Karlsruhe Institute of Technology

Constraints on Transport Models for Galactic Cosmic Rays and their Implications for the Anomalous Positron Abundance

Simon M. Kunz

Zur Erlangung des akademischen Grades eines
DOKTORS DER NATURWISSENSCHAFTEN
an der Fakultät für Physik des Karlsruher Instituts für Technologie

genehmigte

DISSERTATION

von

Dipl. Phys. Simon Michael Kunz
aus Karlsruhe

Tag der mündlichen Prüfung: 14.11.2014

Referent: Prof. Dr. W. de Boer
Institut für Experimentelle Kernphysik

Korreferent: Prof. Dr. G. Quast
Institut für Experimentelle Kernphysik

I declare that I have developed and written the enclosed thesis completely by myself, and have not used sources or means without declaration in the text.

Karlsruhe, October 27, 2014

.....

Simon M. Kunz

Contents

List of Figures

List of Tables

List of Abbreviations

AGN	Active Galactic Nuclei
CMB	Cosmic Microwave Background
CR	Cosmic Ray
DM	Dark Matter
ICRC	International Cosmic Ray Conference
ISM	Interstellar Medium
ISRF	Interstellar Radiation Field
ISS	International Space Station
LAT	Large-Area-Telescope
LB	Local Bubble
LHC	Large Hadron Collider
LIS	Local Interstellar Spectrum
LOS	Line-of-Sight
MCMC	Markov chain Monte Carlo
MHD	Magnetohydrodynamics
MH	Metropolis-Hastings
MTM	Multiple-Try-Metropolis
MW	Milky Way
Ndof	number of degrees of freedom
NN	Next-Neighbour
PDF	Probability Density Function
PFIII	Proposal Function III
PFII	Proposal Function II
PFI	Proposal Function I
PSR	Pulsar
RM	Faraday Rotation Measure
SM	Standard Model of Particle Physics
SNR	Supernova Remnant
UHECR	Ultra-High-Energy Cosmic Ray

1. Introduction

In 1912 Victor F. Hess measured an increasing ionizing rate with altitude. He concluded that this was due to radiation which had to hit the atmosphere from above [1]. Nowadays, this finding is associated with the discovery of cosmic rays (CR), an energetic radiation reaching the Earth from outer space.
During the last one hundred years great efforts have been made to investigate the characteristics of this radiation including not only its particle composition and energy spectrum, but also its origin and acceleration mechanisms. CR measurements are either performed by balloon-borne or space-based experiments to avoid the disruptive influence of the Earth's atmosphere or by ground-based experiments for which the particles properties have to be reconstructed from the secondary produced particles within the atmosphere. With a share of 99%, the majority of CRs are nuclei, mainly hydrogen and helium nuclei and a small fraction of heavier nuclei. About 1% are electrons and a very small fraction are antimatter particles like positrons and antiprotons. The measured energy spectrum of CRs covers several orders of magnitude in flux and energy. Its slope can be described by a power-law in energy, however, with two conspicuous features known as the *knee* and the *ankle* at which the spectral shape changes, respectively. The knee at $\sim 10^{16}$ eV is assumed to mark the transition from the differently produced galactic to extragalactic CRs. The ankle at $\sim 10^{18}$ eV indicates the existence of a new, extragalactic component that may originate from Active Galactic Nuclei (AGN) [2]. The particles with the highest energies, called *Ultra-High-Energy Cosmic Rays* (UHECRs), reach energies of up to $\sim 10^{21}$ eV and are the particles with the highest energies ever detected. Such particle energies are far above energies current particle accelerators can produce. Therefore, CRs form a unique and important research field in high energy particle physics and resulted in many particle discoveries in the first half of the last century like the positron [3], the muon [4], the pion [5] and the kaon [6].
Speculations about a possible connection between the origin of galactic CRs and Supernovae were already expressed in 1934 by Baade and Zwicky [7]. In fact, the CR luminosity of about $3 \cdot 10^{40}$ erg/s could be explained if galactic Supernovae with an average rate of 2 to 3 explosions per century transfered only about 10% of their initial kinetic energy into CR energy. In 2013 gamma-ray observations with the FERMI-LAT experiment revealed characteristic pion-decay signatures from proton-proton collisions in supernova remnants (SNR) [8]. This detection gave direct evidence that, at least in part, CR protons are produced and accelerated by these objects. The particle acceleration is believed to occur via diffusive shock acceleration induced by a shock front formed by the supersonic shells of SNRs [9]. This process, known as *first-order Fermi acceleration*, is based on the reflection

of charged particles on irregularities in the magnetic field. The reflection results in multiple crossings of the shock front whereby the particles gain more energy each time they cross the shock front. The energy spectrum of particles accelerated in this way follows a power-law in energy and corresponds to the initial particle spectrum before it is modified by propagation processes.
The propagation of charged, galactic CR particles is dominated by their scattering off irregularities in the galactic magnetic field which leads to a random-walk-like movement and a confinement in the Galaxy [10]. This process can be described by a diffusion equation. On their way through the Galaxy the particles additionally lose energy by different energy loss mechanisms, may be reaccelerated by the interaction with magnetohydrodynamical Alfvén waves and may be transported by galactic winds which can blow the particles out of the Galaxy. Furthermore, particle loss and production mechanisms by fragmentation and spallation occur. CR propagation models aim to model these processes and to predict the expected particle fluxes at Earth. These models use realistic distributions of the CR sources, the interstellar gas and the interstellar radiation field.
In 2008 the PAMELA detector revealed an anomalous positron abundance in the cosmic radiation [11] which attracted a lot of attention to the field of CR propagation. While SNRs account for most of the CRs in the Galaxy, they do not produce essential amounts of antimatter and the ratio of positrons to electrons produced in SNRs was found to be only a few percent [12]. In the standard picture of CR propagation positrons are pure *secondary* CRs, produced by interactions of hydrogen and helium nuclei in the gaseous environment of the Galaxy. However, the expected amount of secondary positrons and the energy spectrum are not adequate to explain the rise in the positron fraction, defined as $N_{e^+}/(N_{e^+} + N_{e^-})$, with energy as measured by PAMELA and the existence of a new source of primary positrons is demanded.
Many explanations for the unexpected positron abundance have been proposed in the literature. The most prominent ones are certainly nearby pulsars as astrophysical objects and the annihilation of dark matter (DM) particles by which high energetic positrons and electrons are expected to be produced. In 2013 first results of the AMS-02 experiment were published, which showed that the positron fraction continued to rise with energy, but with a decreasing slope [13]. In 2014 a new measurement by AMS-02 with higher statistics and up to higher energies became available and revealed, that above ~ 200 GeV the positron fraction is no longer increasing with energy [14]. In addition, measurements of the separate fluxes of electrons and positrons with unprecedented accuracy were published [15]. These data call for a renewed discussion of possible source scenarios for the anomalous positron abundance.
In order to search for new phenomena and to quantify a possible signal from the data a reliable background model, i.e. a precise modeling of the involved transport processes, is of crucial importance. This work focuses on the investigation of CR transport related transport parameters and their implications with special regard to the secondary positron production. Wide ranges of transport parameters are examined by a Markov chain Monte Carlo method and constrained by experimental measurements.
This thesis is organized as follows:

- Chapter 2
  A comprehensive review of CR physics is presented starting from the early discoveries in 1912. The detection techniques used nowadays in balloon-borne, space-based and ground-based experiments are discussed. The present state of knowledge about the properties of the cosmic radiation itself and about the sources and acceleration mechanisms is reviewed. The connection between CRs and indirect DM searches by the detection of DM annihilation products is discussed in chapter 2.5.

- Chapter 3
  This chapter introduces the basic concept of CR propagation and the relevant transport processes. The diffusion equation used for modeling CR propagation is derived and an extended, full transport equation in which energy losses, fragmentation, spallation, radioactive decays and secondary particle production are considered is discussed [16]. The properties of our own galaxy which are relevant for CR propagation include the SNR source distribution, the gas distribution, the interstellar radiation field (ISRF) and the galactic magnetic field for which realistic models will be shown. A numerical solution to the transport equation within the environment of the Milky Way (MW) is available from the publicly available software packages `GALPROP` and `DRAGON`. Both codes are quite successful in describing many of the observed CR energy spectra.
  A subchapter is dedicated to important observables which are sensitive to the applied transport processes, i.e. to the transport parameters which are partially only very poorly known and not accessible by theoretical considerations. Of particular importance are so-called secondary-to-primary ratios and ratios of radioactive isotopes which allow to constrain the CR interaction rate and the CR escape time. CR interactions also include photons as by-products which are not deflected by the magnetic field and directly point back to their point of origin. Therefore, measurements of the synchrotron and gamma-ray emission play an important role since they contain information about the CR densities far away from the solar system.

- Chapter 4
  For the investigation and constraining of CR transport parameters a Markov chain Monte Carlo (MCMC) method is developed and used in combination with the `DRAGON` package to efficiently sample a large amount of transport parameters with widely chosen limits. The predictions of different sets of transport parameters are compared to most up-to-date measurements of locally observed nuclei spectra and ratios. Compared to leptons which suffer from large energy losses, nuclei have large propagation lengths of the order of kpc and the parameters to be determined correspond to global and averaged ones throughout the Galaxy. This analysis focuses on the preferred, allowed and excluded parameter values, the correlations between the involved parameters and the implications of the resulting degenerated solution. Special importance is given to the investigation of the role of the particular observables usually used for constraining CR transport parameters.

- Chapter 5
  The obtained models, as derived in the previous chapter, are used to predict the expected secondary positron production and the transport related uncertainty. For a correct estimation of synchrotron induced energy losses the parameters of the magnetic field parameterization are tuned to synchrotron foreground maps of the 9-year data of the WMAP experiment. Furthermore, different cross sections for the positron production as proposed in the literature are compared and the influence of the energy densities of the ISRF and the magnetic field on the expected positron production is discussed. The derived model and its uncertainty are used as a background model for the determination of the demanded primary positron contribution for which new AMS-02 lepton lepton data are used. Finally, the potential positron flux from nearby pulsars and from DM annihilation are investigated and it is checked to which extent these explanations can account for the made observations.

- Chapter 6
  This chapter is dedicated to the diffuse, galactic gamma-ray emission which arises from hadronic and leptonic interactions of CR particles with the interstellar gas and the interstellar radiation field. Data collected during almost four years of observa-

tion by the FERMI-LAT experiment are compared to models derived in the previous chapters. Known discrepancies of the expected gamma-ray emission predicted by models optimized to match locally measured observables are addressed. These include the absolute normalization and the spectral shape of the mostly dominating pion decay induced gamma-ray emission. In addition, the predicted underlying CR density distribution shows a too soft radial gradient, commonly known as the *soft gamma-ray gradient problem* [17], [18]. It is shown to which extend basic transport models can solve these discrepancies.
In the very last chapter the influence of local structures on the proton density and the gamma-ray emission is investigated. Our Sun resides in the so-called *Local Bubble*, a low density region in which the density is approximately one tenth of the average density of the interstellar material [19]. Its origin is believed to be related to multiple supernovae explosions within the past ten to twenty million years [20]. Such a structure may have far reaching implications on the transport of CRs and basic concepts are presented.

2. Cosmic Rays

2.1. The History of Cosmic Rays - Discovery and Exploration

Around the year 1900 the observation of the ionization of gas contained in closed vessels arose the question, whether the ionization could be fully explained by radioactive radiation coming from the Earth, from the vessel itself and from emanations in the gas. To answer this question the Austrian-American physicist Victor F. Hess undertook balloon flights and found in 1912, that the ionizing rate increased with altitude and was several times higher at altitudes of about 5 km than at sea level. He was able to exclude a possible radiation from the Sun by balloon flights during a near-total eclipse in which the moon blocked much of the Sun's visible radiation. Hess concluded, that an ionizing radiation was hitting the Earth from outer space [1]. This was the discovery of CRs and brought him the Nobel Price in physics in 1936. It was shared with Carl Anderson for the discovery of the positron. It took another 15 years until other explanations for the increase, like a significant amount of radioactive radiation in the upper atmosphere, could be excluded: It was proven, that the measured radiation experienced much less absorption than gamma-rays from radioactive elements. During the following years every effort was made to investigate what CRs actually are. In 1927 the latitude dependence of the CR induced ionization was measured and a geomagnetic effect was discovered: The trajectories of incoming charged particles are deflected by the Earth's magnetosphere at different latitudes. As a result it could be shown that primary CRs are charged particles and further investigations during 1930 to 1945 proved, that primary CRs are predominantly protons. In 1930 Bruno Rossi noticed that once in a while his equipment was struck by extensive showers of particles. Even if several apparatuses were placed at large distances to each other, the showers were observed in coincidence in each of them [21]. It was Pierre Auger in 1937 who investigated these extensive showers of particles and he concluded that high energetic primary CR particles interact with air nuclei in the atmosphere, initiating a cascade of secondary interactions that yield a large shower of electrons, photons and other particles [22]. By observations with nuclear emulsions carried by balloons to near the top of the atmosphere in 1948 it was found that the number of relativistic electrons does not exceed $\sim 1\%$ and that CRs contain nuclei of a whole series of elements with approximately 10% helium and 1% heavier nuclei such as carbon and iron [23]. Around the year 1950 the synchrotron nature of the cosmic radio emission was established and it became possible to obtain information on the CR electron component in the Galaxy, far away from the Earth. This linked the CR science to astrophysics and astronomy and the connection between radio astronomy and CRs was no longer under dispute.

In 1949 Enrico Fermi considered CRs as a gas of relativistic particles moving in the dynamic interstellar magnetic fields. The particles may be reflected by the fields either gaining or losing energy, depending on whether a magnetic irregularity (a *magnetic mirror*) is approaching or departing [24]. This kind of acceleration process became known as *Fermi acceleration* and its description was a milestone in understanding CR acceleration mechanisms. Speculations about CR sources were already published in 1934 by Baade and Zwicky [7], who related the appearance of supernovae to the generation of CRs. From then on a variety of potential sources were discussed, including active galactic nuclei, quasars, and gamma-ray bursts.
During the recent decades CR astrophysics could be additionally researched by the development of gamma astronomy. More and more detailed information about the gamma-ray sky could be obtained by the missions COS-B (1975), EGRET (1991-2000) and FERMI (since 2008), that allow to trace CR interactions within the Galaxy. Sophisticated particle detectors for investigating CRs at ground-level, in the atmosphere and space were built to determine the properties of the cosmic radiation in greater detail. Beside Ultra-High-Energy Cosmic Ray (UHECR), also the low energy region is quite interesting, since low fluxes of secondary produced particles like antiprotons and positrons may reveal signals of annihilating Dark Matter (DM) particles. In 2008 the PAMELA detector revealed an anomalous positron abundance in the cosmic radiation [11] which attracted a lot of attention to this field. In 2013 data from the Large-Area-Telescope (LAT) of the FERMI satellite revealed by observations of neutral pion decays, that supernovae are CR sources [8]. However, they may not produce all CRs and the question about CR sources is still under investigation. Especially the sources and acceleration mechanisms of UHECRs with energies above 10^{18} eV, whose majority is not produced within the Galaxy, are subject of current scientific research. For this purpose sophisticated detector systems have been developed and built. For the next couple of years the AMS-02 detector, the FERMI Gamma-Ray Space Telescope and the Pierre-Auger-Observatory on ground will remain the flagships for CR measurements.

2.2. Detection Techniques for Cosmic Rays

CRs can be detected and measured by interactions with matter, magnetic fields and radiation. A direct measurement of primary CRs requires detectors in the upper atmosphere or in space, since the atmosphere is shielding the primary CRs. However, balloon-borne and space-based experiments are limited by their size, i.e. by their effective detection area of the order of m^2, and are therefore only suitable for measurements in the low energy region with high fluxes of about 1 particle/m^2/s. CRs with higher energies but low fluxes of about 1 particle/m^2/yr to even 1 particle/km^2/century can only be measured indirectly by ground-based experiments with large detection areas of the order of 1000 km^2. The Earth's atmosphere is used as a natural calorimeter in which large cascades of secondary particles are induced by primary CR particles. The properties of the primary CR particle have to be reconstructed from the measured secondary particles. Table 2.1 shows different energy ranges typically covered by ground-based, balloon-borne and space-based experiments.
The following chapters will disclose more details on the different detection techniques and will highlight the technological advances by means of current experiments.

Table 2.1.: Typical energy ranges covered by ground-based, balloon-borne and space-based experiments.

Detection method	Energy Range (GeV)
Space-based	10^{-1} - 10^{3}
Balloon-born	10^{2} - 10^{7}
Ground-based	10^{6} - 10^{12}

2.2.1. Ground-based Experiments

Ground-based experiments measure secondary particles produced by interactions of primary CR particles with atoms in the atmosphere. If a high energetic particle strikes the top of the Earth's atmosphere billions of secondary particles including hadrons, electrons, photons and muons are created. They spread and create a forward moving plane of particles, a so called *air shower*, whose intensity is the highest near the axis, see figure 2.1. The atmospheric depth, where the number of particles reaches its maximum is called *shower maximum* X_{max} (g/cm^2). Depending on the initial particle type electromagnetic cascades by gamma-rays, electrons and positrons or hadronic cascades by nuclei and hadrons are induced. In electromagnetic cascades each photon creates an electron-positron pair after a typical length d, and each electron above a critical energy of about 85 MeV loses half of its energy per length by radiating bremsstrahlung. Electrons below the critical energy will be absorbed by the atmosphere. Nuclei and hadrons mainly produce mesons, like pions $\pi^{0,\pm}$ and kaons $K^{0,\pm}$. In each interaction about one third of the energy is allotted to neutral pions, which immediately decay into photons and stimulate an electromagnetic cascade. The other two third of the energy are alloted to charged pions, which decay into muons. When passing through the atmosphere photons in the ultraviolet frequency band are created by the fluorescence effect and can be detected in water tanks at ground level via Cherenkov radiation. If several of these water Cherenkov detectors are penetrated, the direction of the primary CR can be reconstructed by basic geometrics: The densities in the affected detectors allow to determine the longitudinal axis point and the particle's energy and the time differences the angle of the axis. For a precise reconstruction of the properties of air showers Monte-Carlo based air shower simulations are used, e.g. CORSIKA [25].

The **Pierre-Auger-Observatory**, located in the Pampa Amarilla in Argentina, is the largest UHECR detector in the world. It currently consists of 1600 such water Cherenkov detectors creating a detection area of about 3000 km^2. Each water detector uses three large photomultiplier tubes to detect the Cherenkov radiation. They are arranged in groups of four in different sized triangular ground patterns. In addition, 24 fluorescence detectors (optical telescopes) are installed to measure the photons in the ultraviolet frequency band. They use faceted observation, similar to a fly's eye, to produce pixeled pictures at high speed. In fact, the Pierre-Auger-Observatory is the first experiment that combines ground detectors and fluorescence detectors allowing a cross-calibration and a reduction of systematic effects. The work on several upgrades is ongoing and includes three additional fluorescence detecting telescopes (HEAT - High Elevation Auger Telescopes), two higher-density nested arrays of surface detectors combined with underground muon counters (AMIGA - Auger Muons and Infill for the Ground Array) and a prototype radio telescope array for detecting radio emission from the shower cascade in the frequency range 30-80 MHz (AERA - Auger Engineering Radio Array).

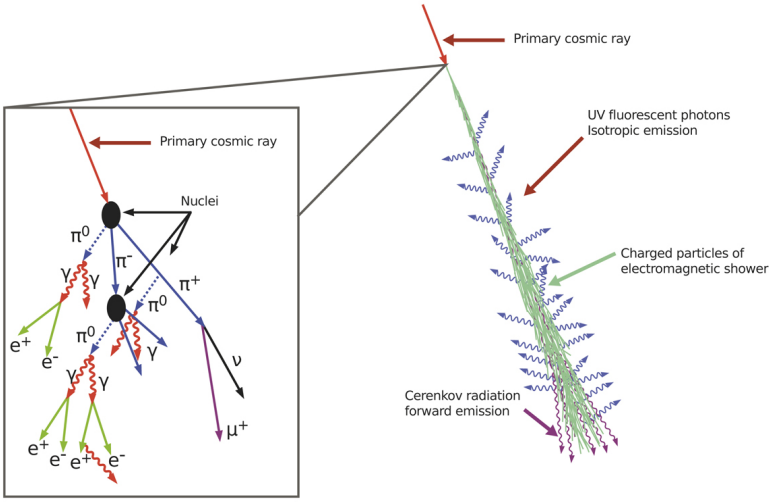

Figure 2.1.: Illustration of an air shower induced by a primary cosmic ray. Fluoresence light and Cherenkov radiation are used by the Pierre-Auger-Observatory to reconstruct the primary CR's properties like its energy and its arrival direction. Figure taken from [26].

2.2.2. Balloon-borne and Space-based Experiments

Balloon-borne and space-based experiments allow the direct measurement of CR particles without the disruptive influence of the atmosphere. However, their effective detection area is limited in terms of financial and technical feasibilitiy. In addition, compared to space-based experiments that have once brought in space relativley large exposure times of several years to decades, balloon-borne experiments suffer from limited flying times of only a few weeks and have to be repeated to collect a sufficient amount of data. These kind of experiments are therefore only suitable for measurements of relatively low energetic CRs with energies of 10^{-1} to 10^{7} GeV with high fluxes. However, CRs with energies up to 10^{3} GeV are believed to be almost exclusively of galactic origin and are therefore of special interest for the investigation of propagation processes of galactic CRs.
In order to measure the particles properties like their mass, momentum, energy and charge, sophisticated detector systems have been developed and built. Typical detector systems include calorimeters, emulsion chambers, scintillators, tracking devices, Cherenkov detectors and transition radiation detectors.

In the following three currently operating detector systems, whose data are used in this work, will be briefly discussed: The CREAM balloon experiment, the LAT of the FERMI satellite and the AMS-02 detector installed on the International Space Station (ISS).

The **CREAM** (**C**osmic **R**ay **E**nergetics and **M**ass) experiment was designed to measure CR elemental spectra during a series of ultra-long duration balloon flights. Up-to-date six flights above 38 km altitude and of several weeks duration between 2004 and 2010 were successfully undertaken. The three main components of the system are [27]

- a Timing Charge Detector, which measures the yield of light produced by the particle in a plastic scintillator. The light yield is a function of the particle charge and velocity;
- a Transition Radiation Detector, in which transition radiation is produced, when a charged particle passes through the boundary of two different media. The signal is a function of the charge and the Lorentz factor γ of the particle;

- a calorimeter, in which a particle initiates a shower and deposits its energy. From the energy deposit the particle's inital energy is determined.

The total weight of the detector system, an important quantity for any balloon payload, is only 1143 kg. Its main scientific achievements include measurements of the energy spectra and relative abundances of CR nuclei at high energies.

The **FERMI-LAT** was designed for measurements of gamma-rays. It was launched in June 2008 and is from that time on measuring the gamma-ray sky with a formerly unprecedented accuracy. Compared to its scientific achievements the detector system is extraordinary simple. The detection principle is based on electron-positron pair conversion. If a photon hits one of the thin tungsten foils at the top of the detector electron-positron pair conversion can occur and the charged particles pass through interleaved layers of silicon strip detectors. These alternate in the x and y direction and the induced signals in different layers allow to track the direction of the inital photon. At the lower edge of the detector the particles deposit their energy in a cesium iodide calorimeter and the initial photon energy can be reconstructed. A discrimination of the relatively rare gamma-rays from charged cosmic rays is accomplished by a plastic anticoincidence detector on top of the instrument, in which charged particles entering the detector cause a flash of light. Figure 2.2 shows a cutaway of the 2789 kg weighting detector. The instrument stands out due to a wide field of view of 20% of the sky, an angular resolution of a few hundredth of a degree for the highest-energy photons and about 3 degrees for 100 MeV photons. Its effective detection area is about 7000 cm^2 at 1 GeV, decreasing with lower and higher energies.
Although the FERMI satellite has no onboard magnet, the collaboration was able to measure the CR electron and positron spectra, as well as the positron fraction. They distinguished the two oppositely charged particles by the shadow of the Earth, and its offset direction for electrons and positrons due to the geomagnetic field. At energies below ~ 10 GeV, a significant fraction of the incoming particles are deflected back to interplanetary space by the magnetic field, known as the geomagnetic cutoff. The value of the geomagnetic cutoff rigidity depends on the detector position and viewing angle. In addition, the east-west effect caused by the Earth's geomagnetic field results in a region of particle directions from which positrons can arrive, while electrons are blocked and vice versa. The measurements derived by using these naturally discriminating mechanisms are not very precise, but the anomalous positron abundance that was previously measured by PAMELA could be confirmed [28]. The scientific achievements of the FERMI-LAT cover a wide range of fields, including the discovery of new radio and gamma-ray pulsars, the discovery of the *fermi bubbles* and the assurance that SNR are sources and accelerator for CRs, to mention only a few.

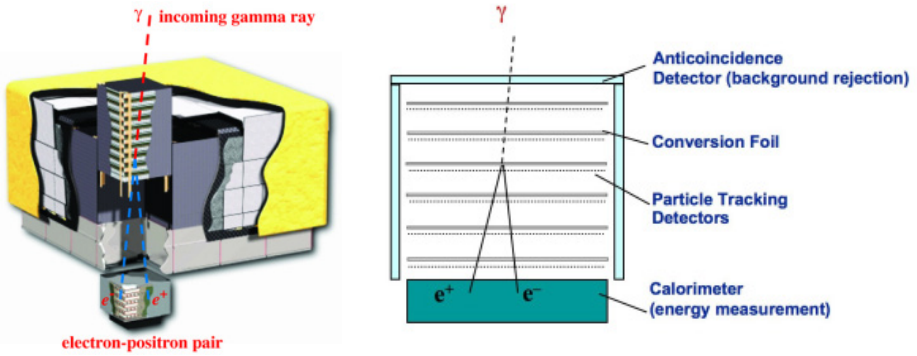

Figure 2.2.: Photon detection principle of the FERMI-LAT. Shown is a cutaway of the detector by which the simple detection principle becomes apparent. After pair-conversion of the photon the tracks and the energy of the electron-positron pair are measured and the arrivial direction and the photon energy are reconstructed. The detector is only 0.72 m deep and 1.8 m x 1.8 m square. Figures taken from [29].

The **AMS-02** (**A**lpha **M**agnetic **S**pectrometer) is a state-of-the-art, general purpose, high energy particle detector mounted on the ISS. Its main purposes are the search for antimatter, DM and the extension of the knowledge of CR properties in general. It was transported to the ISS in May 2011 by the last flight of the Endevaour Space Shuttle and will be operated until the end of the ISS's operating life time, currently confirmed until 2024. Compared to current competitive detectors the AMS-02 detector outstands by its redundant particle identification methods. By a combination of the measurements of different types of subdetectors the CR properties up to TeV energies can be reconstructed with an unprecedented accuracy. These include the sign and absolute value of the charge, the energy, the mass and the momentum. In contrast to FERMI, the sign of the charge can be directly measured by a permanent magnet mounted in the detector's core. The main subdetectors from top to bottom, as illustrated in figure 2.3, are

- a Transition Radiation Detector, which uses the effect of transition radiation for separating particles according to their mass.
- A Time-of-Flight detector, composed by two scintillation planes above and below the permanent magnet, allows the measurement of the velocity, the direction and the charge of the particle and also acts as a trigger system for charged particles.
- A Tracker consisting of seven silicon planes inside the magnet volume and two planes outside. By the measurement of the particle deflection its rigidity and the sign of the charge can be reconstructed.
- An Anti-Coincidence-Counter, that vetoes particles entering the detector laterally.
- A Ring-Imaging-Cherenkov-Detector, which uses Cherenkov radiation for the measurement of the velocity and the charge.
- An Electromagnetic Calorimeter measures the energy of electrons, positrons and photons by an induced electromagnetic shower and the deposited energy. Energies of nuclei have to be inferred from the rigidity measurement of the Tracker.

One of the main challenges for measurements of the low abundant positrons and antiprotons is the achievement of a sufficiently large rejection power to reduce the number of misidentified particles. By exploiting the redundant measurements of the Transition Radiation Detector and the Electromagnetic Calorimeter the AMS-02 detector is able to efficiently supress misidentified protons in the positron sample with a resulting positron

purity above 99% [30].
The scientific achievements up-to-date include precision measurements of the positron fraction in the energy range from 0.5 to 500 GeV [14], measurements of the lepton sum flux ($e^+ + e^-$) up to 1 TeV [31] and separate electron and positron fluxes up to 700 GeV and 500 GeV, respectively [15]. The anomalouse rise, as previously measured by PAMELA and confirmed by FERMI, was measured with unprecedented accuracy allowing a more precise determination of the slope. It was found that it steadily increases from 10 GeV on, however with a decreasing slope starting at $\sim$ 50 GeV. The most-up-to-date measurements indicate a drop of the positron fraction at high energies. Measurements at higher energies are so far limited by low statistics but the trend will be revealed by additional measurements in the future. So far, only 15% of the total expected data are available. The positron fraction revealed no fine structures and no anisotropies in the positron-to-electron ratio were observed [13]. Preliminary results for the spectra of protons, helium and B/C were presented at the International Cosmic Ray Conference (ICRC) in 2013. The analyses are ongoing and are currently finalized for publication [32].

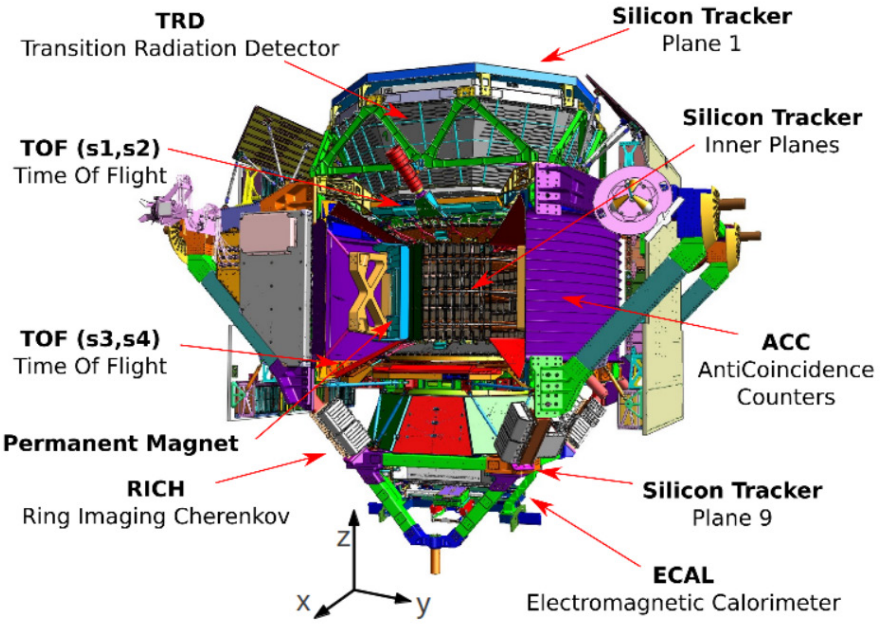

Figure 2.3.: Subdetector system for particle identification of the AMS-02 experiment. The particle's properties are exploited when traversing from the top to the bottom of the 8.5 t weighting detector system. Figure taken from [30].

2.3. The Composition and Energy Spectrum of Cosmic Rays

This chapter is dedicated to the current knowledege of the CR composition and the energy spectrum. CRs include essentially all elements in the periodic table, as well as electrons and positrons. At low energies they mainly consist of protons and light elements with only a small fraction of about 1% of electrons. The fraction of heavier elements like oxygen, magnesium and iron increases significantly with higher energies. The overall nuclei abundances are about 90% protons, 9% helium and 1% of other elements. At about 100 GeV/nucleon (1 PeV/nucleon) the abundances are approximately 56% (15%) protons, 24% (33%) helium and 20% (52%) other elements [33]. The differential energy spectra of different CR species are shown in figure 2.4.
Figure 2.4 shows a compilation of data in a wide energy range complement by experiments on the ground, in the upper atmosphere and in space. The typical and partially

redundant energy ranges covered by theses different kinds of experiments are assigned. The overall particle flux drops dramatically by several orders of magnitude with higher energies and can be well described by power-law distributions. However, the overall spectrum shows two noticeable kinks (or breaks), at which the slope of the sprectum changes, respectively. Their origin is assumed to arise from differently produced CR populations. The first break at an energy of $\sim 10^7$ GeV is called *the knee* and is commonly believed to mark the beginning of the end of CRs with galactic production mechanisms. A transition between galactic CRs produced in e.g. SNRs and extragalactic CRs produced in e.g. Active Galactic Nuclei (AGN) is believed to occure, leading to the change of the slope. Alternative explanations include different energy loss mechanisms below and above the knee, new particle interactions characteristics above 1 TeV/nucleon, a change in the propagation mechansisms or a significant change in the elemental composition [34]. The second break at an energy of $\sim 10^9$ GeV is called *the ankle* at which the spectrum flattens. Only very little is known about the origin of CRs between the knee and the ankle. There seems to be a gap between the top end of galactic and the lower end of extragalactic CRs [35]. Also not much is known about the sources of UHECRs above the ankle. Promising source candidates will be discussed in the next chapter. At an energy of $5 \cdot 10^{10}$ GeV, the so called *Greisen-Zatsepin-Kuzmin limit* (GZK), the theoretical upper limit on the CR energy is reached. By interactions of CRs with the Cosmic Microwave Background (CMB) over long distances pions are produced via the Δ-resonance. Extragalactic CRs with energies larger than the threshold energy, travelling over distances larger than 50 Mpc should never be observed at the Earth and the visible horizon is limited to the GZK-horizon. Observations of CRs above this limit were made by the AGASA experiment. Although not fully understood possible explanations invoke an instrumental error, local sources within the GZK horizon and a circumvention of the GZK limit by heavier nuclei [36].

The arrival direction of CR particles may reveal information about their origin and is therefore closely investigated by almost every CR experiment. The charged particles are, however, deflected by magnetic fields leading to a distorted propagation path and a corresponding loss of information about their origin. Only high energetic protons and nuclei can arrive at Earth without a significant deflection by interplanetary magnetic fields. A measure for the deflection of a particle is the ratio of its gyroradius in the field and the scale of propagation. The gyroradius of a relativistic proton is given by

$$r_g = 3 \cdot 10^9 \gamma (B/10^9 \mathrm{T})\,\mathrm{m}, \tag{2.1}$$

with the Lorentz factor $\gamma = \sqrt{1 - v^2/c^2}$ and the magnetic flux density B in Tesla. A flux density of $B = 10^9$ T and protons with 10^{12} eV ($\gamma = 10^3$) give gyro-radii of 20 Astronomical Units (1 AU corresponds to the distance Sun-Earth). Particles with high energies are therefore more likely revealing information about their arrival direction at the solar system. In fact, the distribution of arrival directions of particles with energies of 10^{13} - 10^{14} eV was found to be remarkably uniform. Anisotropies, studied by Hillas in 1984, have only been detected at a level of 0.1% [37] , see figure 2.5. Recently, the ICE-Cube collaboration studied the large-scale anisotropy of TeV particles by the relative intensity of the cosmic-ray-induced muon flux [38], [39]. They found the arrival direction to be anisotropic with a first-harmonic amplitude of $A_1 = (6.4 \pm 0.2\,(stat.) \pm 0.8\,(sys)) \cdot 10^{-4}$ [38]. However, the origin of the large-scale anisotropy remains unclear. The Compton-Getting effect, by which an anisotropy is induced due to the relative motion of the solar system around the Galactic Center, was found to be not the primary source for the observed anisotropy. An ICE-Cube analysis of small-scale anisotropies, that could be associated to CR sources, exhibits several localized regions, in which significant excesses and deficits

in the CR intensities with median energies of 20 TeV were found [40]. The scales of the regions were found to lie between 15 degrees and 30 degrees and studies, in which the excesses are tried to be associated with possible sources, are ongoing. One of the two most significant excesses coincides with the location of the Vela pulsar at a distance of about 300 pc. However, the gyroradius of 10 TeV protons in a magnetic field of the order of μG is approximately only 0.01 pc, many orders of magnitude smaller than the distance to Vela. Therefore, charged particles from Vela will have lost all their directional information when arriving at the Earth. Over the next few years a large amount of collected events with the ICE-Cube detector will allow to study possible time dependencies of the anisotropy and may reveal additional information on small-scale anisotropies.
In 2007, results from the Pierre-Auger-Observatory showed a strong correlation between the directions of 27 events above $6 \cdot 10^{19}$ eV and the locations of AGNs, lying at distances to Earth within $\sim$ 75 Mpc [2]. The hypothesis of an isotropic distribution of these CRs could be rejected with a confidence level of at least 99%.

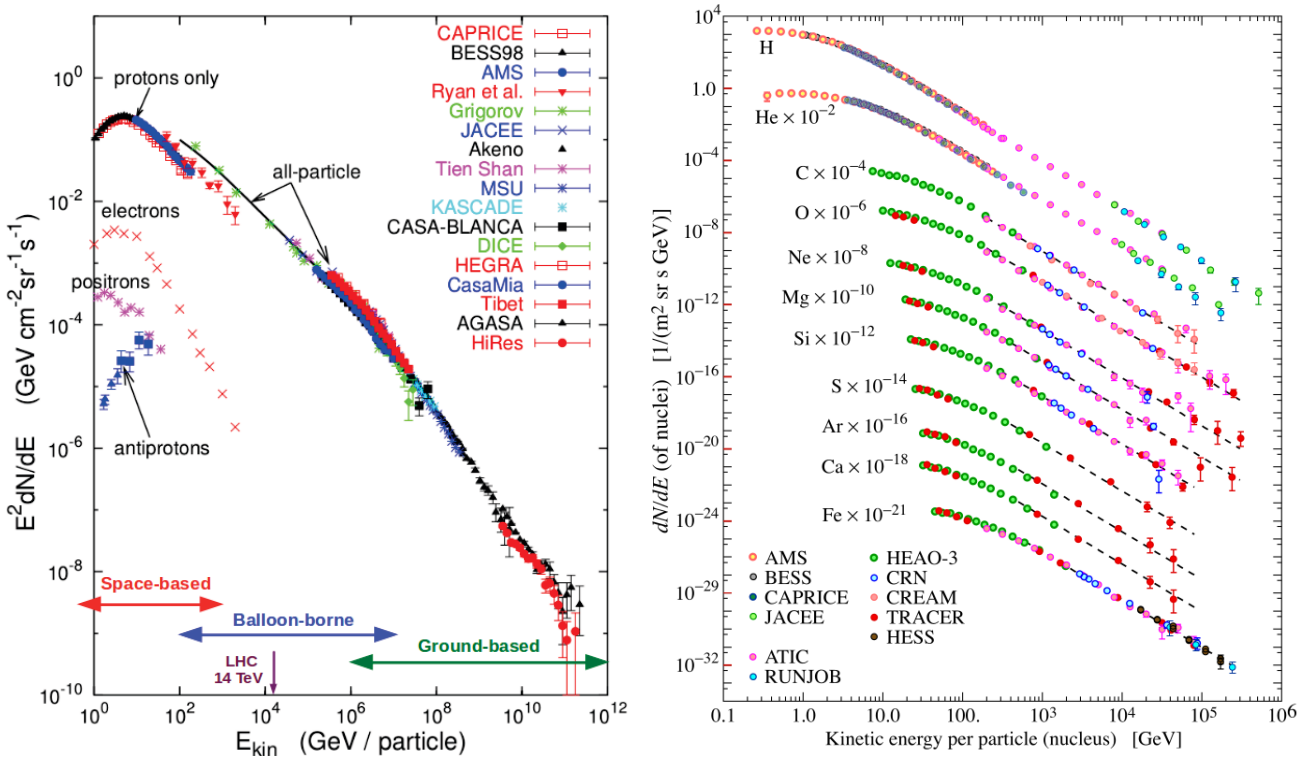

Figure 2.4.: The energy spectrum and abundances of cosmic rays. **Left:** In the energy spectrum two features at energies of $\sim 10^7$ and $\sim 10^9$ GeV are present, known as *the knee* and *the ankle*. They are believed to originate from transitions between differently produced CR populations. The GZK-Cutoff, a theoretical upper limit on the energy CR particles can reach, is at $5 \cdot 10^{10}$ GeV. **Right:** The abundancies of several CR species shown as differential energy spectra. The scaling factors used to display the spectra are shown in the figure. Figures taken from [35] (modified) and [41].

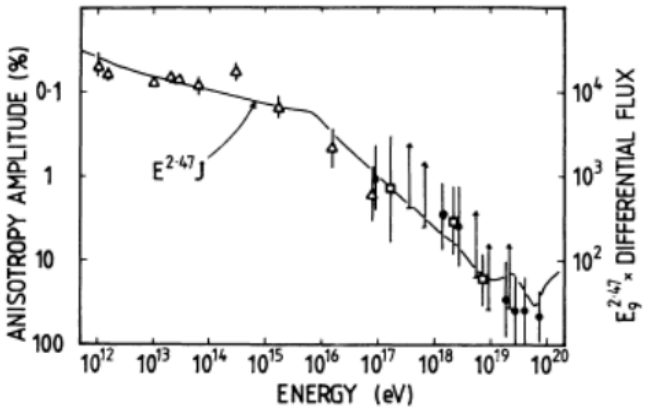

Figure 2.5.: Arrival directions of Cosmic Rays. Shown is the amplitude of the anisotropy in the distribution of CR arrival directions as a function of energy. A best-fitting sine wave has been fitted to the data and the percentage amplitude of the harmonic was calculated. The solid line represents the shape of the differential CR spectrum as used by Hillas in 1984. Figure taken from [37].

2.4. Sources and Acceleration of Cosmic Rays

The previous chapter already emblaced, that the arrival direction of CRs could reveal information about their possible sources. In this chapter possible candidates for galactic and extragalactic CRs sources and their theoretical and experimental motivations will be reviewed. Also the CR acceleration mechanisms, that are strongly connected to the sources, will be emphazised.

2.4.1. Galactic Cosmic Rays

CRs with energies of up to 10^3 GeV are believed to be almost exclusively of galactic origin. The most promising candidates from the theoretical and experimental point of view are SNRs. Speculations about a connection between Supernovae and CRs were already remarked in 1934 by Baade and Zwicky [7]. In fact, the energy content of CRs of about $3 \cdot 10^{40}$ erg/s could be explained if Supernovae with an average rate of 2 to 3 explosions per century within the Galaxy would only transfer about 10% of their initial kinetic energy of $3 \cdot 10^{41}$ erg/s into CR energy. SNRs are the remainder of Supernovae explosions and provide an efficient acceleration mechanisms by a supersonic expansion of a sphere of hot gas into the Interstellar Medium (ISM).

The dynamical evolution can be divided into four stages [10]:

(i) The energy liberated in the Supernova is deposited in the envelope of the star which is heated to high temperatures of millions of Kelvin and ejected with velocities of $(10-20) \cdot 10^3$ km/s. The expanding gas remains undecelerated as long as the mass of the interstellar gas swept up in the expansion is much less than the mass of the ejected gas. The temperature in the sphere decreases adiabatically since the sphere expands. During the supersonic expansion a shock front is formed ahead the expanding sphere.

(ii) As soon as the swept-up mass becomes larger than the ejected mass a deceleration occurs that significantly changes the temperature, density and pressure distributions inside the sphere. The outer shells of the sphere are decelerated first so that the material in the inner parts of the sphere can catch up and increase the matter density at the boundary. This comes along with a reheating of the matter located at the outer layer and the deceleration actually feeds the energy content of this layer by converting kinetic energy.

(iii) After further expansion the temperature behind the shock front drops below 10^6 K and cooling by line emission of heavy ions becomes important. The resulting compression to preserve pressure balance at the shock front increases and the shell forms a dense snowplough.
(iv) The expansion velocity becomes subsonic and the SNR is either dispersed by random motions in the ISM or, in case of a former massive star with more than eight solar masses, collapses into a neutron star.

CR particles are acclerated in the shock front by a mechanism called *diffusive shock acceleration* or *first-order Fermi acceleration*, named by Enrico Fermi who proposed the mechanism in 1949. The more general case of acceleration of particles in the environment of moving magnetized gas clouds without the presence of a shock front is called *second-order Fermi acceleration* or *diffusive reacceleration*. Both Fermi acceleration mechanisms are based on the reflection of charged particles on irregularities in a magnetic field. Magnetized clouds are assumed to move randomly with a velocity V and the particles can stochastically gain energy in these reflections. It is more convenient to treat the basic principle of second-order Fermi acceleration first, before shock front acceleration is discussed.

Second-order fermi acceleration (diffusive reacceleration)

The magnetized cloud is taken to be infinitely massive and its velocity remains unchanged after collisions with particles. The momentum frame of reference is taken to be centered at the moving cloud with velocity V. In this frame the energy of a particle is [10]

$$E' = \gamma_V (E + V\, p\, cos(\theta)), \tag{2.2}$$

with the Lorentz factor of the moving mirror $\gamma_V = (\sqrt{1 - V^2/c^2})^{-1}$ and the angle $\theta \sphericalangle (\vec{V}, \vec{p})$. The x-component of the relativistic momentum is

$$p'_x = p' cos(\theta) = \gamma_V \left(p\, cos(\theta) + \frac{V\, E}{c^2} \right). \tag{2.3}$$

In a collision with a particle the particle's energy is conserved and its momentum in x-direction is reversed: $p'_x \rightarrow -p'_x$. A transformation to the observer's frame gives

$$E'' = \gamma_V (E' + V\, p'_x). \tag{2.4}$$

The change of the particle's energy can be derived by substituting equations 2.2 and 2.3 in 2.4 and exploiting that $p_x/E = v\, cos(\theta)/c^2$:

$$E'' = \gamma_V^2\, E \left(1 + \frac{2\, V\, v\, cos(\theta)}{c^2} + \left(\frac{V}{c} \right)^2 \right). \tag{2.5}$$

An expanding to the second order in V/c gives

$$\Delta E = E'' - E' = E \left(\frac{2\, V\, v\, cos(\theta)}{c^2} + 2 \left(\frac{V}{c} \right)^2 \right). \tag{2.6}$$

Since the particles are randomly scattered the mean increase can be derived by averaging over a random distribution of angles θ. However, there is a slightly larger probability for

head-on collisions in comparison with collisions from behind. For $v \sim c$ the probability is proportional to $\gamma_V(1 + (V/c)\,cos(\theta))$. Averaging over all angles between 0 to π gives the average energy gain per collision:

$$\left\langle \frac{\Delta E}{E} \right\rangle = \frac{8}{3}\left(\frac{V}{c}\right)^2 \tag{2.7}$$

Equation 2.7 is the famous result derived by E. Fermi, in which the average increase in energy is second-order in V/c. The most important characteristic of fermi-accelerated particles is their energy spectrum following a power-law in energy.

First-order fermi acceleration (diffusive shock acceleration)

This acceleration mechanism involves shock waves like supersonic shells of SNRs. A high flux of particles is assumed to be present in front and behind the shock front with velocities much larger than the one of the shock front. Due to diffusive scattering by streaming instabilities or turbulent motions on each side of the shock front, the particles pass through the shock by which they gain small amounts of energy, independent on whether they pass from behind the shock to the front or the other way around. A particle's energy after it passed through the shock is

$$E' = \gamma_V\,(E + p_x V), \tag{2.8}$$

where the x-coordinate is taken to be perpendicular to the propagation of the shock. In case of a non-relativistic shock and a relativistic particle the gained energy is

$$\begin{aligned} \Delta E &= p\,V cos(\theta), \\ \frac{\Delta E}{E} &= \frac{V}{c}\,cos(\theta). \end{aligned} \tag{2.9}$$

The normalized probability distribution $P(\theta)$ of a particle crossing the shock front at angles of $\theta = 0...\pi/2$ is

$$P(\theta) = 2\,sin(\theta)\,cos(\theta)\,d\theta. \tag{2.10}$$

The average energy gain per shock front crossing is then given by

$$\begin{aligned} \left\langle \frac{\Delta E}{E} \right\rangle &= \frac{V}{c}\int_0^{\pi/2} 2\,cos^2(\theta) sin(\theta) d\theta \\ &= \frac{2}{3}\frac{V}{c}. \end{aligned} \tag{2.11}$$

Equation 2.11 shows that the average increase in energy is first-order in V/c. CRs can gain high energies by crossing the shock front many, many times, see figure 2.6. A feature of this mechanism is an energy spectrum following a power-law in energy of the form $N(E) \propto E^{-\alpha}$ with a spectral index of $\alpha \lesssim 2$. Let β be the fractional change of the kinetic energy at each shock front crossing. After n crossings a particle with an initial energy of E_0 will have the energy $E = E_0 \cdot \beta^n$. With the probability P for remaining in the shock front crossing region after each crossing the initial number of particles N_0 is after n crossings reduced to $N = N_0 \cdot P^n$. This results in

$$\frac{N}{N_0} = \left(\frac{E}{E_0}\right)^{\frac{log(P)}{log(\beta)}} \tag{2.12}$$

and leads to a power-law in energy with

$$\frac{dN}{dE} \propto E^{-1+\frac{log(P)}{log(\beta)}} \tag{2.13}$$

and $\alpha = 1 - \frac{log(P)}{log(\beta)}$. It can be shown that $\frac{log(P)}{log(\beta)} \approx -1$ and thus $\alpha \approx 2$. The spectral index can also be associated to the Mach number $M = v_{shock}/v_{sound}$ of the outflowing shock with $\alpha = 2 + 4/M^2$ in case of a mono-atomic gas. Shocks with Mach numbers of the order of $M = 3 - 6$ can account for spectral indices of $\alpha \approx 2.2$ as typically found by modeling of CR propagation processes.

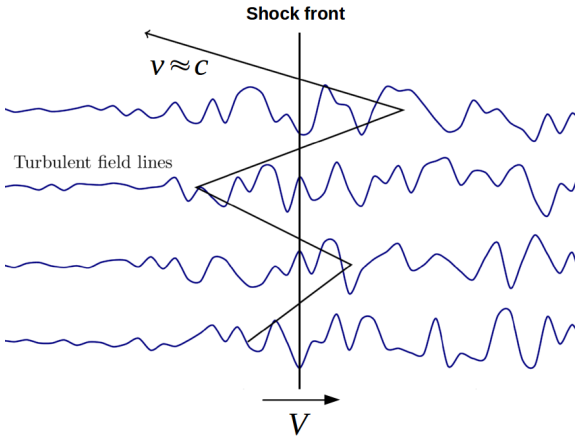

Figure 2.6.: Illustration of diffuse shock acceleration. Each time a particle crosses the shock front moving with V it gains a small fraction of energy proportional to V/c. Figure taken from [42] (modified).

Experimental indications supporting the SNR source hypothesis

Radio and gamma-ray observations of SNRs provide convincing evidence that these are indeed sources of galactic CRs. The energy spectrum of the radio emission was found to be a power-law and was identified with the synchrotron radiation of ultra-relativistic electrons, accelerated by shock waves [43]. Especially in young SNRs the intensity of the radio emission was found to be so high that the energy density of electrons and magnetic fields greatly exceeds values one would expect by compressing the electron flux and magnetic fields in a shock. The conclusion was, that the particles and fields must originate within the SNR itself. X-ray observations of SNRs by the ROSAT observatory revealed shell-like morphologies, that have also been resolved by TeV gamma-ray observations with HESS [44], see fig. 2.7. The observed gamma-ray spectrum up to 100 TeV by HESS gave also direct evidence for the presence of large fluxes of particles with typical CR energies. However, these particles could not be directly associated to electrons or protons. The first evidence came in 2013 when gamma-ray observations with the FERMI-LAT revealed characteristic pion-decay signatures from proton-proton collisions in SNRs [8], as shown in figure 2.8. This detection gave direct evidence that CR protons are accelerated in SNRs, although the expected $1/E^2$ spectrum was not observed and the fits with Bremsstrahlung and a break in the electron spectrum differ not that much. The characteristic pion-decay spectrum in combination with the hard $1/E^2$ spectrum was first observed in the FERMI-LAT data more recently in the star-forming region in the disc [45]. In the star-forming

regions one expects a strong contribution from CRs trapped in sources, since in this case, both the CR density and the gas density are enhanced by large factors.

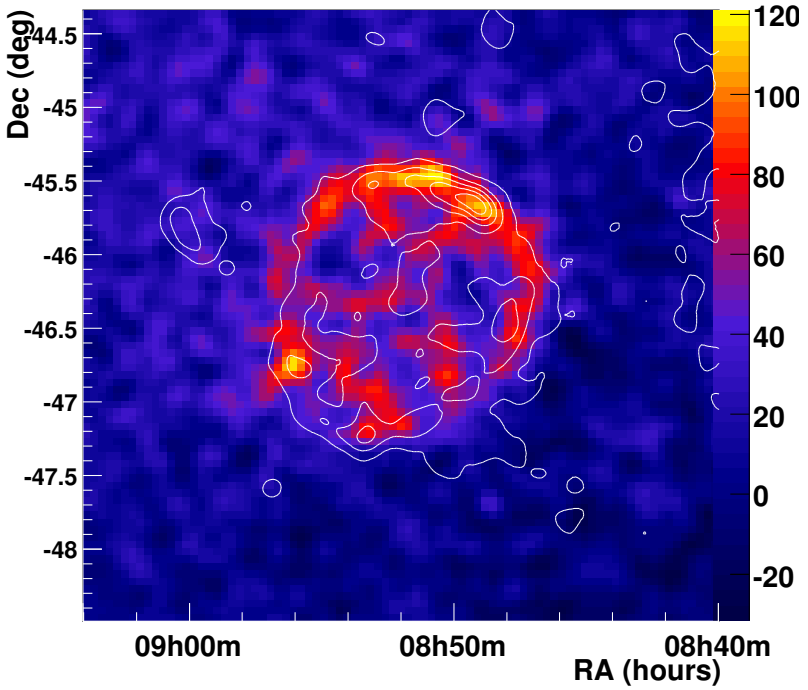

Figure 2.7.: HESS observation of TeV gamma-rays from the SNR RX J0852.0. The morphology exhibits a thin shell similar to features observed in X-rays. Contours of the X-ray emission from ROSAT are superimposed by the white lines. Figure taken from [44].

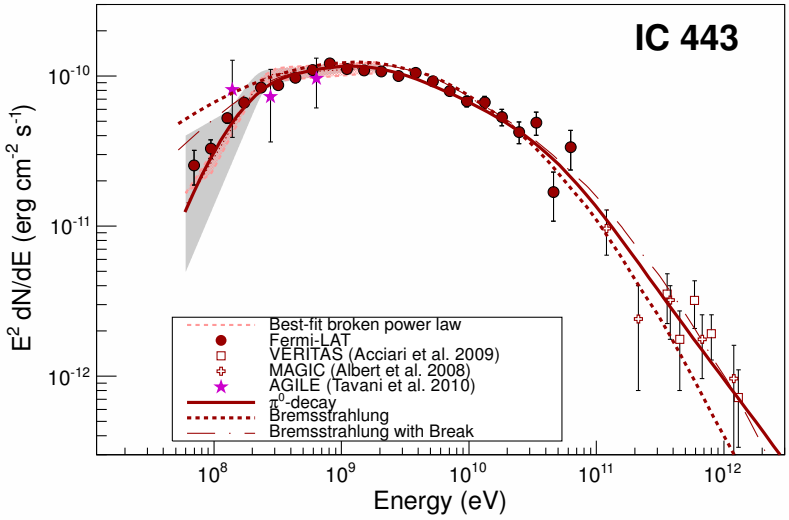

Figure 2.8.: FERMI-LAT gamma-ray measurements of the SNR IC443. Solid lines denote the best-fit pion-decay, dashed lines the best-fit bremsstrahlung and dash-dotted lines the best-fit bremsstrahlung spectra if a low-energy break in the electron spectrum is assumed. The spectral measurements allowed the identification of the π^0 decay features and gave direct evidence for the acceleration of protons in SNRs. Figure taken from [8].

High energy leptons from pulsars

Supernovae explosions of massive stars with more than eight solar masses can result in collapses into neutron stars, so called pulsars. They were accidentially discovered in 1967 by J. Bell and A. Hewish by radio observations of the sky [10]. The most famous example is the *Crab Nebula*, which originated from a supernova explosion of a massive star with an estimated mass of eight to twelve solar masses 7260 years ago.
An evolving neutron star retains at first most of the angular momentum of the former star. However, since its radius is much smaller it is rotating rapidly. The rotational energy generates an electrical field from the movement of the strong magnetic field and leads to the acceleration of protons and electrons on the surface and an emanating beam of electromagnetic radiation from the poles of the magnetic field. The direction of the beam is oriented along the magnetic axis, which does not necessarily coincide with the rotational axis, see figure 2.9. Such a misalignment leads to the typical stable and sharp pulsed emission with periods of milliseconds to seconds as observed in radio and gamma-rays. As a results of the electromagnetic radiation which is extracted from the rotational energy the rotation speed slows down until the mechanism stops after typically 10^5 to 10^8 years.
While conventional SNRs account for most of the CRs in the Galaxy, they do not produce essential amounts of antimatter like positrons or antiprotons. In fact, the ratio of positrons to electrons produced in SNRs was actually found to be only a few percent and the ratio of antiprotons to protons to be only of the order of 10^{-5} [12]. The anomalous rise in the positron fraction gave hints, that essential amounts of positrons and electrons are present, which cannot be explained by conventional SNR sources and the secondary production of positrons [46]. Pulsars are attractive primary source candidates [47]. Particles are initially extracted from the surface by the intense rotation induced electric fields and later transformed into electron-positron pairs through electromagnetic cascading. The electron-positron pairs finally end up as part of the relativistic magnetized wind emanating from the pulsar. However, since electrons and positrons suffer large energy losses due to synchrotron radiation and bremsstrahlung their bigger part must originate at close distances to the Earth of the order of less than 1 kpc. Therefore only nearby pulsars could account for the additional contribution. Estimates for the expected flux exist (see e.g. [47]), but the predictions crucially depend on pulsar parameters that are not well known and only slightly constrained by experimental measurements and theoretical appraisals. Some import properties are the age τ, the spectral index α_p, the spin-down luminosity $\dot{E}$ as a measure for the rate of loss of rotational kinetic energy and the efficiency η by which the rotational energy is transformed to electron-positron pair production. Two characteristic pulsar properties, the pulse period P and its temporal change, denoted as $\dot{P}$, can be measured directly by radio and gamma-ray observations and can be related to some of the pulsar properties [10]:

$$\begin{aligned} \tau &= \frac{P}{(2\,\dot{P})} \\ \dot{E} &= 4\pi I \dot{P} P^{-3} \\ B_s &= \left(\frac{3\mu_0 c^3 M}{80\pi^3 R^4}\right)^{1/2} \sqrt{P\dot{P}}. \end{aligned} \tag{2.14}$$

μ_0 is the constant of permeability, M and R are the pulsar's mass and radius, $I = \frac{2}{5}MR^2$ is the momentum of intertia and B_s the strength of the magnetic field at the surface.

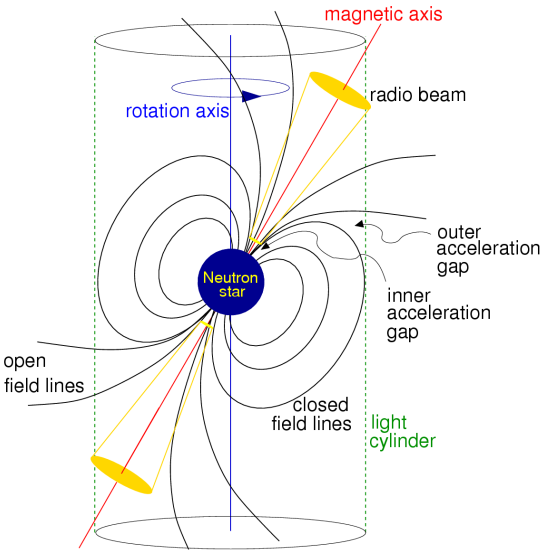

Figure 2.9.: Schematic model of a rotating pulsar in which the magnetic and rotation axes are misaligned. Pulsed radio beams are emitted from the poles of the magnetic field. Typical properties are masses of $M \approx 1.4\,M_{\odot}$, radii of $r \approx 10$ km and magnetic flux densities of 10^5 to 10^9 T. Figure taken from [48].

2.4.2. Extragalactic Cosmic Rays

Extragalactic CRs are high energy particles with energies of 10^{15} eV and more. Those are not produced within the Galaxy, but can propagate into our solar system and can be detected at Earth. However, due to the lack of statistics only very little is known about the origin and composition of these CRs, especially about UHECRs with energies above 10^{18} eV. Their origin and acceleration mechanisms are so far not ascertained beyond doubt and are subject to intense scientific investigations. Estimates, based on theoretical and numerical models, predict that these CRs predominantly consist of light nuclei, mostly protons [49]. In general, efficient acceleration mechanisms are diffusive shock acceleration and acceleration in a very high electric field, generated by fast rotating compact magnetized objects. However, diffusive shock acceleration was found to only account for particles of up to about 10^{17} eV, but not much beyond [50]. Therefore, SNRs are unlikely to be the sources of these CRs. Shocks on larger scales (extragalactic shocks) are therefore invoked, including extragalactic objects like AGNs. In these compact regions in the center of galaxies energetic particle production might take place. The inner cores of AGNs with magnetic fields of the order of 10^3 G and sizes of a few 10^{-5} pc could theoretically account for particles of a few tens of EeV [51]. However, under realistic conditions these energies are unlikely to be achieved due to energy losses like synchrotron and Compton processes and photon-pion production by interactions with the intense AGNs radiation field. Results from the Pierre-Auger-Observatory published in 2007 showed a strong correlation between the directions of 27 events above $6 \cdot 10^{19}$ eV and the locations of AGNs, lying at distances to Earth within $\sim$ 75 Mpc [2]. However, AGNs cannot be pinned down with certainty. The actual sources could rather be located closely to the AGNs as a result of gravitational clumping. Other source candidates typically considered are

- fast rotating, highly magnetized neutron stars. Young neutron stars with spin periods of < 10 ms and magnetic fields of 10^{13} G at the surface could accelerate particles by magnetohydrodynamical forces rather than from stochastic processes as in astrophysical shocks. In theory they should be able to accelerate iron nuclei up to 10^{20}

eV [52];

- Radio Galaxies, by which CRs are accelerated at the termination shocks of giant jets. They should be efficient enough for acceleration of up to 10^{20} eV and no adiabatic deceleration takes place, since the shocks are already inside the extragalactic space [53];
- Gamma-Ray Bursts, which are flashes of gamma-rays by extremely energetic explosions in distant galaxies [54];
- Colliding galaxies with numerous shocks and magnetic fields of the order of 20 μG [55];
- Galaxy clusters, which could account for acceleration of up to 10^{20} eV. The majority of the lower energy CRs will remain in the cluster and only particles with the highest energies can escape [56].

This list is by far not complete and only the most promising source candiates are listed. A review including further source candidates is given in [57].

2.5. Cosmic Rays and Dark Matter

One of the today's most puzzling mysteries in astronomy and cosmology is the nature of Dark Matter (DM). Hints on its existence were found by J. Oort in 1932 [58], who investigated the orbital velocities of stars in the Milky Way (MW). According to the virial theorem the kinetic energy of objects should, on average, be the half of their gravitational binding energy. Oort found that the orbital velocities of stars cannot be explained by the visible mass and that an additional matter component was needed. Similar results were found in 1933 by F. Zwicky, who investigated the orbital velocities of the Coma galaxy cluster by its mass-to-light ratio [59]. 80 years after its discovery many further independent evidences were found. These include

- the observed rotation curves of different galaxies, including the one of the MW,
- obervations of gravitational lensing, by which light from a distant source is bent due to a massive object or a large amount of mass,
- observations and analyses of angular fluctuations in the CMB,
- the fast structure formation in the Universe.

From the combination of the different observations, including precise CMB measurements by PLANCK, it is generally accepted that about 84.5% of the total matter content in the Universe consists of DM, while the visible, baryonic matter makes up only 15.5% [60]. The total energy content of the Universe is, however, dominated by the so called Dark Energy which makes up about 68.3%. Therefore the mass contributes with only 31.7% (26.8% DM and 4.9% ordinary matter). The observations imply that DM underlies only the weak and the gravitational forces and does not participate in interactions of the strong and the electromagentic forces. Numerical simulations of structure formations were performed and support the assumption that the major component of DM must be cold [61], i.e. non-relativistic. The local DM density ρ_{local}^{DM} could be determined by analyses of the rotation curve of the Milky Way and was found to be between 0.2 and 0.4 GeV cm^{-3} [62]. The DM distribution in galaxies is believed to consist of a giant DM halo, much larger than the visible structures, and small gravitationally bound sub-structures called minihalos or clumps.

The particle nature of DM is still unknown and the Standard Model of Particle Physics (SM) does not provide a convenient candidate. A hypothetical DM particle candidate is called WIMP (**W**eakly **I**nteracting **M**assive **P**article), denoted with χ, which was in thermal equilibrium in the hot, early Universe. In the state of thermal equilibrium the WIMPs were able to annihilate and were steadily produced by other particles. As the Universe expanded and therefore cooled down the average thermal energy decreased and the equilibrium abundance dropped exponentially according to the Boltzmann equation. Once the expansion rate of the Universe exceeded the annihilation rate the WIMPs were no longer be able to annihilate. This point in time marks the *freeze-out* of the WIMPs (at $T \approx m_\chi/20$) from which on their cosmological abundance was fixed and represents the *relic density*, denoted with $\Omega_\chi\, h^2$ with the Hubble constant h in units of 100 km/(s Mpc). Thermodynamics and statistical mechanics can be used to describe the particle reactions from which the relic density for WIMP particles in the 100 GeV/c^2 mass range as a function of the thermally averaged annihilation cross section $\langle \sigma v \rangle$ can be derived [63]:

$$\Omega_\chi h^2 \simeq \frac{3 \cdot 10^{-27}\, cm^3\, s^{-1}}{\langle \sigma v \rangle}. \tag{2.15}$$

Measurements of the anisotropy of the CMB and of the spatial distribution of galaxies lead to a value of the relic density of $\Omega_\chi h^2 = 0.112 \pm 0.006$ [41]. The measured value of the relic density leads to annihilation cross sections typical for cross sections of the weak scale which became known as the *WIMP miracle*. Since the particles were non-relativistic at the time of the freeze-out WIMP particles are referred to *cold DM*.

Many attempts to identify DM particles with known or theoretically motivated particles have been undertaken. A detailed review is for example given in [64]. For instance neutrinos that are assumed to be massless in the SM were found to have to be massive by the confirmation of neutrino flavour changing oscillations [65]. However, neutrinos could only account for a small fraction of the observed DM, due to experimental upper limits on the sum of the masses of the three neutrino generations. Furthermore, neutrinos were relativistic at the time of decoupling and would form *hot DM*, which is not supported by numerical simulations of structure formations. Other candidates are hypothetical axions, introduced to solve the strong CP-problem, i.e. the absence of CP-violation in strong interactions compared to weak ones. From direct searches and the dynamic of the Supernova 1987a it is assumed that axions must be very light ($m_A \leq 0.01$ eV) [64] and that they interact only very weakly and were therefore not in thermal equilibrium in the early Universe. In 1921 T. Kaluza tried to unify gravitation and electromagnetism by introducing additional spatial dimensions. The theory provides a viable DM candidate in form of the lightest Kaluza-Klein Particle (LKP). The LKP may account for the observed matter and its mass should lie in the range between 400 and 1200 GeV. Another candidate is provided by supersymmetrical extensions of the SM. The lightest of the additional hypothetical particles is called LSP (lightest supersymmetrical particle) and is stable if the R-parity is conserved. The R-parity is an additional multiplicative quantum number in supersymmetric models and its conservation implies that supersymmetric particles can be created and decay only in pairs, by which the stability of the LSP is assured. In many models this particle is the neutralino which is, with masses of roughly 10 to 10000 GeV and cross sections of the weak interaction, the leading WIMP candidate.
Most of the WIMP's properties, like its mass and its cross section for interactions with other particles, are unknown and sophisticated experiments are built to detect them. Three principal detection methods can be applied (see also figure 2.10):

- The direct WIMP production at particle collider experiments like at the Large Hadron Collider (LHC) at CERN. Although the direct production channel is sup-

pressed they could be produced by the decay of formely produced heavier supersymmetric particles and detected by missing transverse energy.

- The direct detection of WIMP scattering processes by cryogenic detectors (e.g. EDELWEISS) or noble liquid detectors (e.g. XENON) located in underground laboratories for CR background reduction. If a WIMP hits an atom of the absorber a tiny amount of heat, scintillation light and/or ionization is produced. The detection principle for such WIMP scattering processes is based on the detection of these signals. Mostly combined detection methods are used to determine or constrain the mass of the WIMP and the cross section from potential interactions with the target material.
- The indirect detection by the detection of SM particles originating from WIMP annihilations, see figure 2.11.

What all these detection principles have in common are large background contributions and consequently challenging background rejection and signal identification methods have to be applied. Direct searches suffer from large background contributions from neutrons, muons, photons and electrons originating from CRs or natural radioactive radiation.

In indirect searches the signal strength crucially depends on the DM density. While the signal strength in case of decaying DM particles and direct DM searches is proportional to the DM density, it is proportional to the squared density for annihilating DM particles. Even though the large, diffuse DM halo contains most of its mass, the main annihilation contributions therefore result from the bound and denser substructers, whose properties are, however, not well known. The contributions of protons and electrons from WIMP annihilations are exceeded by far by the contributions from primary CR sources. Therefore, only less abundant antimatter particles which are produced in interactions of the primary CRs with the ISM like antiprotons and positrons can be used. WIMP induced gamma-rays which directly point back to their origin may also be detected in the diffuse component of the gamma-ray sky, but are as well overlayed by large contributions originating from pion decays, inverse Compton scattering and bremsstrahlung. Of crucial importance for any indirect DM search is a precise understanding of the involved processes and a precise modeling of the astrophysics of CRs.

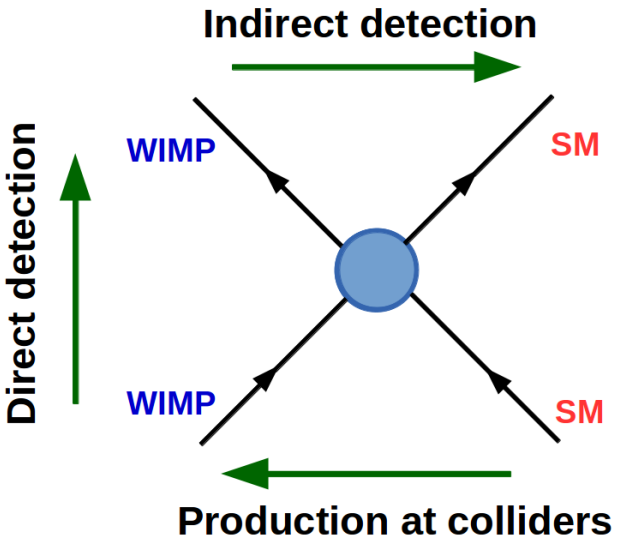

Figure 2.10.: Illustration of Dark Matter detection principles. The green arrows indicate the direction of time and show, how the diagram can be interpreted in three different ways: Direct production by two initial SM particles and two resulting WIMPs, direct detection by the scattering of a WIMP and a SM particle and indirect detection by an annihilaton of two WIMPs resulting in two particles of the SM.

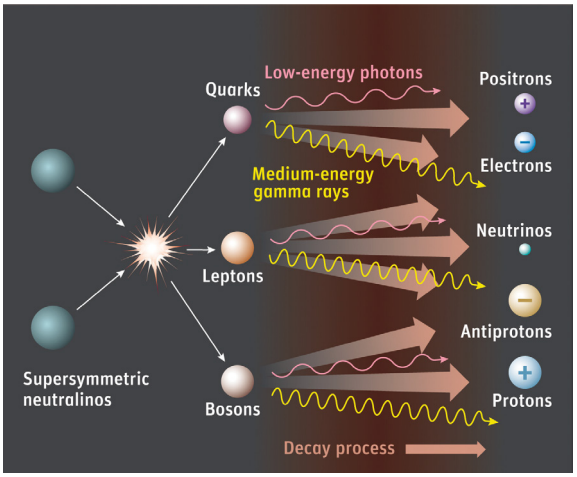

Figure 2.11.: Illustration of Dark Matter Annihilation. In case of annihilating DM particles, e.g. supersymmetric neutralinos, known particles of the SM are produced that may be detected in indirect DM searches. Credit: Sky & Telescope, Gregg Dinderman.

3. Cosmic Ray Propagation

In this chapter, the basic concept of CR propagation is presented. After an introduction to the relevant transport processes, the mathematical framework for modeling CR propagation in form of an extended diffusion equation is introduced and a detailed description for each physical process is given. Subsequently, the environment of the MW in terms of relevant properties for CR propagation within our Galaxy is addressed. In section 3.2.4 numerical and analytical solutions to the transport equation are discussed and the `GALPROP` and the `DRAGON` software for modeling CR propagation are introduced. Finally, the link to experimental observations, which directly allow to test the theoretical predictions, is pointed out and important observables are discussed.

3.1. Introduction to Cosmic Ray Propagation

After being produced and accelerated by their sources, CR particles are injected into the ISM and then propagate through the Galaxy. They underly several processes, modifying the initial particle spectrum and the particle composition. The dominating process of these propagation (or transport) processes is diffusion by the scattering of charged particles off magnetic turbulences in the galactic magnetic field, leading to a random walk like dispersion. In addition, CR particles scatter on randomly moving magnetohydrodynamic (MHD) waves, leading to a stochastic acceleration (diffusive reacceleration). During propagation through the gaseous Galactic Disc, CRs interact with the ISM and consequently lose or gain energy and produce secondary particles, gamma-rays and synchrotron radiation. Furthermore energy losses and particle losses by fragmentation, radioactive decays and escape from the Galaxy have to be taken into account. Convective transport due to the common movement of the scattering centers away from the galactic plane, may also play an important role, since convection not only transports CRs, but also produces adiabatic energy losses in case the wind speed increases in greater distance to the Galactic Disc. Additionally, CR particles propagating through our solar system are affected by low energetic charged particles coming from the Sun. This process, called *solar modulation*, modifies the particles spectra in the low energy region up to about 30 GeV/nucleon and strongly depends on the varying solar activity.

3.2. Modelling of Cosmic Ray Propagation

3.2.1. Transport Processes

3.2.1.1. Diffusion and diffusive Reacceleration

The propagation of charged particles in the ISM is dominated by their interaction with the magnetic and electric fields in the cosmic plasma. Therefore, the interactions of a collection of relativistic charged particles with a magnetized plasma have to be analyzed. For a given electric field $\vec{E}$ and magnetic field $\vec{H}$, the momentum distribution $f(\vec{r},\vec{p},t)$ of CR particles follows the kinetic equation [66]

$$\frac{\partial f}{\partial t} + (\vec{V}\cdot\vec{\nabla})f + Ze(\vec{E} + \frac{\vec{V}}{c}\times\vec{H})\cdot\frac{\partial f}{\partial \vec{p}} = 0, \tag{3.1}$$

in case particle collisions are neglected. $\vec{p}$ is the momentum, Ze is the charge of the particle and $\vec{F} = Ze(\vec{E} + \frac{\vec{V}}{c}\times\vec{H})$ the Lorentz force. A well known approach is the *quasilinear approximation*, in which the electric and magnetic fields are separated into their average values and fluctuations, corresponding to an ensemble of waves with random phases:

$$\vec{H} = \vec{H_0} + \vec{H_1}, \qquad \langle\vec{H}\rangle = \vec{H_0}, \qquad \langle\vec{H_1}\rangle = 0, \qquad \langle\vec{E}\rangle = 0 \tag{3.2}$$

The distribution f is also composed by an average and a fluctuating part:

$$f = \langle f\rangle + f_1, \qquad \text{with } \langle f_1\rangle = 0. \tag{3.3}$$

By averaging formula 3.1 over the ensemble of waves and the assumption of small amplitudes ($f_1 \ll \langle f\rangle$), one obtains

$$\frac{\partial f_1}{\partial t} + (\vec{V}\cdot\vec{\nabla})f_1 + \frac{Ze}{c}(\vec{V}\times\vec{H_0})\cdot\frac{\partial f_1}{\partial\vec{p}} = -Ze(\vec{E} + \frac{\vec{V}}{c}\times\vec{H_1})\cdot\frac{\partial\langle f\rangle}{\partial\vec{p}}. \tag{3.4}$$

It is practical to make use of the Fourier transformed fields in space coordinates:

$$\begin{aligned}\vec{E}(t,\vec{r}) &= \sum_\alpha \int d^3k e^{-i\omega^\alpha(\vec{k})t + i\vec{k}\cdot\vec{r}}\vec{E}^\alpha(\vec{k}),\\ \vec{H_1}(t,\vec{r}) &= \sum_\alpha \int d^3k e^{-i\omega^\alpha(\vec{k})t + i\vec{k}\cdot\vec{r}}\vec{H_1}^\alpha(\vec{k}),\end{aligned} \tag{3.5}$$

in which the summation over various kinds of waves in the plasma with the dispersion relation $\omega = \omega^\alpha(\vec{k})$ for each wave type is taken into account. By introducing cylindrical coordinates $p_\parallel$, $p_\perp$ and ϕ, one can derive a scattering condition for which particles are scattered by the waves:

$$\omega^\alpha(\vec{k}) - k_\parallel V_\parallel - s\omega_H = 0, \qquad \text{with} \quad s = 0, \pm1, ... \tag{3.6}$$

The integer s corresponds to cyclotron resonances of different orders. This *resonance condition* states that the frequency of the wave is an integer multiple of the frequency of the cyclotron rotation of the particle in the regular magnetic field $\vec{H_0}$. Thus, scattering between the particle and the wave occurs only if the wavelength is comparable to the particle's gyroradius. In case of wavelengths much shorter than the gyroradius the particle

circles around the direction of the regular field $\vec{H}_0$. For comparable wavelengths the interaction occurs at the harmonics $s = 0, \pm 1$. Two types of oscillation modes are relevant for scattering processes in the ISM: Alfvén waves with the dispersion relation $\omega^\alpha(\vec{k}) = \pm|k_\parallel|v_A$ and fast magnetosonic waves with $\omega^\alpha(\vec{k}) = \pm k v_A$. Both Alfvén and magnetosonic waves propagate along the magnetic field with the *Alfvén velocity*, but with opposite circular polarisation. In order to obtain a closed equation, the following assumptions are made:

- The characteristic time scale to establish isotropy is larger than the scattering rate,
- the characteristic distances are larger than the relaxation length of the fluctuations,
- the distribution function has a small anisotropic component: $\bar{f} = f_0 + \delta f(\mu)$, with the cosine of the pitch angle μ and $f_0 = \frac{1}{2}\int_{-1}^{1} d\mu \bar{f}$,
- the energy densities of waves propagating along the field and in the opposite direction are equal.

Following [66], the diffusion-reacceleration equation in one spatial dimension, including a source term Q, reads

$$\frac{\partial f_0}{\partial t} = \frac{\partial}{\partial x} D_{xx} \frac{\partial f_0}{\partial x} + \frac{1}{p^2}\frac{\partial}{\partial p} p^2 D_{pp} \frac{\partial}{\partial p} f_0 + Q \tag{3.7}$$

with the coefficients

$$\begin{aligned} D_{xx} &= \frac{v^2}{2}\int_0^1 d\mu \frac{1-\mu^2}{2\nu_\mu} \\ D_{pp} &= p^2 \left(\frac{v_A}{v}\right)^2 \int_0^1 d\mu (1-\mu^2)\nu_\mu \end{aligned} \tag{3.8}$$

with the Alfvén velocity v_A as a characteristic phase velocity of weak disturbances propagating in a magnetic field and $\mu = cos(\theta)$ with the pitch angle θ, i.e. the angle between $\vec{p}$ and $\vec{H}$. The scattering rate ν_μ can be expressed by

$$\nu_\mu \approx 2\pi^2 |\omega_H| \frac{k_{res} W^\alpha(k_{res})}{H_0^2} \tag{3.9}$$

with the cyclotron angular frequency ω_H, the resonant angular wavenumber k_{res} and the wave energy density $W^\alpha(k_{res})$ at resonance.

Equation (3.7) was derived by assuming that the particles move in a turbulent, magnetized plasma. This leads to diffusion of the particles in space along the direction of the regular magnetic field and to diffusive reaccleration, corresonding to diffusion in momentum space. The concept of CR diffusion explains why energetic charged particles have highly isotropic distributions and why they are well confined in the Galaxy.

If the spectrum of waves shows a power-law behaviour, corresponding to

$$W(k) \propto \left(\frac{k}{k_0}\right)^{-s}, \tag{3.10}$$

and the regular and the random fields are taken to be equal, the diffusion coefficient of particles along the field is given by

$$D_{xx} = D_0 \frac{v}{c} \left(\frac{\rho}{\rho_0} \right)^{\delta}, \tag{3.11}$$

D_0 being the *diffusion constant*, $\rho = \frac{p}{Ze}$ the particle rigidity, ρ_0 a reference rigidity and δ handling the rigidity dependence of the diffusion term (e.g. $\delta = \frac{1}{3}$ for a Kolmogorov and $\delta = \frac{1}{2}$ for a Iroshnikov-Kraichnan MHD turbulence spectrum). Typical values found by valuation and fitting to CR data for particle energies of several GeV are $\delta \approx 0.2$ to 0.8 and $D_0 \approx 10^{28} - 10^{29} \mathrm{cm}^2/\mathrm{s}$, depending on the model setup [67], [68].

In addition to diffusion and diffusive reacceleration there are other transport processes, as well as energy losses and particle losses that have to be taken into account, thus the diffusion equation (3.7) has to be extended. In the following, the convective transport process is motivated and energy loss, particle loss and particle production processes are discussed.

3.2.1.2. Convection

The existence of galactic winds in many galaxies proposes a large scale motion of the interstellar gas with a 'frozen' magnetic field, in which CRs may play an imortant role [69], [70]. They may not only diffuse, but can be carried by a convective outflow with a certain convection velocity $\vec{V_c}(\vec{r}, t)$. For a long time, this convective outflow from the Galaxy was assumed to be insignificant, since pure diffusion models were in general successful in describing most of the CR observations. However, following publications about the self-confinement of CRs [71], the CR hydrodynamic equations and analyses of hydrodynamic stability as well as the dynamics of the ISM showed that the convective velocity might be small near the galactic plane, but the wind is accelerated by gaseous, CRs and MHD wave pressures. As a result the wind velocity can reach several hundred km/s far away from the Galactic plane, with an almost linearly increasing wind velocity with distance, as was shown by numerical calculations [70]. Also, the interpretation of soft X-ray emission in the galactic halo gave evidence for the existence of a galactic wind, since hot gas at high galactic latitudes was found by ROSAT observations [72] which was not expected due to the gravitational bound.

3.2.1.3. Energy Losses, Particle Losses and Secondary Production

During propagation through the ISM, CR particles are subject to a number of energy loss mechanisms, causing a distortion of their initial energy spectra. These loss mechanisms involve interactions with matter, magnetic fields and radiation and have to be well understood in order to obtain information about the particles history. Whereas nuclei predominantly suffer from energy losses by ionization and Coulomb scattering, leptons additionally lose energy from bremsstrahlung and synchrotron processes, leading to faster energy losses and therefore shorter propagation lengths.
Of great interest are energy loss processes including gamma-rays and synchrotron radiation as by-products, since these photons can be used as tracer for the galactic CR distribution, see chapter 3.3.2.
In this chapter the main energy loss mechanisms and particle number changing modes are reviewed. A detailed description of the particular energy loss processes according to [73] and [74] is summarized in Appendix A.

Any charged particle experiences an electrostatic interaction if passing through the Coulomb field of another charged particle. In CR physics, this is typically an interaction between a very fast particle and a slow, cold particle. The energetic particle is decelerated, it suffers energy losses called **Coulomb losses** or **ionization losses** depending on the interaction

partner. For protons and other nuclei these are the dominating energy loss processes. In addition, collisions of nuclei with hydrogen, helium or heavier nuclei within the ISM can cause inelastic scattering processes by which the parent nucleus gets destroyed and new CR particles, so called **secondary particles**, are produced:

$$n_1 + (p, He) \rightarrow n_2 + X, \tag{3.12}$$

in which n_1 and n_2 are the mother and the daughter nucleus. The destruction of an existing CR particle according to the total cross section is called *fragmentation* and the production of a new particle according to the branching fraction of the corresponding channel is called *spallation*. The partial cross sections for the production of different elements and isotopes as a function of energy are best determined from collider experiments in which beams of high energy particles interact with target nuclei. Fragmentation is included in the transport equation (3.19) by associating a fragmentation rate $\frac{1}{\tau_f}$ to the cross section.

For the computation of the source function for secondary CRs, the sum over all present species j and the integral over the nucleon momentum is required:

$$q(p) = \frac{c}{4\pi}\frac{dn(p)}{dt} = \frac{c}{4\pi}\sum_{i=H,He} n_i \sum_j \int dp' \beta n_j(p') \frac{d\sigma_{ij}(p,p')}{dp}, \tag{3.13}$$

with the gas density n_i, the differential production cross section $d\sigma_{ij}(p,p')/dp$ of species j with hydrogen (i=H) and helium (i=He), the CR density $n_j(p')$ of species j and the total momentum of the nucleus p'.

Radioactive isotopes can be produced directly in the CR sources (e.g. ^{26}Al), as well as by fragmentation of heavier nuclei (e.g.^{10}Be). Instable isotopes are of special interest for CR propagation models, since the known half life enters the model, allowing the determination of a characteristic time scale in which the isotopes propagate through the Galaxy (see chapter 3.3.1). The number of instable, radioactive isotopes $N(t)$ after a time t with an inital population of N_0 and a half life of $\tau_{1/2}$ is given by the exponential decay law:

$$N(t) = 2N_0 e^{-\frac{t}{\tau_{1/2}}}. \tag{3.14}$$

In case of relativistic speeds, $\tau_{1/2}$ has to be replaced by $\gamma\tau_{1/2}$. Most of the decay modes are β^+ and β^- decays, leading to an emission of a neutron or a proton, respectively. Additionally, *K-capture* processes can occur, in which a proton-rich nuclues absorbs one of the orbital electrons (usually from the K or L electron shell), therefore changing a proton to a neutron and forming a new element. The missing orbital electron has to be caught in the ISM, which, however, is not rich in electrons. Therefore, the lifetime of a K-capture isotope can be significantly longer than the one measured in the laboratory. Some isotopes (e.g. ^{26}Al, ^{54}Mn, ^{56}Ni) underly both β-decay and K-capture with relativley short half lifes. In this combined case, both half lifes have to be taken into account and the 'naked' nucleus, i.e. the electron-free nucleus, can decay via $\beta^{\pm}$. Radioactive decays are included in the transport equation (3.19) by associating a decay rate τ_f. The source function for the daughter isotopes can be calculated by

$$\frac{\partial N_i}{\partial t} = \sum_{i<j} \frac{N_j}{\tau_{i,j}}. \tag{3.15}$$

Here, $\tau_{i,j}$ is the probability that a nucleus of type j decays into a nucleus of type i. A summary of the most important radioactive isotopes created in spallation processes is shown in table 3.1.

Table 3.1.: Summary of important radioactive isotopes. Shown are the corresponding decay mode(s) and half-lifes. Table taken from [10] and updated using [75].

Isotope	**Decay mode**	**Half-life (yr)**
^{10}Be	β^-	$1.387 \cdot 10^6$
^{14}C	β^-	5700
^{26}Al	β^+	$8.73 \cdot 10^5$
	K-Capture	$8.45 \cdot 10^6$
^{36}Cl	β^-	$3.01 \cdot 10^5$
	K-Capture	$1.59 \cdot 10^7$
^{54}Mn	β^-	$(6.3 \pm 1.7) \cdot 10^6$
	K-Capture	312 days

Bremsstrahlung is electromagnetic radiation produced by the deceleration of a charged CR particle when deflected by another charged particle of the ISM. The loss of kinetic energy of the moving particle is balanced by the emission of a photon (see Appendix A for details):

$$e + (e, p) \rightarrow e' + (e', p') + \gamma \tag{3.16}$$

Synchrotron radiation is produced when a charged, high energetic CR particle is forced to propagate in a curved path by the galactic magnetic field. Since the particle's mass m determines the synchrotron induced energy loss term with $\delta E \propto m^{-4}$ electrons and positrons lose their energy much faster compared to protons and other nuclei.

Inverse Compton scattering occurs if high energetic electrons or positrons scatter on low energetic photons of the ISRF, mainly photons from the CMB, stars and dust. Energy from the electron or positron can be transferred to the photon, increasing the photon energy:

$$e^{\pm} + \gamma \rightarrow e^{\pm'} + \gamma' \tag{3.17}$$

For an illustrative comparison of the energy dependence and the hierarchy of the different energy loss mechanisms, figure 3.1 shows the energy loss times for nuclei, electrons and positrons. For electrons and positrons at low energies Coulomb and ionization losses dominate, leading to total energy loss times between $4 \cdot 10^6$ and $3 \cdot 10^8$ years between 10^{-3} and 10^{-1} GeV. Above several hundred GeV inverse Compton and synchrotron losses become dominant and the loss time decreases to about 10^6 years at $2 \cdot 10^2$ GeV. For even higher energies above 10 GeV the loss times are comparable to the CR escape time of $\sim 10^7$ years. For nuclei the energy loss time exceeds this escape time in the whole energy range.

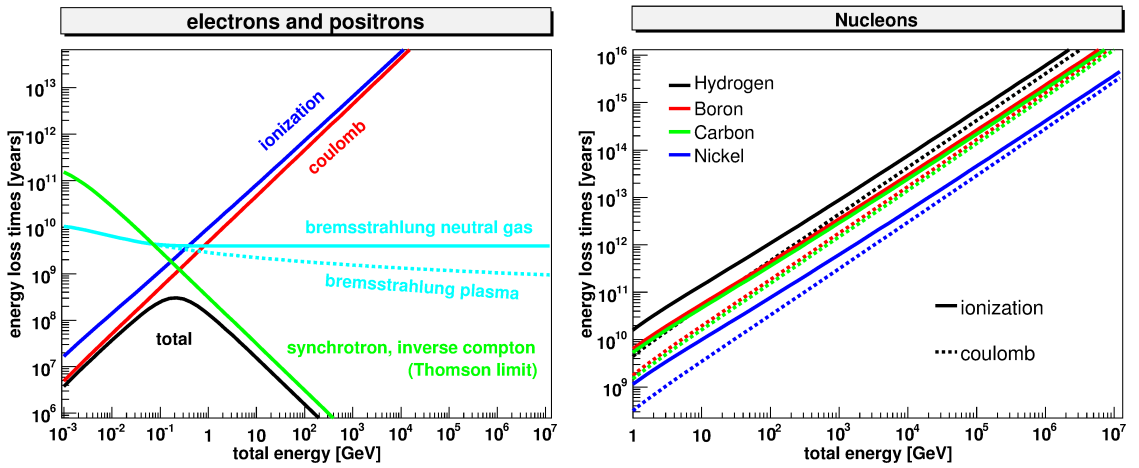

Figure 3.1.: Characteristic energy loss time scales. The energy loss times for electrons **(left)** and nuclei **(right)** are calculated in the Thomson limit, i.e. the energy density of photons and the magnetic field are identical (1 eV/cm^3). The loss times refer to equal gas densities of the neutral and ionized component of the ISM ($n_H = n_{H_{II}} = 0.01$ /cm^3) and a He to H ratio of 0 (no Helium). Figure taken from [76].

Energy Loss Length

Typical propagation lengths of protons and other nuclei are of the order of several kpc, depending on the particle's energy. In contrast, leptons have much shorter propagation lengths due to the large energy losses. A quantity linking the energy losses and propagation distance is the *energy loss length*. It is defined as the distance an electron propagates until it loses about 50% of its energy. With a diffusion coefficient parameterized as $D = D_0(E/E_0)^\delta$ and an average energy loss rate of $dE/dt \equiv b(E) = -\beta E^2$ the energy loss length λ can be expressed by

$$\lambda^2(E) = \int_{E/2}^{E} \frac{D(E)}{b(E)} dE = \frac{D_0 E^{\delta-1}}{(1-\delta)E_0^\delta \beta}. \tag{3.18}$$

In [77] the influence of the energy loss length to the solution of the diffusion-loss equation in different parts of the energy spectrum was studied. Bulanov et al. found that in case of low energetic particles with energy loss lengths much larger than the halo size energy losses are negligible. The spectrum is steepend from the initial index $(-\alpha)$ to $(-\alpha - \delta)$ as in the hadronic case. In the intermediate region the energy losses lead to a spectrum steepened to $(-\alpha - \delta/2 - 1/2)$ and the volume the particles are located in is limited by the loss length. At high energies the energy loss length drops drastically. The spectrum is steepened to $(-\alpha - 1)$ and the particles are confined to a thin volume around the sources. Figure 3.2 illustrates the spatial distribution of 100 MeV and 10 TeV CR electrons as a function of r and z. The density distribution along z is broader at 100 MeV, because the 10 TeV electrons are confined to the sources due to the large energy losses. In the model setup used in [78] typical propagation lengths are $r < 1$ kpc for 100 GeV electrons and $r < 0.2$ kpc for 10 TeV electrons.

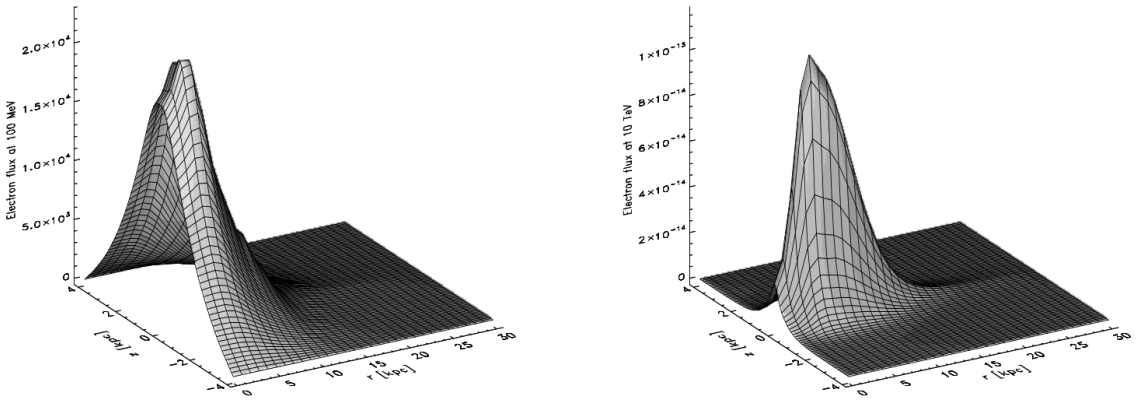

(a) 100 MeV (b) 10 TeV

Figure 3.2.: Spatial density distribution of 100 MeV and 10 TeV CR electrons. While the 100 MeV electrons spread spatially, the 10 TeV electrons are confined to a small area due to large energy losses. Figure taken from [78].

3.2.2. The Transport Equation

The *diffusion equation* for a particular particle species is given by equation (3.7). The full *transport equation*, including a convective transport mode, energy losses, particle losses and secondary particle production reads

$$\begin{aligned}\frac{\partial \psi}{\partial t} = q(\vec{r}, p, t) + \vec{\nabla} \cdot (D_{xx} \vec{\nabla} \psi - \vec{V_c} \psi) + \frac{\partial}{\partial p} p^2 D_{pp} \frac{\partial}{\partial p} \frac{1}{p^2} \psi \\ - \frac{\partial}{\partial p} [\dot{p} \psi - \frac{p}{3} (\vec{\nabla} \cdot \vec{V_c}) \psi] - \frac{1}{\tau_f} \psi - \frac{1}{\tau_r} \psi.\end{aligned} \tag{3.19}$$

Here, $\psi(\vec{r}, p, t)$ is the CR density per unit of total particle momentum p at the position $\vec{r}$ with $\psi(\vec{r}, p, t) dp = 4\pi p^2 f(\vec{p}) dp$, $q(\vec{r}, p, t)$ is the source term including the primary source, as well as spallation and decay contributions, D_{xx} is the spatial diffusion coefficient (assumed to be isotropic, i.e. the same in all directions), D_{pp} is the diffusion coefficient in momentum space for diffusive reaccleration, $\vec{V_c}$ is the convection velocity, $\dot{p}$ is the momentum gain/loss rate, τ_f is the fragmentation time scale and τ_r the time scale for radioactive decay. Equation (3.19) is a partial differential equation with two spatial partial derivatives. It depends on a multitude of parameters which determine the CR energy spectra and densities in the Galaxy. These parameters are not or only slightly accessible by theory and can only be constrained by a comparison of model predictions with experimental observations. The most important parameters are

- α, the injection index, determines the initial CR energy spectrum with which the particles are injected into the ISM,
- δ, which dictates the rigidity dependene of the diffusion coefficient and is related to the spectrum of turbulences,
- D_0, the diffusion constant, which is related to the turbulence level in the ISM,
- v_A, the Alfvén velocity, which determines the efficiency of the stochastic reacceleration mechanism,
- V_c, the convection velocity, by which CR particles may be carried away from the galactic plane,

- L, the halo height, which limits the height of the diffusion halo and acts as a boundary.

Chapter 3.3 gives an overview of how different observations can be used to constrain the particular transport parameters. Before solutions to the transport equation are presented, the properties of our Galaxy relevant for CR propagation are summarized.

3.2.3. The Milky Way

At first, this chapter gives a short description of the geometrical structures of galaxies, including the *Milky Way*. Then the properties of the MW that are relevant for CR propagation are discussed. These include the CR source distribution, the interstellar gas distribution, the interstellar radiation field, the magnetic field and the solar modulation.

In general, galaxies are complex, gravitationally bound systems, typically consisting of hundreds of millions or billions stars. Beside stars they contain interstellar gas and dust, forming the ISM, and an important but only very poorly known component, the so called DM (see chapter 2.5). Between large spaces with only a few or no galaxies, the *voids*, compound systems from pairs, small groups to giant galaxy clusters containing over a thousand of galaxies were observed. A wide variety of different galaxy morphologies exist, categorized into three main types: *elliptical*, *spiral*, and *irregular*. Our own Galaxy is a typical spiral galaxy in which the visible components form a spiraling pinwheel. It consists of a rotating disc of stars and the ISM, along with a central bulge of in general older stars. The disc itself is composed of curving arms, the so called *spiral arms*, in which most of the visible matter is located, see figure 3.3. The radius of the disc, in which the spiral arms are located, is about $r \approx 25 - 30$ kpc with a thickness of only $d \approx 400 - 600$ pc. Our solar system is located at a distance of $r_{Sun} = 8.33 \pm 0.35$ kpc [79] away from the Galactic Center close to the inner rim of the Orion arm and $d_{Sun} = 5 - 30$ pc [80] away from the central plane. The MW is moving with $v_{MW} \approx 550$ km/s through space with respect to the photons of the CMB, whereas our solar system moves with an orbital speed of $v_{Sun} \approx 220$ km/s. This gives an orbital period of $T_{Sun} \approx 240 \cdot 10^6$ years [81].

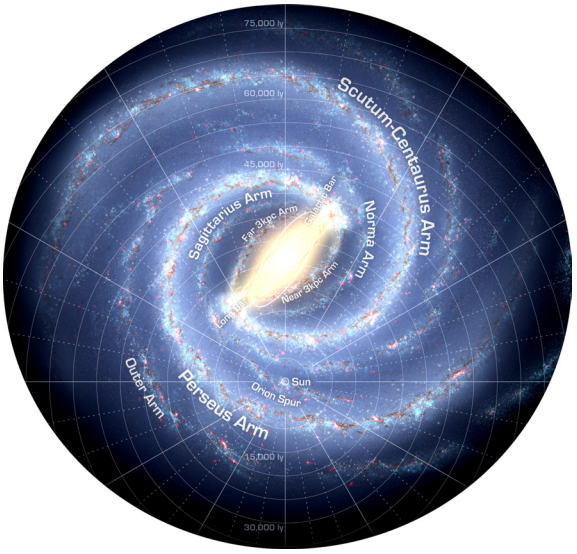

Figure 3.3.: Artist's view of the Milky Way's spiral arm pattern. The Galaxy's two major arms (Scutum-Centaurus and Perseus) can be seen attached to the ends of a thick central bar, while the two now-demoted minor arms (Norma and Sagittarius) are less distinct and located between the major arms. Whereas the major arms consist of the highest densities of both young and old stars, the minor arms are primarily filled with gas and pockets of star-forming activity. Figure taken from [82].

3.2.3.1. Source Distribution for Cosmic Rays

As already discussed in detail in chapter 2.4.1, SNRs are the most promising primary sources for galactic CRs. For modelling CR propagation a distribution of SNRs within the MW has to be adopted. In the literature several source distributions, often based on Pulsar (PSR) and SNR radio surveys, are proposed, see e.g. [83], [84]. A class of possible distributions can be written as

$$q(r,z) = q_0 \left(\frac{r}{r_{Sun}}\right)^{\alpha} \cdot e^{-\beta\frac{(r-r_{Sun})}{r_{Sun}}} \cdot e^{-\frac{|z|}{z_0}}, \tag{3.20}$$

with the radial distance to the Galactic Center r, the vertical distance to the Galactic Disc z and the model dependent factors q_0, α, β and z_0 (e.g. Lorimer et al. found : $\alpha = 1.9$, $\beta = 5$, $z_0 = 0.2$ kpc [83]).

A selection of these distributions is shown in figure 3.4. For a better comparison between the different source distributions the absolute abundance is normalized to the same value at $r = 8$ kpc. It should be noted, that the absolute abundance is not essential, since the modelled particle fluxes are usually normalized to the experimental data.

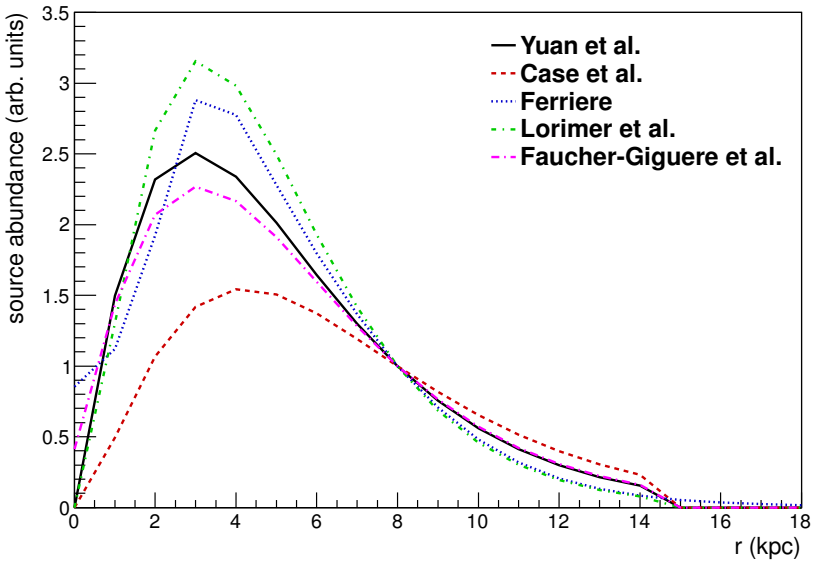

Figure 3.4.: Proposed SNR distributions. Shown are the proposed models by Lorimer et al. [83], Case et al. [84], Ferierre [85], Yuan et al. [86] and Faucher-Giguere et al.[87] within the Galactic Disc ($z = 0$ kpc). Averaged over all directions, the maxima of all distributions lie at distances between 2.5 and 4.5 kpc to the Galactic Center. Above 15 kpc the source abundance drops to zero or decreases exponentially.

3.2.3.2. Interstellar Gas Distribution

The mass of the interstellar gas contributes with only 5% to the visible mass in the MW. It consists of about 89% hydrogen, 9% helium and 2% heavier elements such as carbon, nitrogen, oxygen and iron (commonly summarized to 'metals' in an astrophysical context). Most of the gas is concentrated in the galactic plane, moving in circular orbits, with an overall gas density of about 10^6 particles/m^3. However, there are wide variations in terms of density and temperature throughout the ISM due to dynamical heating processes (e.g. supernova explosions, stellar winds, ultraviolet radiation) and cooling processes (e.g. bremsstrahlung) [10].

The gas content of the ISM is composed of multiple phases, distinguished by whether the matter is ionic, atomic, or molecular. Hydrogen is present in form of atomic hydrogen (HI), molecular hydrogen (H_2) and ionized hydrogen (HII). For predictions about secondary particle production and energy losses of CR particles, an appropriate knowledge of these distributions is of crucial importance. Therefore primary trace methods and the deduced density profiles for each hydrogen phase will be discussed.

Atomic hydrogen

Neutral, atomic hydrogen in the ISM has a temperature of 100 K to about 3000 K and emits line radiation at a frequency of $\nu_0 = 1420.41$ MHz ($\lambda_0 = 21.1$ cm). This radiation occurs through an almost completely forbidden hyperfine transition in which the spins of the electron and proton change from parallel to antiparallel. Although this transition is very rare the so called *21-cm line radiation* can be used as a tracer for the interstellar HI distribution, since it is highly abundant and therefore radiating steadily. It also allows the investigation of the dynamics of HI. Is the gas moving relative to the observer, Doppler shifts of the 21-cm-line can be measured and conclusions about the relative motion can be drawn. Recent measurements of the whole sky yield full 3-dimensional models of the density as a function of the position in the Galaxy, showing that the HI distribution is also following the spiral arm patter of the MW as stars do [88]. Its structure was found to be very extensive with over- and underdensities. In particular an underdense region is believed to enclose our solar system, known as the *Local Bubble* [89]. Its origin is most likely connected to supernova explosions in the solar neighbourhood. This strucure might also affect CR propagation in a not negligible way.

Molecular hydrogen

Molecules can emit line radiation corresponding to transitions between electronic, vibrational and rotational excited states. These molecular line emissions yield information about the denser regions of the interstellar gas than the 21-cm line, since molecules are fragile and can be dissociated by optical and ultraviolet photons. For this reason, molecular line emissions are predominantly found in dense molecular clouds with number densities of about 10^9 to 10^{10} m^{-3}.
H_2 is difficult to detect by infrared and radio observation due to the absence of an electric dipole moment. However, carbon monoxide (CO) can be used as tracer for H_2: CO molecules are excited by collisions with hydrogen molecules. The presence of line radiation of previously excited CO states implies the presence of H_2 allowing the determination of the H_2 number density. CO is, next to H_2, the second most abundant molecule and emits strong line radiation at $\lambda = 2.6$ mm caused by the rotational transition $J = 1 \rightarrow J = 0$, J being the angular momentum quantum number. A full 3-dimensional mapping of the galactic H_2 distribution by using CO as a tracer was done by Pohl et al. in 2007 [90].

Ionized hydrogen

The mechanisms for ionization of hydrogen are photoexcitation and photoionization at energies above the ionization energy $E_I = 13.6$ eV of hydrogen. Due to the large cross section of hydrogen atoms for ionization by high energy photons, photoionization is the dominating ionization process. For tracing the HII distribution intensities of hydrogen recombination lines can be used: Regions of ionized hydrogen can be observed in the radio band due to bremsstrahlung processes and in the optical band due to recombination of hydrogen and helium ions with free electrons. The dominant spectral line is the $H\alpha$ line with a wavelength of $\lambda = 656.3$ nm emitted by atomic hydrogen when the electron falls into a lower atomic shell ($n = 3$ to $n = 2$) after recombination. Those radiative transitions in which an electron from a higher excitation state ($n > 1$) cascasdes down the ground state ($n = 1$) happen very frequently, leading to the assumption that HII regions

are composed of a mix of electrons and ionized hydrogen, permanentely recombining into hydrogen atoms.
Figure 3.5 shows the radially averaged gas number density distributions for HI, H_2 and HII as a function of the radial distance to the Galactic Center [91].

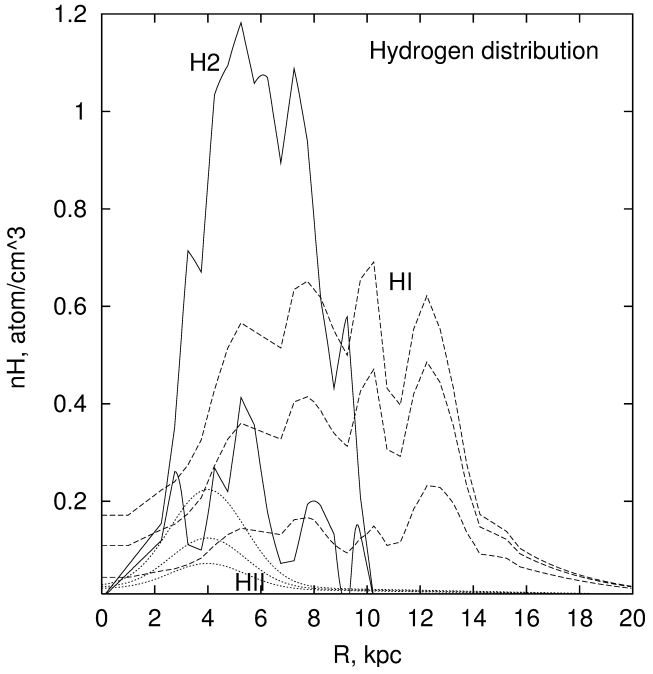

Figure 3.5.: The averaged gas number density distributions for HI (dashed), H_2 (solid) and HII (dots) for different heights of $z = 0, 0.1, 0.2$ kpc (decreasing density). Figure taken from [91].

Helium and coronal gas

Helium is with 9% the second most common element in the ISM. Its distribution follows that of hydrogen with a constant factor He/H of about 0.11. So-called *coronal gas* accounts for up to 70% of the fractional volume of the ISM. Tracing this hot, ionised, gaseous component is done using absorption lines of highly ionized metals. With temperatures of $T \sim 10^5$ to 10^6 K and densities of 10^{-4} to 10^{-3} atoms/cm^3 this extenuated component is of minor importance for CR propagation, especially compared to the uncertainties of the much more important hydrogen distribution.

3.2.3.3. Interstellar Radiation Field

In order to calculate photon induced energy losses an appropriate model for the galactic ISRF as a function of (r, z, ν) is required. The components the ISRF consists of are mainly photons from stars and from the CMB. These photons are scattered, absorbed and re-emissioned in the infrared band by dust in the ISM. The most detailed calculation by Strong et al. [92] includes a spatial and a wavelength dependence over the whole Galaxy. It is steadily extended by new relevant astronomical information on stellar populations, the galactic structure, and the interstellar dust [93], [94]. Figure 3.6 shows the energy density of the three components of the ISRF as a function of r and z.

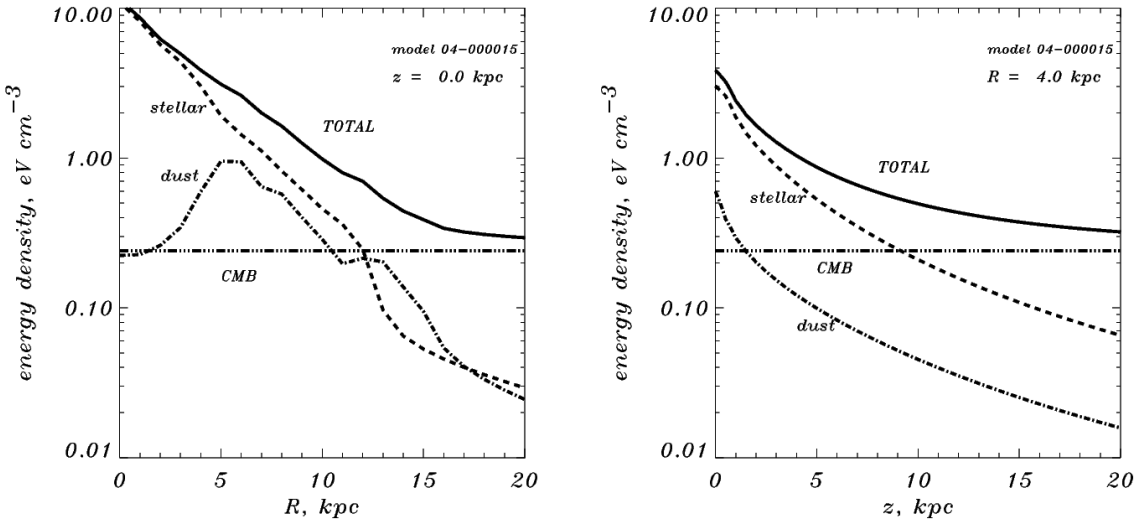

Figure 3.6.: Energy density of the three components of the ISRF. Shown are the contributions of stars (dashed), dust (dash-dot), the CMB (dash-3-dots) and the total contribution (full line) as a function of r in the galactic plane at $z = 0$ kpc **(left)** and as function of z at $r = 4$ kpc **(right)**. Figures taken from [92].

3.2.3.4. Magnetic Field

Galactic magnetic fiels are a fundamental component of the ISM. They affect the gas flows in spiral arms and the star formation by providing the transport of angular momentum required for the collapse of gas clouds. Furthermore, they significantly contribute to the total pressure of the ISM, preventing a gravitational collapse of the Galaxy. They play also an important role for CR propagation, since they dictate the scattering rate in the context of diffusion and are responsible for the large energy losses of electrons and positrons. If the diffusion equation is used to model propagation, the properties of the magnetic field are considered by the diffusion coefficient and the Alfvén velocity. However, for the calculation of synchrotron losses a parameterization of the galactic magnetic field as a function of (r, z) is required.

The structure of the galactic magnetic field consists of a *regular* and a *random (or turbulent)* component [95]. The regular component is believed to be generated and maintained by the *dynamo* mechanism: a weak seed field can be amplified to a large-scale field by a transfer of mechanical energy to magnetic energy [96]. The small-scale fluctuations in the magnetic field with coherence lengths of the order 100 pc, are produced by turbulences of the large-scale field, thermal instabilities, compression of magnetic fields by SNR shock fronts and stellar winds and self generated fields by the dynamo mechanism at small scales.

Tracing the MW's magnetic field is a challenging task, since it is a three-dimensional vector field that varies on multiple scales throughout the Galaxy. Furthermore, the related observables are not only sensitive to the magnetic field itself, but also to other quantities that are concealed by various effects. The total strength of the galactic magnetic field can be determined from the intensity of the total synchrotron emission orthogonal to the Line-of-Sight (LOS). However, this method is superimposed by the uncertainty of the CR electron density in the Galaxy. Polarization of thermal emission of dust shows directly the magnetic field projected in the sky plane, since dust particles are predominantly orientated along the ambient magnetic field inducing a polarization. Within a few kpc to the Sun also the polarization of starlight can be used, that is scattered by dust particles when traveling from a star to the Earth. For measuring the parallel component the splitting of spectral lines in an emission or absorption region can be used *(Zeeman splitting)*. Another method

uses Faraday Rotation Measures (RM). Faraday rotation occurs if polarized radio waves travel through a magnetized medium. The Faraday effect causes a rotation of the plane of polarization which is proportional to the component of the magnetic field in the direction of propagation. The RM is the integrated line-of-sight component of the magnetic field, weighted by the thermal electron density. The RM of pulsars and extragalactic radio sources can therefore be used to probe the magnetic field in our Galaxy, see e.g. Pshirkov et al. 2011 [97], Farrar et al. 2012 [98].

According to radio, synchrotron, optical polarization and Zeeman splitting data the average strength of the total magnetic field in the MW is about 6 μG near the Sun and about 10 μG in the inner galaxy (see [99] and references therein). Radio filaments near the Galactic Center and dense clouds of cold molecular gas yield fields with strengths of up to several mG. Outside the central region, the large-scale field is mostly parallel to the plane of the Galactic Disc. The overall field structure follows the spiral arms, but several distortions near star-forming regions were discovered [100]. Figure 3.7 shows a model of the MW's large-scale magnetic field derived by RMs of known pulsars and extragalactic sources.

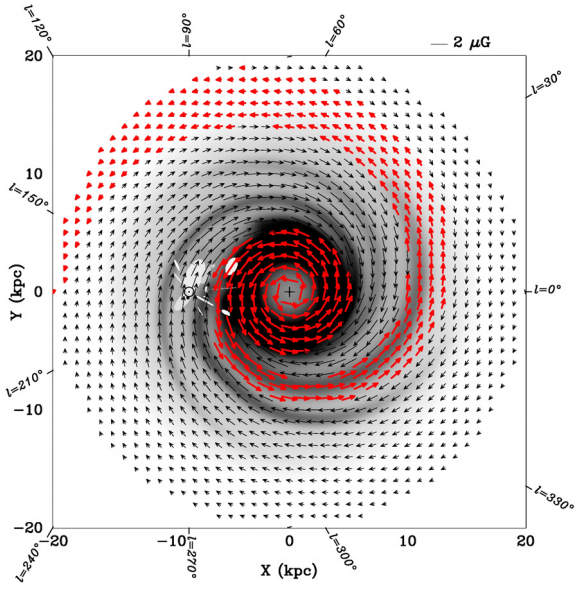

Figure 3.7.: Model of the large-scale magnetic field in the MW within the Galactic Disk. The positions of the solar system and interstellar clouds are indicated by white colours. The overall magnetic field structure follows the optical spiral arms and is symmetric with respect to the galactic plane. The strength of the field increases towards the galactic centre region. The reversal of the field inside the solar circle is shown in red. Credit: MPIfR, X.H. Sun and W. Reich [101].

For calculations of synchrotron losses in a cylinder-symmetrical setup Strong et al. proposed a simple, effective parametrization of the total magnetic field [92]:

$$B(r,z) = B_0\, e^{-(r-r_{Sun})/r_0} \cdot e^{-|z|/z_0}. \tag{3.21}$$

The parameters B_0, r_0 and z_0 can be adjusted to best reproduce measurements of the synchrotron emission in the Galaxy. For a sufficiently well description of the synchrotron emission at 408 MHz the values were found to be $B_0 = 6.1$ μG, $r_0 = 10$ kpc and $z_0 = 2$ kpc [92]. However, new data of the synchrotron emission at higher frequencies by WMAP make a renewed investigation of the sustainability of such a simplified model necessary.

3.2.3.5. Solar Modulation

During the propagation of CRs within our solar system their energy spectra are modified by interactions of the CR particles with the solar wind, a stream of charged particles released from the upper atmosphere of the Sun. It mostly consists of electrons and protons with low energies between 1.5 and 10 keV forming the *heliosphere*, a large bubble-like volume surrounded by the ISM. The strength of the modulation depends highly on the solar activity and modifies the low energy region of the particles spectra up to 20 - 30 GeV/nucleon. As a measure for the solar activity neutron monitors can be used. Such ground-based detectors measure the number of high energetic charged particles pitching on the Earth's atmosphere. In times of strong solar activity fewer galactic CRs reach the Earth and vice versa. Figure 3.8 shows the deviation to the averaged count rate during the last 50 years, in which the 11-year cycle of the Sun's activity becomes apparent.

The prediction for the Local Interstellar Spectrum (LIS) of each particle species has to be corrected corresponding to the respective solar activity. In 1968, Gleeson and Axford [102] derived the so-called *force-field-approximation*, in which the modulation of CRs is approximated as a motion in an effective, radial electric field. The strength of the modulation according to the solar activity can be described by a single parameter, the effective *modulation potential* Φ_{eff}. However, this parameter is model dependent and does not represent the solar potential itself. Nevertheless, reference values for the effective modulation potential for different experiments can be found in the literature, where a particular transport model was used [103]. This directly allows to compare the influence of solar modulation on datasets, recorded within periods of different solar activity.

For a given particle species with a mass m, a kinetic Energy of E_{kin}, a mass number A and a charge number Z the flux at Earth Φ is derived from the interstellar flux Φ_{LIS} by

$$\Phi(E_{kin}, A, Z) = \frac{(E_{kin} + m)^2 - m^2}{\left(E_{kin} + m + \frac{Z|e|}{A}\Phi_{eff}\right)^2 - m^2} \, \Phi_{LIS}(E_{kin} + \frac{Z|e|}{A}\Phi_{eff}, A, Z). \quad (3.22)$$

The force-field-approximation is quite successful in describing many of the existing observations. Figure 3.9 shows the proton spectrum at low energies as measured by the PAMELA detector during the years between 2006 and 2009 [104]. The force-field-approximation with different effective modulation potentials in combination with an unbroken proton injection spectrum can explain the data sets reasonably well.

Equation 3.22 does not depend on the sign of the charge of the particle species. However, recent measurements of the PAMELA experiment on electrons, positrons, protons and antiprotons gave hints that a charge sign dependent modulation could be realized in nature [105]. A more sophisticated treatment of the solar modulation is implemented in the not yet publicly available `HelioProp` software, which solves the the transport equation in the solar system accounting for charge-dependent drifts in the presence of a time-dependent current sheet [106].

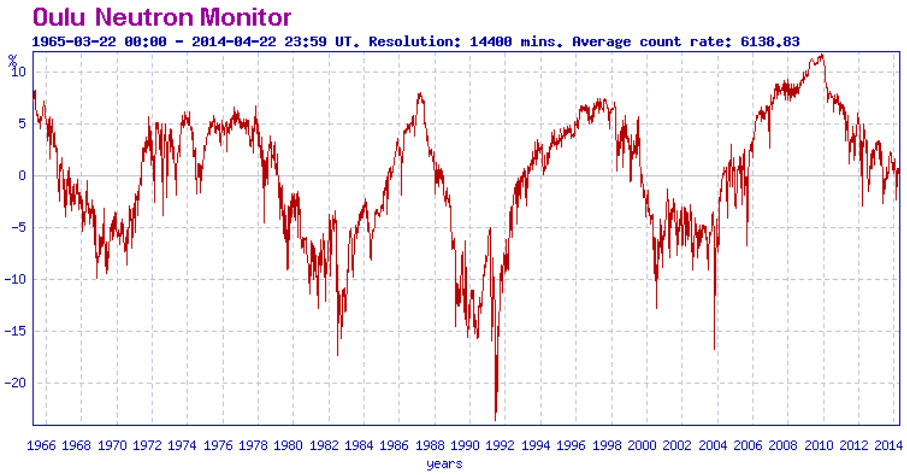

Figure 3.8.: The periodically varying solar activity. Shown is the deviation to the averaged count rate of CRs between 1965 and 2014, in which the 11-year cycle of the Sun's activity becomes apparent. Note, that the shown CR count rate is proportional to the inverse of the Sun's activity. The figure was produced with data from the Oulu Neutron Monitor [107].

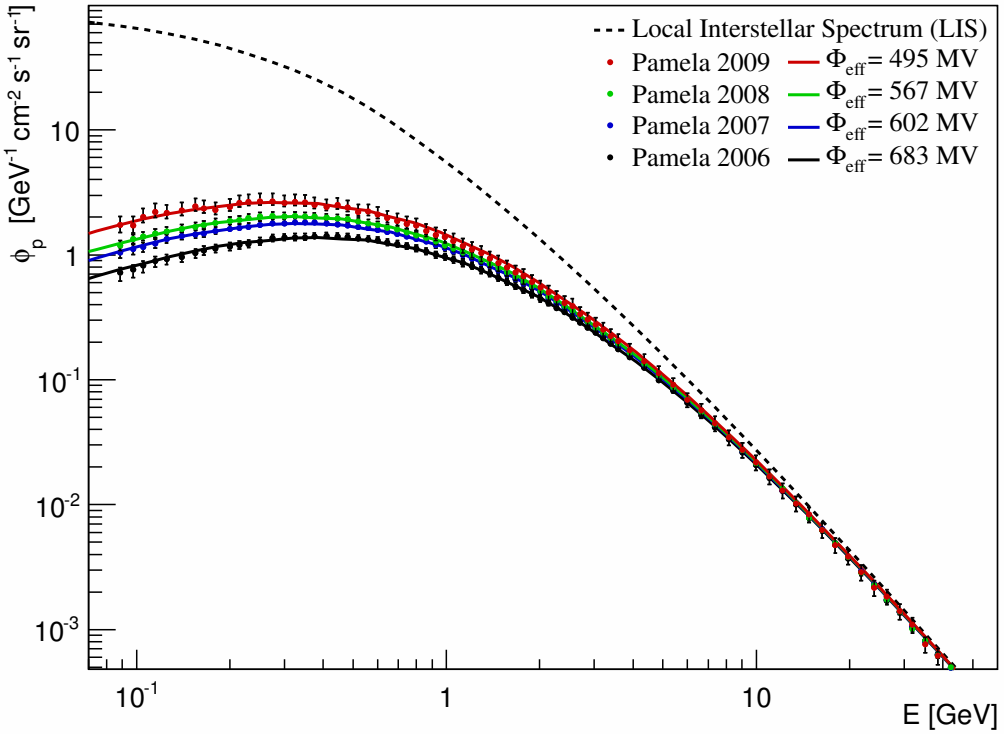

Figure 3.9.: The year-binned low energy proton spectrum as measured by PAMELA. The coloured lines were derived by disposing the force-field-approximation to the assumed LIS. The effective modulation potentials were fitted to the data and decrease with time corresponding to the decreasing solar activity from 2006 to 2009. Above energies of ~ 30 GeV the influence of the solar wind is negligible. Data taken from [104].

3.2.4. Solving the Transport Equation

Solutions to the transport equation (3.19) can be found numerically. Analytical and semi-analytical solutions require simplifying assumptions, e.g. an arbitrary gas distribution and energy losses cannot be considered at once. The explicit analytical solution approach for cylinder-symmetric 2D diffusion-convection models including secondary particle production and a source distribution was derived in 1976 by Ginzburg and Ptuskin [108]. In this approach many approximations and simplifications had to be made, e.g. energy losses were not taken into account. Semi-analytical solutions in 2D, including energy losses and reacceleration, can be expressed by a Green's function that has to be integrated over the sources [109]. The gas model, however, restricts to a simple, constant density within the disk. An analytical solution for the time-dependent case and a generalized gas distribution, but without energy losses, was proposed in [110].
Despite of their restrictions, analytical and semi-analytical solutions are in general fast to compute and can be useful to obtain insights into the relations between the involved quantities and for rough estimations. However, with today's computing power numerical solutions are very attractive, since they provide the CR distribution over the whole Galaxy, including an arbitrary gas distribution and energy losses, in a reasonable time.
In this work two solutions to the transport equation are used: An analytical solution for electrons and positrons originating from point like pulsars and numerical solutions as implemented in the `GALPROP` [111] and the `DRAGON` [112] code.

3.2.4.1. Analytical Solution for a Point like Source

For the computation of electron and positron densities of a point like source a simplified transport equation, in which convection and diffusive reaccleration are neglected, is given by [113]:

$$\frac{\partial N_e(E,t,\vec{r})}{\partial t} = D(E)\nabla^2 N_e + \frac{\partial}{\partial E}(b(E)N_e) + Q(E,t,\vec{r}). \tag{3.23}$$

Here N_e is the electron density, $D(R) = D_0(R/R_0)^\delta$ is the rigidity dependent diffusion coefficient, $b(E) = b_0E^2$ with the constant $b_0 = 1.4 \cdot 10^{-16}$ GeV^{-1}s^{-1} is an approximation for the energy loss term, including the dominant synchrotron and inverse Compton loss mechanisms [47] and $Q(E,t,\vec{r})$ is the source term. For a source at a distance $|\vec{r}|$ at a time $t > t_0$ the source term has the form

$$Q(E,t,\vec{r}) = Q_0 \left(\frac{E}{1GeV}\right)^{-\Gamma} \cdot e^{-\frac{E}{E_{cut}}} \delta(t-t_0)\delta(\vec{r}). \tag{3.24}$$

Q_0 is a normalization parameter, Γ the spectral index of the injected particle flux and E_{cut} the cut-off energy. An analytical solution to equation (3.23) can be derived [113] and is given by

$$\begin{aligned} N_e(E,t,\vec{r}) = \frac{Q_0}{\pi^{3/2}R_{diff}^3(E,t)} \left(1 - \frac{E}{E_{max}(t)}\right)^{\Gamma-2} \left(\frac{E}{1GeV}\right)^{-\Gamma} \\ \cdot exp\left[-\frac{E}{E_{cut}}\frac{1}{1-E/E_{max}} - \left(\frac{|\vec{r}|}{R_{diff}}\right)^2\right] \end{aligned} \tag{3.25}$$

with

$$R_{diff}(E,t) \simeq 2\left(D(R)t\frac{1-(1-E/E_{max})^{1-\delta}}{(1-\delta)E/E_{max}}\right)^{\frac{1}{2}}. \tag{3.26}$$

$E_{max}(t) = (b_0 t)^{-1}$ is the maximal energy an electron, injected with an arbitrarily large energy, has after a time t due to the already discussed energy loss mechanisms.

3.2.4.2. The GALPROP Code

A publicly available software package, which solves the transport equation numerically, is the `GALPROP` code [111]. In their pioneering work starting in 1996 the authors A. Strong and I. Moskalenko 'put all together' allowing the computation of CR densities including convection, diffusive reacceleration, energy losses, nuclear fragmentation and secondary production. They used most up-to-date data on cross sections, source and gas distributions and the ISRF, for which a model was specially developed. In `GALPROP` the transport equation (3.19) is solved for the steady-state case by the numerical *Crank-Nicholson implicit second-order scheme* [114]. For the derivatives in r, z and p *operator splitting* is adopted. For the cylinder-symmetrical 3 dimensional problem (r,z,p) or the cartesian 4 dimensional problem (x,y,z,p) the transport equation can be finite-differenced in the form

$$\begin{aligned}\frac{\partial\Psi_i}{\partial t} &= \frac{\Psi_i^{t+\Delta t}-\Psi_i^t}{\Delta t}\\ &= \frac{\alpha_1\Psi_{i-1}^{t+\Delta t}-\alpha_2\Psi_i^{t+\Delta t}+\alpha_3\Psi_{i+1}^{t+\Delta t}}{\Delta t}+q_i.\end{aligned} \tag{3.27}$$

The α_i with $i=1,2,3$ are called *Crank-Nicholson-coefficients*. The index i refers to the discrete spatial grid and t and Δt to the quantity at a time t and $t+\Delta t$, respectively.

For a time step of Δt the updating scheme is given by

$$\Psi_i^{t+\Delta t} = \Psi_i^t + \alpha_1\Psi_{i-1}^{t+\Delta t} - \alpha_2\Psi_i^{t+\Delta t} + \alpha_3\Psi_{i+1}^{t+\Delta t} + q_i\Delta t. \tag{3.28}$$

This leads to a tridiagonal system of equations that has to be solved for $\Psi_i^{t+\Delta t}$:

$$-\alpha_1\Psi_{i-1}^{t+\Delta t} + (1+\alpha_2)\Psi_i^{t+\Delta t} - \alpha_3\Psi_{i+1}^{t+\Delta t} = \Psi_i^t + q_i\Delta t. \tag{3.29}$$

At each iteration the spatial boundary conditions are applied, in which the particle density is forced to zero at the boundaries. For the cylinder-symmetrical case they read

$$\begin{aligned}\Psi(R_{max},z,p) &= 0,\\ \Psi(R,-z_{max},p) &= 0,\\ \Psi(R,z_{max},p) &= 0.\end{aligned} \tag{3.30}$$

The solution is computed for each particle species, starting from the heaviest one in order to take contributions from spallation processes and radioactive decays to the lighter species into account. After the nuclear chain reached hydrogen, the lightest element, electron and positron densities are calculated. The procedure for each species is repeated for all timesteps Δt. Usually the calculation starts with a large Δt of the order of $\sim 10^3$ Myr and continues with $\Delta t/4$ until a minimum timestep of the order of $\Delta t_{min} = 100$ yr is reached. For reasonable solutions for leptons the minimum timestep should be of the order of 1 yr [78]. The reason is that different physical processes have different intrinsic time scales

that have to be accounted for. The runtime increases significantly with smaller time steps, therefore a reasonable compromise between the computation time and the precision of the calculation has to be made. The computation ends if the given maximum number of timesteps is reached or a particular criterion of convergence is fulfilled. Usually, the time scale is required to be large compared to the timescales of diffusion and energy losses.

3.2.4.3. The DRAGON Code

`DRAGON` (**D**iffusion of cosmic **ra**ys in **g**alaxy modelizati**on**) is a publicly available software package written by C. Evoli, D. Gaggero, D. Grasso and L. Maccione. It is based on the `GALPROP` codes v.50p to v.54 and uses basically the same solving algorithm, the same nuclear cross sections and the same ISRF. However, it is written in pure C++ and uses the advantages of this modern programming language in contrast to `GALPROP`. The computations are performed in a highly optimized way by using 34 classes. Large amounts of data are passed as pointers to structured objects, leading to an efficient memory management and thus fast computations. This makes the `DRAGON` code attractive for statistical analyses of transport models. The code is also steadily extended in terms of performance (e.g. OpenMPI parallelization) and physically motivated features. For instance a realistic 3D distribution of the MW's spiral arm pattern was adopted allowing the source distribution, the gas distribution and the ISRF to follow the spiral arm pattern [106]. Anisotropic, position dependent diffusion in three spatial dimensions granting the specification of an arbitrary function of position and rigidity for the diffusion coefficient in the parallel and perpendicular direction to the regular magnetic field was presented in [115].

The Cosmic Ray group at KIT under the supervision of Dr. I. Gebauer is in close contact to the authors of `DRAGON` and is involved in upgrading and extending the code. Beside smaller bug fixes and optimizations the main contributions of the KIT group, all of which were adopted to the currently available official version, are

- the implementation of a non-equidistant spatial grid, which allows the investigation of small scale structures,
- the implementation of local structures, in which deviations of the gas distribution or transport parameters may be applied,
- an update of the electron capture implementation,
- an additional model for the MW's spiral arm density.

Furthermore, sophisticated tests in terms of convergence of the obtained solutions were performed and critial issues were indicated and handed down to the authors for further improvements of the code.

3.3. Constraining Observations

This chapter gives an overview of how transport models, i.e. the particular transport parameters, can be constrained by experimental observations. First, the influence of the established transport parameters on the energy spectrum of nuclei and leptons are discussed and the special roles of secondary-to-primary ratios and ratios of radioactive isotopes are emphasized. Afterwards, the diffuse galactic gamma-ray emission, the synchrotron emission and their constraining potential for transport models are highlighted.

3.3.1. Local Spectra of Nuclei and Leptons

Constraining of transport models is in many cases only of limited suitability due to degeneracies of the transport parameters. For instance, an increase of the diffusion constant D_0 corresponds to less effective scattering which leads to a quicker escape of CRs. This can be counterweighted by an increase of the halo height L, so that the escape time remains the same.

The slope of the energy spectrum of a primary hadron at energies above ~ 10 GeV depends on the initial injection index α and the rigidity dependence of the diffusion coefficient, dictated by δ. The effect of δ is a steepening of the initial slope of the spectrum. This can be shown in a simplified leaky-box-model in which the loss of CRs propagating in a box is treated by a non-zero probability of escape when encountering the boundary:

$$\frac{\partial N}{\partial t} = \frac{N}{\tau_{esc}(E)} + Q(E), \tag{3.31}$$

with the particle density $N(E)$ at an energy E and the time τ_{esc} cosmic rays spend in the Galaxy. With $\tau_{esc} \propto E^{-\delta}$ the steady-state solution, i.e. $\frac{\partial N}{\partial t} = 0$, gives

$$N(E) \propto E^{-\alpha-\delta}. \tag{3.32}$$

The energy region below $\sim$ 10 GeV is affected by v_A, which reaccelerates low energy particles and V_c, which decreases the particle flux at the solar position by a convective transport. Primary particles are only partially suitable for constraining transport parameters. However, a matching shape and normalization to the locally measured spectra and abundances are of crucial importance for an appropriate prediction of the expected secondary particle production. Measurements of secondary particles (e.g. antiprotons) allow to examine these predictions.

Of fundamental importance for constraining transport parameters are measurements of *secondary-to-primary* ratios (e.g. Boron/Carbon) and ratios of *radioactive isotopes* (e.g. $^{10}Be/^{9}Be$). They allow to constrain the CR interaction rate and the CR escape time.

Secondary-to-primary ratios do not show the degeneracy of equation 3.32. For secondary particles one gets $N(E) \propto E^{-\alpha-2\delta}$ and the slope of the ratio is proportional to $E^{-\delta}$. At low and intermediate energies these ratios are also strongly affected by D_0 and v_A: A larger value of D_0 leads to a lower ratio because of the faster escape of the primary nuclei from the Galaxy and consequently less secondary produced particles. However, an increase of the halo height can increase these ratios again because the CR particles spend more time in the Galaxy and more secondary particles are produced. A measure for the averaged thickness of the matter CRs have to traverse on their way from their sources to Earth, is the *grammage* χ, defined as the gas column density along the path of CRs:

$$\chi = \int n_H c \tau_{esc}. \tag{3.33}$$

High energy particles traverse typically about $10\,\mathrm{g/cm^2}$ of matter on their way through the solar system [116] corresponding to a density of ≈ 0.2 atoms/cm^3. In fact, the average gas density seen by CRs was found to be substantially lower that the Galactic Disc average of 1 atom/cm^3 [116]. This indicates that CRs are confined in the Galaxy and spend substantial parts of their lifetime in regions with low densities, like in the halo of the Galaxy.

The relative abundance of **radioactive isotopes** is sensitive to the halo height L. The larger the halo is, the longer it takes for nuclei to reach the Earth. In case of radioactive isotopes the relative abundance decreases with time. Ratios of radioactive instable to radioactive stable isotopes, called *cosmic clocks*, allow the determination of the local age of CRs. Especially isotopes with lifetimes near the CR escape time (e.g.^{10}Be) are of particular importance. Beryllium is a pure secondary element, produced by spallation processes of Carbon (C), Nitrogen (N) and Oxygen (O). Whereas the ^{9}Be isotope is stable against radioactive decay, the ^{10}Be isotope decays via β^{-}-decay with a half-life of $\tau_{^{10}Be} = 1.39$ Myr [75]. Measurements of several cosmic ray isotopes are consistent with cosmic ray escape times of $\tau_{esc} \approx 10^{7}$ yr at non-relativistic energies [116].

The most precise measurements up-to-date for the energy spectra of protons, antiprotons, electrons and positrons in a wide energy range are published by the PAMELA collaboration, see figure 3.10. Measurements of the ratios B/C and $^{10}Be/^{9}Be$ were accomplished amongst others by the experiments HEAO [117],[118], ACE [119], CREAM [117] and ISOMAX [120]. Figure 3.11 illustrates quantitavely the influcence of some of the most important transport parameters on the expected particle spectra at Earth. For a fair comparison the proton spectrum of each prediction was normalized to the according data and the LIS (no solar modulation) is shown. It becomes apparent that the different observables are affected in different ways and with different strengths by the transport parameters. For instance, while the diffusion constant D_0 crucially affects the proton spectrum and B/C the ratio $^{10}Be/^{9}Be$ is only marginally affected. In turn, $^{10}Be/^{9}Be$ and B/C show a strong dependence on the halo height L: CR particles spend more or less time in the Galaxy and more or less secondary particles are produced by interactions with the gas and by radioactive decays. The slope at high energies of B/C is basically determined by δ, as already reasoned before. Figure 3.12 shows additionally the influence of the transport parameters on the proton density distributions in r and z direction. The proton density is forced to zero by the boundary conditions at $r = 20$ kpc and $z = L$. While the radial shape is significantly influenced by almost all transport parameters the shape in z direction is basically determined by the halo height L.

For **leptons** fast energy losses by synchrotron radiation and inverse Compton scattering result in shorter propagation lenghts than e.g. for protons (see chapter 3.2.1.3). Therefore locally measured, high energetic leptons, coming from close sources, may have underlain local propagation modes, that may be different from the global galactic ones. Especially for analyses of positrons, it is important to use an appropriate model matching the proton, helium and B/C data to make sure that the total positron contribution is predicted correctly and which is matching the locally electron data and synchrotron data to make sure that the energy losses are estimated correctly and possible local transport modes are considered.

The constraining power of locally measured particle spectra is limited to predictions at Earth. CR densities far away from the Earth are only indirectly accessible via the detection of CR interaction products, which will discussed in the following chapter.

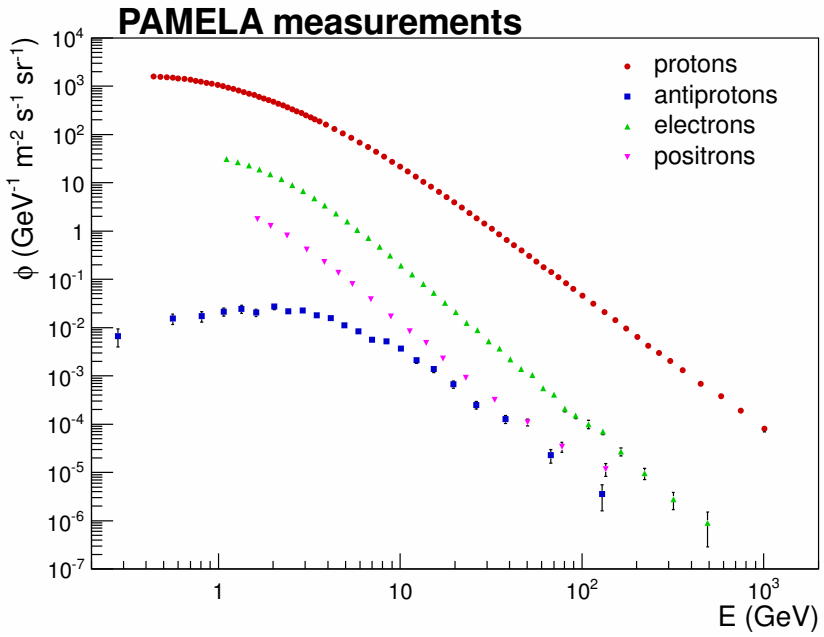

Figure 3.10.: PAMELA measurements of the spectra of protons [121], antiprotons [122], electrons [123] and positrons [124].

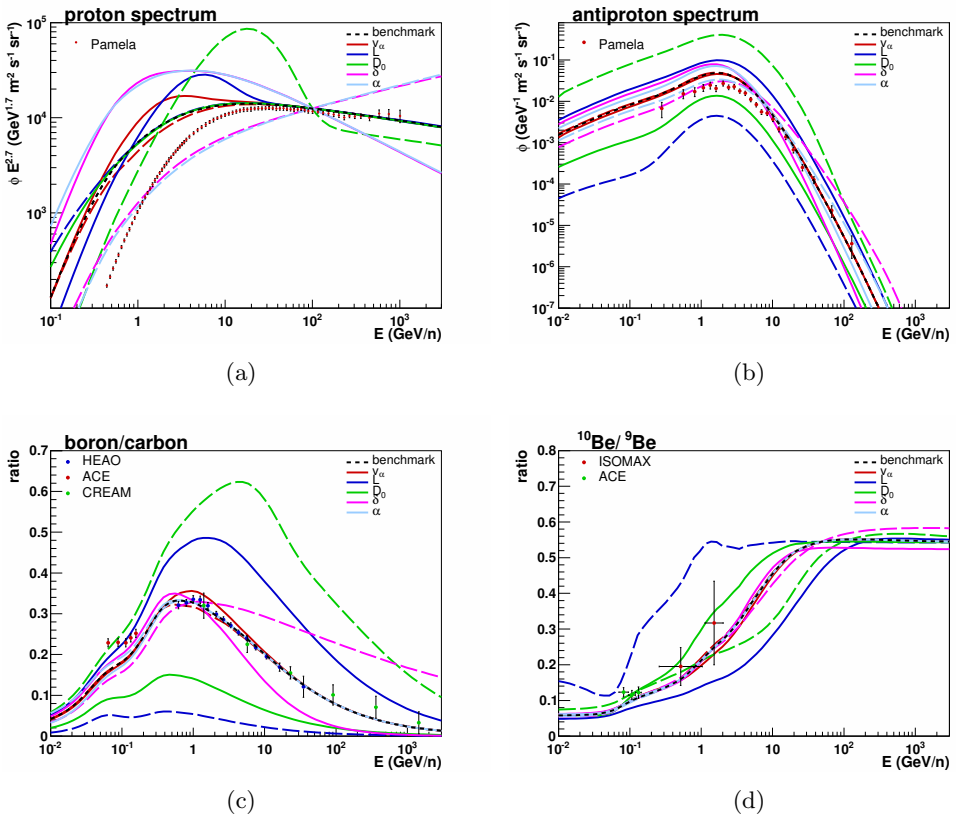

Figure 3.11.: Influence of transport parameters on the expected energy spectra at Earth. The black dashed line corresonds to a benchmark model produced with the DRAGON code, from which changes to the transport parameters have been applied to derive the colored lines. Each color corresponds to the change of a different transport parameter, either increased (solid lines) or decreased (dashed lines). For a fair comparison the proton spectrum was normalized to the according data. See text for interpretation.

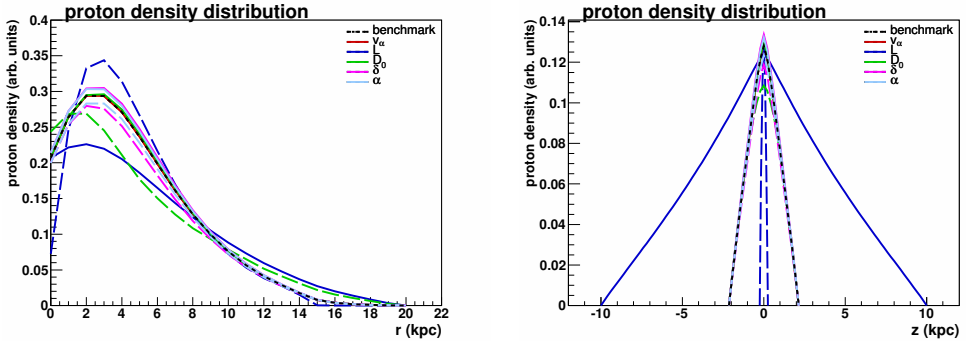

Figure 3.12.: Influence of transport parameters on the expected proton distribution. Shown is the proton distribution at an energy of 91 GeV as a function of r at $z = 0$ kpc **(a)** and as a function of z at $r = 8.0$ kpc **(b)**. The proton density is forced to zero at $r = 20$ kpc and $z = L$. While the radial shape is significantly influenced by almost all transport parameters the shape in z direction is basically determined by the halo height L.

3.3.2. Gamma-Ray and Synchrotron Emission

The diffuse, galactic gamma-ray emission arises from interactions of CR particles with the interstellar gas and the ISRF. The dominant contributions are produced by hadronic and leptonic interactions of mainly protons, helium, electrons and positrons. The largest contribution in the GeV energy range originates from decaying π^0 mesons, which are produced in hadronic proton-proton collisions leading to the production of two high energetic photons:

$$(p, He) + (p, He) \rightarrow \pi^0 + X \rightarrow \gamma\gamma + X \tag{3.34}$$

The *emissivity*, which is the number of particles emitted per unit of volume, time, energy and interaction, can be caluclated for a hydrogen target by [125]

$$Q_{\pi^0}(E_{\pi^0}) = cn_H \int_{E_p^{min}(E_{\pi^0})}^{E_p^{max}} dE_p n_p(E_p) \frac{d\sigma(E_p, E_{\pi^0})}{dE_{\pi^0}}, \tag{3.35}$$

with the differential cross section of π^0 production from proton-proton collisions $\frac{d\sigma(E_p,E_{\pi^0})}{dE_{\pi^0}}$. If the proton energy is much larger than its mass, the photon emissivity can be approximated by

$$Q_\gamma(E_\gamma) \simeq \frac{2}{\alpha}\sigma_0 c n_H Y(\alpha) n_p(E_\gamma), \tag{3.36}$$

where $Y(\alpha)$ is a function of the proton spectral index α, commonly called *spectrum-weighted moment* or *yield*. It is a dimensionless quantity and corresponds to the averaged number of photons produced in a volume of 1 cm^3 per second and per interaction, e.g. $Y(2.2) = 0.103$ [126].

The dominant leptonic production mechanisms are the dominant energy loss mechanisms for electrons and positron and were already discussed in chapter 3.2.1.3: Bremsstrahlung (equation 3.16), inverse Compton scattering (equation 3.17) and synchrotron emission. The contribution of leptonically produced gamma-rays from Bremsstrahlung and inverse Compton scattering processes to the diffuse emission can be dominant in the sub-GeV energy range. Synchrotron radiation is maximal in the MeV region, but gives only very small contributions to the overall gamma-ray spectrum. A large contribution results from photons of extragalactic origin. This photon flux is isotropic and dominates the diffuse gamma-ray spectrum at low and high energies in directions with low CR proton, CR electron and gas densities, e.g. at the galactic poles.
In contrast to charged CRs, which are deflected by the galactic magnetic field, gamma-rays point directly back to their production position. Therefore, observations of diffuse gamma-rays provide important information that can be used to trace the CR spectra and densities even at distant locations. The proton density distribution in combination with the gas distribution can be traced by diffuse gamma rays (as measured by e.g. FERMI) and the electron density in combination with the magnetic field by sychrotron data (as derived by e.g. WMAP data).

The expected gamma-ray emission for a given model, including the CR density distribution computed in steady-state, the gas distribution and the ISRF, can be obtained by integrating the expected emissivity along the line-of-sight for an observer at the solar position. The CR particle densities used for the expected gamma-ray flux are usually normalized to locally measured particle densities. However, if the locally measured densities represent a local over- or underdensity in the Galaxy the expected gamma-ray flux can be over- or

underestimated and a different normalization has to be applied.

The most up-to-date data of the gamma-ray sky is provided by the FERMI-LAT experiment. Figure 3.13 shows a skymap of almost four years of observation of the diffuse, galactic gamma-ray emission. The diffuse component was derived from the raw data by subtracting energy and spatial templates of all known point sources[1]. The data were taken from the Fermi Science Support Center (FSSC) and processed using the *fermi-science-tools* software [29]. Details on the data taking period and the used event class can be found in table 3.2.

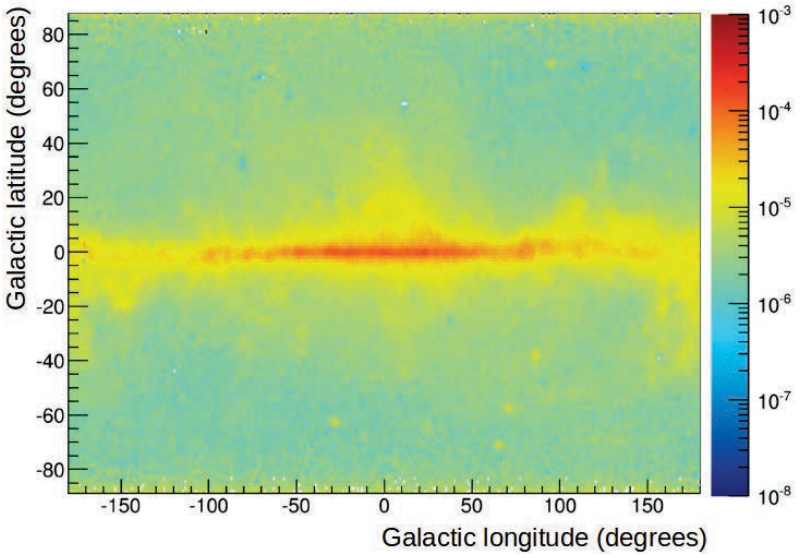

Figure 3.13.: The diffuse component of the FERMI gamma-ray sky in the energy range 0.4 - 0.56 GeV. The flux shown on the z-axis is given in units of ($\mathrm{GeV}^{-1}\mathrm{m}^{-2}\mathrm{s}^{-1}\mathrm{sr}^{-1}$). The largest contributions arise from the Galactic Disc and the Galactic Center, in which the CR density and the gas density are expected to be maximal. Relicts from insufficient point source models (e.g. the Blazar PKS 2326-502 at $l = -28.0°$, $b = -62.3°$) can be excluded by spatial masking but are not significant if the total flux in large regions is examined.

Table 3.2.: Specifications used for the processing of FERMI data.

Start date	2008-08-04 15:43:36.00
End date	2012-04-26 00:34:36.00
Max. zenith angle	100°
Event class	2
IRF	P7SOURCE_V6
ROI-Based Zenith Angle Cut	no
Relational Filter Expression	DATA_QUAL>0, LAT_CONFIG==1
Energy Range	0.1 - 100 GeV

The synchrotron emission cannot be measured directly due to overlayed contributions from the CMB, emission from dust and thermal bremsstrahlung from ionized hydrogen. The latter is called *free-free radiation* which is produced by free electrons scattering off ions without being captured.
A model for the synchrotron dominated emission at a frequency of 408 MHz was derived

[1] In collaboration with Dr. M. Weber

in 1981 by Haslam et al. [127]. For the complete all-sky coverage four different radio continuum surveys from the Jodrell Bank Mk1A telescope, the Effelsberg 100 metre telescope and the Parkes 64 metre telescope were composed. The original map as well as a a filtered map, in which also strong point sources were removed, are publicly available [128]. The filtered 408 MHz map in units of the antenna temperature is shown in figure 3.14. The relation between the antenna temperature $T(\nu)$ and the intensity $I(\nu)$ is given by

$$T(\nu) = \frac{I(\nu)c^2}{2\nu^2 k_B}, \tag{3.37}$$

with the frequency ν and the Boltzmann's constant k_B.

Maps of the synchrotron emission in different, higher frequency bands were derived by fitting templates of the foreground components (synchrotron, dust, free-free emission, CMB) to WMAP data [129]. Figure 3.15 shows a sketch of the antenna temperatures of the particular contributions in different frequency bands. Below 60 GHz the main contributions to the total emission are synchrotron radiation and free-free emission. Above 60 GHz the synchrotron emission is much less contributing and the total emission is completely dominated by thermal dust emission and free-free emission. Foreground maps derived by PLANCK data in the high frequency bands centered at 100, 143, 217, 353, 545 and 857 GHz will allow a more precise determination of the particular contributions and are expected to be published soon.

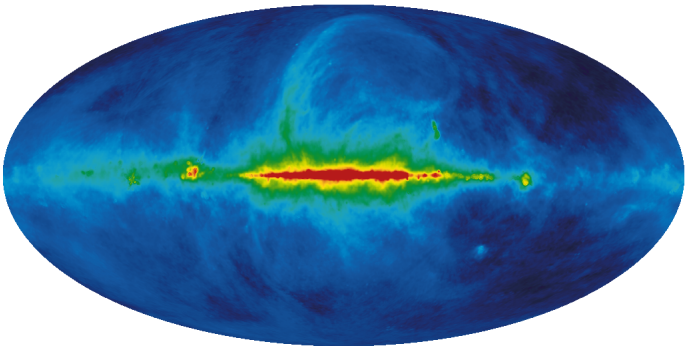

Figure 3.14.: The synchrotron dominated Haslam 408 MHz all-sky map in healpix format[130]. It has been derived by composing several radio continuum surveys and contributions from strong point sources have been mitigated. The temperature shown on the logarithmic z-axis ranges from 10 to 250 K . Figure taken from [128].

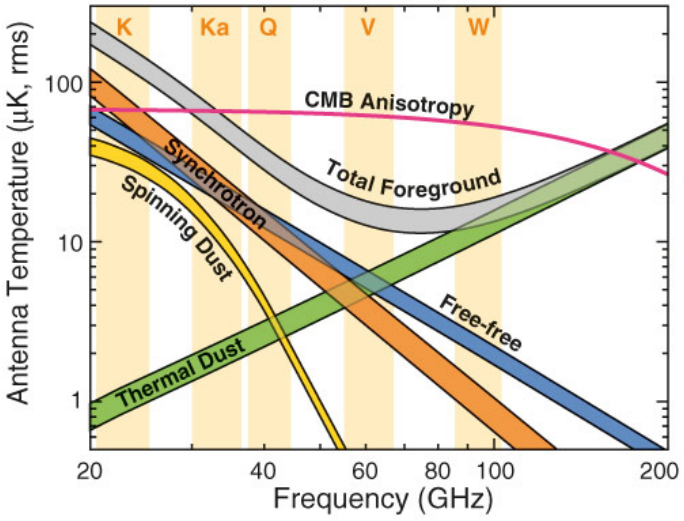

Figure 3.15.: Contributions to the photon emission in the frequency range between 20 and 200 GHz as derived by 9 year data of WMAP. The frequency bands in which WMAP is measuring the photon emission are shown by the orange bands. Above frequencies of ~ 60 GHz the total emission is completely dominated by thermal dust emission and free-free emission. Figure taken from [128].

4. Constraining Transport Parameters

4.1. Motivation and Approach

Transport models for galactic CRs based on diffusion and reacceleration are in general successful in describing most of the observations made nowadays. However, they depend on a large number of transport parameters that are partially only very poorly known and only accessible by experimental observations. In 2004, Strong et al. made every effort to determine transport parameters of diffusion-reacceleration models by comparing the models predictions computed with `GALPROP` with the most up-to-date data at that time. They proposed a model which became known as the *Conventional GALPROP model* and which is used to the present day as the basis of many analyses. However, even if experimental observations are matched, large known and unknown correlations between the transport parameters and subsequently degenerated solutions complicate a precise modeling of the transport processes and call the models implications into question. For the search for new phenomena in galactic CR physics a reliable background model, i.e. a precise knowledge of the involved transport processes and the related transport parameters, is of crucial importance in order to investigate, quantify and identify a possible signal. Uncertainties of the related transport parameters resulting from the uncertainties of the experimental data have to be taken into account. Current CR precision measurements by PAMELA, FERMI and AMS-02 may give deeper insights into the transport processes and make a revisiting of the potentials and limitations of current transport models necessary. The aim of this study is to answer to following questions:

- How large is the degree of conformity of the predictions of current diffusion-reacceleration-convection transport models to different current experimental measurements?
- How large are the correlations of the transport parameters and which implications follow from the resulting degeneracies of the obtained solutions?
- How well can the transport parameters be constrained and are there conform, exotic combinations of transport parameters which are not known and were not considered so far?

Since the investigation of transport parameters is problem of high dimensionality with typically 6 to 16 free parameters and the computation of the solution of the transport equation is generally slow, simple minimization or scan algorithms are not feasible. Therefore statistical sampling methods, like MCMC, are commonly adopted. Such analyses were

already made in the past, however, either simplified models with semi-analytical solving methods were used [131] or, in case fully numerical solutions have been applied, relatively strong constrained models have been analyzed, e.g. [68].

In this work MCMC sampling methods are used to investigate extraordinary wide ranges of transport parameters. The investigated model setup depends on 16 free parameters, describing the particles injection spectrum, the properties of the diffusion and diffusive reacceleration processes, a possible convective transport mode and the diffusion volume. The solution to the full transport equation is obtained by using the `DRAGON` code, taking into account energy losses, particle losses and secondary particle production for which realistic distributions of the galactic gas and the galactic magnetic field are used. The large computational effort is handled by a great number of modern computing nodes[1]. The hardware in combination with a sophisticated MCMC algorithm allows an evaluation of several models in parallel by which more information about the parameter space can be obtained while the computation time is kept down. In addition, iterative steps with different proposal algorithms are used in order to increase the sampling efficiency by taking advantage of already collected information about the parameter space. The predictions of each evaluated model are compared to the latest, most precise measurements of primary nuclei, secondary nuclei, ratios of secondary-to-primary nuclei and ratios of radioactive nuclei and the degree of conformity, i.e. the model's goodness, is quantified.

4.2. A Markov Chain Monte Carlo Interface to DRAGON

In this section a MCMC interface to the `DRAGON` code is introduced. At first, the basic principle of MCMC is highlighted. Afterwards, different decision algorithms and proposal algorithms used in this work will be addressed and their realization through the usage of different computing tools is described.

4.2.1. Principle of Markov Chain Monte Carlo

Especially for the investigation of high dimensional problems and time consuming computations simple minimizing or scan algorithms reach their limits in terms of feasibility. Bayesian methods have become increasingly popular in modern statistical analyses in a broad spectrum of scientific fields. Especially MCMC methods enjoy great popularity since they are in general easy to implement and to analyze. MCMC methods are based on bayesian statistics and are a class of algorithms that allow the estimation of an unknown Probability Density Function (PDF). For this purpose a *Markov chain* is constructed by sampling the parameter space that has the unknown PDF as its equilibrium distribution. Hence, the time a Markov chain spends in a particular region of the parameter space is directly proportional to the unknown PDF leading to an efficient sampling of interesting regions. The accuracy by which the equilibrium distribution is described by the sampled distribution depends on the number of accepted states. Therefore, the Markov chain should be as long as possible and ideally infinite.
Bayes theorem follows from the bayesian interpretation of the probability. The probability quantifies the state of belief connected to a hypothesis and can have values different from 0 and 1, in opposition to the frequentist's view. In a general form the Bayesian theorem for two states A and B can be expressed by

$$P(A|B) = \frac{P(B|A) \cdot P(A)}{P(B)}. \tag{4.1}$$

[1] bwGRID - Computing Grid of Baden-Württemberg

Herein P(A) and P(B) are the probabilities for A and B and P(A|B) and P(B|A) are the probabilities of A given B and B given A, respectively. The theorem links the degree of belief before and after accounting for evidence.

Assume a set of N parameters which represents a particular model:

$$\theta = \{\theta_1, \theta_2, ..., \theta_N\} \tag{4.2}$$

The degree of belief in the model is obtained by comparing the model's predictions with experimental data. Applying Bayes theorem gives

$$P(\theta|data) = \frac{P(data|\theta) \cdot P(\theta)}{P(data)}. \tag{4.3}$$

$P(\theta|data)$ corresponds to the desired PDF and $P(data)$ is the data probability which does not depend on the model's parameters so that it can be taken as a normalization factor. $P(data|\theta)$ is the likelihood $\mathcal{L}$ of the model describing the data. $P(\theta)$ is the prior probability, i.e. the degree of believe before observing the data. In order to obtain information about the single parameters θ_i the posterior density is integrated over all other parameters, called *marginalization*.
In practice, a Markov chain is generated by starting from a set of parameters with arbitrary values $\theta^0 = \{\theta_1^0, \theta_2^0, ..., \theta_N^0\}$. A MCMC proposal algorithm that for instance draws numbers from a simple Gaussian distribution in each dimension centered at the current value, proposes a new set of parameters θ^1. Whether the proposed model is added to the Markov chain or not is decided by a MCMC decision algorithm which takes the likelihoods of both models θ^0 and θ^1 into account. An often used algorithm is the *Metropolis-Hastings* algorithm [132] which uses the ratio of the likelihoods as a decision probability. Depending on the decision a new model is proposed either from θ^0 or from θ^1 in case the proposed model was added to the chain. The procedure is repeated until a sufficient amount of samples is collected and the length of the chain is sufficient for a statistical analysis.
MCMC sampling algorithms are in general easy to implement, however a reasonable configuration and a precise inspection and understanding of the behaviour of the algorithm is of crucial importance. Of particular importance is to ensure that the whole parameter space can be examined, e.g. if the step size of the proposal algorithm is chosen to be too small the algorithm will stuck in a certain region of the parameter space and will never explore regions that might be interesting as well. There is also the complicating fact that each parameter influences the likelihood differently strong and a characteristic step size for each parameter has to be found independently. The number of accepted models divided by the number of rejected models, the so called *acceptance rate*, has to be examined with due care. It strongly depends on the chosen step size and the acceptance criterion and indicates the *efficiency* of the Markov chain. If it is too high by choosing too small step sizes or a too slacky acceptance criterion the Markov chain has to be run very long until it represents the equilibrium distribution. The same applies to too low acceptance rates where only few models are added to the chain and the Markov chain has to be run very long until a sufficient amount of samples is collected. As a rule of thumb the acceptance rate should not fall below 10% and not exceed values of 50% for a reasonable efficiency. In fact, in can be shown theoretically that the ideal acceptance rate for an one-dimensional Gaussian distribution is about 50%, decreasing to approximately 23% for an N-dimensional Gaussian target distribution [133]. The quoted numbers refer to *local* acceptance rates at states where the Markov chain is believed to sample the equilibrium distribution. The

global acceptance rate usually decreases first until it approaches constant values. The reason is that randomly chosen starting points typically not yield large likelihoods and the chain has first to rummage to interesting regions before a certain, characteristic level of likelihoods is reached. This process is called *burn-in* and the models which were added to the chain during this period should not be used for a statistical analysis since the sampled distribution does not represent the desired equilibrium distribution.
In order to increase the efficiency of MCMC many sophisticated decision algorithms and proposal algorithms were developed and can be found in the literature. The following sections will highlight a selection of decision algorithms, namely the Metropolis-Hastings and the Multiple-Try-Metropolis algorithm, and three proposal algorithms that build on one another as used in [131].

4.2.2. Decision Algorithms

A widely used algorithm is the Metropolis-Hastings (MH) algorithm, which is, however, only usable to a restricted extent for high dimensional applications. As will be shown, the covered distance increases proportional to the square root of the number of dimensions leading to either high rejection rates or only locally moving Markov chains. The Multiple-Try-Metropolis (MTM) algorithm accounts for the dimensionality of the problem by utilizing multiple trials to bias the local sampling. In the following sections both algorithms will be discussed in detail.

Metropolis-Hastings Algorithm

The MH algorithm was proposed in 1970 [132] and is due to its simplicity a widely used algorithm in many MCMC applications. It dictates the acceptance probability from a current state x^0 to a proposed state x^* by which the proposed state is added to the Markov chain. Once in equilibrium the algorithm ensures, that the chain samples the target distribution. The probability for proposing a particular state x^* from the current state x^0 is given by $\pi(x^*|x^0)$. The acceptance probability α for an arbitrary, not necessarily symmetrical, proposal function than reads

$$\alpha = min\left(1, \frac{P(x^*)}{P(x^0)}\frac{\pi(x^*|x^0)}{\pi(x^0|x^*)}\right). \tag{4.4}$$

In case a symmetrical proposal function like a Gaussian distribution is used, i.e. $\pi(x^*|x^0) = \pi(x^0|x^*)$, the acceptance probability simplifies to

$$\alpha = min\left(1, \frac{P(x^*)}{P(x^0)}\right). \tag{4.5}$$

For the computation of the acceptance criterion only the likelihoods of the states x^0 and x^* enter the formula and any information about the chain's history is neglected. Since the ratio of likelihoods is used, the absolute normalization cancels.
Although the algorithm converges to the state of equilibrium in the limit of infinite sampling, the process can be very slow since a proposal function has to be assumed without any knowledge about the desired target distribution. Especially in high dimensional applications the algorithm is only of limited suitability as will be discussed in more detail. If in two dimensions x and y a Gaussian proposal function with a mean of 0 and a variance of 1 is assumed, the mean displacement is $\Delta x = \Delta y = 0$. However, the average square of the displacement is nonzero:

$$< \Delta x^2 > = \frac{1}{\sqrt{2\pi}} \int_{-\infty}^{\infty} x^2 e^{-\Delta x^2/2}\, dx = 1. \tag{4.6}$$

The square of the total average distance is

$$< r^2 > = < \Delta x^2 + \Delta y^2 > \tag{4.7}$$

and increases with the number of dimensions. In case of N dimensions and identical averaged displacements in each dimension, it can be written as

$$< r^2 > = \ N \ r_{rms}^2 \tag{4.8}$$

with the root-mean-squared step size r_{rms}^2. Therefore, the distance, calculated by $R = \sqrt{< r^2 >}$, increases with the square root of N:

$$R \ = \ \sqrt{N} \ r_{rms}. \tag{4.9}$$

This implies that if appropriate parameter step sizes for each dimension are chosen the resulting total distance R will lead to a high rejection rate. On the other hand, if the step sizes are reduced for an appropriate value of R and a reasonable acceptance rate the speed with which the chain moves through the parameter space is limited and a full exploration is prohibited.

Multiple-Try-Metropolis Algorithm

The MTM algorithm was proposed in 2000 [134] and aims to prevent the insufficiencies of the MH algorithm for high dimensional problems. It is based on utilizing multiple trial proposals to bias the local sampling. From the current state of the chain x^0 a whole set of k states $\{x^1, x^2, ..., x^k\}$ is proposed and evaluated. According to the likelihoods one state x^* is chosen from which a second set of k-1 states $\{y^1, y^2, ..., y^{k-1}\}$ is proposed and evaluated. The *weight* w between two states x and y is defined as

$$w(x, y) = P(x)\pi(x, y)\lambda(x, y). \tag{4.10}$$

P(x) is the likelihood of state x, $\pi(x, y)$ is probability for proposing state x from y and $\lambda(x, y)$ is an arbitrary, non-negative symmetric function in x and y. The simplest choice is $\lambda(x, y) = 1$.

The acceptance probability α for adding state x^* to the chain is given by

$$\alpha = min \left(1, \frac{\sum_{i=0}^{k} w(x^i, x^0)}{w(x^0, x^*) + \sum_{i=0}^{k-1} w(y^i, x^*)} \right). \tag{4.11}$$

In case a symmetrical proposal function is chosen, i.e. $\pi(x, y) = \pi(y, x)$, it is convenient to choose $\lambda(x, y) = \frac{1}{\pi(x,y)}$ and therefore $w(x, y) = P(x)$. It can be shown that the algorithm fulfills all necessary MCMC properties and converges to the state of equilibrium [134]. By comparing whole sets of models much more information about the surrounding regions in parameter space enter the acceptance criterion leading to a faster convergence. It accounts for the dimensionality of the problem leading to relatively large step sizes while the acceptance rate can be kept reasonably high. Figure 4.1 illustrates the principle of both the MH and the MTM algorithm.

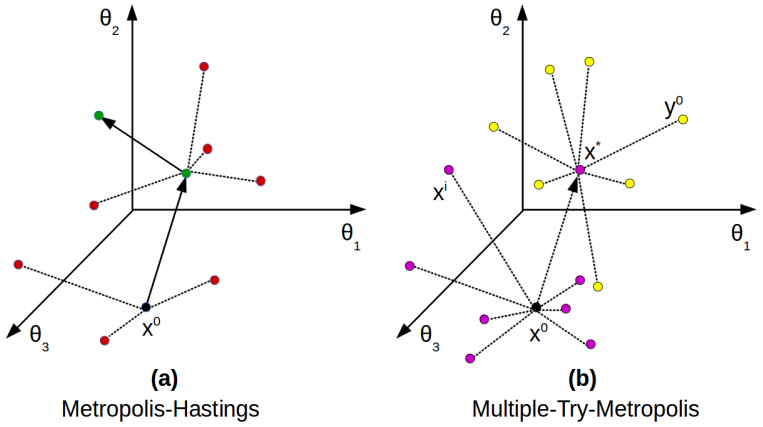

Figure 4.1.: Illustration of the Metropolis-Hastings and the Multiple-Try-Metropolis algorithm in three dimensions. The Multiple-Try-Metropolis algorithm stands out by utilizing multiple trials to bias the local sampling. To account for the dimensionality of the problem two sets of trail states (purple and yellow points) are proposed and for a single decision much more information about the surrounding regions in parameter space enters the acceptance criterion.

4.2.3. Proposal Algorithms

In the following, three different proposal algorithms as used in [131] and in this work will be discussed. They allow to exploit information on the parameter space obtained with the one(s) before leading to an increase of the efficiency of the Markov chains as necessary for time consuming applications.

Gaussian Distribution

If no information about the desired target distribution is available a common choice is to propose states according to a simple Gaussian distribution separately in each dimension, further referred to as Proposal Function I (PFI). The means of the symmetric distributions are chosen to the current state and the chosen variances correspond to the step sizes. The mean step in each dimension is 0, independent of the chosen step size. Therefore the most probable proposed state is always the current state.

Multivariate Normal Distribution

In case the N-dimensional covariance matrix is known or can be approximated, the proposal of states can be performed by drawing numbers according to the multivariate normal distribution, further referred to as Proposal Function II (PFII). Information about correlations and appropriate, characteristic steps sizes of the parameters are contained in the covariance matrix, allowing an efficient sampling of the parameter space. However, if a single covariance matrix is used, the correlations and characteristic step sizes are averaged and assumed to be identical in the whole parameter space, which is not the case in many applications.

Binary-Space-Partitioning-based

If sufficient information about the parameter space is available the parameter space can be partitioned in binary cells by which a binned map of the unknown PDF can be obtained. Each state in the parameter space is than represented by a state for which the likelihood is already known. The more information are used, the smaller are the bins and the better is the resolution. Proposed states are directly drawn from the binned approximation of the desired target distribution, further referred to as Proposal Function III (PFIII). While PFI and PFII are symmetrical proposal functions, this holds not for the binary-space-partitioning based and equations 4.4 and 4.10 have to be applied.

4.2.4. The DMCMC software package

For the realization of a MCMC based sampling of transport parameters, a MCMC interface to the DRAGON code was developed and named DMCMC. The class-based software package contains all decision and proposal algorithms mentioned above and allows a simple configuration of those. Of particular advantage is the implemented openMP (Open Multi-Processing) based parallelization by which the steady-state solution of several transport models can be calculated in parallel. This is applied to the evaluation of the two sets of transport models as used by the MTM algorithm. Information about the evolution of the MCMC is stored after each decision process and includes the outcome of the decision, the model's parameters and its degree of conformity to the data sets of the considered observables. Figure 4.2 shows a flow chart of the interface containing the most important steps.

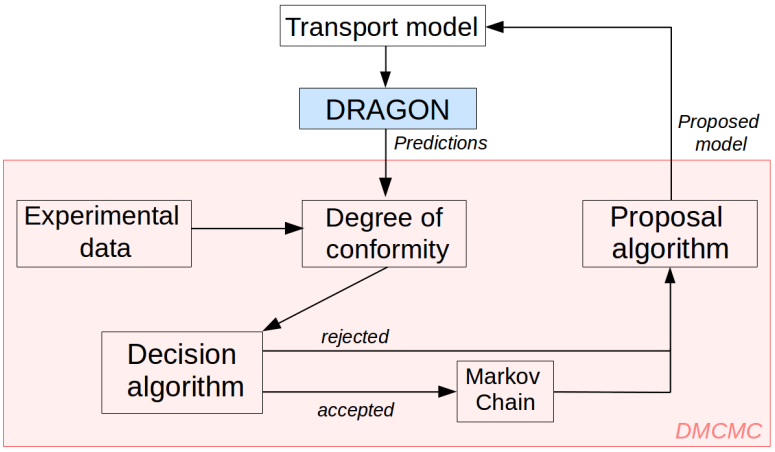

Figure 4.2.: A flow chart of the MCMC interface to DRAGON. After the predictions of an initial transport model computed with DRAGON are given to DMCMC, the degree of conformity with experimental data is determined and the decision algorithm decides whether the model is added to the Markov chain or not. The proposal function proposes a new model that is given to DRAGON for evaluation and the process repeats until the Markov chain is sufficiently long.

χ^2 Calculation

In order to quantify a model's goodness for describing the data a χ^2 calculation is performed. A model's total χ^2 value is the sum of the individual χ^2 values obtained for the different observables. Since these are sensitive to different transport parameters each χ^2 value is normalized to the corresponding number of data points for a fair weighting of the observables. The quantity used to define a model's goodness, denoted as $\bar{\chi}^2$, is defined accordingly and re-weighted by the number of data point and observables:

$$\bar{\chi}^2 = \frac{N^d}{N^o}\left(\sum_j^{N^o}\frac{\chi_j^2}{N_j^d}\right) \quad \text{with}$$
$$\chi_j^2 = \sum_{i=0}^{N_j^d}\left(\frac{\phi_{i,j}^D - \phi_{i,j}^M}{\sigma_{i,j}^D}\right)^2 . \tag{4.12}$$

The index j runs over all observables N^o and the index i over all data points N_j^d of observable j. $\phi_{i,j}^M$ is the model's prediction and $\phi_{i,j}^M$ the corresponding experimental measurement

with uncertainty $\sigma^D_{i,j}$. A descriptive quantity is the χ^2 value reduced to the number of degrees of freedom (Ndof). The latter are calculated by the total number of data points minus the number of free parameters of the applied model. The value of $\chi^2/Ndof$ represents the level of agreement between the measurements and the model and is used to determine the goodness of a model. For a reasonable description of the data $\chi^2 \approx Ndof$ is expected since the mean of the corresponding χ^2 distribution is equal to Ndof. Values of $\chi^2/Ndof \gg 1$ indicate a poor description of the data by the hypothesized model.

Technical Details

In the following, technical details about the generation of pseudo random numbers and the realization and implementation of the proposal functions are given. Pseudo random numbers for the Monte Carlo method are generated by the Mersenne-Twister pseudo random number generator [135] as implemented in the class *TRandom3* which is part of the object oriented data analysis framework `ROOT` [136]. For the generation of random numbers according to a given multivariate normal distribution the upper triangular Cholesky factor is calculated as follows. The multivariate normal distribution for a N-dimensional covariance matrix A at $\vec{x}$ with a variance of $\vec{\mu}$ has the form

$$f(\vec{x}, \vec{\mu}, A) = \frac{1}{\sqrt{(2\pi)^N |A|}} \, exp\left(-\frac{1}{2}(\vec{x}-\vec{\mu})^T A^{-1} \, (\vec{x}-\vec{\mu})\right). \tag{4.13}$$

Herein $|A|$ is the determinant of the covariance matrix A. In order to draw a random vector $\vec{x}$ from the distribution a vector $\vec{y}$ is created whose elements are a sample of the 1-dimensional normal distribution with mean 0 and variance 1. The upper triangular Cholesky factor R of A is determined so that $A = R^T \cdot R$. The random vector can be calculated by $\vec{x} = \vec{\mu} + R^T \cdot \vec{y}$.
The binary-space-partitioning is performed by a data structure called *kd-tree*, which stands out by allowing fast access to the data. The structure is built by the `ROOT` class *TKDTree*. For the proposal of states according to the binned approximation of the PDF, now represented by the kd-tree, a Gibbs-sampler is used. A random state θ^{rnd} is produced and its Next-Neighbour (NN) in parameter space θ^{NN} is identified. According to a probability α_{NN} the random state θ^{rnd} is either proposed for evaluation or discarded. α_{NN} is given by

$$\alpha_{NN} = min\left(1, \frac{P_{NN}}{P_{max}}\right). \tag{4.14}$$

Herein P_{NN} is the probability of the NN of the initial random state and P_{max} is the maximal probability of all states contained in the kd-tree. The procedure is repeated until a random state is proposed for evaluation.

4.2.5. Performance Optimization

The `DMCMC` package was tested and optimized on performance using a realistic transport model setup. The applied configuration by which a good coverage and efficiency were achieved will be discussed in the following.

Coverage

In order to propose models according to 1-dimensional Gaussian distributions appropriate variances dictating the average step sizes have to be provided. The chain's coverage of the parameter space was analyzed for different step sizes by the inspection of so called *trace*

plots showing the temporally evolution of transport parameters. It was found, that an appropriate coverage is achieved if the variances of the parameters are set to 80% of the parameter range as illustrated in figure 4.3.

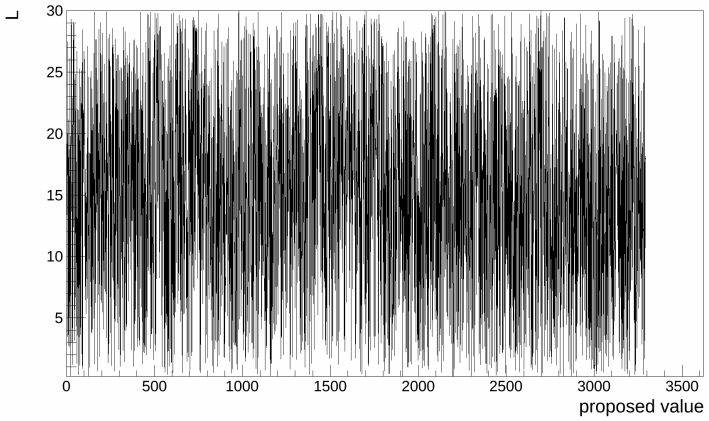

Figure 4.3.: Trace plot of the halo height L. Shown is the evolution of the proposed values for L with time. A reasonable coverage of the whole allowed range of 0.25 kpc $<$ L $<$ 30 kpc is achieved by using variances of 80% of the allowed range.

Sampled Distribution

The quantity usually maximized by a MCMC is the likelihood $\mathcal{L}$ or rather the log-likelihood, connected to χ^2 by

$$\mathcal{L} \propto e^{-\chi^2/2}. \tag{4.15}$$

However, Markov chains running on the likelihood derived with a realistic transport model setup showed, that the likelihood distribution is highly non-uniform and changes dramatically on small scales. The obtained χ^2 values covered more than 20 orders of magnitude. The consequences are either acceptance rates of 0, i.e. the chains immediately stuck in a certain region of the parameter space, or insufficiently moving chains if the step sizes are chosen to be exceedingly small. A possible way out is the artificial softening of the real likelihood distribution. The transformation of the distribution, from now on called *fitness distribution*, was determined empirically by demanding reasonable acceptance rates and a sufficient coverage. The best performance was achieved by defining a model's fitness $\mathcal{F}$ to

$$\mathcal{F} \equiv \frac{1}{(\bar{\chi}^2/N^d)^n} \quad \text{and} \quad n \approx 2.7. \tag{4.16}$$

Sampling according to the fitness distribution instead to the likelihood distribution is a strong intervention to the MCMC algorithm. The derived distributions do not represent a PDF in the proper sense which prohibits a statistically correct interpretation of the states associated to the Markov chain in terms of confidence.

By using the defined fitness and the chosen variances all demands in terms of performance and efficiency could be matched. An illustration of the performance of the MH and MTM algorithm can be found in Appendix B.1.

4.3. Transport Model Setup

The solution to the transport equation is obtained for a cylindrical symmetry. In r-direction the grid resolution is set to $\Delta r = 1$ kpc and in z-direction to $\Delta z = 200$ pc, independently of the halo height L. Typical runtimes for the applied resolution vary from several minutes to several hours, depending on the chosen halo height. The model depends on 16 free parameters describing diffusion, diffusive reacceleration, convection, the halo height, beyond which free escape of particles is assumed, and a twice broken injection spectrum. In addition, 4 parameters accounting for the solar modulation of CR particles are included.

The applied SNR distribution is the one proposed by Yuan et al. [86] as it is a good compromise to other, more extreme distributions proposed in the literature, see figure 3.4. It should be noted that the choice of the SNR distribution only marginally affects the modeled spectra at Earth, but highly influences the proton distribution and therefore the expected gamma-ray flux in the Galaxy.
The nuclei injection spectrum is described by a power law in momentum $dq(p)/dp \propto p^{-\alpha}$. It is assumed to be equal for all nuclei species and is allowed to be broken twice at ρ_0, ρ_1 leading to three slopes α_0, α_1, α_2.
The spatial diffusion coefficient is taken to be constant and isotropic in the Galaxy and is parameterized by

$$D_{xx}(\rho) = D_0 \beta^\eta (\frac{\rho}{\rho_0})^{\delta(\rho)}, \tag{4.17}$$

with $\rho = p/(Ze)$ being the rigidity of the particle of charge Z and momentum p. The normalization is given by the diffusion constant D_0. The rigidity dependence given by δ is allowed to be different below and above the rigidity ρ_b, leading to $\delta(\rho \leq \rho_b) = \delta_l$ and $\delta(\rho > \rho_b) = \delta_h$. The reference rigidity is fixed to the commonly used value $\rho_0 = 4$ GV. η dictates the low energy behaviour of $D(R)$ and is phenomenologically motivated. It can take low energy effects like the dissipation of Magnetohydrodynamics (MHD) waves originating from their resonant interaction with CRs into account, which is not considered in the derivation of the diffusion equation. The strength of diffusive reacceleration is given by the Alfvén velocity v_A according to equation 3.8.

Since the spatial dependence of a possible convection velocity $V_c(r, z)$ is basically unknown, 4 parameters are dedicated for its description. The radial dependence of the convection velocity is allowed to be proportional to the source strength of CRs, i.e. to the assumed SNR distribution as first used in [76]. This takes care of the increased CR pressure close to the maximum of the source distribution. The strength of the radial dependence is dictated by α_r:

$$V_c(r, z) \propto Q(r)^{\alpha_r} \tag{4.18}$$

The z-dependence of $V_c(r, z)$ is described by three parameters, namely v_0, v_b and dV_c/dz, which allow a parabolic shape and a smooth transition from the base velocity v_b at $z = 0$ kpc to v_0 at $z = 0.1$ kpc. The gradient by which V_c increases above $z = 0.1$ kpc is given by dV_c/dz, see figure 4.4.

The solar modulation is treated by the force-field approximation introduced in chapter 3.2.3.5. Since its strength is strongly model dependent the effective modulation potentials are fitted to the corresponding data sets after the particles were propagated. They are allowed to be different for data sets recorded during different epochs of the solar activity

and oppositely charged particles. The potentials do not enter the MCMC process directly, i.e. they are not part of the proposal process.

Table 4.1 lists the transport parameters and the selected limits for the MCMC sampling. The parameter ranges were chosen exceedingly wide, especially for the diffusion constant, the rigidity dependence, the Alfvén velocity and the halo hight. For handling several orders of magnitude of the diffusion constant it is convenient to use $log(D_0)$ instead of D_0 and many results are quoted dimensionless as $log(D_0)$. Also shown are the 4 modulation potentials and the applied limits used for the optimization. The used observables and data sets are listed in table 4.2. For a description of the sensitivity of the chosen observables to the transport parameters and their constraining power the reader is referred to chapter 3.3.

A note on the transport model setup

Using a model setup with such a high number of degrees of freedom seems to be exaggerated, since successful models with much less degrees of freedom are already known and usually preferred. However, known and unknown degeneracies of the obtained solutions and the negligence of possible transport processes like convection call the models implications into question. This study does primarily not aim to find a best-fit model as this would only allow model dependent statements. Instead, a wide parameter space of transport parameters is investigated in which many uncertainties are included in order to draw reasonable conclusions about the preferred values and limits of the major transport parameters. If the data prefer less complicated models like for instance models with an unbroken injection spectrum, the MCMC will automatically concentrate on these kind of models and the evaluated models will simplify in a very natural way. The same holds for whole transport processes which are allowed to vanish by a respective choice or a natural MCMC based preference of the corresponding transport parameters.

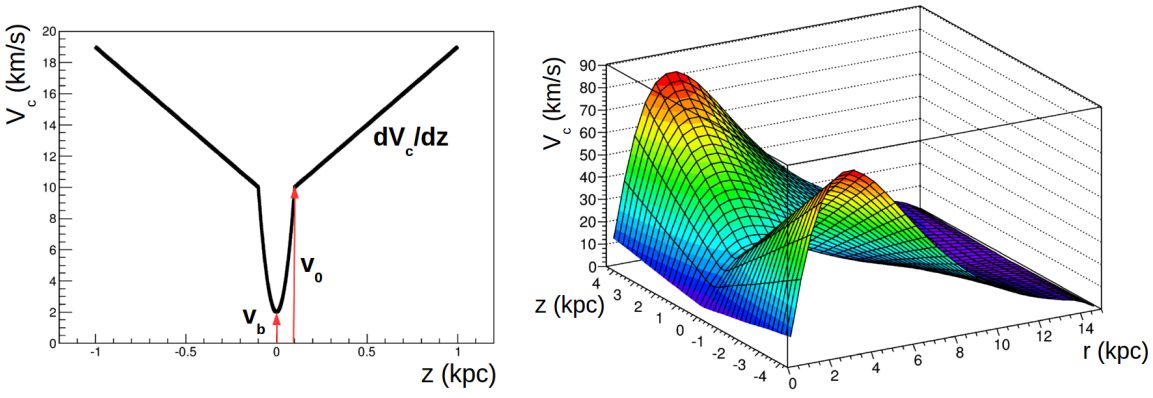

(a) (b)

Figure 4.4.: Illustration of the parametrization of the convection velocity. The z-dependence **(a)** is fixed by v_0, v_b and dV_c/dz describing a parabolic shape with a smooth transition from v_b at z=0 kpc to v_0 at z=0.1 kpc. In **(b)** the r-dependence is coupled to the SNR source distribution with strength $\alpha_r = 1$. The butterfly shaped increase in z is caused by dV_c/dz ($v_b = v_0$).

Table 4.1.: The 16 transport parameters and their selected limits used for the MCMC sampling. Extraordinary wide limits were chosen to investigate a large parameter space. The lower panel shows the 4 modulation potentials used in the force-field-approximation that are fitted for each model to the corresponding data and do not enter the MCMC directly.

Parameter	Unit	Lower limit	Upper limit
D_0	$10^{28}\mathrm{cm}^2/\mathrm{s}$	10^{-3}	10^4
δ_l/δ_h	1	0.0/0.0	1.2/1.2
ρ_δ	GV	0.0	3500
L	kpc	0.25	30.0
η	1	-2.0	2.0
v_α	km/s	0.0	70.0
v_0	km/s	0.0	200.0
$f_b \equiv v_b/v_0$	1	0.0	1.0
dV_c/dz	km/s/kpc	0.0	100.0
α_r	1	0.0	1.0
ρ_0	GV	0.0	100.0
ρ_1	GV	100.0	1000.0
α_0	1	0.0	3.0
α_1	1	0.0	3.0
α_2	1	0.0	3.0
Φ_p	MV	0.0	1000.0
Φ_{pb}	MV	0.0	1000.0
$\Phi_{B,C}$	MV	0.0	1000.0
$\Phi_{^{10}Be,^9Be}$	MV	0.0	1000.0

Table 4.2.: Considered observables and used experimental data sets.

Observable	Experiments
Proton spectrum	PAMELA [121]
Antiproton spectrum	PAMELA [122]
Proton/Antiproton	PAMELA [122]
Boron/Carbon	ACE [119], CREAM[117], ISOMAX[120]
^{10}Beryllium/^{9}Beryllium	HEAO [118], ISOMAX [120]

4.4. Results of the Markov Chain Monte Carlo

The transport parameters of the employed model were sampled with the MTM algorithm in the framework of the `DMCMC` package using the entire constraining power of the observables listed in table 4.2. The three proposal functions were used one after another to collect information about the parameter space that were used by the following one. For each of them, several hundred Markov chains with identical configuration were run until a sufficient number of accepted models was achieved and the sampled distributions didn't change essentially anymore. The collected information about the parameter space obtained up to this point were additionally used to sample transport parameters for each individual observable separately, using directly the binary-space-partitioning-based proposal function. Table 4.3 shows an overview of the executed Markov chains and the obtained number of sampled and accepted models, respectively. In total, about 14 million transport models

have been evaluated. These include beside the listed ones also models evaluated during test-phases and phases of optimization. Details on the performance of the Markov chains, especially in terms of the individual proposal functions, can be found in Appendix B.3.

In this chapter the large amount of data is analyzed whereat special importance is given to the preferred, allowed and excluded parameter ranges as well as to trivial and non-trivial correlations between the transport parameters. At first, the obtained density distributions are analyzed for the different observables and the preferred parameter ranges are qualitatively illustrated. Subsequently, the parameter space and the sampled models are analyzed quantitatively by their χ^2 value. A selection of the most interesting, data-conform models is presented and their implications are discussed. Finally, a reduced, minimal transport model setup is constructed and its potential and implications are discussed. For reasons of clarity and comprehensibility not all transport parameters will be discussed with the same attention in this chapter. Some of the parameters were found to be of minor importance and their discussion is shifted to the Appendix.

Table 4.3.: Summary of the executed Markov chains. Shown are the used observables, the applied proposal functions and the number of sampled and accepted models for each case. The proposal function III-A is based on a kd-tree containing all sampled models derived with I and II. The kd-tree for III-B was built by using all sampled models from I, II and III-A. Noticeable are the varying acceptance rates depending on the proposal function and the target distribution, respectively.

Observables	Proposal function	Markov chains	Sampled models	Accepted models	∅ acceptance
all	I	270	1,421,149	15,393	0.17
all	II	520	1,072,938	30,521	0.43
all	III-A	480	5,042,021	24,221	0.07
p	III-B	100	1,174,626	6,304	0.08
$\bar{p}$	III-B	100	1,001,171	16,433	0.25
$\bar{p}/p$	III-B	100	906,033	5,155	0.09
B/C	III-B	100	706,047	2,205	0.05
$^{10}Be/^{9}Be$	III-B	100	990,002	21,023	0.32

4.4.1. Density Distributions

The majority of the sampled models do not describe the experimental data sufficiently well and the same holds for the accepted models. However, the latter have been accepted by the decision algorithm and their statistical entirety represents a probability distribution which can be used to assign values of transport parameters to a certain probability. Since the sampling algorithm was based on the models fitness instead of their likelihood for reasons of performance (see chapter 4.2.5) the sampled distribution does not correspond to a PDF in the proper sense, but rather to a fitness-density-distribution. This prevents a statistically correct interpretation of the obtained distribution in terms of probability and a bayesian analysis is prohibited. Nevertheless, the maxima of the projected distribution on the parameters axes yield a good approximation for their most probable value and qualitative information about the probability of certain values of the individual transport parameters can be obtained. The maxima of the projected distributions represent values for which the largest potential is expected for describing the data, or in other words, values for which it is easiest. However, these values do no necessarily coincide to values of well data describing models, especially if correlations between the transport parameters exist.

On the other hand, flat distributions point either to a lack of statistics, i.e. the Markov chains have not been run long enough, to an insignificant influence of the particular parameter, but can also be caused by parameter correlations and the resulting degeneracy of the solution.
Figures 4.5 to 4.12 show the distribution of the accepted models sampled by Markov chains using all observables and individual observables for all considered parameters. The distributions were derived by a projection on the corresponding, binned parameter axis. Models accepted during the burn-in phase were not used and were subtracted before. For an estimation of the burn-in length the Gelman-Rubin diagnostic was applied, see appendix B.2 for details. The distributions are based on 18,586 (all observables), 5,109 (p), 15,233 ($\bar{p}$), 3,966 ($\bar{p}/p$), 1,119 (B/C), 19,823 ($^{10}Be/^{9}Be$) models.

D_0 and L

Figure 4.5 shows that whereas p and $^{10}Be/^{9}Be$ prefer rather high values of above $log(D_0) = 1.5$ all other observables prefer lower values of the order of $log(D_0) = -0.5$. It is not surprising that the distribution obtained with Markov chains including all observables has its maximum in an intermediate range of about $log(D_0) = 0.1$ where the best compatibility between the different experimental data sets is expected. The rather large values of D_0 as preferred to describe the proton spectrum is affiliated to less needed fine tuning of the other parameters. To which extent the models are conform with the data will be discussed in the next chapter.
The preferred halo heights L of most of the single observables do not show a clear preference. Solely $^{10}Be/^{9}Be$ disfavours values below $L = 14$ kpc and shows a relatively flat distribution above. The distribution derived by using all observables yields preferred values of around $L = 10$ kpc, slightly decreasing for lower and larger values, whereas a constant plateau above $L = 20$ kpc is present. This beaviour seems to be contradictory since obviously no single observable prefers values of $L = 10$ kpc as they do in common. This can be ascribed to the correlation between D_0 and L: The halo height is indirectly constrained by the natural concentration of a much more narrow range of D_0 as demanded for agreement with the different observables.

v_α, ρ_b, δ_l, δ_h and η

Figures 4.6 and 4.7 show the corresponding distributions for v_α, ρ_b, δ_l and δ_h. While B/C prefers values of the order of $v_\alpha = 30$ km/s, p and $\bar{p}$ prefer much lower values of $v_\alpha \approx 4$ km/s. The overall preferred range lies by trend in the lower allowed region, compatible with $v_\alpha = 0$ km/s, and is steadily decreasing towards higher values. The preferred values for δ_l are rather high at the order of $\delta_l = 0.9$ which is basically forced by B/C, $\bar{p}$ and $^{10}Be/^{9}Be$ that prefer even larger values. p prefers lower values below $\delta_l = 0.5$ whereby the distribution of $\bar{p}/p$ has its maximum consistently in the intermediate range $0.7 < \delta_l < 0.9$. The distribution of δ_h is indeed maximal in the range $0.6 < \delta_h < 1.0$, but is also washed out and much more flat due to the fact that the transition from δ_l to δ_h at ρ_b lies predominantly at high rigidities of $\rho_b > 2000$ GeV at which no sensitivity to the data is achieved. Both the high values of ρ_b and the similarity of δ_l and δ_h suggest that the rigidity dependence may be sufficiently described by a single parameter $\delta = \delta_l = \delta_h$ and a break is redundant.The distribution of η shows a maximum in the range -1.8 < η < -1.2 and decreases towards higher values with slightly, locally preferred region at around $\eta = 0.7$. This can not be affiliated to the particular single observables all of which prefer larger values if considered separately.

Injection spectrum

The injection index α_0 shows a clear preference to values of $\alpha_0 \approx 2.35$ and α_1 to slightly higher values of $\alpha_1 \approx 2.45$ which is forced by the proton and antiproton data. α_2 is

much less constrained and shows two preferred sectors around $\alpha_2 \approx 0.8$ and $\alpha_2 \approx 2.75$. Important are the positions of the breaks ρ_0 and ρ_1 at which the transitions between the injection indices occur. ρ_0 shows a relatively flat distribution with only slightly preferred values of 40 GeV $< \rho_0 <$ 55 GV as well as around $\rho_0 \approx 94$ GV. Values close to 0 make ρ_0 and α_0 redundant and can be neglected. ρ_1 prefers the range 680 GeV $< \rho_1 <$ 780 GV. This is affiliated to the non-power-law-like slope of the proton spectrum as measured by PAMELA at kinetic energies above several hundred GeV.

Convection

The overall preferred convection velocity is found to be rather low. The distribution of v_0 shows preferred values compatible with $v_0 = 0$ km/s with decreasing probability towards larger values. This is demanded by all observables except p which does not show a clear preference. A similar behaviour is shown by dV_c/dz whose probability is also decreasing towards larger values but, however, prefers non-zero values in the range $2 < dV_c/dz <$ 16 km/s/kpc. This is a consequence of the contradictive demands of B/C which prefers much larger values of $dV_c/dz \approx 90$ km/s/kpc and $^{10}Be/^{9}Be$ demanding values compatible with $dV_c/dz = 0$ km/s/kpc. The base convection velocity v_b at $z = 0$ kpc described and sampled as the fraction of v_0 with $f_b = v_b/v_0$, shows two maxima above and below $f_b = 0.4$, whereat B/C demands rather low values of $f_b < 0.1$. In opposition to $^{10}Be/^{9}Be$ lower values are by trend also slightly preferred by the other observables. The strength by which the radial convection velocity follows the SNR distribution, described by α_r, shows a quite flat distribution which can be affiliated to the low convection velocities in general by which the parameter's sensitivity is reduced. A slight concentration is found to be at values below $\alpha_r = 0.4$ but a meaningful conclusion can not be drawn.

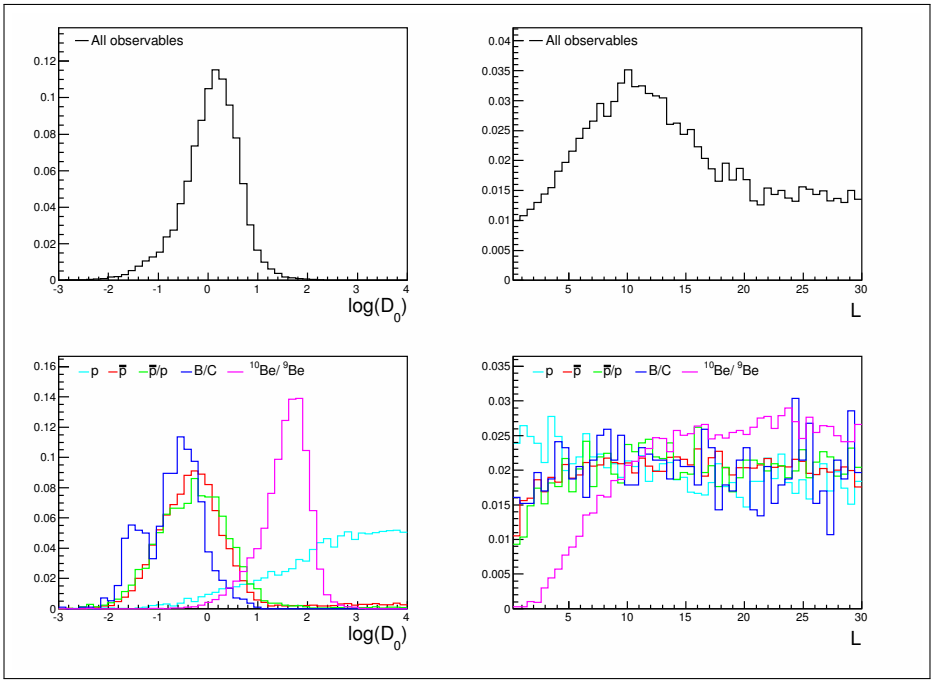

Figure 4.5.: Density distributions for D_0 **(left)** and L **(right)**. The distributions represent the normalized number of models accepted by the MCMC algorithm projected on the binned parameter axis. Shown are distributions obtained by Markov chains in which all observables were considered **(top)** and respective distributions obtained by considering particular observables exclusively **(bottom)**.

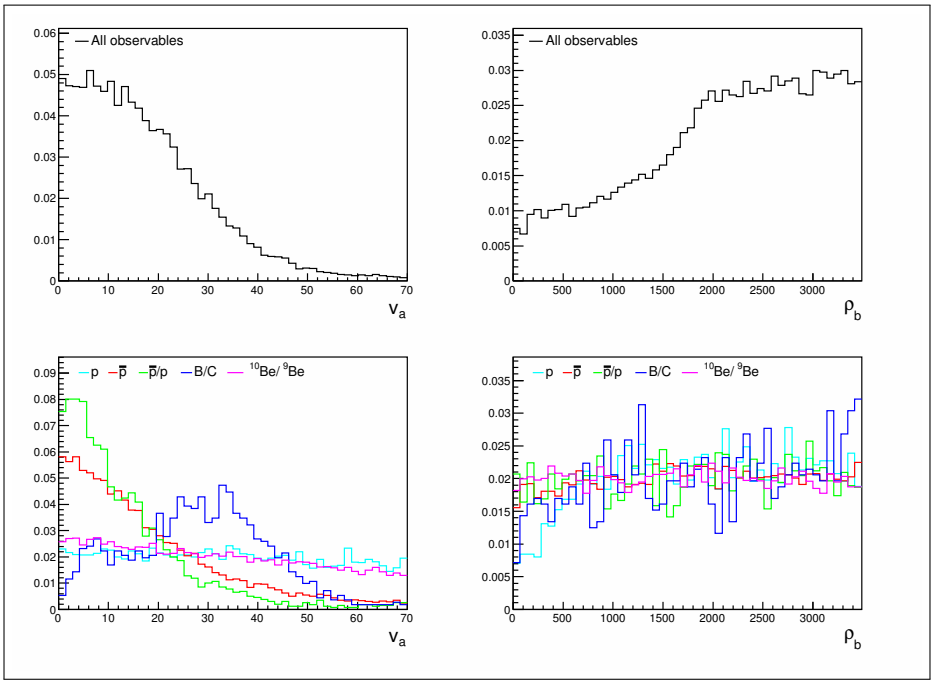

Figure 4.6.: Density distributions for v_α **(left)** and ρ_b **(right)**. The distributions represent the normalized number of models accepted by the MCMC algorithm projected on the binned parameter axis. Shown are distributions obtained by Markov chains in which all observables were considered **(top)** and respective distributions obtained by considering particular observables exclusively **(bottom)**.

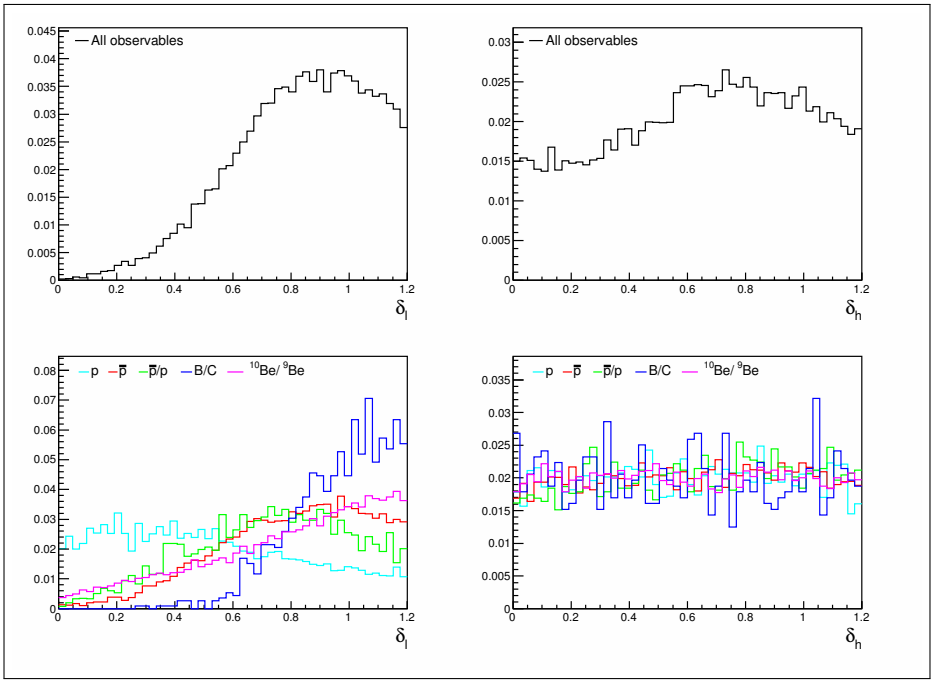

Figure 4.7.: Density distributions for δ_l **(left)** and δ_h **(right)**. The distributions represent the normalized number of models accepted by the MCMC algorithm projected on the binned parameter axis. Shown are distributions obtained by Markov chains in which all observables were considered **(top)** and respective distributions obtained by considering particular observables exclusively **(bottom)**.

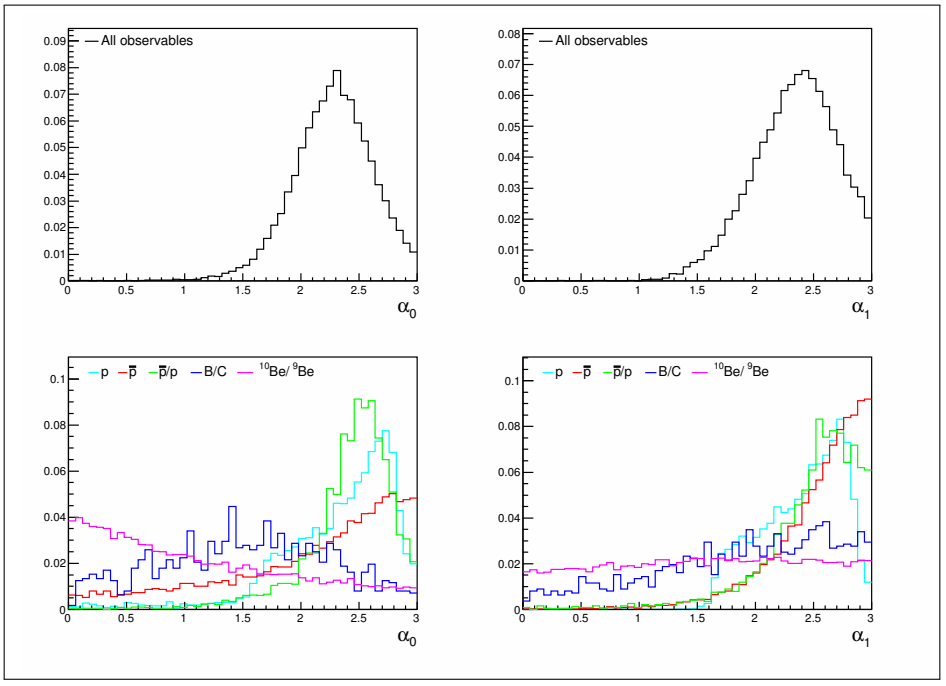

Figure 4.8.: Density distributions for α_0 **(left)** and α_1 **(right)**. The distributions represent the normalized number of models accepted by the MCMC algorithm projected on the binned parameter axis. Shown are distributions obtained by Markov chains in which all observables were considered **(top)** and respective distributions obtained by considering particular observables exclusively **(bottom)**.

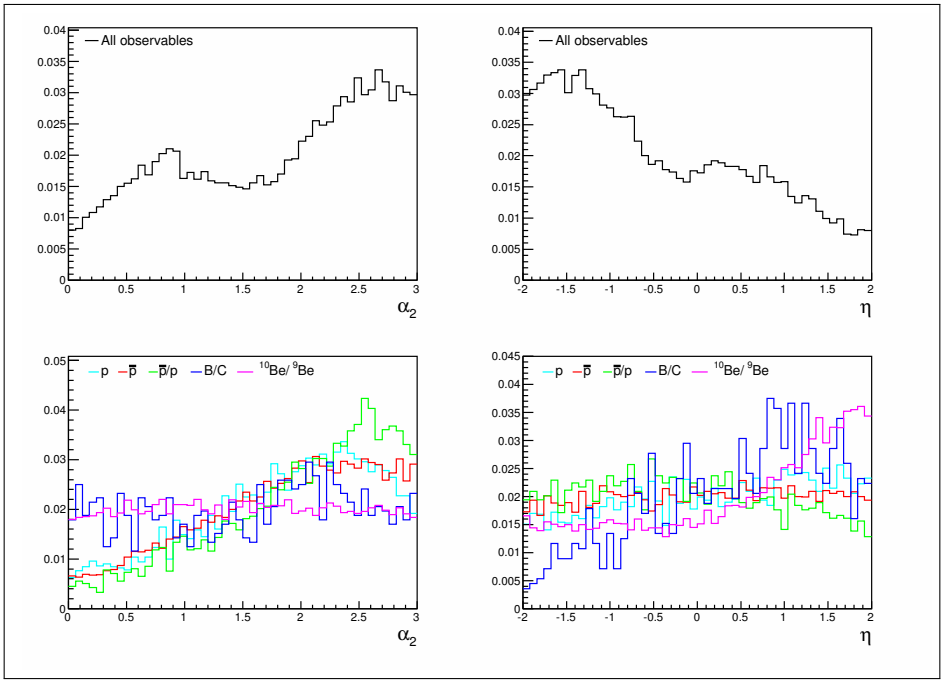

Figure 4.9.: Density distributions for α_2 **(left)** and η **(right)**. The distributions represent the normalized number of models accepted by the MCMC algorithm projected on the binned parameter axis. Shown are distributions obtained by Markov chains in which all observables were considered **(top)** and respective distributions obtained by considering particular observables exclusively **(bottom)**.

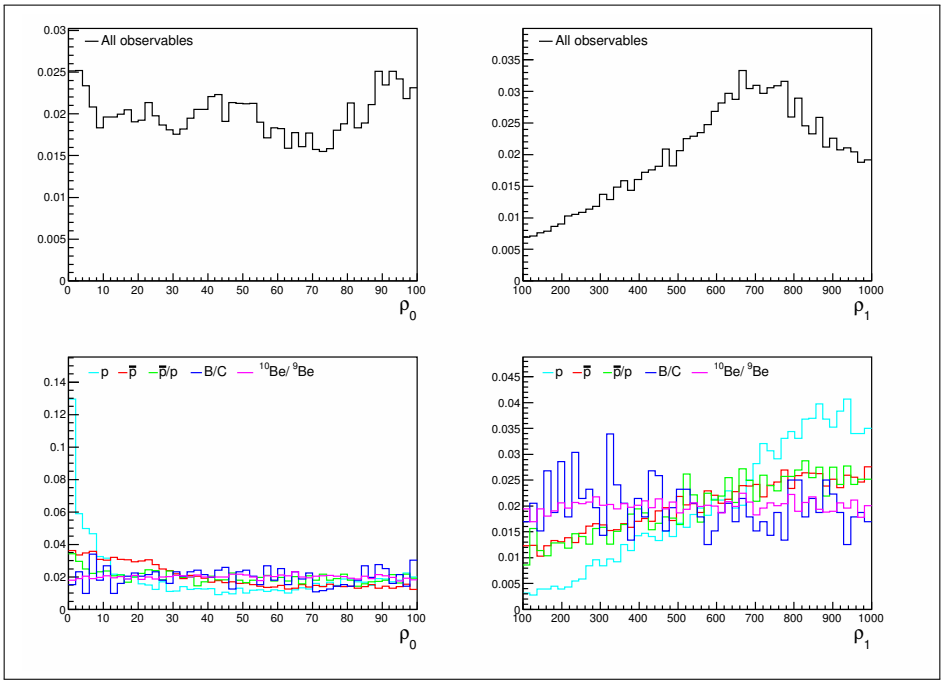

Figure 4.10.: Density distributions for ρ_0 **(left)** and ρ_1 **(right)**. The distributions represent the normalized number of models accepted by the MCMC algorithm projected on the binned parameter axis. Shown are distributions obtained by Markov chains in which all observables were considered **(top)** and respective distributions obtained by considering particular observables exclusively **(bottom)**.

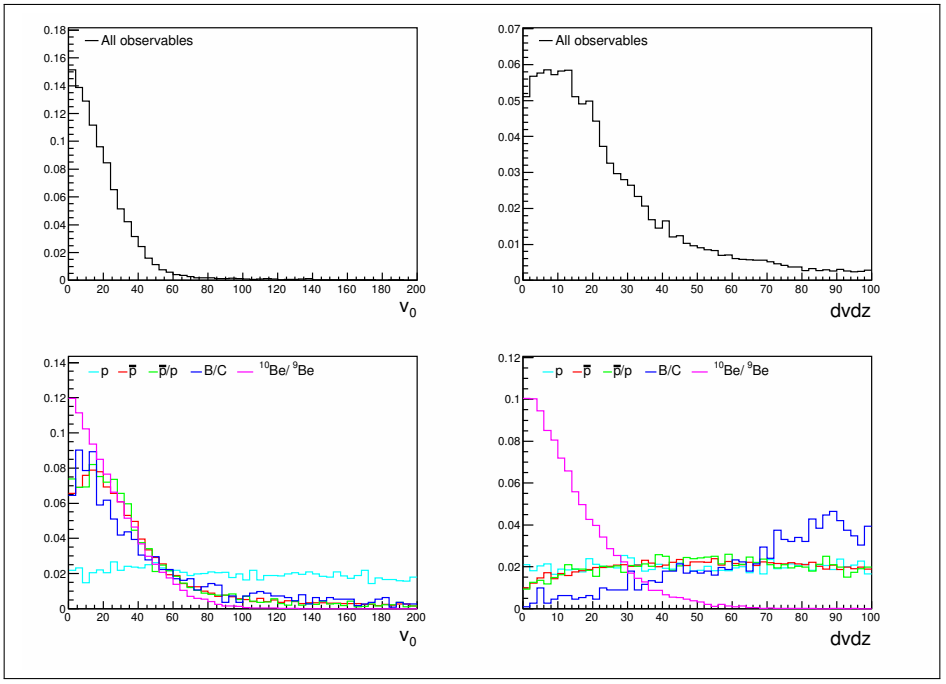

Figure 4.11.: Density distributions for v_0 **(left)** and dV/dz **(right)**. The distributions represent the normalized number of models accepted by the MCMC algorithm projected on the binned parameter axis. Shown are distributions obtained by Markov chains in which all observables were considered **(top)** and respective distributions obtained by considering particular observables exclusively **(bottom)**.

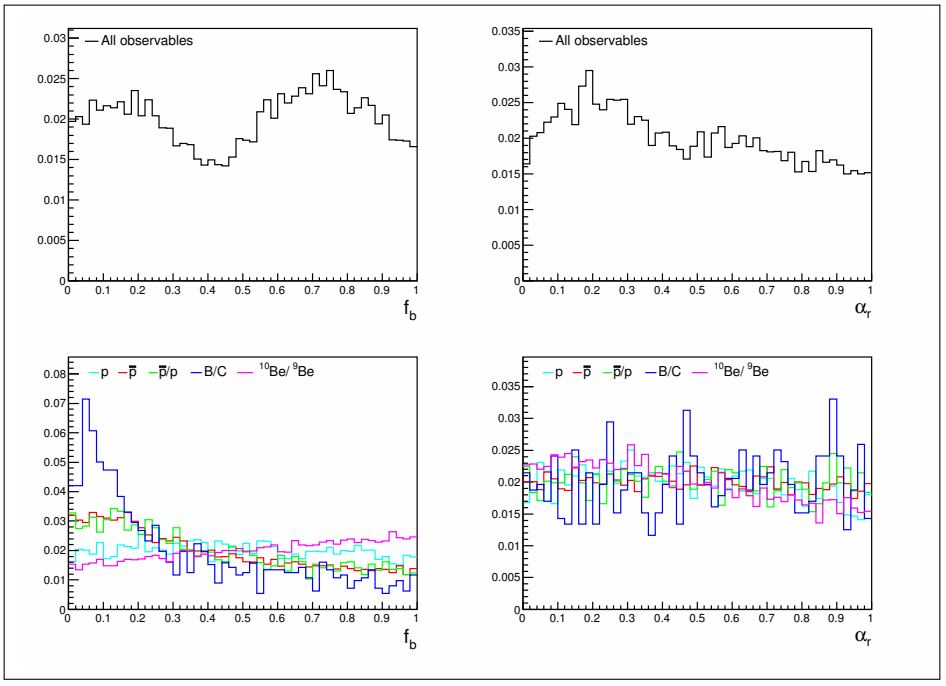

Figure 4.12.: Density distributions for f_b **(left)** and α_r **(right)**. The distributions represent the normalized number of models accepted by the MCMC algorithm projected on the binned parameter axis. Shown are distributions obtained by Markov chains in which all observables were considered **(top)** and respective distributions obtained by considering particular observables exclusively **(bottom)**.

4.4.2. χ^2-Analysis

This analysis is not restricted to the accepted models and incorporates the whole data set, consisting of 13,947,437 models. By using the MCMC technique different regions in the parameter space were sampled with a different intensity by its nature. This results by trend in lower averaged χ^2 values in regions which were strongly biased by the MCMC, i.e. in regions favoured by the entirety of the observables and the particular ones. The parameter space is now analyzed by the obtained minimal $\chi^2/Ndof$ values, illustrated by a projection of the transport parameters in binned, 2-dimensional planes. For reasons of clarity, only the representations in parameter planes yielding the most conspicuous behaviour are shown (see fig. 4.13). The remaining illustrations can be found in Appendix C.2. For a direct affiliation of the observed behaviour to a particular observable the projections are also shown for the χ^2 values of each observable separately in Appendix C.1. In the following, the influence on the models predictions and the found correlations of the dominating transport parameters are discussed.

Figure 4.13 shows the representation in the parameter planes (D_0, L), (D_0, v_α), (D_0, dV_c/dz), (D_0, δ_l), (α_1, δ_l) and (α_0, v_α). Overlayed are the top 97 models marked by stars. Apparent are large areas containing a substantial amount of models with comparable values of $\chi^2/Ndof \approx 1$. Also smooth transitions to areas with much higher values exist, indicating a sufficient degree of granularity. No appreciable local minima lying outside these areas are visible and the closeness of the structures suggests, that local minima within the global one are continuously connected. The correlations are non-trivial and are the result of the complex interplay between the transport parameters at different scales. They strongly depend on the absolute parameter values, e.g. the quadratic-like correlation between D_0 and L as visible in fig. 4.13(a) is strongly apparent at rather low values of $L < 5$ kpc but indistinguishable at higher values. Although the corresponding density distribution of L emblazed preferred values of around $L = 10$ kpc, no concentration of a multitude of powerful models within the enormously large parameter range is apparent. Instead, these models are equally distributed in the whole range making it impossible to exclude any of the tolerated halo heights. A discriminated examination of the χ^2 values of the particular observables emblazes how the constraining powers of the observables assemble, see fig C.8. The correlation is visible for $\bar{p}$, B/C and $^{10}Be/^{9}Be$. While the absolute value of L is not constrained by any observable, D_0 is strongly bounded below by p and B/C and bounded above by B/C.

Figure 4.13(b) shows the rejuvenescence of the range of D_0 towards higher values of v_α. The fact that by increasing v_α the range of D_0 is more constrained explains why the sampled density distribution of v_α (fig. 4.6) is maximal at low values. However, also in this case the found minimal χ^2 values show in fact a worsening above $v_\alpha = 45$ km/s but no clear preference for values below. The most constraining observables for v_α are again p and B/C: The proton spectrum strongly disfavours high v_α for low D_0. B/C disfavours high v_α for high D_0, see fig. C.9. The observed behaviour is explained by a stronger CR confinement and shorter propagation lengths for low D_0. Diffusive reacceleration is more efficient for short scattering lengths by which D_0 is correspondingly more constrained the higher v_α is.

v_α is also correlated with α_0 and α_1. While v_α is allowed to be higher the lower α_0 is, the opposite behaviour is shown by α_1 due to the different energy scale at which α_0 and α_1 influence the spectrum. The observables most sensitive to this correlation are $\bar{p}/p$ and B/C, see fig. C.13.

Figures 4.13 (a) - (c) show the remaining transport parameters for which the strongest

correlations were found. The largest data-conform values for dV_c/dz are found for low values of D_0, so an increase of dV_c/dz can be counterweighted by a non-linearly lowering of D_0. The same holds for v_0 for which the largest, data-conform values are found for rather low values of D_0. It is explained by the faster escape of CR particles due to high convection velocities which is balanced by a stronger confinement resulting from lower D_0. Since both the convection velocity and v_α are correlated with D_0, high convection velocities also accompany by trend with low v_α and vice versa. This is demanded by $\bar{p}$ and B/C as shown in fig. C.10.

The observed correlation between D_0 and δ_l is caused by their influence on the diffusion coefficient. An increased diffusion coefficient due to a higher normalization D_0 can be counterweighted by its rigidity dependence up to a certain extent. Surprisingly, many of the observed data-conform models involve exceedingly large values of δ_l and δ_h which had not been expected before. However, due to the transition from δ_l to δ_h none of the found values can be expected to hold for the whole rigidity range. The most sensitive observable and also the one holding the strongest contraining power on δ_l and δ_h is B/C.

The correlations between the injection indices and δ_l and v_α illustrate that very similar model prediction can be achieved by choosing different injection spectra and a corresponding choice of the relevant strengths of the transport processes. By trend, harder injection spectra, i.e. lower injection indices, require higher values for δ_l and v_α. Due to the normalization of the propagated spectra harder injection spectra accompany with a reduced population of less energetic particles by which an enhanced diffusive reacceleration or a correspondingly adjusted rigidity depended diffusion is required.

Some parameters of the model setup were found to play only a minor role. Especially α_r and f_b were found to show no preference at all even in case of high convection velocities. Since their influence is overlocked by those of the dominating parameters no reasonable insights can be drawn from the chain point density distributions. Also the χ^2 analysis did not yield any useful information about preferred or excluded values.

It was shown that the constraining power of the used observables is strongly limited due to the uncertainties of the experimental measurements and more important due to the large parameter correlations and degeneracies. The strengths of the correlations differ strongly depending on the position in the parameter space and are additionally washed out by the great number of free parameters. A reasonable determination of the allowed regions implies a full exploration of the boundaries of the regions in which the majority of the promising models lie. However, to explicate this for the applied, high-dimensional transport model setup requires an exceedingly large computational effort which cannot be performed within a decent time. Instead, this was performed for a reasonably constrained, minimal model setup for which the limits and correlations can be determined more precisely. The results will be presented in chapter 4.5.
The implications of the unconstrained model setup are illustrated by a set of the top 97 models with strongly differing sets of transport parameters, as marked by the stars in fig. 4.13. These models are characterized by yielding a maximal average deviation to each data set of 1σ and describe the data reasonably well. The parameter ranges covered by the corresponding models as well as the parameter set of the best-fit model are listed in table 4.4. Fig. 4.14 shows the predicted energy spectra and ratios. The LIS of each model is shown as a gray line while modulated spectra are shown in blue. The dashed and solid lines correspond to the LIS and the modulated spectrum of the best-fit model, respectively. The derived spectra are in good agreement within the uncertainty of the experimental

measurements. The predictions for the LIS of the proton spectrum are characterized by a large spread at low energies all of which can be aligned with the data by applying a corresponding modulation strength between 211 and 892 MV. At energies above a few hundred GeV the PAMELA data show a non-power-law like slope which is accounted for by the break in the injection spectrum at typically 650 - 800 GV (see fig. 4.10). The snappy behaviour of the best-fit model and some other models in the ratios B/C and $^{10}Be/^{9}Be$ at energies above $\sim$ 300 GeV/n is affiliated to the break in the rigidity dependence. The fact, that the breaks lie predominantly above energies at which no or only a slight sensitivity to the data is given suggest, that a break is redundant. Fig. 4.15 shows the profiles of the predicted proton densities as a function of r and z. The densities throughout the Galaxy differ strongly and are only constrained at the Sun's position. Especially the gradient in z-direction shows an exceedingly wide spread due to the large range of the halo height of the models. This directly demonstrates the disability of constraining the shape of the overall large scale particle densities by locally measured nuclei.

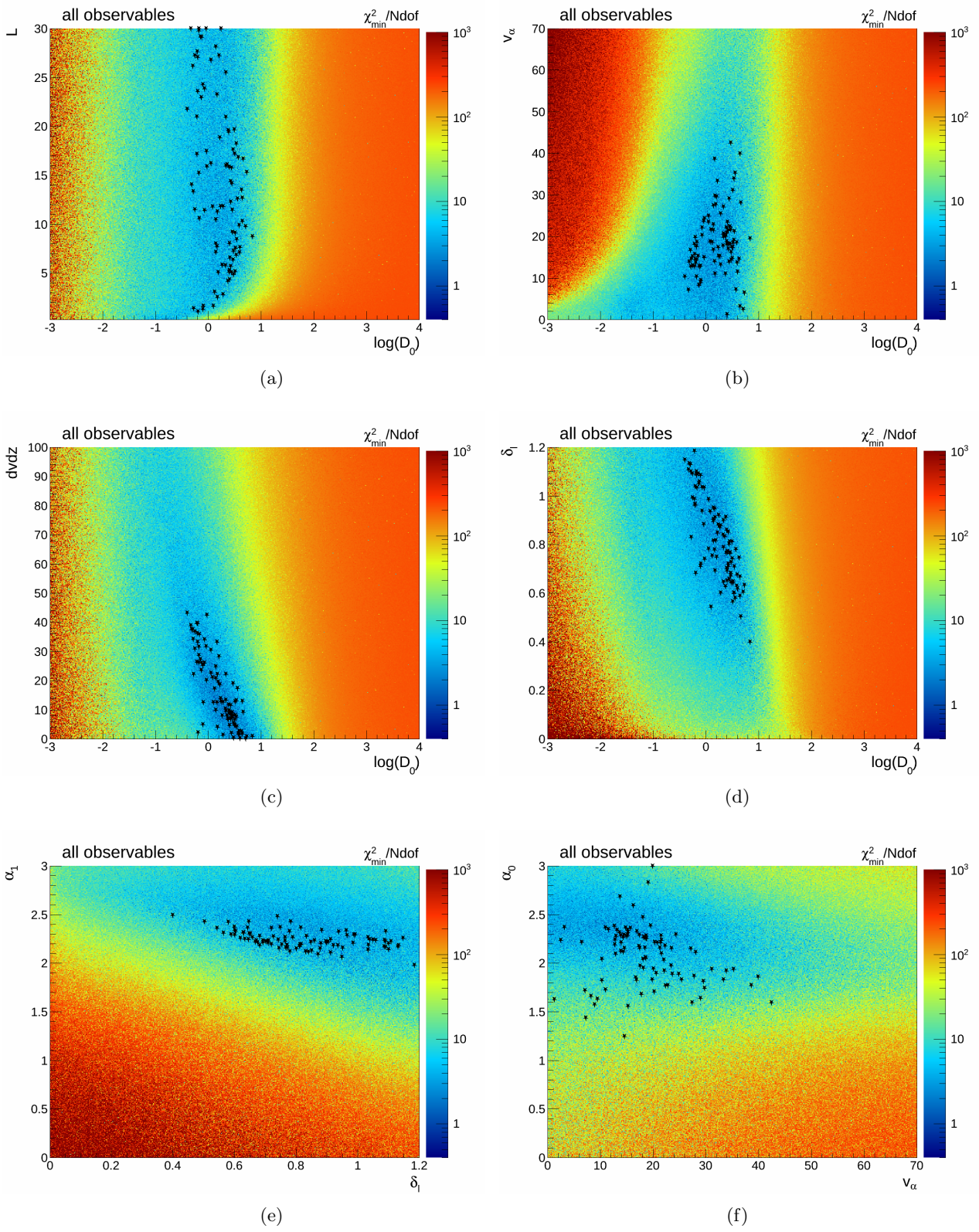

Figure 4.13.: Minimal $\chi^2/Ndof$ values projected on 2-dimensional parameter planes. Overlayed are the parameters of the top 97 models marked as stars all of which yield an average deviation to the each data set of $\leq 1\sigma$.

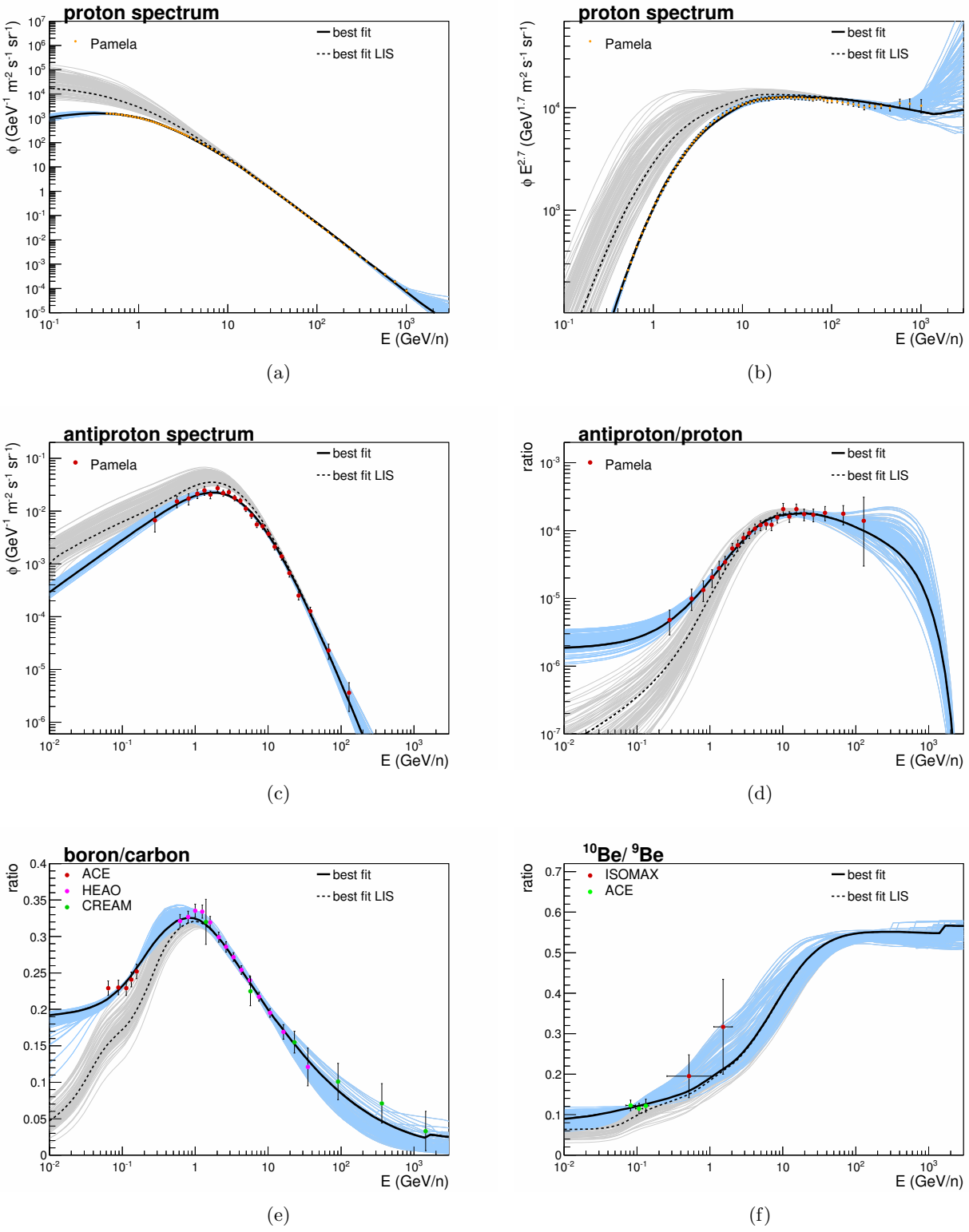

Figure 4.14.: Energy spectra and ratios of the top 97 models all of which yield an average deviation to the each data set of $\leq 1\sigma$. The best-fit model is shown in black while the remaining models are shown in blue. The gray lines correspond to the local interstellar spectrum (LIS) and represent the model predictions without accounting for solar modulation.

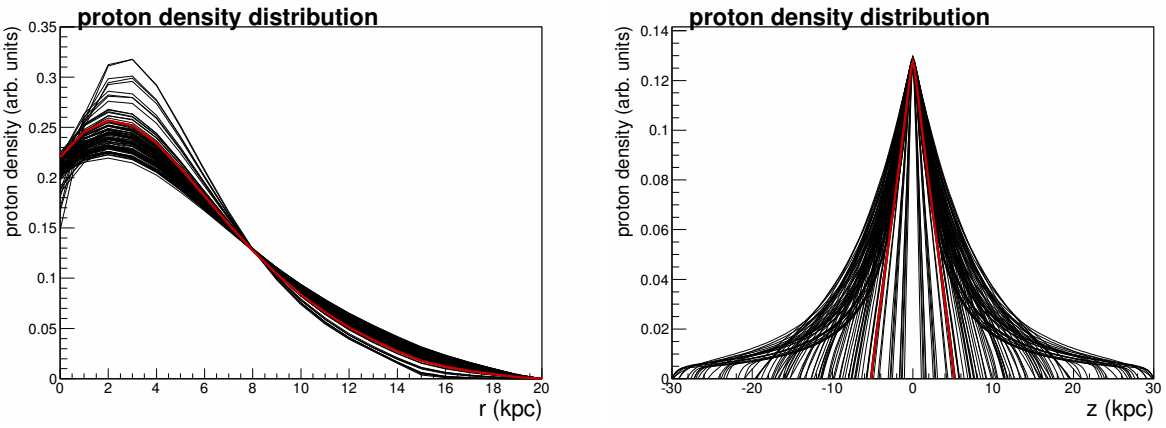

(a) (b)

Figure 4.15.: Proton density distributions for $E = 91$ GeV protons as predicted by the top 97 models. In (a) the distribution is shown as a function of r at $z = 0$ kpc and in (b) as a function of z at $r = 8.0$ kpc. The best-fit model is shown in red, respectively.

Table 4.4.: Parameter ranges of the top 97 models sampled by MCMC and the parameters of the best-fit model. The models are characterized by an average deviation to the each data set of $\leq 1\sigma$

Parameter	Unit	Lower limit	Upper limit	best-fit
D_0	$10^{28}\mathrm{cm}^2/\mathrm{s}$	0.40	6.96	3.28
δ_l	1	0.40	1.19	0.56
δ_h	1	0.01	1.20	0.24
ρ_δ	GV	32.80	3488.00	1431.00
L	kpc	1.05	30.00	5.19
η	1	-2.00	1.58	0.49
v_α	km/s	1.29	42.50	31.14
v_0	km/s	0.14	16.85	2.14
$f_b \equiv v_b/v_0$	1	0.02	1.00	0.97
dV_c/dz	km/s/kpc	0.13	43.18	12.85
α_r	1	0.03	1.00	0.40
ρ_0	GV	0.56	100.00	12.77
ρ_1	GV	132.80	1000.00	155.87
α_0	1	1.25	3.00	1.94
α_1	1	1.98	2.49	2.31
α_2	1	0.14	2.72	2.33
Φ_p	MV	211	892	412
Φ_{pb}	MV	359	1000	523
$\Phi_{B,C}$	MV	16	336	216
$\Phi_{^{10}Be,^9Be}$	MV	0	828	153

4.5. Minimal Transport Model Setup

In the previous chapter a 16-dimensional transport model was analyzed and the roles of the transport parameters and the used observables were highlighted. Including uncertainties from less dominating parameters, large ranges of the dominating transport parameters were found to be and found not to be suitable for describing experimental data. The diffusion constant was found to be the dominant transport parameter. A clearly preferred range of the order of $(0.4 \leq D_0 \lesssim 7)\ 10^{28}\mathrm{cm}^2/\mathrm{s}$ outside of which no data-conformity was achieved could be identified and excluded. However, the injection spectrum and the rigidity dependence of the diffusion coefficient were allowed to be broken and hence no reasonable conclusion about values holding for the whole energy range can be drawn. Even though this could be realized in nature, from a physical point of view it is more convenient and instructive to investigate the potential and limitations of elementary models and extend those, if necessary. In this chapter the derived knowledge is used to construct a reasonably constrained, minimal transport model setup, ignoring subordinate parameters as well as redundant features. The main differences to the previously incorporated transport model setup are

- an unbroken nuclei injection spectrum,
- an unbroken rigidity dependence of the diffusion coefficient,
- a complete negligence of the convective transport mode.

The 6 remaining parameters of the minimal model setup are D_0, δ, L, η, v_α and α. The applied limits as well as the treatment of the solar modulation remain unchanged. For the investigation of this relatively low-dimensional parameter space, a modified MCMC was used incorporating exceedingly small step sizes as well as a restricted acceptance criterion. This approach allows to explore the auspicious parameter ranges in more detail, especially in terms of their boundaries. In total 840,610 models were sampled by Markov chains starting at different, but well chosen positions in the parameter space. The chains were found to move slowly but steadily by which connections between previously found local minima were brought to light.
Although the minimal model setup incorporates much less degrees of freedom it was found to be in no way inferior to the 16-dimensional setup in accounting for experimental observations. In fact, by sampling a much more reduced paramter space a large amount of exceedingly well data describing models could be obtained.

Figure 4.16 shows the obtained minimal $\chi^2/Ndof$ values, illustrated by a projection of transport parameters in binned, 2-dimensional planes. Apparent are in general harder constrained regions and less washed out correlations compared to the 16-dimensional setup. For the majority of the parameters also clear borders are visible over which the chains were precluded to cross. Solely L deprives from a reasonable restriction upwards and merely very low values of $L < 0.4$ kpc are disfavoured. The hardest constraints result from the proton spectrum and the B/C ratio which are responsible for almost all parameter limitations. The constraining power of $^{10}Be/^{9}Be$ could not be fully exploited due to the limited amount of available data and its quality by which $^{10}Be/^{9}Be$ plays a minor part. Also the data on $\bar{p}$ and $\bar{p}/p$ are fraught with large uncertainties and their change in χ^2 by parameter deviations is subordinate compared to the ones by p and B/C. In fig. C.21 and C.22 the minimal χ^2 values are shown separately for p and B/C. Any observed parameter limitation can be affiliated to p or B/C: $\chi^2_{B/C}$ is strongly sensitive to D_0 and L leading to the narrow preferred band and sharp borders as shown in fig. 4.16(a). While χ^2_p is only marginally sensitive to D_0 and L it crucially determines the allowed combinations of α and δ which are highly correlated. However, the proton spectrum is not suitable for limiting the particular values of α and δ. A lower and upper limitation of δ is given by B/C whereby

the limitation of α and δ as shown in fig. 4.16(b) is demanded by the combination of p and B/C. The parameter v_α is upper bounded by both p and B/C. However, the upper limit strongly depends on the corresponding values of η, α and δ. The largest values of v_α can be realized by low δ and a corresponding choice of η and α. η is upper bounded by B/C but the maximal allowed value again depends on the choice of v_α and δ and can be achieved for low v_α and intermediate δ.

Figure 4.18 shows the energy spectra and ratios of the best-fit model as well as the spectra and ratios of the top 13,400 models, all of which yield a maximal average deviation of 1σ to each data set. The spectra and ratios are reasonably well described by the models with differing sets of transport parameters. The parameter limits of the model selection and the parameter values of the best-fit model are listed in table 4.5. Also shown in fig. 4.17 are the correlation coefficients for the entirety of the 13,400 models. In the lower left triangular of the correlation matrix the Pearson correlation coefficient is shown, quoting the strength of the linear correlation or dependence between two parameters. In the upper right triangular of the matrix the Spearman's rank correlation coefficient is shown which is a measure for the strength of a monotonic relationship between two parameters and is also sensitive to quadratic correlations. In case a linear correlation is present the two correlation coefficients are comparable. The quoted numbers quantify the degree of the correlation as illustrated in fig. 4.16. Almost all transport parameters are strongly correlated. The largest exists between D_0 and L with a monotonic relationship of 99%. δ and α are linearly correlated with -98%. Beside these obvious and expected correlations also concealed correlations are brought to light illustrating the complex interplay of the transport parameters. For instance the halo height shows a linear correlation to α of 0.21 and to δ of -0.21. This is a result of the link between L, α and δ via D_0.
Shown in fig. 4.19 are the model predictions for further nuclei spectra and ratios which were, however, not taken into account during the MCMC sampling and the model selection. On the one hand, experimental measurements of heavy nuclei suffer from large uncertainties and are often only available at rather low energies with the interfering influence of the solar wind. On the other hand, precise predictions are prevented by large uncertainties of the elemental abundances which have to be assumed. In principle these can be tuned to available measurements to match the data, but the tuned values crucially depend on the assumed transport model and consequently do not hold for arbitrary models. The applied elemental abundances are those proposed by [137] which are commonly adopted in CR propagation calculations.
Fig. 4.19(a) and 4.19(b) shows the spectra of ^3He and ^4He for the 13,400 models and the best-fit model tuned to match p, $\bar{p}/p$, B/C, $^{10}Be/^9Be$ only. A good agreement between the data and the model at energies above $E = 5$ GeV/n is achieved. The deviations at lower energies are a result of the insufficiency of the force-field-approximation for strong solar modulations. The shown IMAX92 data were recorded in 1992 during a phase of high solar activity, see fig. 3.8. Also shown is the ratio of $^{26}Al/^{27}Al$, a ratio of an unstable to a stable isotope. The ratio holds a strong constraining power since the degeneracy of the solution is less distinctive. However, no experimental measurements at high energies are available for constraining transport parameters. A measurement of the secondary-to-primary-ratio $^{54}Fe/^{56}Fe$ by CRISIS at around 753 GeV/n is compatible with the predictions within the large data uncertainty. Also shown is O/C, a ratio of primary produced elements. The high energy measurements are partially contradictory but the matching of the slope of the HEAO3 data suggests, that the assumption of identical injection spectra for each element species is justified. The secondary-to-primary-ratio SubFe/Fe is shown in fig. 4.19(f). SubFe is an acronym for the sum of the elements Scandium (Sc), Titanium (Ti) and Vanadium (V) all of which are secondary produced nuclei by spallation processes of Fe. At energies around 2 GeV/n the ratio is underestimated by the models, probably due to an

too imprecise modeling of the spallation processes. At high energies the model predictions widen beyond the data uncertainty by which the transport parameters can be further constrained. Additional demands on the SubFe/Fe ratio were applied to the 13,400 models resulting in 10,050 remaining models describing the ratio at high energies reasonably well, as shown in fig. 4.20. The limits of these models are additionally listed in table 4.4. The parameters which could additionally and perceptibly be constrained by SubFe/Fe are δ, α and η. The best-fit model is not affected by the additional constraint and remains the same.

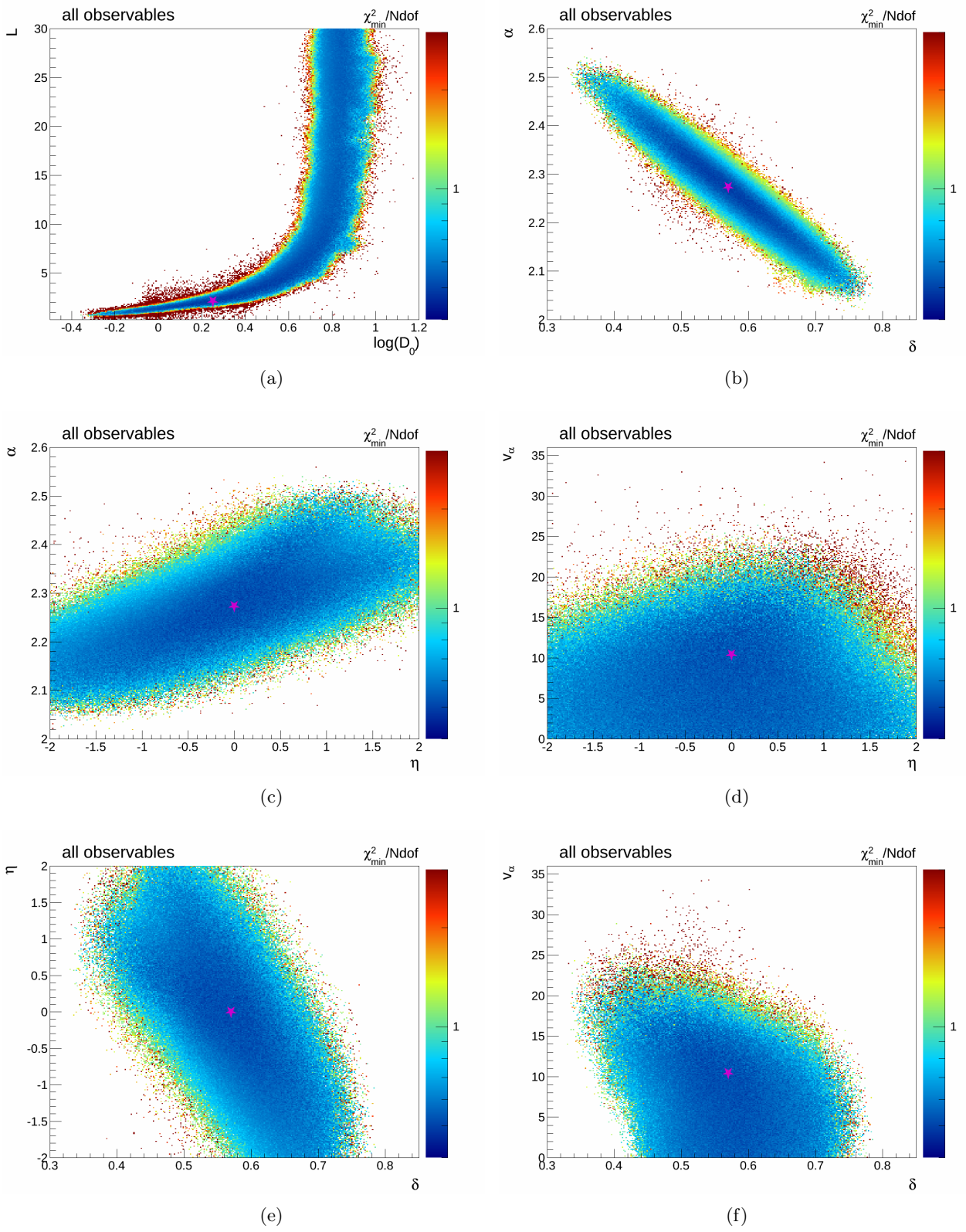

Figure 4.16.: Minimal $\chi^2/Ndof$ values projected on 2-dimensional parameter planes for the minimal model setup. Overlayed are the parameter values of the best-fit model marked as star.

Table 4.5.: Parameter ranges of the top 13,400 models of the minimal transport model setup sampled by MCMC. The limits were derived by demanding an average deviation to the each data set of $\leq 1\sigma$. Also shown are the limits of a subset of 10,050 models* including additional constraints from SubFe/Fe.

Parameter	Unit	Lower limit	Upper limit	Lower limit*	Upper limit*	best-fit
D_0	$10^{28}\mathrm{cm}^2/\mathrm{s}$	0.58	8.55	0.58	7.81	1.79
L	kpc	0.85	29.98	0.85	29.88	2.15
D_0/L	$10^{28}\mathrm{cm}^2/\mathrm{s/kpc}$	0.21	1.09	0.22	1.02	0.83
δ	1	0.39	0.71	0.49	0.68	0.57
v_α	km/s	0.00	19.90	0.00	18.65	10.42
η	1	-1.90	1.21	-1.74	1.07	0.00
α	1	2.11	2.47	2.14	2.36	2.27
Φ_p	MV	437	927	453	832	639
Φ_{pb}	MV	483	983	612	980	837
$\Phi_{B,C}$	MV	52	302	52	288	138
$\Phi_{^{10}Be,^9Be}$	MV	0	1000	0	1000	162

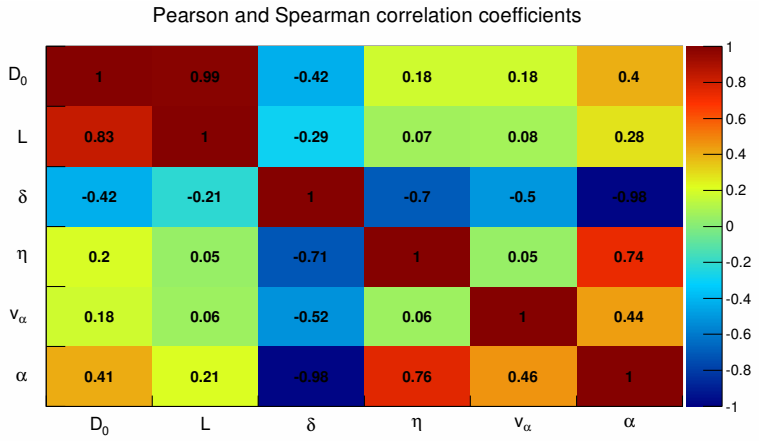

Figure 4.17.: Correlation matrix for the 6 parameters of the minimal model setup. The lower left triangular shows the Pearson correlation coefficients indicating the strength of a linear correlation. The upper right triangular shows the Spearman's rank correlation coefficient indicating the strength of a monotonic relationship.

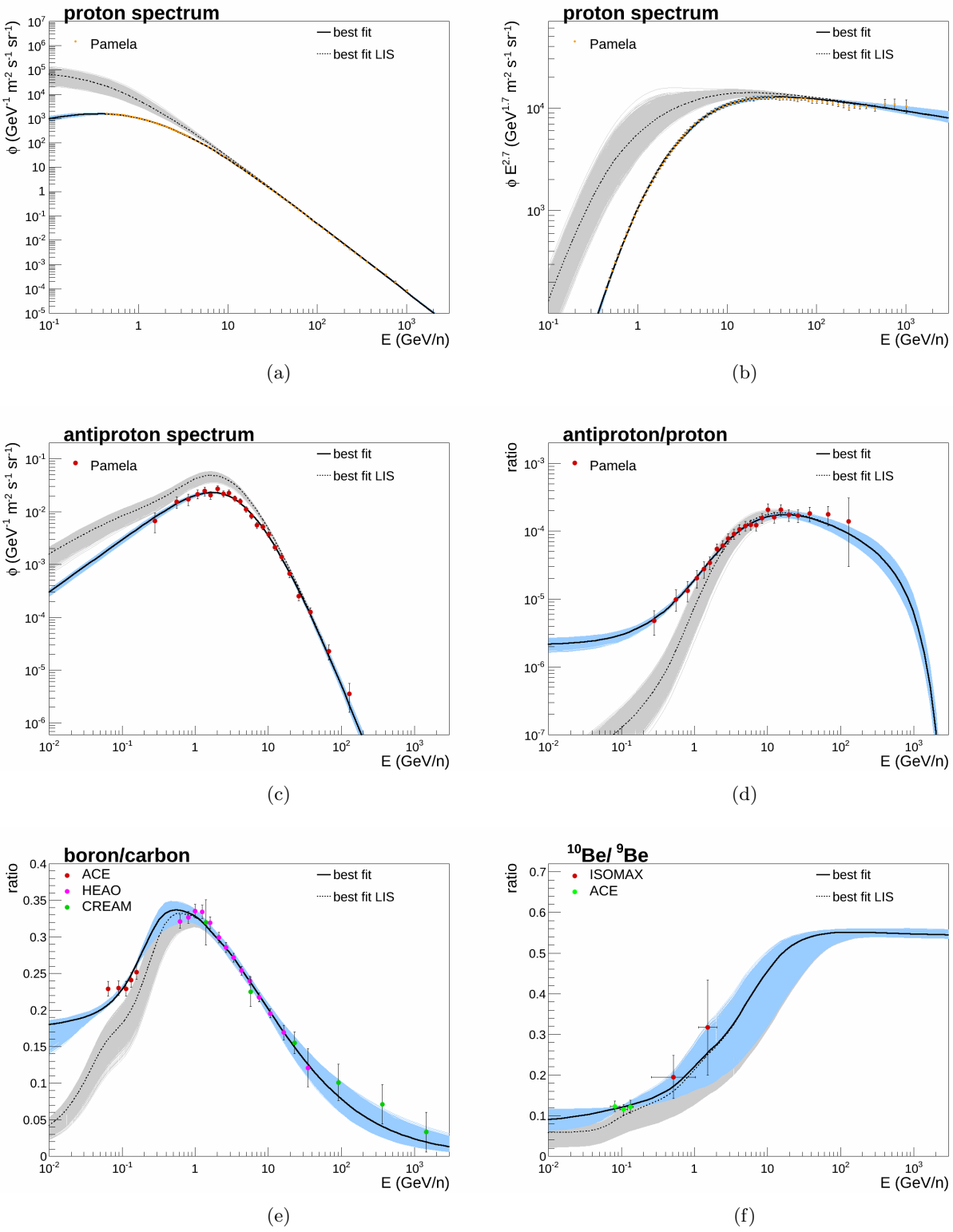

Figure 4.18.: Energy spectra and ratios of the top 13,400 models of the minimal transport model setup. Those models yield an average deviation to each data set of $\leq 1\sigma$. The best-fit model is shown in black and the remaining models are shown in gray and blue. The gray lines correspond to the local interstellar spectrum (LIS) and represent the model predictions without accounting for solar modulation.

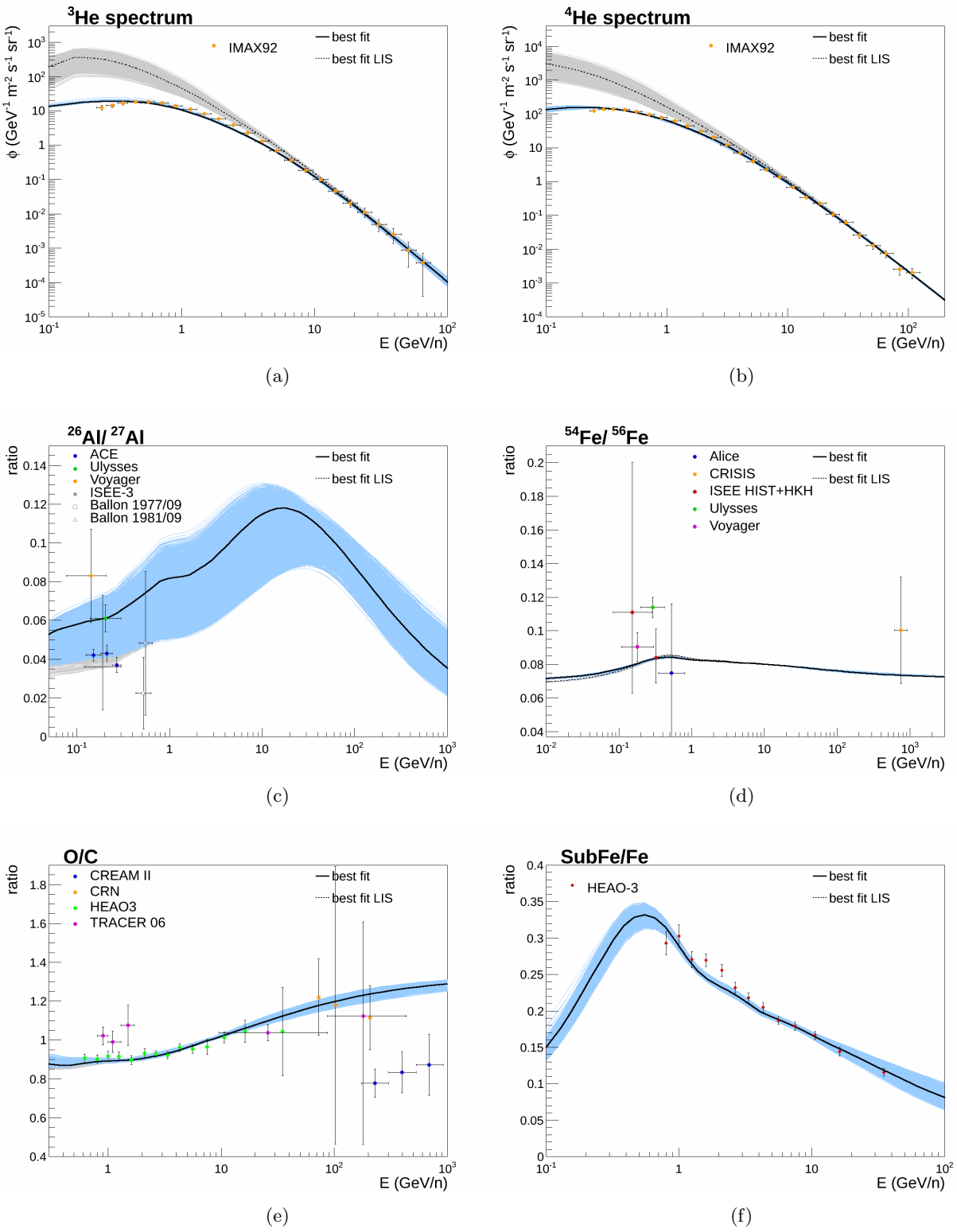

Figure 4.19.: Model predictions for various nuclei spectra and ratios of the best-fit model and the top 13,400 models tuned to match experimental measurements of p, $\bar{p}/p$, B/C, $^{10}Be/^{9}Be$. The gray lines correspond to the local interstellar spectrum (LIS) and represent the model predictions without accounting for solar modulation. Data taken from [103].

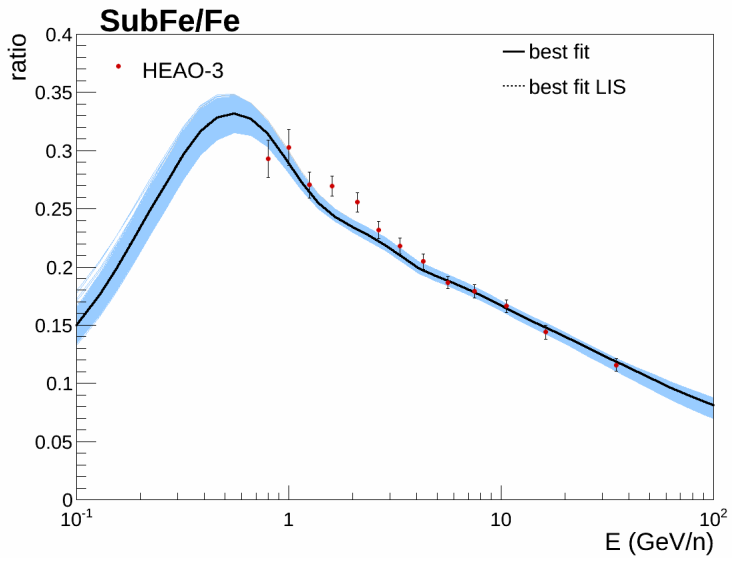

Figure 4.20.: The SubFe/Fe ratio of a subset of 10,050 models including constraints from SubFe/Fe at high energies.

4.6. Summary and Comparison to other Studies

For the investigation and constraining of transport parameters a MCMC method was used to sample transport models incorporating wide ranges of transport parameters. The suitability of particular parameter values were compared to most up-to-date measurements of p, $\bar{p}$, $\bar{p}/p$, B/C and $^{10}Be/^{9}Be$ and the parameters were constrained. Special importance was given to the role of the particular observables. The constraining power and the preferred parameter values of each observable as well as of their entirety were highlighted. A large number of around 10,000 transport models were derived which can explain the experimental measurements and can be further used for studies of different aspects like the secondary positron production (chapter 5) and the diffuse gamma-ray emission (chapter 6). In the following, the main results of this study are summarized and compared to similar studies.

The diffusion constant is one of the major transport parameters which crucially affects the predictions for all observables. As shown in fig. 4.5 a clear prefered parameter range could be identified. The data can be described within their experimental uncertainties by adopting a common value of D_0. The constraining power was found to be limited due to uncertainties from experimental measurements and the large degree of degeneracy resulting from strong parameter correlations. The halo height L was found to be highly correlated with D_0. Within the constrained range of D_0 halo heights from $L = 0.85$ kpc up to the maximal tolerated value of $L = 30$ kpc were found to be data-conform. Although reasonable models including rather high convection velocities accompanied by low D_0 were sampled, a convective transport mode was found to be not preferred and not necessarily demanded by any observable. The limits for the injection index, the rigidity dependence of the diffusion coefficient and the Alfvén velocity as listed in table 4.4 were found to be restricted strongest by p and B/C.
A simplified model setup characterized by an unbroken injection spectrum, an unbroken rigidity dependence and the absence of a convective transport mode was found to be completely sufficient for describing the experimental observations of locally measured spectra and ratios. In this low dimensional model setup tighter restrictions on the transport parameters could be achieved: The range of D_0 could be constrained to $(0.58 \leq D_0 \leq 8.55)$

$10^{28}\mathrm{cm}^2/\mathrm{s}$. The MHD turbulence level described by δ was found to be data-compatible in the range $0.39 \leq \delta \leq 0.71$ and in the range $0.49 \leq \delta \leq 0.68$ if constraints from SubFe/Fe are taken into account. A Kolmogorov spectrum ($\delta = 1/3$) can therefore be excluded and the results point to an Iroshnikov-Kraichnan spectrum with $\delta = 1/2$. Compatible Alfvén velocities were found ranging from $v_\alpha = 0$ km/s up to $v_\alpha \leq 20$ km/s and are upper bounded by the proton spectrum and B/C. The best data-conformity was achieved for $v_\alpha \approx 10$ km/s. The range of the nuclei injection index is $2.11 \leq \alpha \leq 2.47$ and is stronger constrained if SubFe/Fe is taken into account leading to $2.14 \leq \alpha \leq 2.36$. This result is in agreement from what is expected from the first-order-fermi-acceleration shock-front theory of SNRs with super- and hypersonic shock front Mach numbers of around $M = 3$ to 6.

Results of a study focusing on the constraining of transport parameters by B/C and antiproton data were published in [138]. Therein, the `DRAGON` code was used to solve the transport equation for diffusion-reacceleration models similar, but not identical, to the ones used in this work. For instance the diffusion coefficient was assumed to decrease exponentially with z and only halo heights between 2 and 6 kpc were considered. Due to different model setups comparisons to other studies are often only possible to a limited extend. Nevertheless, the limits on the major transport parameters found in [138] are similar to the limits derived in this study. For the strength of diffusive reacceleration the authors found $10 \leq v_\alpha \leq 20$ km/s with a best-fit value of $v_\alpha = 15$ km/s. In opposition to this work v_α was found to be bounded below which is most likely a consequence of the different considered energy ranges and the allowed freedom of η. The quoted limits on δ are $0.3 \leq \delta \leq 0.6$ with a best-fit value of $\delta = 0.5$ which point also to a Iroshnikov-Kraichnan spectrum as found in this work. Limits on D_0 and L are merely given for the ratio in units of $10^{28}\mathrm{cm}^2\mathrm{s}^{-1}\mathrm{kpc}^{-1}$ and are $0.6 \leq D_0/L \leq 1.0$. The corresponding values found in this work are $0.22 \leq D_0/L \leq 1.02$ whereby models with much lower values of 0.22 were found to be suitable in the much larger parameter space. In agreement with the conclusion drawn in the present work, a convective transport mode was also found to be not required to interpret CR nuclei and antiproton data.

In [68] a Bayesian analysis of transport parameters by using MCMC and nested sampling was performed with the `GALPROP` code. The employed diffusion-reacceleration model incorporated a broken nuclei injection spectrum for a better description of the low energy tail of the proton spectrum. As already pointed out in [78] this results in much higher preferred Alfvén velocities. The preferred models in [68] are characterized by high v_α between 34.2 and 42.7 km/s and consequently low values for δ between 0.26 and 0.35. Also D_0 assigns to rather high values of $(5.54 \leq D_0 \leq 11.20)$ $10^{28}\mathrm{cm}^2\mathrm{s}^{-1}$ with halo heights between 3.2 and 8.6 kpc. The comparison of the results demonstrates the uncertainty of the major transport parameters on the chosen model setup and explains the partially contradictory results found by different groups.

Analyses using semi-analytical solutions to the transport equation were published in [109], [131] and [67]. However, a reasonable comparison is aggravated due to the simplified gas and source distributions as well as by the fact that diffusive reacceleration takes place only in the thin Galactic Disk with height z_d in these models. In [109] transport parameters of a model setup with an unbroken nuclei injection spectrum were investigated and constrained using B/C. In contradiction to the study presented here the authors exclude any model without a convection velocity or without diffusive reacceleration. However, δ was found to be restricted to the range $0.45 \leq \delta \leq 0.85$ with a best fit value of $\delta = 0.70$ by which a Kolmogorov-like turbulence spectrum is also excluded by this study. In [67] a MCMC method was used to determine the preferred values of transport parameters taking into

account B/C and the isotopic ratios $^{10}Be/^{9}Be$, $^{26}Al/^{27}Al$, $^{36}Cl/Cl$. The conclusion of this study is that models including convection are more-likely than pure diffusion-reacceleration models. The authors found that the former implies $\delta \approx 0.8$ and the latter $\delta \approx 0.2$, independent on the halo height. The halo heights for which the data could be best matched were found to be $L \approx 8$ for convection models and $L \approx 4$ for pure diffusion-reacceleration models. These values are fraught with large uncertainties depending on the applied model setup.

In this chapter it was shown to which extend current experimental measurements allow to constrain transport models for galactic CRs. Even though the particular observables were found to partially prefer different values of transport parameters (e.g. $^{10}Be/^{9}Be$ prefers a higher diffusion constant than B/C), current transport models are able to consistently describe the made observations within the experimental uncertainties. Parameter ranges inside which an agreement of the transport model predictions with experimental measurements could be obtained were given and a large amount of around 10,000 data-conform transport models were presented. A more precise determination of transport parameters requires more precise measurements of nuclei spectra and ratios which are eagerly-awaited by the community. Results from the AMS-02 experiment which is currently measuring the spectra of nuclei with a previously unachieved precision are awaited to be published soon. By combining the high precision measurements of various observables sensitive to different transport modes will allow to further disentangle the large observed degeneracies of transport parameters. Of particular importance will be measurements of B/C up to high energies which will allow to further constrain the rigidity dependence of the diffusion coefficient and thus the nuclei injection spectrum. This observable holds also the strongest constraing power on the diffusion constant and the halo hight.

5. Propagation of Leptons

Recent experimental measurements of CR electrons and positrons by PAMELA gave hints on new physics which drew great attention to field of CR propagation. Positrons which are assumed to be produced purely secondary were found to be not sufficient to explain the high measured positron fluxes and the rise in the positron fraction, defined as $\frac{e^+}{e^+ + e^-}$. A falling slope of the positron fraction is expected since the positron energy spectrum of secondary produced positrons should fall more steeply than the electron energy spectrum. Compared to nuclei, CR electrons and positrons suffer from large additional energy losses due to synchrotron radiation, inverse Compton scattering and bremsstrahlung. A precise modeling of lepton propagation is therefore a challenging task and requires the consideration of uncertainties related to the imprecise knowledge of transport parameters, energy losses and cross sections. For the the calculation of the secondary positron production by interactions of nuclei with the ISM most up-to-date cross section models on p-p, p-He, He-p and He-He are used as derived by Kamae et al. in 2006 [139]. These are compared to commonly used cross section models as implemented in `GALPROP` which were derived by Strong et al. in 1998 [140].
Energy losses by synchrotron radiation are estimated by a comparison to most-up-to date foreground maps on synchrotron radiation from WMAP data. Uncertainties related to the energy density of the magnetic field and the ISRF are inspected and compared to uncertainties from global transport parameters. The implications of the derived uncertainties on global transport parameters are used to predict and to constrain the expected positron flux and to compare the predictions to current experimental measurements.
The predictions are used to characterize the additional positron contribution (further referred to as 'signal') which is needed to explain the data. Finally, two of the most promising signal candidates are put to the proof: high energetic electrons and positrons from nearby pulsars and electrons and positrons originating from DM annihilation. Implications and consequences of both explanations will be compared and discussed.

5.1. Uncertainties from Cross Sections, Energy Losses and Transport Parameters

Secondary CR electrons and positrons are the final product of decays of charged pions and kaons which are created in collisions of CR particles with the interstellar gas. Needed for the computation of the expected positron production are therefore reliable cross section models. Several models, mainly based on analyses of the galactic, diffuse gamma-ray

emission, were proposed in the past (Stecker 1970 [141], Badhwar et al. 1977 [142], Dermer 1986 [143]) and a combined model was implemented in GALPROP by Strong et al. 1998 [140]. However, an analysis of the galactic, diffuse gamma-rays by Kamae et al. in 2006 emblaced [139] that previous models had left out the diffractive interaction and the Feynman scaling violation in the non-diffractive inelastic interaction. Additionally, it was found that most previous calculations assumed an energy-independent p-p inelastic cross section, whereas recent experimental data have established a logarithmic increase with the proton energy. Fig. 5.1 shows a comparison of the expected local interstellar positron spectra from proton interactions for the cross section models proposed by Kamae et al. and as implemented in GALPROP v54. In agreement to what other groups found, the absolute positron flux computed with the cross sections by Kamae et al. is lower than predictions with the cross sections implemented in GALPROP. Also shown in the figure is the energy dependent distinction illustrated by the ratio of the predicted positron fluxes. For lepton related analyses in this work the cross section model by Kamae et al. is used exclusively, since it is the most sophisticated and most convincing model available up to now.

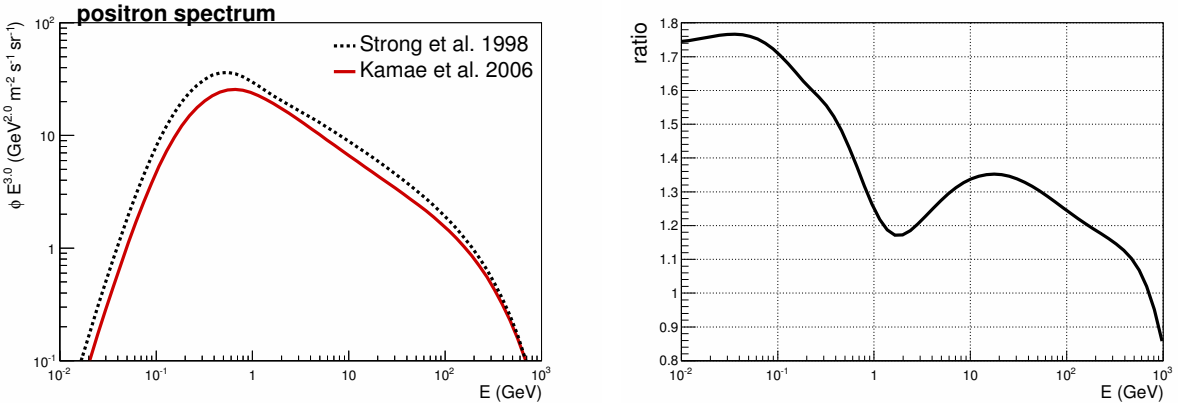

(a) (b)

Figure 5.1.: Comparison of positron production cross sections. In **(a)** the local interstellar positron spectrum from proton interactions is shown for cross section models proposed by Strong et al. and Kamae et al.. In **(b)** the ratio of the positron predictions is shown by which the energy dependent distinctions are illustrated.

For a correct estimation of synchrotron induced energy losses the parameters of the applied magnetic field (eq. 3.21) were tuned to best match the synchrotron foreground maps of 9-year WMAP data and the Haslam synchrotron map. The positron and electron densities derived by solving the transport equation for a reasonable transport model were extended by additional components to describe the electron and positron data measured by PAMELA and the high energy positron fraction measured by AMS-02. The synchrotron emission in particular directions of the sky was calculated by the integration of the emissivity along the LOS. Details on the calculation, the fitting procedure and the results can be found in Appendix D. A previous tuning done in [92] incorporated the Haslam synchrotron map only and the authors demonstrated a reasonable description of the synchrotron radiation by applying the used magnetic field parameterization with the values $B_0 = 6.1\ \mu G$, $r_0 = 10$ kpc and $z_0 = 2$ kpc. These values could be verified and were found to describe the Haslam synchrotron profiles at 408 MHz along the galactic latitude and longitude well. However, the WMAP maps predict a much higher synchrotron emission at high frequencies and the emission was found to be significantly underestimated for Haslam-conform models in regions in or close to the Galactic Disk. It was found that the parameters of the magnetic field could not be tuned to simultaneously match the overall

observed spectral shape of the synchrotron emission in various sky directions, see fig. D.24. More sophisticated models for the magnetic field proposed by Pshirkov et al. 2011 [97] and Farrar et al. 2012 [98] were checked but were found to be not able to improve the situation a priori. The values for which the best match of the Haslam and WMAP synchrotron spectra in the considered sky regions could be achieved are $B_0 = 10.5$ μG, $r_0 = 7.97$ kpc and $z_0 = 0.79$ kpc. Beside a much stronger field strength at the solar position, the field is characterized by a faster decrease with r and z from the Galactic center in case WMAP foreground maps are taken into account. The synchrotron emission is by far not perfectly described and the results call for a more extensive study. However, this study does not aim to perfectly model the synchrotron emission but rather to estimate the synchrotron induced energy losses during lepton propagation.

For an estimation of energy loss related influences and uncertainties on the expected positron flux the energy densities of the magnetic field and the ISRF (dust and starlight) were diversified by 30%. Fig. 5.2 shows the influence on the resulting positron prediction. Also shown is the uncertainty related to CR transport by two models with the minimal transport model configuration constrained by the global observables and yielding the largest and lowest positron flux in the energy range 10 - 1000 GeV. The transport related uncertainty is found to be the dominant uncertainty in a wide energy range. The predicted absolute positron flux is strongly related to the transport parameters. Fig. 5.3 shows scatter plots of the predicted secondary positron flux at $E = 30.5$ GeV as a function of the halo height and the diffusion constant for the 10,050 models constrained by global observables. The large uncertainty on the positron flux is ascribed to the large uncertainties of D_0 and L whereby the largest contribution is predicted by models with low D_0 and low L and vice versa. The behaviour is explained by shorter propagation lengths and thus less energy losses due to a stronger confinement induced by lower D_0. The halo height assigns to values according to D_0 to match the CR interaction rate and the CR escape time as dictated by B/C and $^{10}Be/^{9}Be$. The positron predictions of models of the 16-dimensional model setup are shown in fig. 5.4 and compared to those of the minimal setup. While in the energy range between 8 and 20 GeV the spread is comparable due to very similar limits of D_0, the high dimensional models show a wide spread at energies below and above. This is related to the breaks in the nuclei injection spectrum and the resulting highly non-power-law like proton spectrum which crucially determines the expected positron spectrum. In the minimal setup the propagated, local interstellar positron spectra in the energy range between 4 and 40 GeV can be described by power-law-shaped energy spectra with spectral indices between 3.53 and 3.68, as found by fits to the propagated spectrum. Also shown in fig. 5.4(b) is the positron spectrum of an extended model additionally tuned to gamma-ray measurements, see chap. 6.2. This model includes not only a single broken nuclei injection spectrum, but also a convective transport mode both leading to the digressive spectral shape. Even though a slightly harder positron spectrum is predicted the model does not imply an exceptional positron production.

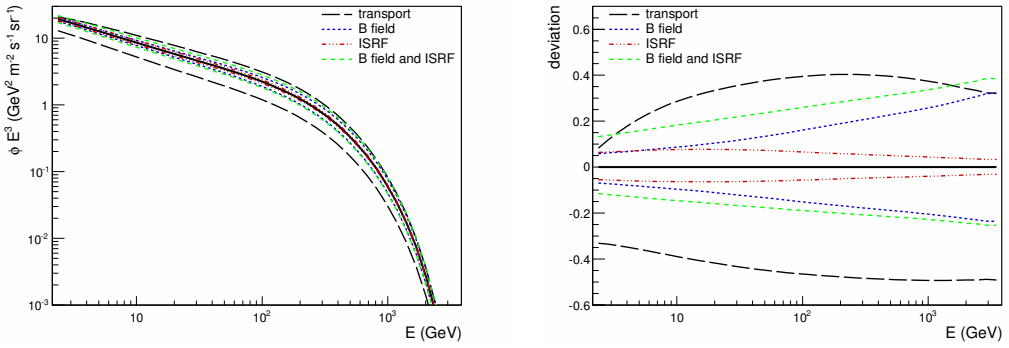

(a) (b)

Figure 5.2.: Illustration of the influence on the positron flux related to transport and energy loss mechanisms. In **(a)** the expected positron flux is shown for the best-fit model on global observables (solid black line) and two models yielding the minimal and maximal secondary positron contribution (dashed black lines). Uncertainties related to energy losses by synchrotron radiation and inverse Compton scattering are estimated by applying variations of 30% to the magnetic field, to the ISRF and to both. In **(b)** the relative deviation to the initial model is shown.

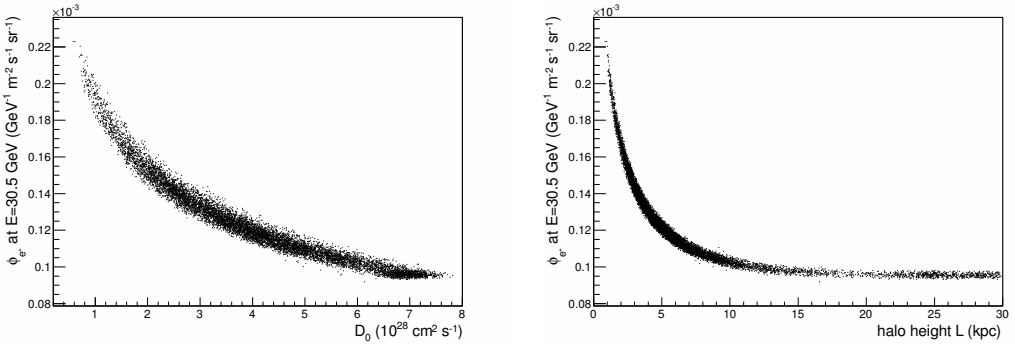

(a) (b)

Figure 5.3.: The dependence of the positron flux prediction at $E = 30.5$ GeV on the diffusion constant **(a)** and the halo height **(b)**. The behaviour is explained by shorter propagation lengths and thus less energy losses due to a stronger confinement induced by lower D_0. The halo height assigns to values according to D_0 to match the CR interaction rate and the CR escape time as dictated by B/C and $^{10}Be/^{9}Be$.

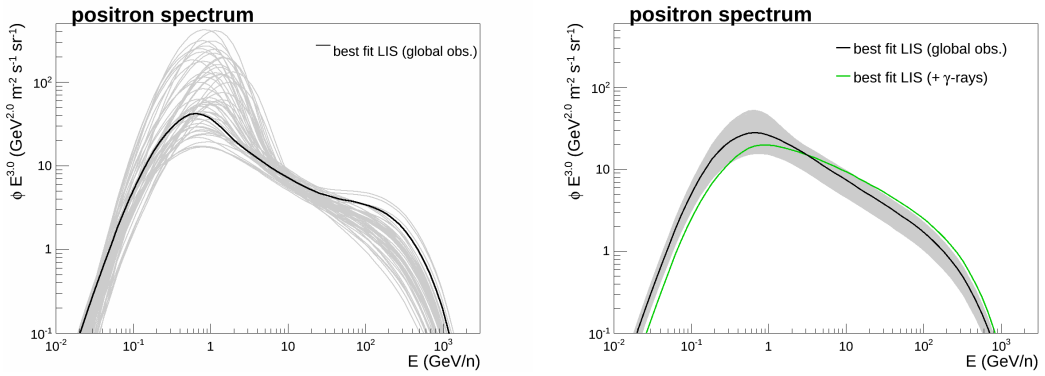

(a) (b)

Figure 5.4.: Positron predictions of models of the 16-dimensional **(a)** and the minimal transport model setup **(b)**. Each shown model is constrained by experimental measurements of p, $\bar{p}$, $\bar{p}/p$, B/C, $^{10}Be/^{9}Be$ and SubFe/Fe. While in the energy range between 8 and 20 GeV the spread is comparable, the high dimensional models show additionally a wide spread at energies below and above due to the breaks in the nuclei injection spectrum. The resulting highly non-power-law like proton spectrum crucially determines the expected positron spectrum. Also shown in **(b)** is the prediction of an extended model additionally tuned to gamma-ray measurements. The model includes not only a single broken nuclei injection spectrum, but also a convective transport mode both leading to the digressive spectral shape.

5.2. The Anomalous Rise in the Positron Fraction

Measurements of the rise of the positron fraction at high energies were first published in 2009 by the PAMELA collaboration [11]. The rise could be confirmed by FERMI in 2012 [28] and further measurements of the fraction by AMS-02 with an unprecedented accuracy were published in 2013 [13]. Recently, AMS-02 measurements of the positron fraction up to higher energies [14] as well as precise measurements of the separate fluxes of electrons and positrons were published [14]. A measurement of the lepton sum flux $(e^+ + e^-)$ as used in this work was accepted for publication [31]. The insufficient description of the data by the assumption of purely secondary produced positrons is illustrated in fig. 5.5.
Numerous explanations for the rise of the positron fraction are proposed or disproved in the literature. In [144] several hypotheses like an anomalous primary electron source spectrum, spectral features in the proton flux, an anomalous energy-dependent behaviour of the diffusion coefficient and rising cross sections at high energies were put to the proof. Those explanations were found to be at least strongly disfavored if not ruled out. In [145] a possible acceleration of secondary positrons by nearby SNRs is discussed. The authors found that no more than $\sim 25\%$ of the observed rise in the positron fraction can result from this secondary acceleration scenario since other secondary CR species like B and $\bar{p}$ would also be accelerated leading to a rise in B/C and $\bar{p}/p$ which is not observed. There is the general presumption that the rise is caused by a flux of primary produced positrons, most-likely injected in the form of electron-positrons pairs whether or not originating from astrophysical or exotic sources. From an astrophysical point of view several primary sources come into question (see [146] for an early review). These include molecular gas clouds which interact with hadronic CRs leading to $e^{\pm}$ production by the secondary production of $\pi^{\pm}$ and $K^{\pm}$ and subsequent decays.
The most plausible and favoured astrophysical explanation is certainly the $e^{\pm}$ production in the magnetosphere of nearby pulsars. Strong, rotation induced electric fields extract particles from the surface and $e^{\pm}$ pairs are generated through electromagnetic cascading which end up in the relativistic magnetized wind emanating from the pulsar. Especially

at high energies above 50 GeV merely a few sources like Geminga or Monogem may contribute dominantly to the observed positron flux. However, the complex astrophysics and the not well known pulsar properties prohibit robust predictions.
Beside these astrophysical explanations also particle physics related explanations by the annihilation or decay of DM particles are considered and studied excessively, see e.g. [147], [148], [149] to mention only a few. If a new, DM like particle was found in direct production experiments, an indirect evidence is in any case imperative in order to affiliate the astronomical and cosmological observations to this particle. For certain annihilation/decay channels the particle spectra can be calculated and limits on the DM mass and the annihilation cross-section/lifetime can be obtained.
Each explanation has to be consistent with other CR constraints, for instance with measurements of the antiproton flux. Standard DM annihilation/decay models with relatively low DM masses below a few hundred GeV/c^2 are contradictory to antiproton measurements why 'leptophilic' DM models [150] are often assumed. Those models incorporate couplings to leptons but not to gauge bosons or quarks whereby no antiprotons are expected from these DM annihilation/decay models. Since the $e^{\pm}$ production by pulsars is purely electromagnetic no antiprotons are expected from those sources and a tension to antiproton measurements does not occur in a very natural way.

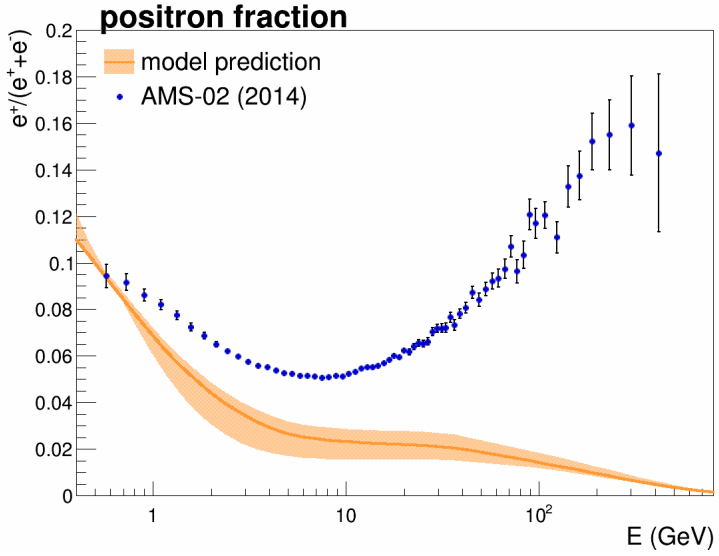

Figure 5.5.: The insufficient description of the positron fraction by purely secondary produced positrons. Shown are the best-fit model (solid line) and the transport related uncertainty derived from constraints on global observables in the minimal transport model setup. For a comparison the data and the model are integrated over the energy bin width. The electron injection spectrum and the charge-dependent modulation potentials were optimized to the data.

5.3. Signal Characterization

In this chapter a general signal characterization is performed by a quantification of the discrepancy to the data. It is assumed that electrons and positrons related to the signal are exclusively produced in pairs.
In a first approach the $e^{\pm}$ energy spectra of the background contribution are assumed to follow power-laws in energy. In addition, a common source Φ_s is modeled as a power-law with a cut-off at the energy E_{cut}. The electron and positron fluxes at Earth are accordingly given by the following parameterizations:

$$\begin{aligned} \Phi_{e^+} &= C_{e^+} E^{-\gamma_{e^+}} + \Phi_s \\ \Phi_{e^-} &= C_{e^-} E^{-\gamma_{e^-}} + \Phi_s \\ \Phi_s &= C_s E^{-\gamma_s} e^{-E/E_{cut}}. \end{aligned} \tag{5.1}$$

The parameters C_{e^+}, C_{e^-} and C_s are the normalizations for the electron and positron power-laws and the common source. The respective spectral indices are γ_{e^+}, γ_{e^-} and γ_s. The parameter E_{cut} enters the minimization in the form of $1/E_{cut}$ in order to ensure that the χ^2 distribution around the minimum can be described by a second order polynomial. For the fit the AMS-02 data sets of the lepton sum flux and the positron fraction were used exclusively. Compared to separate fluxes those measurements can be done with reduced systematic uncertainties: Measurements of ratios, like the positron fraction, do not require the knowledge of the effective detection area of the detector since it cancels in the computation. A discrimination of the sign of the charge of the particles is redundant for measurements of the flux of $(e^+ + e^-)$ by which the measurement can be performed up to higher energies.
The modulation potentials for solar modulation were assumed to be charge dependent and the same potentials for each data set were used since both data sets were recorded during periods of similar solar activity. It was checked that data set dependent potentials did not significantly change the results.
It was found that a simple power-law parametrization of the electron background does not lead to a reasonable description of the data why a break and an additional spectral index were introduced[1].

Fig. 5.6 illustrates the result of the fit where the lines correspond to the background and signal contribution, respectively. The model predictions and the data for the separate fluxes are shown for consistency reasons only. The corresponding parameter values and their uncertainties as derived from the fit are listed in table 5.1 and are compatible with an analysis in [151]. The best-fit cut-off energy is around $E_{cut} = 1.2$ TeV, but is afflicted with the largest uncertainty of 87% upwards and 32% downwards. By the combination of the spectral index of the electron background contribution and a rather high value of E_{cut}, as demanded by the lepton sum flux, the positron fraction is overshot by the model at the highest energies and does not follow the decreasing trend. This behaviour is affiliated to the large uncertainty of the high energy measurements of the positron fraction and to the fact, that the sum flux measurement up to higher energies has smaller relative errors, but shows a rather smooth behaviour. Within the experimental uncertainties of the sum flux measurement, no drop is observed and the fit is dominated by these data. At the lowest energies an inconsistency between the first data point of the electron and positron flux to the data of the positron fraction and the sum flux can be observed and was confirmed in [151].

[1] In fact, the data are also impossible to describe with properly propagated electrons if an unbroken electron *injection spectrum* is assumed. This points either to an anomalous transport mode above $E \approx 30$ GeV, at which a break is required, but could also be the result of an anomalous acceleration mechanism or of a superimposition of sources with different acceleration mechanisms.

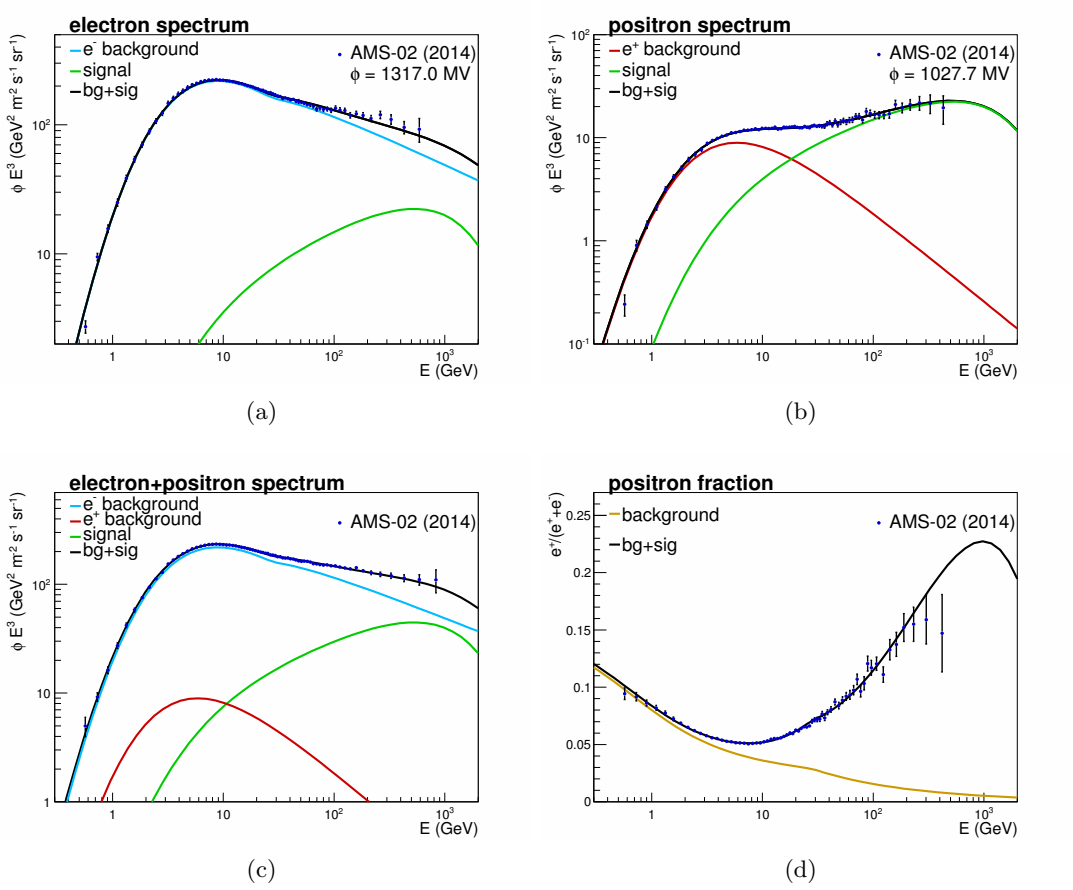

Figure 5.6.: Power-law parameterized model fluxes optimized to recent AMS-02 measurements of the lepton sum flux and the positron fraction. While the lepton sum flux and the positron fraction **(a,b)** yield a combined $\chi^2/Ndof$ of 74.78/129, the separate electron **(b)** and positron **(b)** data yield 55.25/62 and 35.39/61, respectively. The change of slope of the positron fraction is not described by the model due to the smaller relative experimental uncertainties of the sum flux up to higher energies which dominate the fit.

Table 5.1.: Best-fit parameter values for the positron fraction and the lepton sum flux with power-law parameterizations of the fluxes. Especially the parameter E_{cut} is afflicted with large uncertainties of around 87% upwards and 32% downwards.

Parameter	Best-fit value
C_{e+}	108.44 ± 18.06
γ_{e+}	3.87 ± 0.08
C_{e-}	2436.30 ± 136.20
γ^0_{e-}	3.73983 ± 0.02
γ^1_{e-}	3.40056 ± 0.01
ρ_{e-} (GeV)	28.67 ± 0.96
C_s	2.30 ± 1.02
γ_s	2.56 ± 0.10
E_{cut} (GeV)	$1185.53^{+1034.87}_{-376.89}$
ϕ_{e+} (MV)	1027.65 ± 42.08
ϕ_{e-} (MV)	1316.98 ± 20.39
$\chi^2/Ndof$	74.78/129

It was found that appropriate values for E_{cut} strongly depend on the electron spectral index and thus on the break position. In fact, a better description of the high energy data with still reasonable values for $\chi^2/Ndof$ could be obtained by fixing the break position to higher energies of around 40 GeV. However, this influences the preferred value of E_{cut} and thus reasonable conclusions on this parameter cannot be drawn. Shifting the minimal energy for the fit to higher energies and neglecting the low energy data reduces the influence of the solar modulation, but was found to be not constructive since the low energy data are of crucial importance for constraining the positron background contribution (see also [151]).
Fig. 5.7 shows the fit result where the break position was fixed to $\rho_{e^-} = 40$ GeV and all other parameters were left free. This break position was optimized in terms of $\chi^2/Ndof$ by demanding a description of the high energy data within the experimental uncertainties. In this case, the best-fit model yields $\chi^2/Ndof = 106/129$ and the high energy data can be matched. The colored bands correspond to the uncertainty of E_{cut} which was determined by a set of E_{cut} values while data conformity at the highest energies was demanded. The minimal, best-fit and maximal value for E_{cut} are (500, 1276, 2000) GeV with corresponding, overall $\chi^2/Ndof$ values of (112.0, 105.8, 105.9)/129. Note, that the fits with the medium and maximum value for E_{cut} lead to indistinguishable values for $\chi^2/Ndof$ by which the strong correlations and the magnitude of the large uncertainty of E_{cut} become obvious. So far, only 15% of the total expected data from the AMS-02 are available and the situation will improve with more collected statistics.
The analysis showed, that simple power-law assumptions of CR particle fluxes can in principle account for the current available observations, but do a priori not lead to satisfying, i.e. robust, conclusions. The shown model represents merely a parameterization of the data without any predictive power. A more adequate examination implies the consideration of transport processes and energy losses that modify the initial power-law like particle spectra. A possible signal may also originate from several and different kind of sources so that the assumption of a single power-law-like signal is obsolete. However, the simplistic assumption of power-law modeled fluxes used up to now gives hints on the characteristics of the demanded signal at low energies. In particular, in these models the additional positron flux starts to dominate over the background contribution at rather low energies of around 20 GeV.

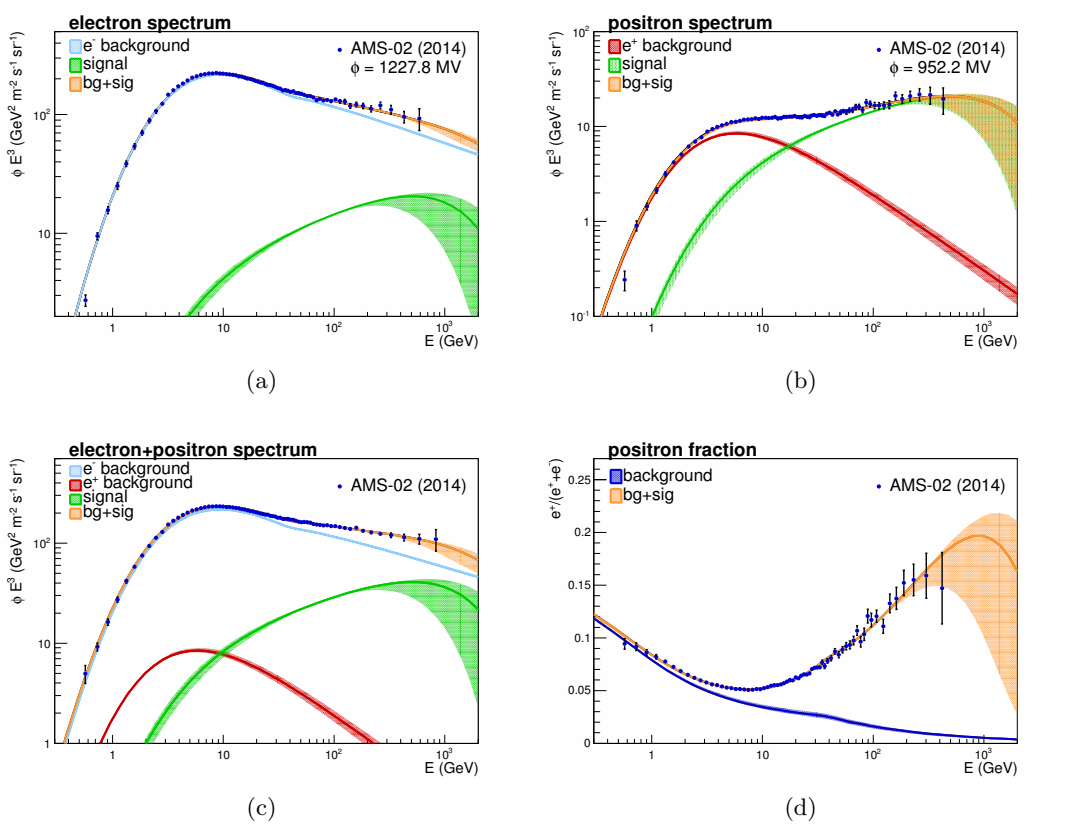

Figure 5.7.: Power-law parameterized model fluxes optimized to recent AMS-02 measurements of the lepton sum flux and the positron fraction at high energies. The break position of the electron background power-law was compared to the best-fit model increased to $E = 40$ GeV, necessary to account for the high energy data. The resulting uncertainty on E_{cut} is illustrated by the colored bands.

In a second approach constrained and well-motivated transport models as derived in the previous chapter are used to predict the secondary positron contribution and to quantify the discrepancy to the data, including transport related uncertainties. The background positron contribution is fixed by interactions of nuclei in the ISM and can directly be compared to the separate positron flux as measured by AMS-02. Even though the experimental relative errors of the positron flux are larger compared to those of the sum flux and the positron fraction, the small absolute errors allow to precisely determine the characteristics of the signal without any knowledge on the electron spectrum. Fig. 5.8 shows the positron predictions and the demanded positron contribution needed to account for the observation. While the filled bands illustrate the transport model related uncertainty on the background positron flux and on the demanded signal, the green dashed lines assign to the additional data uncertainty transferred to the signal. The first data point is not matched due to the already mentioned inconsistency of the data. However, it was checked that the positron flux as derived by combining the data of the positron fraction and the sum flux is desribed at low energies.
At 5 GeV the background contribution is comparable to the signal contribution and the latter starts to dominate over the first at the latest at an energy of 15 GeV in case the experimental uncertainties are taken into account. Above 200 GeV the background contribution lies at least one order of magnitude below the signal contribution and is negligible. The fact, that a significant signal contribution is already demanded at rather low energies, as was also the case for the power-law modeled fluxes, will play a central role in analyses of different source hypotheses as will be presented in the the following chapters.

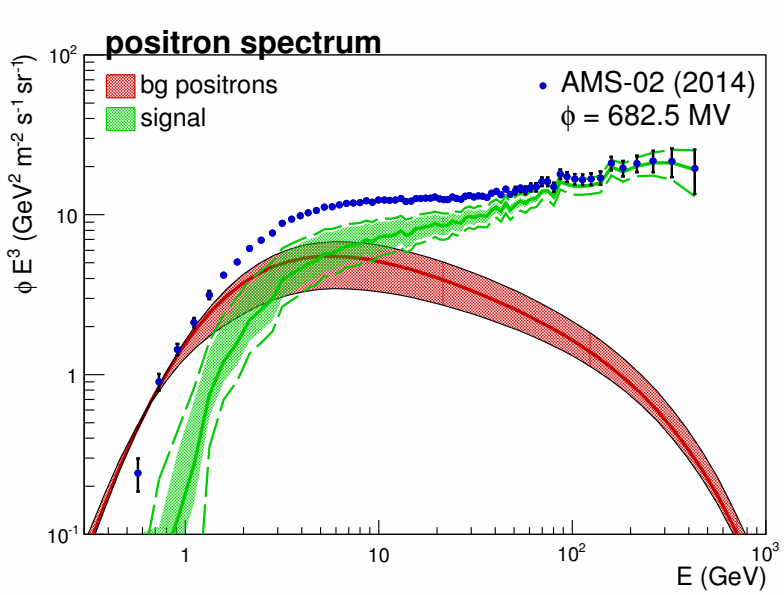

Figure 5.8.: Signal determination from the separate positron flux as measured by AMS-02. While the filled bands illustrate the transport model related uncertainty on the background positron flux and on the demanded signal, the green dashed lines assign to the data uncertainty. The first data point is not in agreement with the positron fraction and the sum flux and is not matched.

5.4. Pulsars as Sources of Electrons and Positrons

In order to investigate the potential electron and positron contributions from nearby pulsars a basic pulsar model is employed and the expected fluxes from 10 nearby pulsars are examined. The overall model is quite basic and depends on a large amount of not well known pulsar parameters which determine the expected fluxes at Earth. This study does not aim to determine these pulsar parameters in a physical meaningful way. It rather discloses the potential of pulsars and the resulting implications in case realistic assumptions are made. The general questions addressed in this study are:

- Are nearby pulsars able to explain current positron measurements if realistic assumptions about the pulsar properties are made?
- How many pulsars are actually needed to explain the data? For instance, can a strong single pulsar account for the observations?
- What are the features and implications of the pulsar explanation? Is the expected dipole anisotropy in agreement with current upper limits?

For the propagation of electrons and positrons from pulsars an analytical solution to the transport equation (eq. 3.25) is used, following closely the model presented in [47]. The model was extended to 3 spatial dimensions for a subsequent, reasonable analyses of the expected anisotropy. The pulsars are treated as point-like sources at (x,y,z) with a source term characterized by a power-law spectrum $\propto E^{-\Gamma}$ and a cut-off energy E_{cut} (eq. 3.24). The normalization of the flux Q_0 is fixed by the total spin-down energy W_0 emitted by the pulsar:

$$\int_{m_e}^{\infty} E \cdot Q(E) dE = \eta W_0, \text{ with } W_0 \simeq \frac{\dot{E} t_{ch}^2}{\tau} \tag{5.2}$$

Herein, m_e is the mass of the electron, $\dot{E}$ is the pulsar spin-down luminosity (i.e. the energy loss rate), t_{ch} is the characteristic pulsar age (the time an ideal magnetic dipole at infinite frequency needs to slow down to the observed frequency), $\tau \approx 10^4$ yr is the characteristic luminosity decay time and η is the efficiency for the production of $e^{\pm}$ pairs for which the commonly used value $\eta = 0.4$ is adopted.
Models of 10 nearby pulsars are investigated which are expected to contribute most to the electron and positron flux. All other (known) pulsars were found to contribute less than 0.1% to the flux at energies of the peak emission [47]. The pulsars properties like their age, their distance and their injection spectrum order the expected flux completely, but are fraught with large uncertainties. Fig. 5.9 illustrates the influence of the pulsar age, distance and $\dot{E}$ on the expected electron or positron flux at Earth by applying variations of 20% to the corresponding parameters of a benchmark model. Especially the distance crucially influences the absolute flux and deviations of about one order of magnitude are already present for a 20% uncertainty, which is typically much lower than current experimental uncertainties. Table 5.2 lists the considered pulsars and their parameters. Also shown are the conservatively combined parameter limits on the distance taken from [47] and from the second FERMI-LAT pulsar catalogue [152] which are used for the fit. The allowed range of the injection indices is taken to be $1 \leq \Gamma \leq 2$ and for the limits of the age and $\dot{E}$ a general uncertainty of 20% is assumed.

For the calculation of the expected dipole anisotropy Δ the following formula as derived in Appendix E is used:

$$\Delta = \frac{3D}{v} \frac{\left|\vec{\nabla} N\right|}{N}. \tag{5.3}$$

Herein, D is the rigidity dependent diffusion coefficient, v is the particles velocity and N is the electron (positron) number density at Earth. The dipole anisotropy is ever calculated for the total flux, i.e. it includes the background electrons (positrons) as well as the entirety of the considered pulsars. A dipole anisotropy of the background electrons is expected due to the source distribution which is the largest between the Galactic Center and the solar position. It drops in the direction to the anti center leading to an effective flux from the direction of the center to the anticenter at Earth. An additional pulsar does not necessarily increase the resulting anisotropy. Depending on the position of the pulsar the total anisotropy can be increased or decreased or even vanish for specific models. The same holds for several pulsars whose combined anisotropy is amplified or weakened depending on their position. Therefore the largest anisotropy is expected in case of one or several pulsars positioned on the connecting line between the Earth and the Galactic Center.

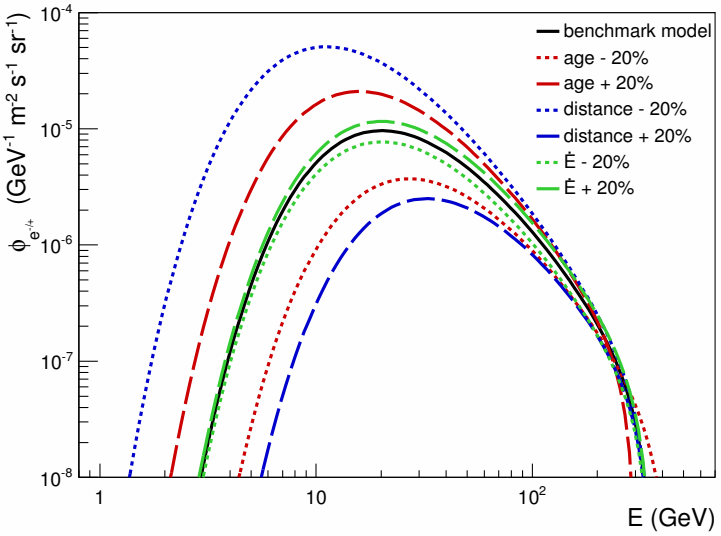

Figure 5.9.: Influence of pulsar parameters on the expected positron flux at Earth. The solid black line corresponds to a benchmark model to which parameter variations of 20% to the age, distance and spin-down luminosity $\dot{E}$ were applied.

Table 5.2.: Pulsar parameters of 10 nearby pulsars which are expected to contribute most to the electron and positron flux at Earth. The limits on the distance were taken from [47] and [152] and were conservatively combined.

Pulsar name	l (°)	b (°)	Distance and limits (kpc)	Age (kyr)	$\dot{E}$ (10^{34} erg/s)
J0357-32	162.76	-16.00	0.82 (0.66 - 0.98)	585	0.6
J1732-31	-3.69	1.01	1.52 (1.21 - 1.83)	120	14.6
J1741-2054	6.43	4.91	1.11 (0.27 - 1.43)	392.1	0.9
J1809-2332	7.39	-1.99	1.45 (0.70 - 2.70)	67	43
J1836+5925	88.88	25.00	0.44 (0.04 - 0.84)	1800	1.1
J2021+4026	78.23	2.09	0.44 (0.38 - 1.95)	76.8	11.4
J0633+1746	-164.87	4.27	0.28 (0.18 - 0.47)	342	3.3
J0659+1414	-158.89	8.26	1.39 (0.25 - 1.56)	110	3.8
J1057-5226	-75.00	6.65	1.02 (0.10 - 1.22)	535	3
J2043+2740	70.61	-9.15	3.35 (1.26 - 4.12)	1200	5.5

5.4.1. Models with One, Two and Three Pulsars

In a first approach the potential from single pulsars for describing the positron fraction at high energies is investigated. The transport parameters of the applied background model were set in such a way to best describe measurements of global observables. The electron injection spectrum of the background electrons was consistently determined using data of the separate electron flux. However, above 43 GeV the injection spectrum is assumed to be featureless, i.e. unbroken, corresponding to a more conservative approach with a less steep slope of the positron fraction given by the background contribution. Within the experimental uncertainties the existence of a break in the electron injection spectrum at higher energies cannot be confirmed or disproved.

By a fit of pulsar parameters within the applied limits to the positron fraction above 100 GeV five pulsars yielding the largest potential positron and electron flux were identified, namely J0633+1746 (Geminga), J0659+1414 (Monogem), J1057-5226, J1809-2332 and J2021+4026. Fig. 5.10 shows the fit result for the Monogem pulsar exemplarily where

the distance and the spin-down luminosity were set to the minimal distance and the maximal spin-down luminosity for a maximal electron and positron contribution, respectively. Whereas the absolute positron flux is barely sufficient to explain the data above 100 GeV an additional description of the slope above 30 GeV was found to be impossible to mimic with a single pulsar. A model with two strong pulsars as shown in fig. 5.11 is able to explain the data above 30 GeV but another pulsar is needed to account for the whole energy range, as shown in fig. 5.12 for a model including three pulsars.
The expected dipole anisotropy in $(e^+ + e^-)$ of the particular model including the three pulsars is shown fig. 5.13 and compared to upper limits as published by the FERMI collaboration [153]. The anisotropy is shown for two cases: First, the three pulsars are assumed to be located on the connecting line between the Sun and the Galactic Center. While the total flux depends only on the distance and remains the same the anisotropy can be taken as the maximal expected anisotropy since an amplification and no cancellation due to the background electrons and positrons occurs. This allows for the fact that the additional electron and positron contribution might not necessarily originate from the named pulsars. Second, the experimentally measured directions of the three named pulsars and resulting cancellation effects are considered. In both cases, the expected anisotropy is in agreement with current experimental upper limits. The predicted dipole anisotropy in the ratio e^+/e^- (see chap. E.2) was additionally compared to the current upper limit as measured by the AMS-02 experiment in an energy range between 16 and 350 GeV, but was found to be roughly one order of magnitude below the quoted value of 0.030 at a 95% confidence level [14].
Although the anisotropy predictions are in agreement with current upper limits the anisotropy from both the background and the pulsars depends on the applied diffusion coefficient, i.e. on D_0 and δ, and may be increased or decreased. Probing the pulsar origin of the additional, primary positrons by the detection of a dipole anisotropy should be handled with due care. It is in principle possible, but at least up to a certain extend a not detected dipole anisotropy should not be used as an exclusion criterion as long as uncertainties on D_0 and δ are not taken into account and the number and strengths of the contributing pulsars are not known. The influence of the diffusion coefficient on the dipole anisotropy will be emphasized in the next chapter by assuming a larger diffusion constant within the framework of a model including possible contributions from ten pulsars.

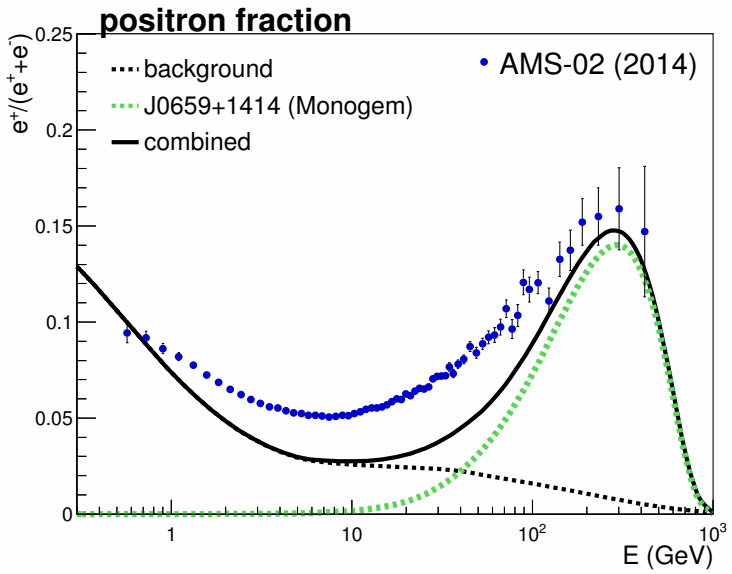

Figure 5.10.: Single pulsar model for the description of the positron fraction. Shown is the potential contribution as can be expected from the Geminga pulsar. A rather steep injection spectrum with a spectral index of ≈ 1 as well as maxed out parameters for the distance and the spin-down luminosity are needed to match the data at high energies.

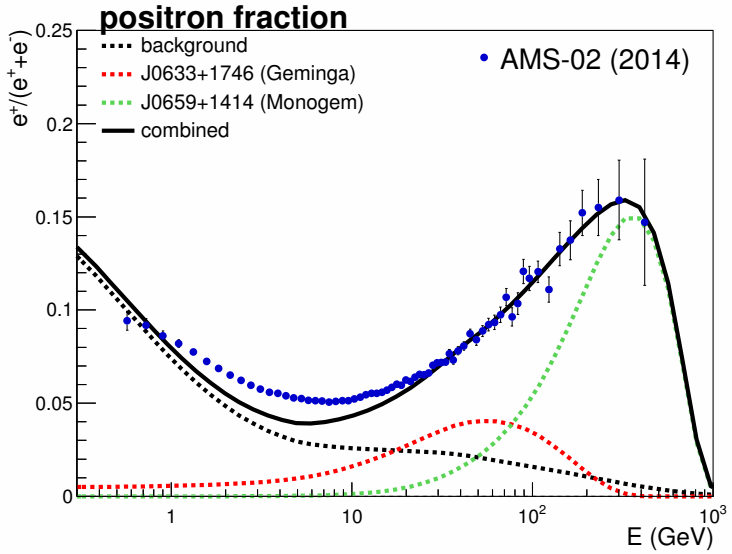

Figure 5.11.: Double pulsar model for the description of the positron fraction. Shown are the potential contributions from the Geminga and the Monogem pulsar. In this model the positron flux at high energies is dominated by Monogem and Geminga plays an overall subordinate, but nevertheless important role at intermediate energies.

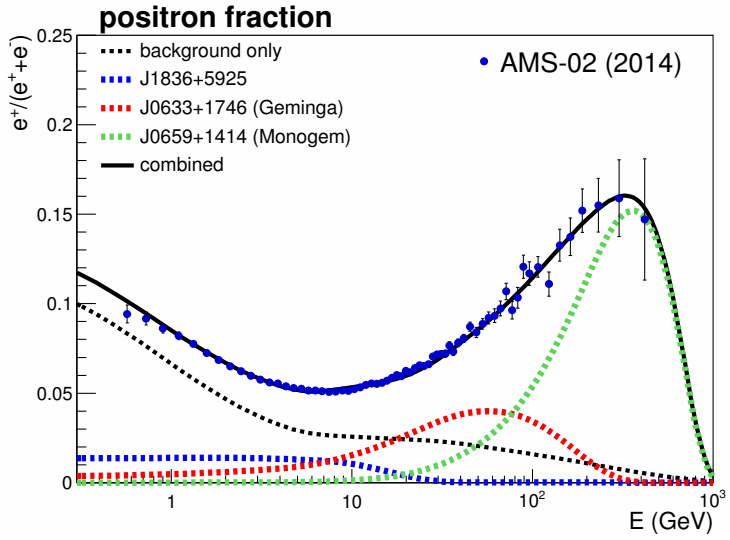

Figure 5.12.: Triple pulsar model for the description of the positron fraction. Shown are the potential contributions from three pulsars needed as a minimal number of pulsars to explain the positron fraction in the whole energy range. The applied modulation potentials are $\phi_{e^+} = 723.5$ MV and $\phi_{e^-} = 806.5$ MV.

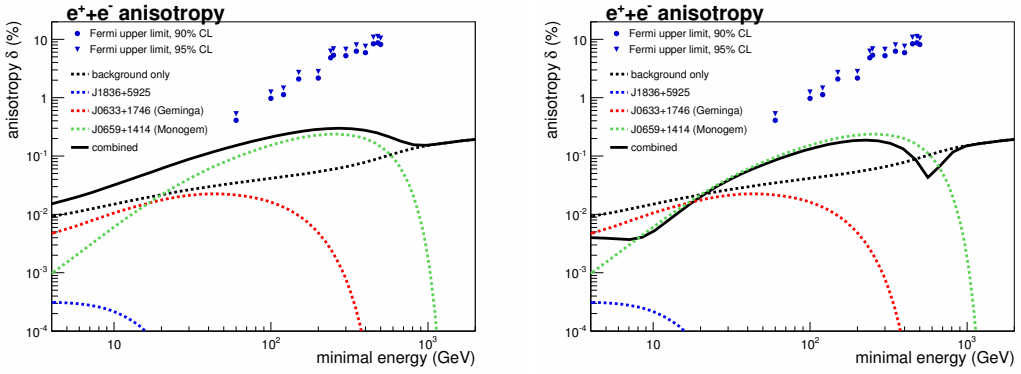

(a) (b)

Figure 5.13.: Expected dipole anisotropy of the triple pulsar model. The anisotropy is shown as a function of the minimal energy in a cumulative energy binning up to 1 TeV and beyond. In **(a)** the anisotropy was calculated assuming the three pulsars to be located on the connecting line between the Sun and the Galactic Center. In **(b)** the directions of the named pulsars and cancellation effects are taken into account by which a reduction as well as a change of the direction of the dipole anisotropy from the galactic anti-center to the center occurs. In both cases, the anisotropy is in agreement with current upper limits from Fermi. Limits taken from [153].

5.4.2. Model with Ten Nearby Pulsars

The full potential of ten known nearby pulsars, which are expected to contribute most to the local positron flux, is now investigated by a fit of the pulsar parameters to the lepton sum flux and the positron fraction. In total, 50 pulsar parameters and two charge-dependent modulation potentials enter the fit whereby the number of degrees of freedom is exceedingly large. Due to the degeneracy of the solution (for instance, a commutation of two similar pulsars by exchanging the corresponding parameters is possible) the derived model is merely one of many possible scenarios. Fig. 5.14 shows the fit results with

$\chi^2/Ndof = 76.58/88$. Noticeable are few dominating pulsars describing the high energy data of the sum flux. The high energy data of the positron fraction are barely matched due to the assumption of an unbroken background electron injection spectrum above 43 GeV, as already discussed in chapter 5.3. Between 1 and 500 GeV the remaining pulsars contribute differently strong in various energy ranges and account for the needed positron contribution in the GeV region. Also shown is the expected dipole anisotropy dominated at high energies by the pulsar J1809-2332 which is located at a galactic latitude of $l = 7.39°$. At low energies the large amount of pulsars lowers the expected dipole anisotropy due to efficient diffusion. The dipole anisotropy expected from this model, which includes rather strong pulsar contributions at high energies as demanded by the lepton sum flux, is also in agreement with current upper limits. However, the diffusion constant and the rigidity dependence of the diffusion coefficient were fixed to $D_0 = 1.79 \cdot 10^{28}\text{cm}^2/\text{s}$ and $\delta = 0.57$ and their uncertainties were not considered. The expected dipole anisotropy of a re-fitted model with the maximal allowed diffusion constant of $D_0 = 7.81 \cdot 10^{28}\text{cm}^2/\text{s}$ and an appropriate rigidity dependence of $\delta = 0.5$ is shown in fig. 5.15. The assumed diffusion coefficient crucially affects the dipole anisotropy and a slight tension to the upper limits is present by which the particular model is disfavoured. This demonstrates that specific models are already sensitive to current upper limits on the dipole anisotropy and that current and future limits can put constraints on the particular models.

Summarized, it was shown that current AMS-02 measurements of the lepton sum flux and the rise in the positron fraction can be explained by additional primary $e^{\pm}$ pairs originating from nearby pulsars. It was found that at least three pulsars are needed to explain the shape of the positron fraction and the positron flux in the whole energy range. The presented models proved that both a further rise and a drop of the positron fraction can be modeled in case reasonable assumptions about the pulsar parameters are made. Future measurements of the slope of the positron fraction up to higher energies will therefore not disprove the pulsar explanation a priori in case a further drop is observed.
An effective dipole anisotropy is expected by all shown models, but its strength was found to be crucially affected by the underlain diffusion coefficient. A model assuming an intermediate, well-motivated diffusion coefficient was found to be in agreement with current upper limits by FERMI and AMS-02, consistent with similar studies in [154] and [155]. Specific models including larger diffusion coefficients were found to exceed current upper limits. In a publication by the FERMI collaboration [153] larger anisotropies were predicted due to a larger, but still reasonable diffusion constant of $D_0 = 5.8 \cdot 10^{28}\text{cm}^2/\text{s}$ as well as the incorporation of FERMI data of the lepton sum flux which show a rather hard energy spectrum and hence higher pulsar fluxes are demanded. These data were found to be not consistent with AMS-02 and at the highest energies [156]. Future experimental upper limits or the detection of a dipole anisotropy will allow to constrain the pulsar and transport models or even challenge the pulsar explanation. A pulsar induced anisotropy is certainly the most auspicious feature to prove or disprove this explanation and to distinguish between this and other, non-point-like source based explanations.

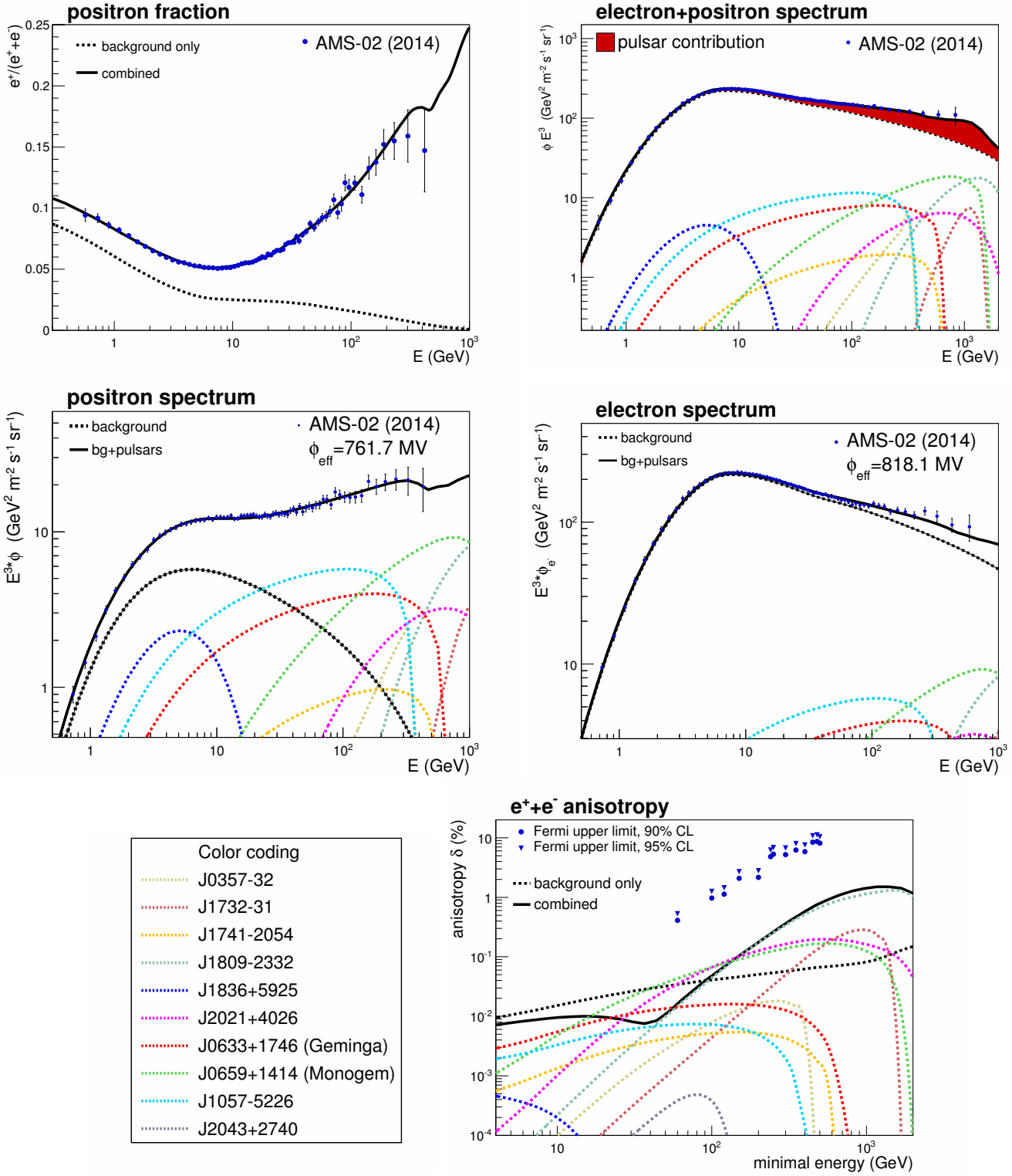

Figure 5.14.: Fit results and expected anisotropy for the ten pulsar model. The pulsar parameters as well as the modulation potentials were fitted to the lepton sum flux and the positron fraction as measured by AMS-02 ($\chi^2/Ndof = 76.58/88$). The separate fluxes are shown for consistency reasons only. The resulting anisotropy is in agreement with current upper limits as given by FERMI.

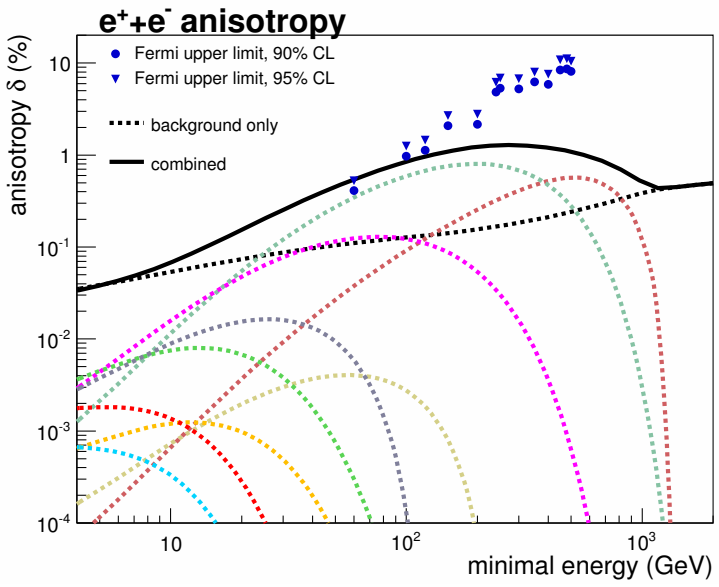

Figure 5.15.: Expected anisotropy for a low diffusion, ten pulsar model. The pulsar parameters were optimized for a rather high value of $D_0 = 7.81 \cdot 10^{28}\mathrm{cm}^2/\mathrm{s}$ by which the role of particular pulsars changed. In this case the anisotropy is slightly in tension with current upper limits and the model is disfavoured.

5.5. Dark Matter Annihilation as a Source of Cosmic Rays

In this chapter the potential $e^{\pm}$ pair production by annihilating DM particles is examined and compared to current lepton measurements by AMS-02 and antiproton measurements by PAMELA. In a previous work by Cirelli et al. [157] a model-independent analysis including experimental measurements by PAMELA, ATIC, HESS and FERMI was performed. The authors disclosed in agreement to other studies that a sufficient amount of positrons requires either

- leptophilic DM particles, i.e. an exclusive annihilation into lepton pairs for a suppression of the antiproton production,
- a DM mass around 1 TeV/c^2 and an annihilation into $\mu^{\pm}$ for a reasonable description of the positron fraction and a compatibility to antiproton measurements,
- large DM masses of 10 TeV/c^2 and an annihilation into $W^{\pm}$ which leads to features in the antiproton spectrum in an energy range not yet accessible. However, such a model was found to be disfavoured by HESS data on the $e^+ + e^-$ spectrum.

An update of this work was published in 2013 including precision measurements of the positron fraction by AMS-02. The indicated flattening was found to favour DM masses below about 1 TeV/c^2 which is, however, not supported by FERMI measurements of the $e^+ + e^-$ spectrum. The already mentioned inconsistency of the FERMI data to AMS-02 data of the $e^+ + e^-$ spectrum as well as the fact that in [157] the background contributions were freely renormalized make a revisiting necessary.
The analysis in the present work gives special importance not only to the highest energies, but also to the intermediate energy range in which already a relatively strong positron contribution is required if no renormalization of the positron background is applied, see fig. 5.8. The analysis is performed model-independent and data-driven, i.e. no particular supersymmetric DM model is assumed. Depending on the DM mass the electron, positron and antiproton spectra resulting from annihilations into different channels to particles of

the SM are used to fit the data and to determine the required relative strengths of the different channels, i.e. the branching fractions.
The differential particle yields defined as the number of particles per annihilation process in a given energy range for certain DM masses, annihilation cross-sections, local DM densities and DM halo profiles are calculated for different annihilation channels with the `DarkSusy` software package version 5.1.1 [158]. `DarkSusy` is an advanced numerical package for DM calculations including resonances, pair production thresholds and coannihilations for supersymmetric neutralino models. External packages like `FeynHiggs`, `ISASUGRA` and `SUSPECT` are incorporated for the computation of masses and mixings of the particles for a variety of models defined by the user. The features of `DarkSusy` were widely broken down and merely the differential particle yields for certain, pure DM channels are used.
For the computation of the differential electron and positron yield in case of a direct DM annihilation into $e^{\pm}$ pairs the DM particles are assumed to be non-relativistic whereby the particle yield in the energy range between E and $E + dE$ can be written as

$$\frac{dN_{e^+}}{dE} = \frac{dN_{e^-}}{dE} = \delta(E - m_\chi). \tag{5.4}$$

An annihilation into light fermion pairs is *helicity suppressed* by a factor of the fermion mass squared $\propto (m_f/m_\chi)^2$ whereby the annihilation into $e^{\pm}$ pairs is expected to be suppressed the strongest compared to $\mu^{\pm}$ and $\tau^{\pm}$. The employed DM halo mass profile is the Navarro-Frenk-White profile (NFW), a model derived from N-body simulations of cold DM halos [159] and one of the most commonly used profiles. A potential enhancement of the signal by the clumpiness of DM is not considered in the halo parameterization. Instead, it is absorbed in scaling factors of the spectral templates. Therefore, the distribution of DM clumps follows directly the applied model of the diffuse component and the overall scaling factor corresponds to a boost factor. The boost factor is defined as the required enhancement due to the clumpiness relative to the diffuse component. Note, that disregarding substructures not only affects the normalization of the $e^{\pm}$ flux but also the spectral shape due to transport effects.
A local DM density of $\rho_{local}^{DM} = 0.3\,\mathrm{GeV/cm^3}$ and a thermally averaged and channel independent annihilation cross section of $\langle\sigma v\rangle = 3 \cdot 10^{-26}\mathrm{cm^3 s^{-1}}$ are assumed, as derived from the kinematics of stars [160] and the relic density, respectively. In order to keep the model parameters at a minimum these values are kept constant whereby the quoted boost factors are ever related to these values. After the initial particle spectra are calculated the particles are propagated by the numerical solution of the transport equation using `DRAGON`. The propagation of particles originating from DM annihilation is hence consistently applied in the same way as for conventional CRs, especially in terms of energy losses.
The fitting procedure is based on a multi-step-fitting-approach in which the free boost factors and modulation potentials are optimized by a χ^2 minimization for certain, fixed DM masses. The considered mass range is $0 < m_\chi \leq 1$ PeV/c^2 within which logarithmically equidistant mass values are examined. The following annihilation channels into leptons, quarks and gauge bosons are investigated:

$$\chi + \chi \rightarrow \begin{cases} e^+ + e^- \\ \mu^+ + \mu^- \\ \tau^+ + \tau^- \\ c + \bar{c} \\ t + \bar{t} \\ b + \bar{b} \\ g + g \\ W^+ + W^- \\ Z^0 + Z^0 \\ Z^0 + \gamma \end{cases}$$

Scans were performed for each channel separately as well as for a combination of all channels for which an optimization of the branching fractions was adopted. The used data for the χ^2 calculation are the lepton sum flux and the positron fraction by AMS-02 as well as the antiproton flux measured by PAMELA. The results are illustrated by the minimized $\chi^2/Ndof$ value as a function of the DM particle mass for a standard and a leptophilic DM annihilation scenario, see fig. 5.16. As indicated by the large $\chi^2/Ndof$ values of $\gg 1$, none of the models is able to describe the spectral shape of the lepton data in the whole energy range without violating constraints from the antiproton flux. This holds for particular exclusive channels as well as for a combination of all considered channels. Selected models including the best leptophilic model, the best-fit model with $\chi^2/Ndof \approx 50$ and a lepton optimized model excluded by antiproton measurements are shown in appendix F for illustration (figs. F.26, F.27, F.28).

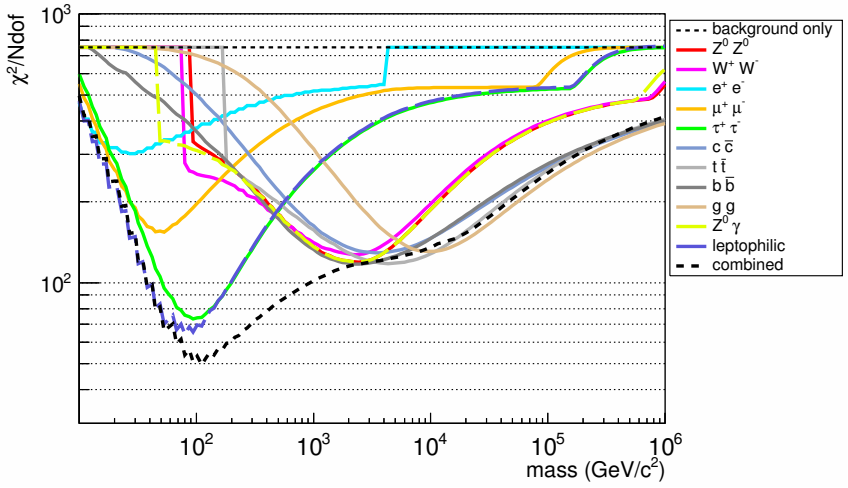

Figure 5.16.: $\chi^2/Ndof$ values as a function of the DM mass for different annihilation channels and an exclusive annihilation into charged leptons (leptophilic DM). Even though the annihilation branching fractions were optimized for a best description of the demanded spectral shape of the lepton data, none of the models is able to describe the AMS-02 measurements in the whole energy range without violating constraints from the antiproton flux. An illustration of selected models is given in appendix F.

Another scenario was studied in which DM annihilation is assumed to account only for the positron contribution at the highest energies and lower energetic positrons originate from other sources, like e.g. from nearby pulsars. Note, that the background positron contribution at the highest energies is negligible and the influence from the background

model is kept at a minimum. A fit was performed including the lepton data above $E = 100$ GeV and constraints from antiprotons. The results of the scan are shown in fig. 5.17. An annihilation into the lepton pairs $\mu^{\pm}$ or $\tau^{\pm}$ favours DM particle masses of around 849 and 2078 GeV/c^2, respectively, whereas the $\tau^{\pm}$ channel is preferred by the resulting spectral shape of the expected $e^{\pm}$ flux. An annihilation into both $\mu^{\pm}$ and $\tau^{\pm}$ favours a DM mass of 1 TeV/c^2 and implies an abrupt drop of the positron fraction, as shown in fig. 5.18. Also shown is the predicted dipole anisotropy largely determined by the local gradient of the applied DM halo profile. It is, compared to a point source induced anisotropy, rather low due to the small local gradient of the DM density profile.
Annihilations into gauge boson pairs favour rather high masses of around 21 TeV/c^2 leading to an production of high energetic antiprotons in an energy range not accessible by the PAMELA data. The particle spectra are shown in fig. 5.19 for a DM particle mass of 21 TeV/c^2 and an exclusive annihilation into $W^{\pm}$, exemplarily. Also shown are data of the $e^+ + e^-$ flux as measured by the HESS experiment which were not considered in the fit. These data clearly show an enhanced flux compared to the AMS-02 data and a highly non-power-law-like spectral shape in the very high energy range not covered by AMS-02. The presented model can explain the high energy lepton data above $E = 100$ GeV and predicts a further rise in the positron fraction. It is conform with antiproton measurements by PAMELA and predicts a significant antiproton contribution above $E = 100$ GeV. Precision measurements of the antiproton flux and the positron fraction up to higher energies by AMS-02 will yield a strong constraining power and will allow to put these kind of models to the proof.

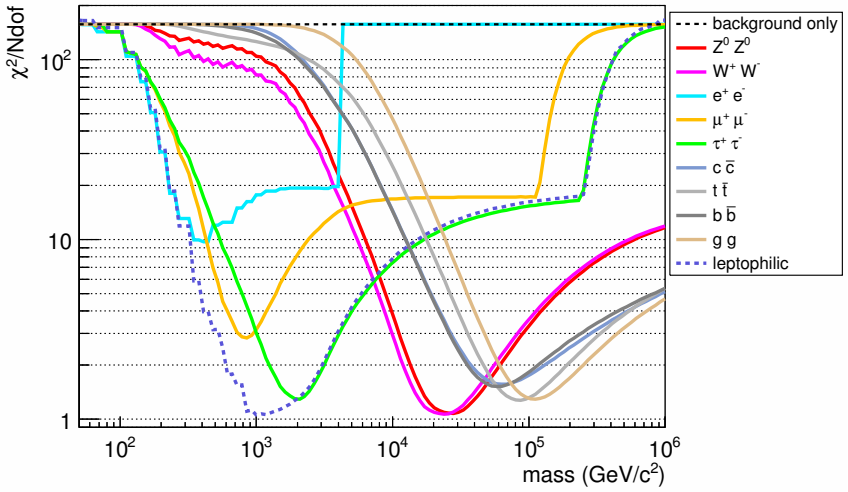

Figure 5.17.: $\chi^2/Ndof$ values as a function of the DM mass for the lepton data above 100 GeV and constraints from antiprotons. The most interesting models are shown in fig. 5.18 and 5.19.

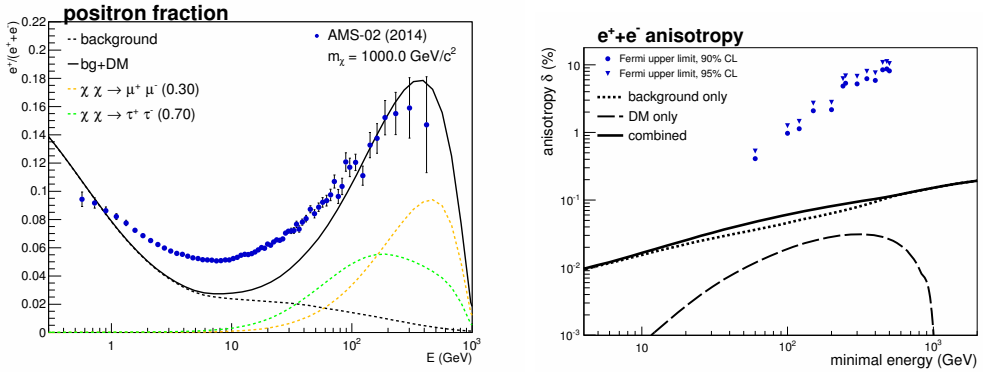

(a) (b)

Figure 5.18.: Best-fit leptophilic DM annihilation model for the lepton data above $E = 100$ GeV which predicts an abrupt drop of the positron fraction **(a)**. In this model DM particles with a mass of 1 TeV/c^2 annihilate with a share of 30% into $\mu^{\pm}$ and with 70% into $\tau^{\pm}$. The contribution was boosted with $b = 1270$. The expected dipole anisotropy **(b)** is compared to a point source induced anisotropy rather low due to the small local gradient of the applied DM halo profile.

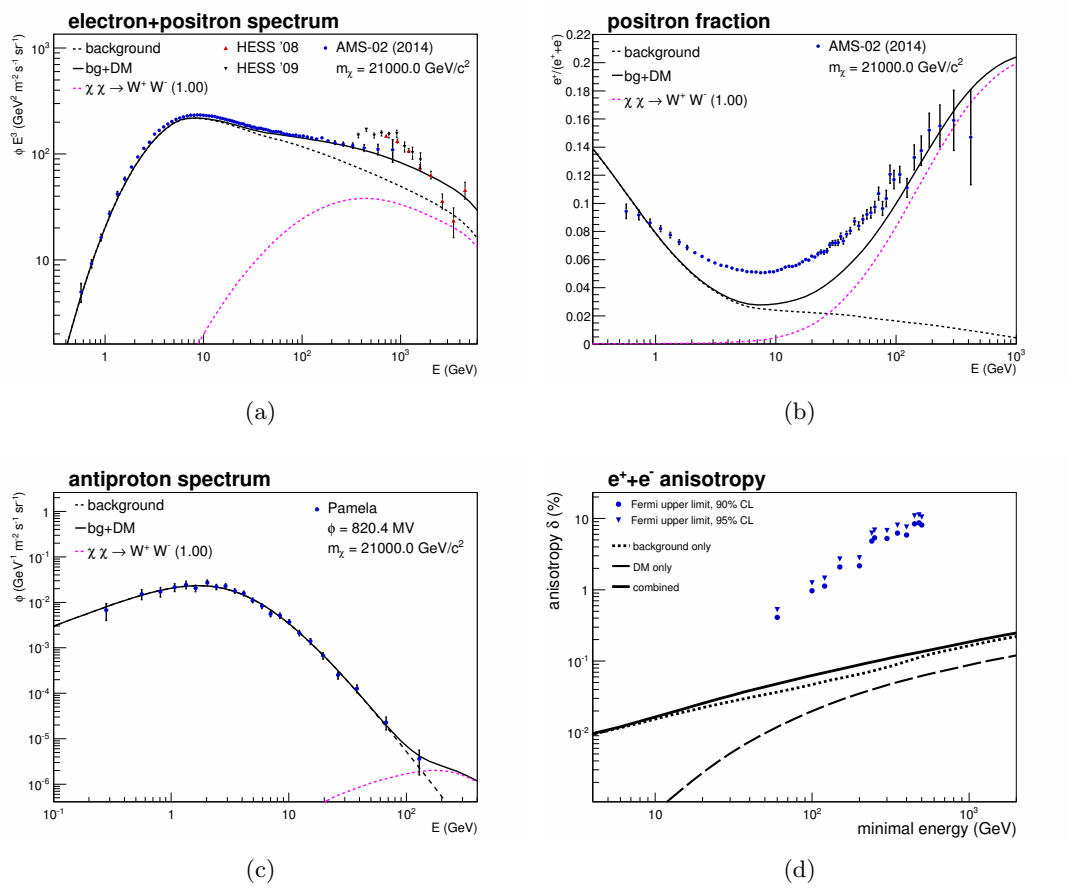

Figure 5.19.: Best-fit DM annihilation model for the lepton data above $E = 100$ GeV and with constraints from antiprotons. By assuming a particle mass of $m_\chi \approx 21$ TeV/c^2, an exclusive annihilation into $W^\pm$ and a boost factor of b=58,884, the model can explain the lepton data above $E = 100$ GeV **(a)(b)** and predicts a further rise of the positron fraction. The model does not violate constraints from antiprotons as measured by PAMELA **(c)**. The $e^+ + e^-$ flux at the highest energies as measured by HESS [161], [162] shows a highly non-power-law-like behaviour and cannot be matched **(a)**. Also in this model the expected dipole anisotropy **(d)** is rather low.

6. Diffuse Gamma-Ray Emission in the Galaxy

Diffuse, galactic gamma-rays arise from hadronic and leptonic interactions of CR particles with the interstellar gas and the ISRF. The largest contribution in the GeV energy range originates from decaying π^0 mesons, which are produced in hadronic collisions of CR hydrogen and helium nuclei with the interstellar gas. Leptonically produced gamma-rays arise mainly by interactions of electrons and positrons with the ISRF (inverse Compton scattering) and with the interstellar gas (Bremsstrahlung). For details about the hadronic and leptonic gamma-ray production mechanisms the reader is referred to chapter 3.3.2. In this chapter the expected gamma-ray emission of models constrained by locally measured nuclei spectra and ratios is compared to gamma-ray measurements by FERMI. The gamma-ray predictions of a large amount of transport models in a minimal transport setup constrained by locally measured nuclei as well as a gamma-ray and nuclei optimized model will be presented. For this purpose the steady-state solutions for the densities of protons, helium, electrons and positrons, normalized to locally measured abundances, are used together with the ISRF and the gas column densities to calculate the emissivity, which is the number of particles per unit of volume, time, energy and interaction. Skymaps for the gamma-ray emission are obtained by the integration of the emissivities along the LOS in a given direction (l,b) for an observer at Earth. The contribution from inverse Compton scattering can be directly calculated using the ISRF and the electron and positron densities. Contributions from Bremsstrahlung and pion decays require models for the galactic H_I and CO (tracer of H_2) distributions as a function of (r,z) for which combined astronomical surveys are used [163], [164]. Those distributions are partitioned into galactocentric rings based on the assumption that the gas obeys a uniform circular rotation curve. This allows to indirectly consider galactic structures for the gas content like for instance the spiral arm structure.

The gamma-ray gradient problem

The all-sky gamma-ray observations are by far not well understood and large discrepancies in terms of the spectral shape of the gamma-ray energy spectrum, the absolute photon flux and the gradient of the emissivity along the galactic longitude within the galactic plane are observed. The latter is called *gamma-ray gradient problem* and implies that the galactocentric radial distribution of CRs is much steeper than the distribution one would expect from gamma-ray measurements which demand significant contributions originating

at large radii [17], [18]. A solution to this problem using EGRET data could be found by the assumption of a sharp rise of the conversion factor between the CO emissivity and the H_2 density with the galactocentric radius, called X_{CO} factor or calibration ratio and defined as $X_{CO} = N(H_2)/W_{CO}$ [165]. Herein, $N(H_2)$ is the molecular hydrogen column density and W_{CO} the integrated intensity of the 2.6 mm emission line of carbon monoxide. A radial rise of X_{CO} up to factors of five to ten leads to an increased gas density at large radii which can balance the the decreasing CR density leading to a better description of the gamma-ray profiles along the galactic longitude. The sharp rise of X_{CO} as used in [165] is illustrated in fig. G.29.
The existence of the gamma-ray gradient problem could be confirmed by the FERMI-LAT collaboration [166]. However, an analysis of the gamma-ray emission in the third Galactic quadrant as measured by FERMI-LAT revealed that the conversion factor X_{CO} is flat over several kpc with $X_{CO} \approx 2 \cdot 10^{20} \mathrm{cm}^{-2} (\mathrm{K\,km\,s}^{-1})^{-1}$ and that no significant differences are present between the local spiral arm and the interarm region. The authors concluded that a larger halo size, or more generally, a flatter CR source distribution than those usually assumed are required. Other scenarios studied in [167] imply anisotropic and spatially non-uniform diffusion and are quite successful without any changes of the source term, the halo height or X_{CO}.
In the present work the assumption of a homogeneous and isotropic diffusion coefficient is retained and a constant value of X_{CO} is assumed. The potential and limitations of this kind of transport models are examined by variations of transport parameters and comparisons to the measurements.

6.1. Predictions for the Diffuse Gamma Ray Emission in the Galaxy

The diffuse gamma-ray emission was calculated for the CR steady-state densities of 10,050 well-motivated transport models of the minimal transport model setup whose transport parameters were constrained by local observations of p, $\bar{p}$, $\bar{p}/p$, B/C, $^{10}Be/^{9}Be$ and SubFe/Fe. The LOS integration was performed with a step resolution of 10 pc. The skymaps were calculated in the *HEALPix* projection [168] with a resolution of 49,151 equal sized pixels covering the spherical sky. For the analyses, the modeled gamma-ray emissions are compared to almost 4 years of FERMI data in various regions of the sky as shown in fig. D.23. Since this study aims to review the predicted large-scale CR densities, regions which are known to comprise anomalous gamma-ray contributions are excluded, namely the Galactic Center, the galactic bar and the *Fermi Bubbles*.
Fig. 6.1 shows the predicted gamma-ray emission and its composition for the best-fit model on local nuclei spectra and ratios as well as the envelopes of a selection of 10,050 models for an illustration of the transport related uncertainty in the minimal transport model setup. Each model of the selection is characterized by an unbroken nuclei injection spectrum which determines the characteristic, decreasing shape of the mostly dominating contribution from pion decays. At the galactic poles (Region F) the gamma-ray emission is dominated by the isotropic, extragalactic contribution for which a model[1] provided by the Fermi Science Support Center (FSCC) was incorporated. None of the gamma-ray spectral shapes of the considered regions can be reasonably described by models of the minimal transport model setup and a harder hadronic component is required in any direction of the sky. Consequently, models with broken nuclei injection spectra have to be considered and the data-conformity to both local nuclei spectra and ratios and gamma-rays will be investigated.
Also shown in fig. 6.2 is the longitudinal profile of the gamma-ray emission within the

[1] iso_p7v6source.txt. Isotropic spectral template from a fit to the all-sky emission for $|b| > 30°$ [29].

Galactic Disc with $|b| < 5°$ in the energy range $0.9 < E < 1.3$ GeV for the best-fit model on local nuclei spectra and ratios. The normalizations of the particular contributions were best possible optimized and the *gamma-ray gradient problem* is shown up due to the too little CR density above around $|l| = 100°$ as predicted by the model.

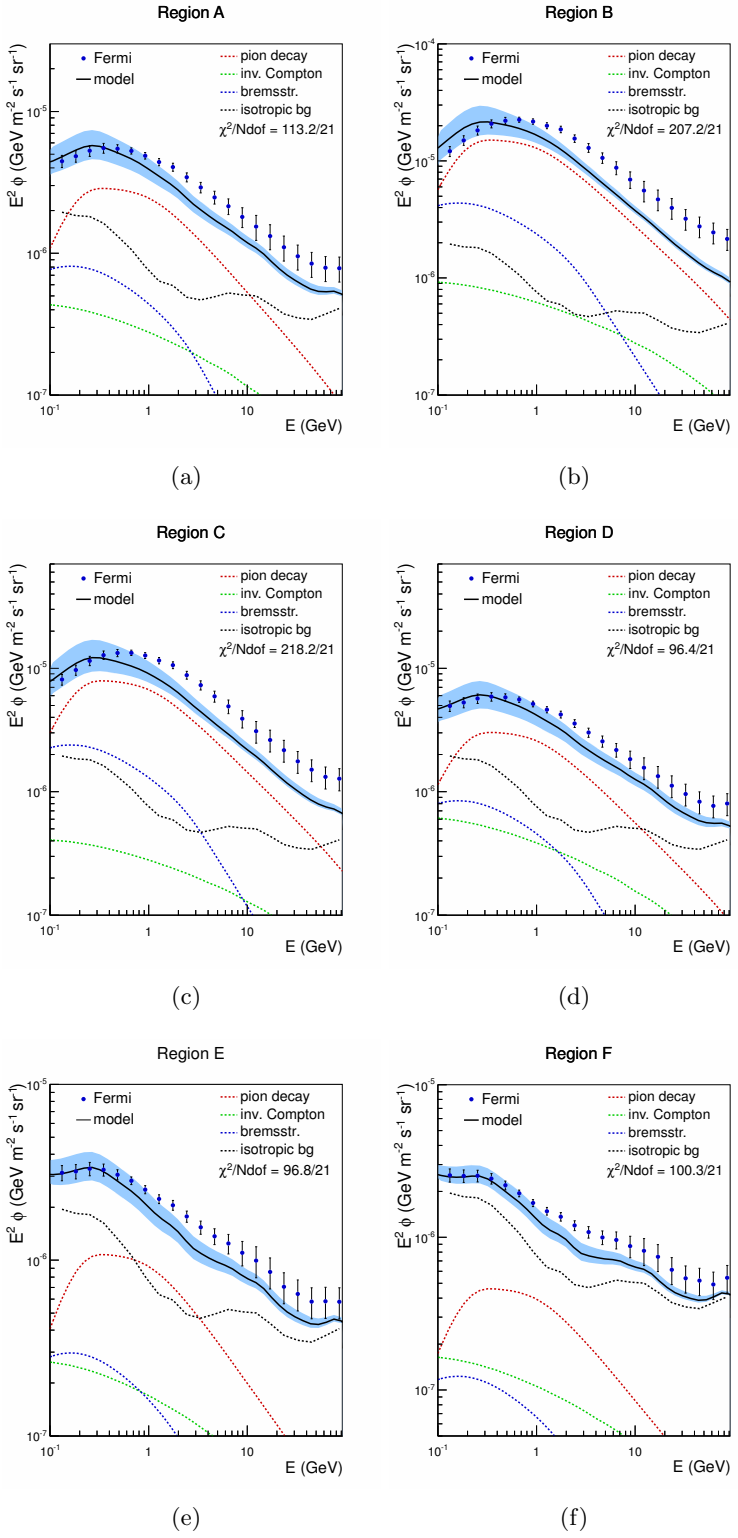

Figure 6.1.: Gamma-ray predictions of transport models of the minimal transport setup in various directions of the sky as defined in Appendix D (fig. D.23). The best-fit model on locally measured spectra and ratios is shown as the black, solid line and the transport related uncertainty is illustrated as the colored band. None of the models all of which imply an unbroken nuclei injection spectrum can account for the spectral shape of the gamma-ray data.

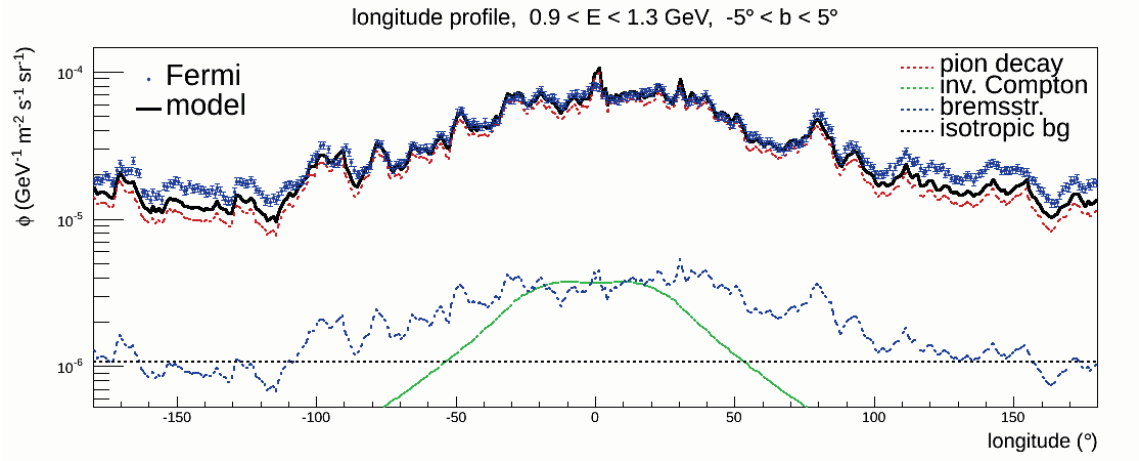

Figure 6.2.: Illustration of the gamma-ray gradient problem. Shown is the longitudinal profile of the gamma-ray emission within the Galactic Disc with $|b| < 5°$ for the best-fit model on local nuclei spectra and ratios. The predicted CR density above around $|l| = 100°$ is not sufficient to explain the gamma-ray measurements.

6.2. Gamma-Ray and Nuclei Optimized Model and its Implications

A MCMC based sampling method optimized for parameter determination was used in combination with an extended model setup in order to examine the possible data-conformity to both locally measured nuclei spectra and ratios as well as gamma-rays. The transport parameters were optimized to the spectra of p, $\bar{p}$, the ratios of $\bar{p}/p$, B/C, $^{10}Be/^{9}Be$ and the energy spectrum and the longitudinal and latitudinal profiles of the gamma-ray emission. Compared to the minimal model setup the extended model setup implies a single broken nuclei injection spectrum to account for the spectral shape of the gamma-ray spectrum as well as a convective transport mode.
It was found that with such a model setup a data-conformity up to a certain extend can be achieved, but only if the normalizations of the proton- and electron density used for the gamma-ray computation are disentangled from the locally observed densities. This could be realized in nature if the solar position represents a local over- or underdense region in terms of the particle density, as will be discussed in chapter 6.3. The normalizations of the gamma-ray contributions were fitted to the data by a template fit procedure. A global scaling was applied for the pion decay contribution, the isotropic background and the leptonic contributions. Since both leptonic contributions depend on the electron density a common scaling was applied absorbing the absolute scale of the electron density. Fig. 6.3 shows the gamma-ray spectrum of the best-fit model found by the MCMC based parameter sampling[1]. Table 6.1 lists the transport parameters of this optimized model and the applied, global scaling factors for the different gamma-ray components. The overall spectrum and the spectra in the considered regions as shown in fig. 6.3 are well described. However, the overall proton density throughout the galaxy must be enhanced by a factor of 1.98 compared to the locally measured density and the overall electron density must be reduced by a factor of 0.58 for a reasonable description of the gamma-ray spectrum. The enhancement of the isotropic background by 13% is justified by the gamma-ray flux at high energies at the galactic poles (region F) where it completely determines the flux. This suggests an underestimation of the implied model as published by the FERMI collaboration. The simultaneous enhancement of the total flux at low energies by the increased isotropic

[1]The computation of gamma-ray skymaps is in general time consuming. The number of sampled models is limited and was found to be not sufficient for a statistical analysis.

component can be counterweighted by a reduction of the pion decay contribution through an increase of the convection velocity with dV_c/dz. Compared to the models derived in the minimal transport model setup the optimized model sticks out by a flatter radial proton density distribution, as shown in fig. 6.4. This is caused by a special combination of the halo height L and the diffusion constant D_0 which was found to be not favoured by the nuclei measurements. The softer gradient has far reaching implications on the longitudinal gamma-ray profile as shown in fig. 6.6. The profile is well described and merely in the range $135° < |l| < 150°$ the emission is slightly underestimated. Close to the galactic anti-center the model predicts a sufficient CR density and the gamma-ray gradient problem is not apparent. The latitue profile of the model is shown in fig. G.30.

Fig. 6.7 shows the locally expected nuclei spectra and ratios of the gamma-ray and nuclei optimized model, however, normalized to the local proton density for the inspection of the spectral shape demanded by the gamma-ray data. The overall slope of the proton spectrum as measured by PAMELA (fig. 6.7(b)) is by far not perfectly described. In the high energy range between $E = 80$ GeV and 550 GeV a softer proton spectrum is predicted and the flux is overestimated. Merely above $E = 550$ GeV the prediction is in agreement with the data. Note, that the PAMELA data show a non-power-law-like behaviour at high energies and a compromise has always to be made in case a featureless proton injection spectrum within this energy range is assumed.

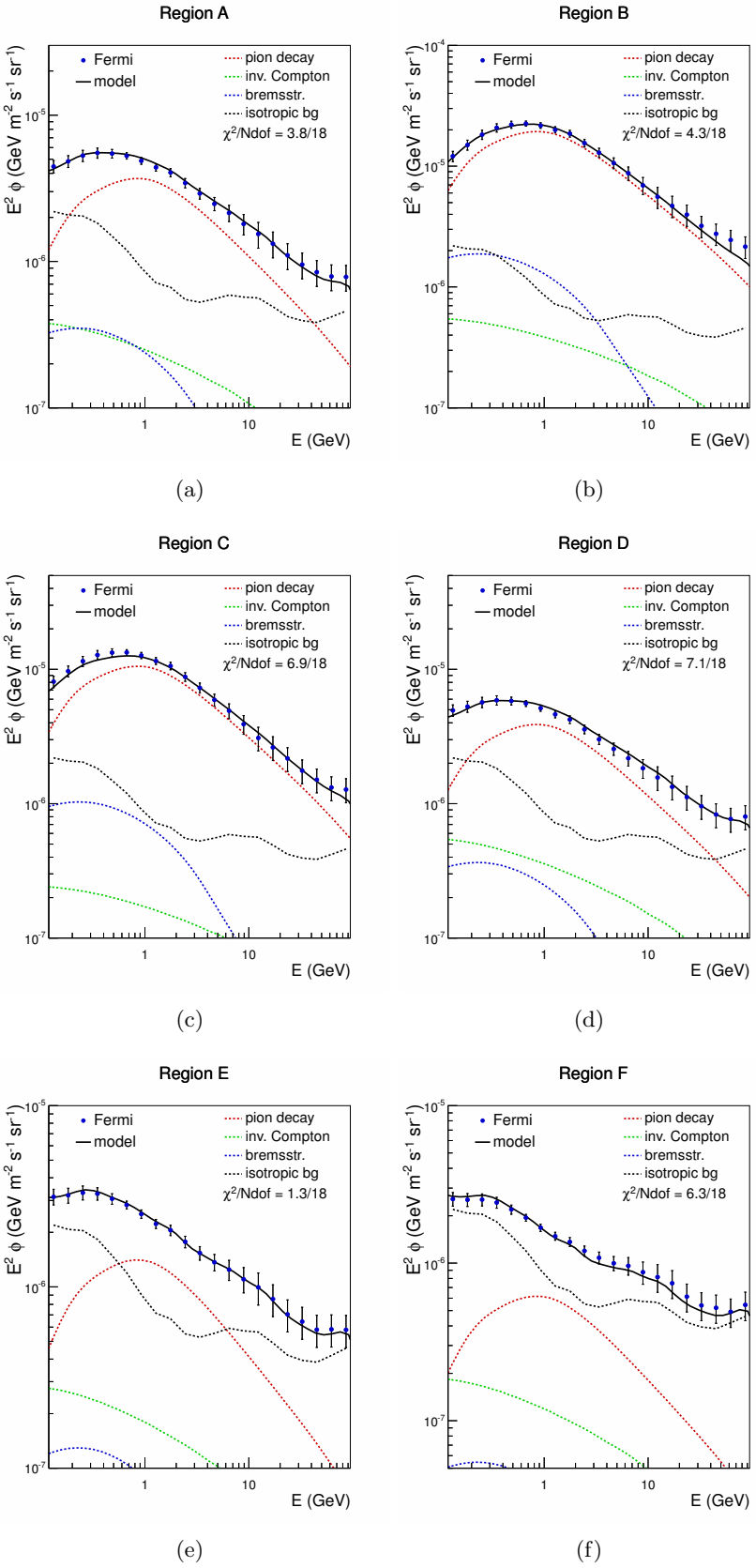

Figure 6.3.: Gamma-ray spectra in various regions of the sky for an optimized model. The model implies a broken nuclei injection spectrum with a break at $\rho = 4.62$ GV and spectral indices of $\alpha_0 = 1.43$ below and $\alpha_1 = 2.16$ above. The global scaling factors for the particular contributions are $C_{pi} = 1.98$, $C_{ic,br} = 0.53$ and $C_{iso} = 1.13$.

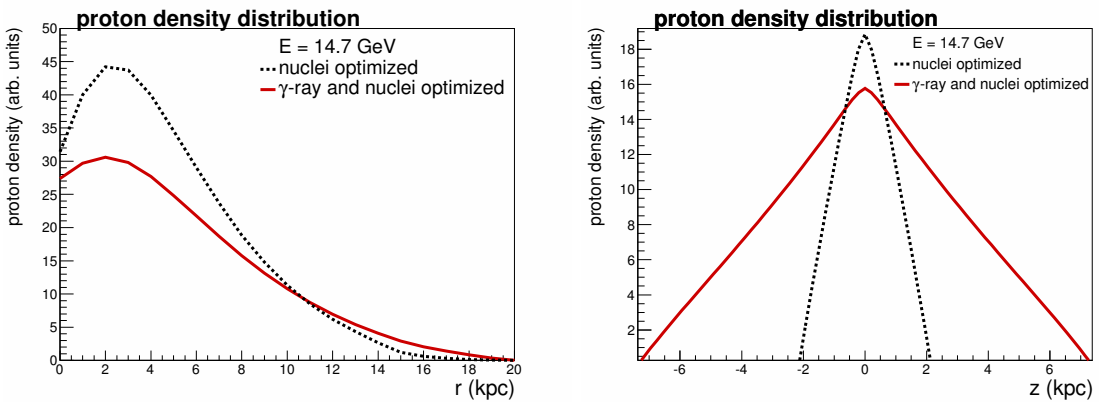

(a) (b)

Figure 6.4.: Proton density profiles for models optimized for nuclei only and additionally for gamma-rays. The densities are normalized to locally measured values and an increase by a factor of about two is needed to account for the gamma-ray observations. In **(a)** the radial proton density is shown at $z = 0$ kpc as a function of r by which the softer gradient of the gamma-ray and nuclei optimized model becomes apparent. None of the selected models of the minimal transport model setup shows a flatter gradient due to the special combination of L and D_0 which is not favoured by nuclei measurements. In **(b)** the profile is shown at $r = 8$ kpc as a function of z illustrating the broader distribution due to the larger halo height of $L = 7.37$ kpc.

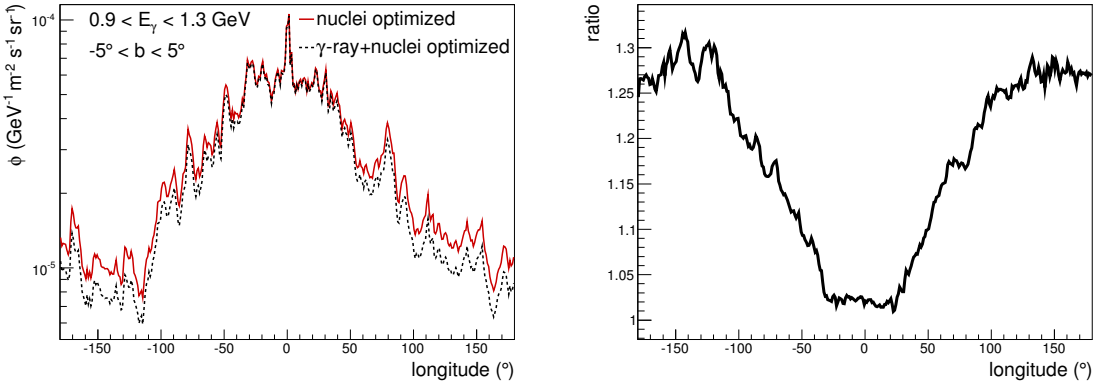

(a) (b)

Figure 6.5.: Longitudinal profile of the pion induced gamma-ray emission between 0.9 and 1.3 GeV and $|b| < 5°$. In **(a)** an enhanced contribution above $|l| = 40°$ is apparent due to the flatter proton density distribution. The ratio shown in **(b)** illustrates the different gradients of the gamma-ray profile leading to an enhanced emission by around 25% in the galactic anti-center.

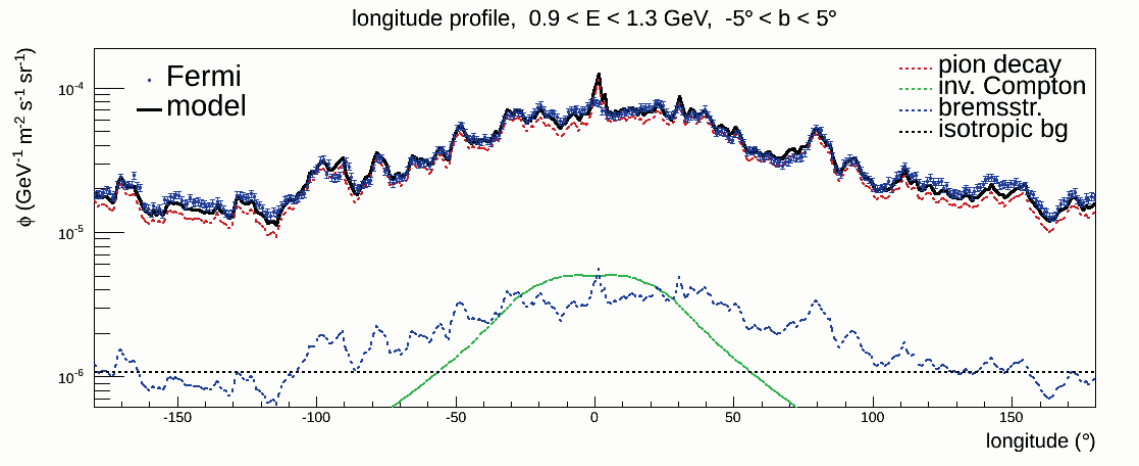

Figure 6.6.: Longitudinal profile of the gamma-ray emission within the Galactic Disc with $|b| < 5°$ for the gamma-ray and nuclei optimized model. The profile is well described and merely in the range $135° < |l| < 150°$ the emission is slightly underestimated. Close to the galactic anti-center the model predicts a sufficient CR density and the gamma-ray gradient problem is not apparent.

Table 6.1.: Parameters of the gamma-ray and nuclei optimized transport model. The model is characterized by a broken nuclei injection spectrum which results in a harder gamma-ray spectrum from pion decays. While the convection velocity at the solar position with 0.78 km/s is rather low the increase by $dV_c/dz = 1.29$ km/s/kpc significantly decreases the contribution from pion decays below $E = 1$ GeV at the galactic poles.

Parameter	Unit	Value
D_0	$10^{28}\mathrm{cm}^2/\mathrm{s}$	4.24
δ	1	0.63
L	kpc	7.37
η	1	-0.53
v_α	km/s	2.23
v_0	km/s	3.71
$f_b \equiv v_b/v_0$	1	0.21
dV_c/dz	km/s/kpc	1.29
α_r	1	0.08
ρ_0	GV	4.62
α_0	1	1.43
α_1	1	2.16
C_{pi}	1	1.98
$C_{ic/br}$	1	0.58
C_{iso}	1	1.13

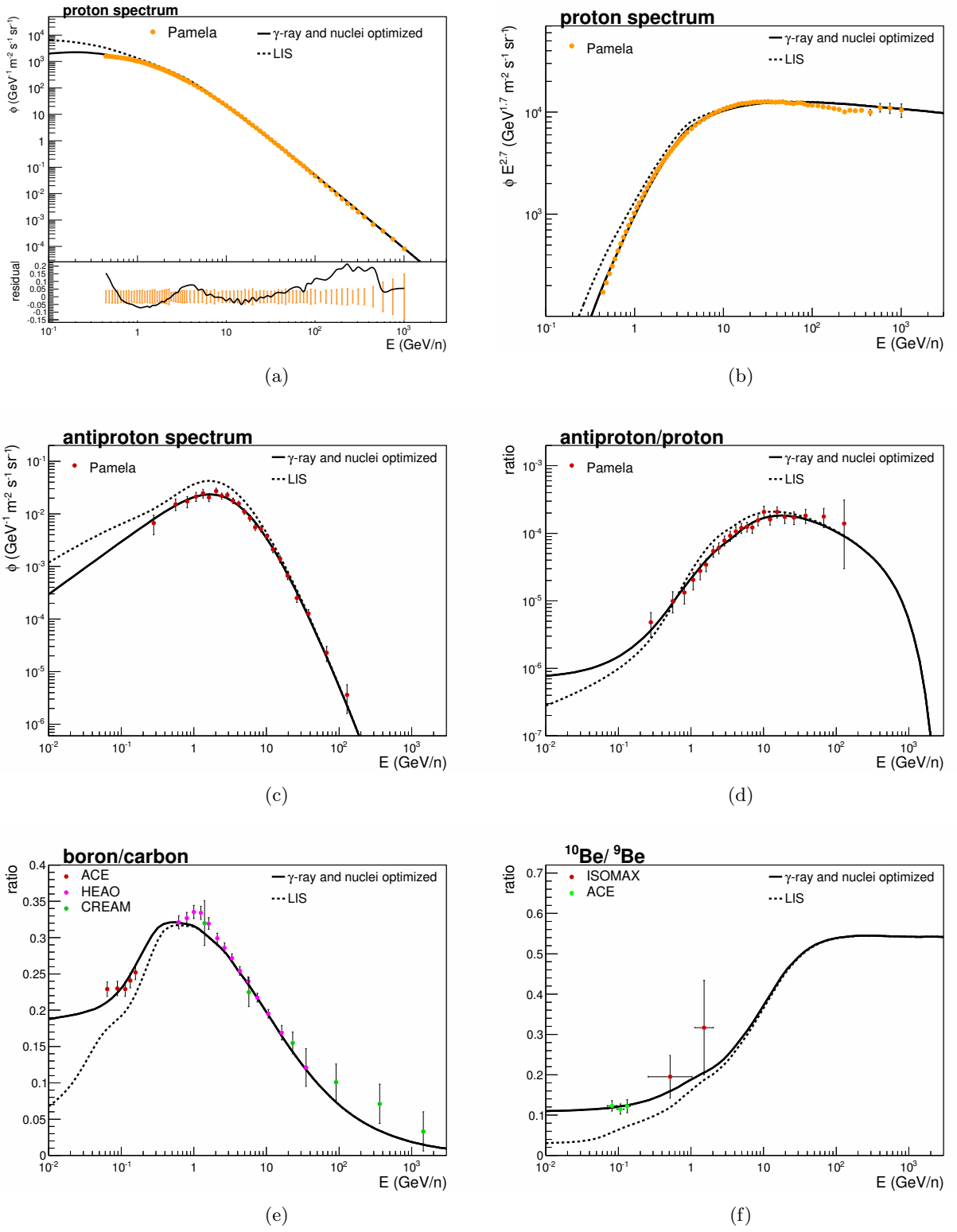

Figure 6.7.: Local energy spectra and ratios as predicted by the gamma-ray and nuclei optimized transport model. The dotted line corresponds to the local interstellar spectrum (LIS) and the solid line to the solar modulated spectrum. The proton spectrum is normalized to the locally observed value.

Fig. 6.8 shows the discrepancy of the optimized model to the data in the region of the Fermi Bubbles which was excluded from the optimization. An additional, hard gamma-ray component is needed which is believed to arise from a freshly accelerated proton

population from star-forming regions, like the Galactic Disc, the galactic bar and the spiral arms. This population interacts with the gas that may be pushed to high latitudes by strong, pressure induced galactic winds in the inner Galaxy [45]. The harder gamma-ray spectrum within the Fermi Bubbles with $\propto E^{-2.1}$ compared to the one originating from the 'old' proton population with $\propto E^{-2.7}$ is explained by the advective environment in which the proton energy spectra are not modified by diffusion. The authors of the cited publication incorporated the presented gamma-ray and nuclei optimized model as a background model for studies of the properties of the Fermi Bubbles and the galactic bar. Since gamma-rays are not absorbed by dust they can be used as tracers for star-forming regions and allow precision determinations of the tilting of the galactic bar. Furthermore, it was found that the bubbles are strongly correlated with the gas distribution, while the spectral shape of the bubble showed that the hadronic CR component dominates over the leptonic component.

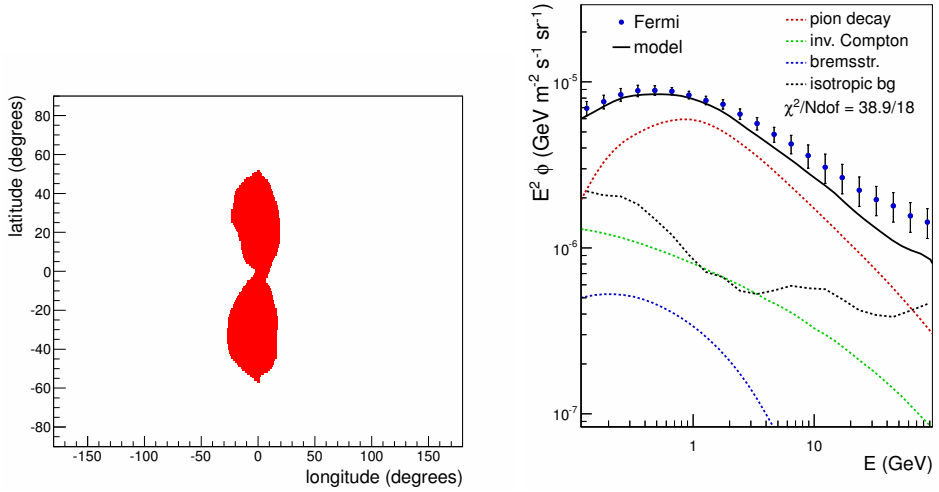

Figure 6.8.: Gamma-ray spectrum within the Fermi Bubbles. A parameterization of the structure is shown on the left [169] while the measured gamma-ray spectrum in comparison to the optimized model is shown on the right. The latitude profile of the gamma-ray emission including the bubbles is shown in fig. G.30.

6.3. The Influence of Local Structures on the Proton Distribution and Gamma-Ray Emission

In the previous chapter it was shown that the gamma-ray spectrum in the bigger part of the sky can be described if the expected hadronic gamma-ray component from pion decays is assumed to be roughly twice as big. However, the proton density needed for the increased pion production is incompatible with local proton measurements. This discrepancy is a known fact and was for instance already pointed out in [76].
It seems reasonable to suppose that the Sun's position represents an extraordinary region in which the proton density may be lower than as expected from CR transport models. In fact, our Sun resides in the *Local Bubble (LB)*, a low density region of gas with radii between 65 to 150 pc into the Galactic plane and extending hundreds of parsecs perpendicular to it [89]. The density inside the LB is about $0.05\,\mathrm{atoms/cm^3}$ which is approximately one tenth of the average density of the ISM [19], [170]. The Sun entered the structure more than five million years ago and is currently moving through the *Local Fluff*, a small overdense region consisting of interstellar clouds. Fig. 6.9 shows a schematic sketch of the LB in comparison to the Sun and various objects in the solar neighbourhood. Its

origin and the observed shape are believed to be related to multiple supernovae explosions within the past ten to twenty million years [20]. The LB is believed to be rather a chimney-like than a bubble-like structure which extends much further into the halo than into the Galactic Disc. This is related to the much lower external pressure from the ISM in the galactic halo. It is compelling to study more realistic diffusion models in which the diffusion coefficient in local structures can be different. A structure like the LB can have far reaching implications on the transport of CRs and studies examining the impact of different transport scenarios on the particle densities and anisotropies by local variations of the gas density and transport parameters are ongoing and will be published soon [171]. The present analysis focuses on the potential influence of the LB on the proton density and the gamma-ray emission. A three dimensional model for the LB was implemented in `DRAGON` allowing local variations of transport parameters and the gas density. A less efficient confinement of the particles inside the LB is investigated, thus an increased diffusion constant within the local structure is applied. Two setups are examined in which the diffusion constant D_0 follows a spherically symmetric and a chimney-like bubble geometry. The absolute bubble dimension as well as the shape at the borders are strongly restricted by the resolution of the spatial grid. Necessary in terms of computation time and memory requirement is the appropriation of a non-equidistant spatial grid allowing an exceedingly high local resolution and a reduced, but nevertheless high enough, resolution in regions far away from the Sun where a substantial amount of CR sources are located. Fig. 6.10 illustrates the applied spatial grid in the plane of the Cartesian x and y coordinates by which a resolution of $\Delta x = \Delta y = \Delta z = 5$ pc around the solar position at (x,y,z)=(8.3,0,0) kpc became feasible.

In a generic approach a simple bubble setup with a bubble radius of $r = 160$ pc as shown in fig. 6.10 was examined. Within the bubble the diffusion constant was increased by factors of 10, 50 and 90 and due to numerical reasons forced to drop smoothly at the borders to the average value assumed throughout the Galaxy. Fig. 6.11 shows the resulting proton density profile for each case as well as for the no-bubble benchmark scenario. Although the bubble's influence is obvious by a flattening of the gradient of the proton density a reduction at the solar position could not be achieved in this setup. A reduction of the proton density requires a passage through which the protons can escape. In the chimney-like setup the bubble border in z-direction was set aside by what an outflow of particles in z-direction was realized. Such a scenario is physically motivated by the absence of the pressure induced counterweight of the ISM above and below the Galactic Disc. Fig. 6.11 shows the profile obtained with this chimney-like structure leading to a significant and sufficient density reduction at the solar position. The shape of the local proton spectrum was found to be only marginally affected by the increased diffusion constant as shown in fig. 6.12.

Although the bubble structure was chosen to be very small compared to the scale of the Galaxy the smoothly increased diffusion constant crucially affects the proton distribution in wide areas far away from the solar position. A significantly reduced proton density is apparent even at large heliocentric distances of several kpc which crucially affects the expected gamma-ray emission from pion decays. For the gamma-ray LOS integration an increased step resolution of 2 pc was applied within and around the bubble structure in order to resolve small-scale gradients of the proton distribution. The resulting all-sky gamma-ray spectrum (region A) for a factor of the diffusion constant of 90 is shown in fig. 6.13 by which the large influence and the insufficient description of the data is illustrated. Calculations incorporating smaller bubble dimension could not be performed due to exceedingly high memory requirements. However, for an estimation of the maximal bubble size constrained by the gamma-ray data the proton density was manually modified. It was found that maximal bubble radii up to around 20 pc which are far below the dimension of the LB are requested in order to not modify the gamma-ray emission too much.

The results reveal that by a local and closed bubble-like modification of the diffusion process the local proton density cannot be reduced by a factor of two. An opened, chimney-like structure with radii of 160 pc can account for the observed proton density, but also crucially affects the proton density in wide regions around the solar position. The lowered proton density also affects the expected gamma-ray emission which can then not be matched. Therefore, a bubble induced modification of the diffusion process can a priori not explain the discrepancy between the locally observed proton density and the one demanded by gamma-ray measurements. However, due to the simplicity of the applied setup, explanations based on local impacts cannot be excluded as a matter of principle and a more extensive study is called. Especially models with strong convection velocities which blow the particles away from the galactic disc are promising and will be extensively studied in future analyses.

Figure 6.9.: Schematic sketch of the Local Bubble. The blue colored regions correspond to regions with decreased gas density in contrast to the yellow regions. Credit: N. Henbest, H. Couper.

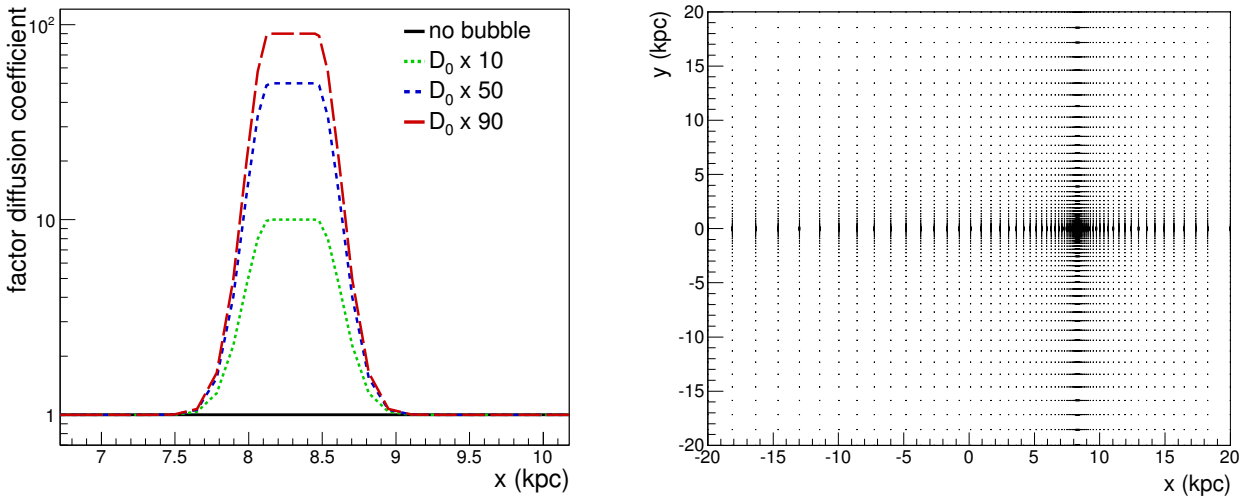

Figure 6.10.: Applied bubble geometry **(left)** and the spatial grid **(right)** needed for an appropriate resolution of the small-scale structure.

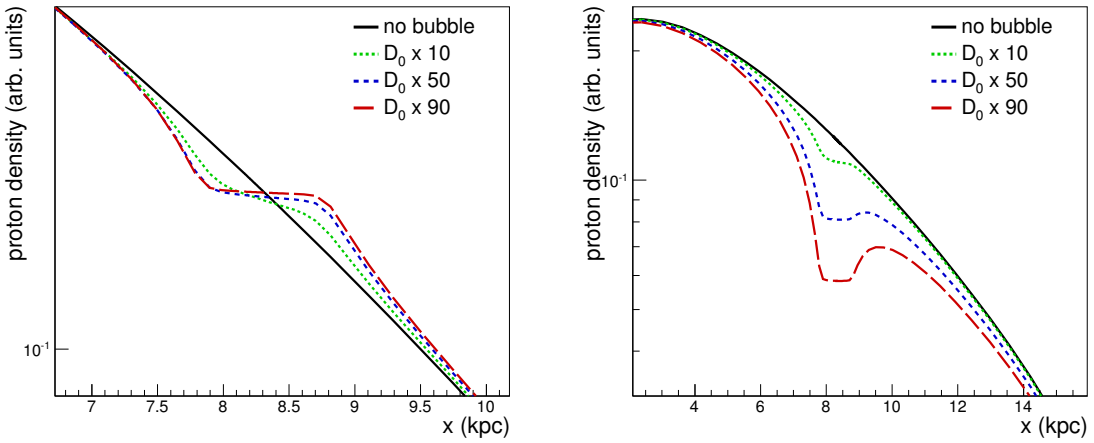

Figure 6.11.: Proton density profiles for the closed, bubble-like **(left)** and the chimney-like **(right)** bubble structure for different factors applied to the local diffusion constant. The local proton density is significantly reduced in case an open, chimney-like geometry is assumed.

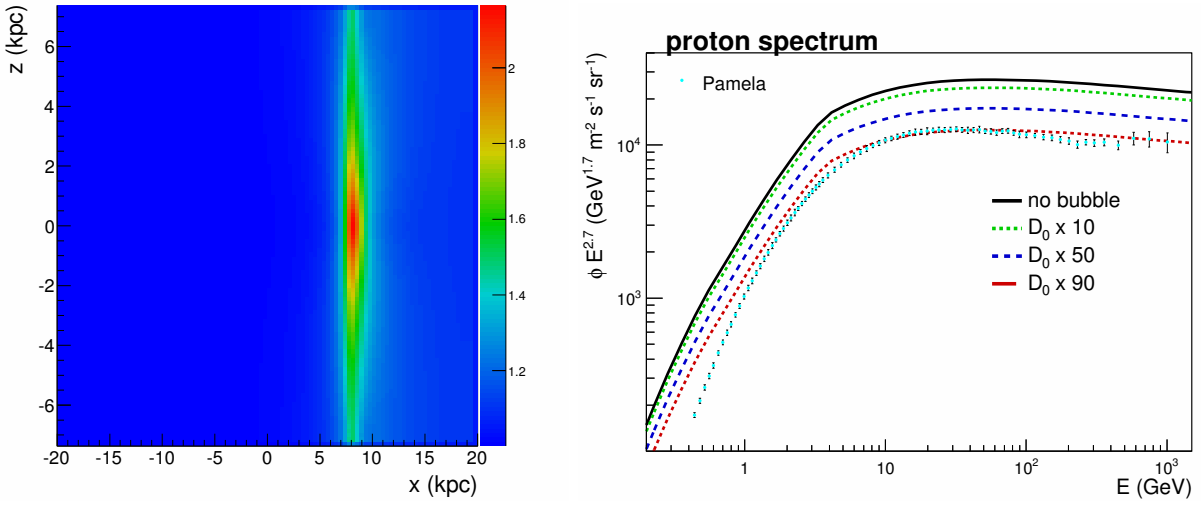

Figure 6.12.: **Left:** The ratio 'no bubble'/'$D_0 \cdot 90$' of the proton density at $E = 91$ GeV in the plane of x-z in which the chimney-like tube is apparent. **Right:** Local interstellar proton spectrum for the chimney-like bubble structure and different factors applied to the local diffusion coefficient. While the spectral shape is only marginally affected, a reduction of the proton density by a factor of about two is realized by a proton outflow towards the galactic poles.

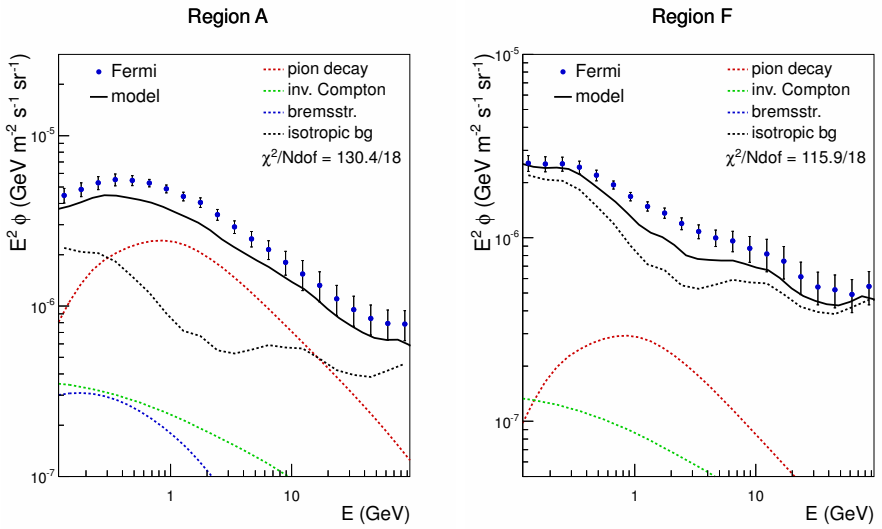

Figure 6.13.: Gamma-ray spectrum in the regions A and F for the chimney-like bubble structure. Whereas the LB locally reduces the proton density to match the locally measured value it also strongly affects the overall gamma-ray spectrum leading to the obvious data-mismatch.

7. Summary, Conclusion and Outlook

Within the last couple of years the field of CR propagation attracted a lot of attention triggered by the detection of an *anomalous positron abundance* in the cosmic radiation. The predicted amount of positrons, which in the standard picture are assumed to be purely produced by interactions of CR nuclei with the interstellar medium, cannot explain the measured rise of the positron fraction. Consequently, *new primary sources* of high energetic positrons are required. Many possible astrophysical and exotic source scenarios were proposed in the literature, but the question of the origin of the anomalous positron abundance has still not been finally answered.
Recently, measurements of electrons and positrons with unprecedented accuracy were published by the AMS-02 collaboration, which called for a renewed investigation of CR transport models in order to discriminate and characterize the observed signal from the expected background.
The major contributions of this thesis include an extensive analysis of current CR transport models, a determination of the uncertainties on the expected secondary positron flux, a characterization of the additional positron contribution as demanded by new AMS-02 data and an investigation of the possible positron contributions and the implications from different source hypotheses.
Since the predicted positron distribution within the Galaxy depends on ill-known transport parameters which describe the propagation processes and determine the underlying nuclei densities, reasonable values and constraints have to be applied in order to make robust predictions. For this purpose a sophisticated Markov chain Monte Carlo interface to the CR propagation software `DRAGON` was developed and widely chosen ranges of 16 transport parameters were investigated. Since the numerical solution of the transport equation is in general slow, the sampling efficiency was increased by the incorporation of a modern, parallelizable decision algorithm which biases the local parameter space. Additionally, three consecutively applied proposal functions were used to exploit already obtained information on the parameter space.

In total, more than 15 million sets of parameters in transport models have been evaluated by means of Markov chain Monte Carlo methods using high-performance computing clusters. The transport parameters were constrained by demanding data-conformity to the entirety of the most up-to-date measurements of sensitive observables, namely the locally measured proton and antiproton energy spectra and the ratios B/C and ^{10}Be/^{9}Be which constrain the CR interaction rate and the CR escape time. It was found that the constraining of transport parameters is restricted due to partially large uncertainties of the

experimental measurements and strong correlations between almost all transport parameters. The diffusion constant, which is a measure for the average scattering length, could be determined to be within one order of magnitude. However, heights of the diffusion halo of up to 30 kpc, beyond which free escape of the particles is assumed, could not be excluded. The high correlation of these two major transport parameters leads to degenerated solutions which are impossible to distinguish by local measurements. Despite the correlations the fitted turbulence spectrum of the magnetohydrodynamical waves clearly points to an Iroshnikov-Kraichnan spectrum ($\delta = 1/2$) in agreement with comparable studies [138]. Although a moderate diffusive reaccleration with Alfvén velocities of up to 20 km/s can lead to a better description of the data, it is not necessarily needed to account for the nuclei measurements. Also a convective transport mode was found to be neither preferred nor demanded.
Model extensions, like the radial dependence of the convection velocity, implemented for this analysis are incorporated in the publicly available `DRAGON` software and are available to scientific community for an easy reproduction of the obtained results. Interesting models found by the Markov chain Monte Carlo sampling built the basis for several analyses performed within the KIT cosmic ray group.
In order to restrict the expected positron flux at Earth, a large amount of transport models, all of which were constrained by locally measured nuclei and are characterized by strongly deviating sets of transport parameters, were used to account for the transport related uncertainties. For a correct estimation of the strong synchrotron energy losses the positrons and electrons suffer from, the parameters of the employed magnetic field model were tuned to match the most up-to-date synchrotron foreground maps as derived from the 9-year WMAP data. A study focusing on the influence of the energy densities of the galactic magnetic field and the interstellar radiation field on the positron spectrum revealed, that even in case those models are afflicted with errors of 30% the uncertainties from the major transport parameters dominate. The parameters with the largest impact on the absolute positron flux are the diffusion constant and the halo height which crucially determine the proton and helium density distributions within the Galaxy and thus the secondary positron production.
The obtained positron predictions were taken as uncertainty on the background in order to quantify the additional positron contribution as required by new AMS-02 lepton data. For the first time consistent and high precision lepton measurements allowed in combination with robust background predictions to deduce spectral information on the required signal. It was found that an additional and significant positron contribution comparable to the background is already required at rather low energies of $E = 10$ GeV. At an energy of 15 GeV the signal contribution starts to dominate over the background. Above 200 GeV the background contribution is negligible and the measured positron flux represents the signal flux (fig. 5.8). This finding was also found to be predicted by power-law modeled fluxes optimized to the data (fig. 5.6).

Nearby pulsars and DM annihilation processes are the most prominent source candidates [113], [63]. It was investigated to which extent these source hypotheses can account for the observations and which implications result from those. For this purpose a widely used pulsar model including 10 known, nearby pulsars which are expected to contribute most to the local positron flux was used. Due to large experimental uncertainties of the pulsar properties, like for instance their distance, robust predictions are however prevented. By an optimization of the pulsar parameters within their experimental limits the AMS-02 lepton data in the whole energy range can be described if at least three nearby pulsars contribute to the positron flux (fig. 5.12). It was found that both, a drop and a further rise of the positron fraction can be obtained if realistic assumptions about the pulsar properties are made.

All studied point source models predict an effective *dipole anisotropy* in the electron and positron flux which was found to be in agreement with current experimental upper limits (fig. 5.13), but may play a seminal role in future source identification analyses. However, such analyses require a better understanding of the strengths and the number of the contributing pulsars and a more precise knowledge of the diffusion related transport parameters in order to challenge the pulsar explanation with future limits if, further on, no anisotropy will be detected.
Even though nearby pulsars provide a quite natural explanation for the positron excess, DM annihilation models are still highly discussed. In case a new, DM like particle was found in accelerator experiments, an indirect evidence is in any case imperative in order to affiliate the astronomical and cosmological observations to this particle. Only this connection ensures that the new particle is indeed what constitutes 85% of the mass of our Universe.
For the study of the potential electron and positron flux from DM annihilation processes, different annihilation channels into leptons, quarks and gauge bosons were considered for a wide range of DM particle masses, respectively. The propagation of the particles from DM annihilation was consistently applied using `DRAGON`. A spectral template fit of the characteristic, propagated positron contributions from the particular annihilation channels to AMS-02 data was performed in order to allow for any possible combination of the annihilation branching fractions.
A description of the lepton data in the entire energy range including constraints from the antiproton flux could not be obtained by the assumption of a pure DM originating signal. Another scenario, in which DM annihilation was assumed to be only the source for the highest positron energies, revealed that either leptophilic models (DM couplings to leptons, but not to gauge bosons or quarks) with DM particle masses of around 1 $\mathrm{TeV/c^2}$ or annihilations into W and Z gauge bosons with DM masses of around 21 $\mathrm{TeV/c^2}$ are preferred (fig. 5.18). While the former predict an abrupt drop of the positron fraction the latter predict a further rise as well as a significant amount of antiprotons, but in an energy range not yet accessible by the available antiproton measurements (fig. 5.19). Precision measurements of the antiproton flux and the positron fraction up to higher energies by AMS-02 will yield a strong constraining power and will allow to put this class of models to the proof.
The expected *dipole anisotropy* of DM induced electrons and positrons was found to be remarkably small due to the small local gradient of the DM density profile. DM substructures in form of clumps may increase the expected dipole anisotropy, but only in case the gradient of the local density distribution is substantially larger than the one of the diffuse component. The feature of a much lower anisotropy fundamentally differs the DM interpretation from point source based explanations and may, to emphasize once more, play a key role in future source identification analyses.

In the last chapter of this thesis the predictions of the obtained transport models on the *diffuse gamma-ray emission* were compared with four years of gamma-ray data collected by the FERMI-LAT experiment. It was found that models with an unbroken nuclei injection spectrum and tuned to the locally measured proton spectrum lead to pion decay induced gamma-rays whose energy spectrum is too soft compared to the data. Therefore, the transport parameters of an extended model setup including a broken nuclei injection spectrum were simultaneously optimized to both the gamma-ray energy spectra in various regions of the sky and the locally measured nuclei spectra and ratios.
An optimized model was presented which describes the considered observations to a satisfactory degree, however, only if the proton and helium densities are disentangled from the locally observed ones by an enhancement of roughly a factor of two. The combination of the diffusion halo height and the correspondingly chosen relatively low diffusion constant

was found to predict a small gradient of the radial proton density distribution (fig. 6.4). It was demonstrated that the *soft gamma-ray gradient problem* can be naturally solved by such an isotropic diffusion model without any changes of the source term and without spatial variations of the conversion factor X_{CO} which was earlier proposed.
It was tried to explain the increase of a factor of two of the interstellar CR density in comparison with the locally observed one by a change in the diffusion coefficient in the *Local Bubble*. A local and sufficient reduction of the proton density could be obtained by a strongly increased diffusion constant within an upwards and downwards opened, chimney-like bubble structure by which a proton outflow in the direction of the galactic poles could be ensured (fig 6.11). However, the proton density distribution was also lowered by the bubble even at large heliocentric radii of several kpc which also affected the predicted gamma-ray emission. An overall, satisfactory explanation could not be obtained. An estimation of the maximal radius such a bubble must have pointed to 20 pc which is below the dimension of the *Local Bubble*. Analyses including models with strong, local convective winds are ongoing and will show if these can solve the observed discrepancy.

The coming months and years will be exciting times for galactic CR related physics. New, high precision measurements of CR nuclei and leptons, all of which are self-consistently and redundantly measured by the AMS-02 experiment, will improve the understanding of the transport processes within the Galaxy.
Of particular importance are not only precise particle spectra up to higher energies, but also upper limit determinations on the anisotropy of different particle species. While the absence of an anisotropy in the lepton flux can constrain or even challenge the pulsar explanation of the positron excess, upper limits on the proton anisotropy may open a new window for constraining transport models.

Bibliography

[1] V. F. Hess, "Nobel Prize in Physics 1936 - Presentation Speech", (1936).

[2] Pierre Auger Collaboration, "Correlation of the Highest-Energy Cosmic Rays with Nearby Extragalactic Objects", *Science* **318** (November, 2007) 938–943, arXiv:0711.2256.

[3] C. D. Anderson, "The Positive Electron", *Phys. Rev.* **43** (Mar, 1933) 491–494.

[4] S. H. Neddermeyer and C. D. Anderson, "Note on the Nature of Cosmic-Ray Particles", *Phys. Rev.* **51** (May, 1937) 884–886.

[5] D. Perkins, "Nuclear Disintegration by Meson Capture", *Nature* **159** (1947) 126–127.

[6] G. Rochester and C. Butler, "Evidence for the Existence of New Unstable Elementary Particles", *Nature* **160** (December, 1947) 855–857.

[7] W. Baade and F. Zwicky, "Cosmic Rays from Super-novae", *National Academy of Sciences of the United States of America Vol. 20, No. 5* (1934) 259–263.

[8] Fermi-LAT Collaboration, "Detection of the Characteristic Pion-Decay Signature in Supernova Remnants", *Science* **339** (2013) 807, arXiv:1302.3307.

[9] A. M. Hillas, "Can diffusive shock acceleration in supernova remnants account for high-energy galactic cosmic rays?", *Journal of Physics G: Nuclear and Particle Physics* **31** (2005), no. 5, R95.

[10] S. Longair, "High energy astrophysics, 3rd edition". Cambridge University Press, 2011.

[11] PAMELA Collaboration, "An anomalous positron abundance in cosmic rays with energies 1.5-100 GeV", *Nature* **458** (April, 2009) 607–609, arXiv:0810.4995.

[12] M. Kachelriess, S. Ostapchenko, and R. Tomas, "Antimatter production in supernova remnants", *Astrophys.J.* **733** (2011) 119, arXiv:1103.5765.

[13] AMS Collaboration, "First Result from the Alpha Magnetic Spectrometer on the International Space Station: Precision Measurement of the Positron Fraction in Primary Cosmic Rays of 0.5-350 GeV", *Phys.Rev.Lett.* **110** (2013) 141102.

[14] AMS Collaboration, "High Statistics Measurement of the Positron Fraction in Primary Cosmic Rays of 0.5–500 GeV with the Alpha Magnetic Spectrometer on the International Space Station", *Phys. Rev. Lett.* **113** (Sep, 2014) 121101.

[15] AMS Collaboration, "Electron and Positron Fluxes in Primary Cosmic Rays Measured with the Alpha Magnetic Spectrometer on the International Space Station", *Phys. Rev. Lett.* **113** (Sep, 2014) 121102.

[16] A. W. Strong, I. V. Moskalenko, and V. S. Ptuskin, "Cosmic-ray propagation and interactions in the Galaxy", *Ann.Rev.Nucl.Part.Sci.* **57** (2007) 285–327, arXiv:astro-ph/0701517.

[17] J. Bloemen, A. Strong, H. Mayer-Hasselwander et al., "The radial distribution of galactic gamma rays. III - The distribution of cosmic rays in the Galaxy and the CO-H2 calibration", *A&A* **154** (January, 1986) 25–41.

[18] A. Strong, J. Bloemen, T. Dame et al., "The radial distribution of galactic gamma rays. IV - The whole galaxy", *A&A* **207** (December, 1988) 1–15.

[19] B. Fuchs, D. Breitschwerdt, M. de Avillez et al., "The search for the origin of the Local Bubble redivivus", *Monthly Notices of the Royal Astronomical Society* **373** (2006) 993–1003, arXiv:astro-ph/0609227.

[20] T. W. Berghöfer and D. Breitschwerdt, "The origin of the young stellar population in the solar neighborhood – A link to the formation of the Local Bubble?", *A&A* **390** (July, 2002) 299–306, arXiv:astro-ph/0205128.

[21] B. Rossi, "Directional Measurements on the Cosmic Rays Near the Geomagnetic Equator", *Phys. Rev.* **45** (Feb, 1934) 212–214.

[22] P. Auger, P. Ehrenfest, R. Maze et al., "Extensive Cosmic-Ray Showers", *Rev. Mod. Phys.* **11** (Jul, 1939) 288–291.

[23] P. Freier, E. J. Lofgren, E. P. Ney et al., "Evidence for Heavy Nuclei in the Primary Cosmic Radiation", *Phys. Rev.* **74** (Jul, 1948) 213–217.

[24] E. Fermi, "On the Origin of the Cosmic Radiation", *Phys. Rev.* **75** (Apr, 1949) 1169–1174.

[25] CORSICA website, "https://web.ikp.kit.edu/corsika/", (2014).

[26] W. Bietenholz, "The most powerful particles in the Universe: a cosmic smash", *ArXiv e-prints* (May, 2013) arXiv:1305.1346.

[27] H. Ahn, P. Allison, M. Bagliesi et al., "The Cosmic Ray Energetics And Mass (CREAM) instrument", *Nucl.Instrum.Meth.* **A579** (2007) 1034–1053.

[28] Fermi-LAT Collaboration, "Measurement of separate cosmic-ray electron and positron spectra with the Fermi Large Area Telescope", *Phys.Rev.Lett.* **108** (2012) 011103, arXiv:1109.0521.

[29] NASA's Fermi Gamma-ray Space Telescope website, "http://fermi.gsfc.nasa.gov", (2014).

[30] M. Heil, "Measurement of the positron fraction in cosmic rays from 0.5 - 350 GeV with the AMS-02 detector on the International Space Station", *Ph.D. thesis* (2013).

[31] AMS Collaboration, "Precision measurement of the e+ + e- flux in primary cosmic rays from 0.5 GeV to 1 TeV with the Alpha Magnetic Spectrometer on the International Space Station", *Accepted for publication in Physical Review Letters* (2014).

[32] V. Vagelli , *personal communication, July 2014.*

[33] B. S. Nilsen, "New Results on Cosmic Ray H and He Composition from the JACEE Collaboration", in *Eighteenth Texas Symposium on Relativistic Astrophysics*, p. 438. 1998.

[34] K. Asakimori et al., "Cosmic-Ray Proton and Helium Spectra: Results from the JACEE Experiment", *The Astrophysical Journal* **502** (1998), no. 1, 278.

[35] T. K. Gaisser, "The Cosmic-ray Spectrum: from the knee to the ankle", *Journal of Physics: Conference Series* **47** (2006), no. 1, 15.

[36] S. Yoshida, "Ultra-high Energy Particle Astrophysics". Nova Science Publishers, 2003.

[37] A. M. Hillas, "The Origin of Ultra-High-Energy Cosmic Rays", *Annual Review of Astron. and Astrophys.* **22** (1984) 425–444.

[38] IceCube Collaboration, "Measurement of the Anisotropy of Cosmic Ray Arrival Directions with IceCube", *Astrophys.J.* **718** (2010) L194, `arXiv:1005.2960`.

[39] IceCube Collaboration, "Cosmic ray Spectrum, Composition, and Anisotropy Measured with IceCube", *Nucl.Instrum.Meth.* **A742** (2014) 35–41, `arXiv:1307.8394`.

[40] IceCube Collaboration, "Observation of Anisotropy in the Arrival Directions of Galactic Cosmic Rays at Multiple Angular Scales with IceCube", *Astrophys.J.* **740** (2011) 16, `arXiv:1105.2326`.

[41] Beringer et al., "Particle Data Group", *Phys. Rev. D86* (2012).

[42] Website of M. Pulupa, "`http://sprg.ssl.berkeley.edu/~pulupa/`", (2014).

[43] K. Koyama, R. Petre, E. V. Gotthelf et al., "Evidence for shock acceleration of high-energy electrons in the supernova remnant SN1006", *Nature* **378** (November, 1995) 255–258.

[44] HESS Collaboration, "HESS Observations of the Supernova Remnant RX J0852.0-4622: Shell-Type Morphology and Spectrum of a Widely Extended Very High Energy Gamma-Ray Source", *Astrophysical Journal* **661** (May, 2007) 236–249, `arXiv:astro-ph/0612495`.

[45] W. de Boer and M. Weber, "Fermi Bubbles and Bubble-like emission from the Galactic Plane", *Astrophys.J.* **794** (2014), no. 1, L17, `arXiv:1407.4114`.

[46] R. J. Protheroe, "On the nature of the cosmic ray positron spectrum", *Astrophysical Journal* **254** (March, 1982) 391–397.

[47] L. Gendelev, S. Profumo, and M. Dormody, "The Contribution of Fermi Gamma-Ray Pulsars to the local Flux of Cosmic-Ray Electrons and Positrons", *JCAP* **1002** (2010) 016, `arXiv:1001.4540`.

[48] D. R. Lorimer and M. Kramer, "Handbook of pulsar astronomy". Cambridge University Press, 2005.

[49] J. P. Rachen, T. Stanev, and P. L. Biermann, "Extragalactic ultra-high energy cosmic rays. II. Comparison with experimental data", *A&A* **273** (June, 1993) 377, `arXiv:astro-ph/9302005`.

[50] P. L. Biermann, "The origin of cosmic rays", *Nuclear Physics B Proceedings Supplements* **43** (June, 1995) 221–228, `arXiv:astro-ph/9501006`.

[51] A. Letessier-Selvon and T. Stanev, "Ultrahigh Energy Cosmic Rays", *Rev.Mod.Phys.* **83** (2011) 907–942, arXiv:1103.0031.

[52] P. Blasi, R. I. Epstein, and A. V. Olinto, "Ultrahigh-energy cosmic rays from young neutron star winds", *Astrophys.J.* **533** (2000) L123, arXiv:astro-ph/9912240.

[53] J. P. Rachen and P. L. Biermann, "Extragalactic Ultra-High Energy Cosmic-Rays - Part One - Contribution from Hot Spots in Fr-II Radio Galaxies", *A&A* **272** (May, 1993) 161, arXiv:astro-ph/9301010.

[54] E. Waxman, "Cosmological Gamma-Ray Bursts and the Highest Energy Cosmic Rays", *Physical Review Letters* **75** (July, 1995) 386–389, arXiv:astro-ph/9505082.

[55] J. Cesarsky, "Cosmic rays with E $> 10^{19}$ eV : Origin and transport", *Astron.Astrophys.* **28** (November, 1992) 51–60.

[56] H. Kang, D. Ryu, and T. W. Jones, "Cluster Accretion Shocks as Possible Acceleration Sites for Ultra–High-Energy Protons below the Greisen Cutoff", *Astrophysical Journal* **456** (January, 1996) 422, arXiv:astro-ph/9507113.

[57] A. Letessier-Selvon and T. Stanev, "Ultrahigh Energy Cosmic Rays", *Rev.Mod.Phys.* **83** (2011) 907–942, arXiv:1103.0031.

[58] J. H. Oort, "The force exerted by the stellar system in the direction perpendicular to the galactic plane and some related problems", *Bull. Astron. Inst. Neth.* **6** (August, 1932) 249.

[59] F. Zwicky, "On the Masses of Nebulae and of Clusters of Nebulae", *Astrophysical Journal* **86** (October, 1937) 217.

[60] Planck Collaboration, "Planck 2013 results. XVI. Cosmological parameters", *Astron.Astrophys.* (2014) arXiv:1303.5076.

[61] V. Springel, S. D. M. White, A. Jenkins et al., "Simulations of the formation, evolution and clustering of galaxies and quasars", *Nature* **435** (June, 2005) 629–636, arXiv:astro-ph/0504097.

[62] W. de Boer and M. Weber, "Determination of the local dark matter density in our Galaxy", *A&A* **509** (January, 2010) A25, arXiv:0910.4272.

[63] G. Jungman, M. Kamionkowski, and K. Griest, "Supersymmetric dark matter", *Phys.Rept.* **267** (1996) 195–373, arXiv:hep-ph/9506380.

[64] G. Bertone, D. Hooper, and J. Silk, "Particle dark matter: Evidence, candidates and constraints", *Phys.Rept.* **405** (2005) 279–390, arXiv:hep-ph/0404175.

[65] Super-Kamiokande Collaboration, "Evidence for oscillation of atmospheric neutrinos", *Phys.Rev.Lett.* **81** (1998) 1562–1567, arXiv:hep-ex/9807003.

[66] V. S. Berezinskij and V. L. Ginzburg, "Astrophysics of cosmic rays". North-Holland, 1990.

[67] A. Putze, L. Derome, and D. Maurin, "A Markov Chain Monte Carlo technique to sample transport and source parameters of Galactic cosmic rays. II. Results for the diffusion model combining B/C and radioactive nuclei", *A&A* **516** (June, 2010) A66, arXiv:1001.0551.

[68] R. Trotta, G. Johannesson, I. Moskalenko et al., "Constraints on cosmic-ray propagation models from a global Bayesian analysis", *Astrophys.J.* **729** (2011) 106, arXiv:1011.0037.

[69] D. Breitschwerdt and S. Komossa, "Galactic Fountains and Galactic Winds", *Astrophysics and Space Science* **272** (2000) 3–13, arXiv:astro-ph/9908003.

[70] V. Dogiel and D. Breitschwerdt, "Cosmic Rays in the Disk and Halo of Galaxies", *ArXiv e-prints* (May, 2009) arXiv:0905.3071.

[71] D. Wentzel, "Cosmic-ray propagation in the galaxy: collective effects", *Ann.Rev.Astron.Astrophys.* **12** (1974) 71–96.

[72] J. Everett, E. Zweibel, B. Benjamin et al., "Cosmic Ray- and Thermal-Pressure Driven Winds: Does the Milky Way Host a Kpc-Scale Outflow?", *EAS Publications Series* **56** (1, 2012) 73–76.

[73] K. Mannheim and R. Schlickeiser, "Interactions of Cosmic Ray Nuclei", *Astron.Astrophys.* **286** (1994) 983–996, arXiv:astro-ph/9402042.

[74] A. Strong and I. Moskalenko, "Propagation of cosmic-ray nucleons in the galaxy", *Astrophys.J.* **509** (1998) 212–228, arXiv:astro-ph/9807150.

[75] B. Pritychenko, E. Betak, B. Singh et al., "Nuclear Science References Database", arXiv:1302.6883.

[76] I. Gebauer, "An Anisotropic Model for Galactic Cosmic Ray Transport and its Implications for Indirect Dark Matter Searches", *Ph.D. thesis* (2010).

[77] S. V. Bulanov and V. A. Dogel, "The Influence of the Energy Dependence of the Diffusion Coefficient on the Spectrum of the Electron Component of Cosmic Rays and the Radio Background Radiation of the Galaxy", *Astrophysics and Space Science* **29** (August, 1974) 305–318.

[78] D. Gaggero, "Cosmic Ray diffusion in the Galaxy and diffuse Gamma emission", *Ph.D. thesis* (2011).

[79] S. Gillessen, F. Eisenhauer, S. Trippe et al., "Monitoring stellar orbits around the Massive Black Hole in the Galactic Center", *Astrophys.J.* **692** (2009) 1075–1109, arXiv:0810.4674.

[80] D. J. Majaess, D. G. Turner, and D. J. Lane, "Characteristics of the Galaxy according to Cepheids", *Mon.Not.Roy.Astron.Soc.* **398** (2009) 263–270, arXiv:0903.4206.

[81] L. S. Sparke and J. S. Gallagher, "Galaxies in the Universe: An Introduction". Cambridge University Press, 2007.

[82] NASA website, "http://solarsystem.nasa.gov/multimedia/", (2014).

[83] D. Lorimer, A. Faulkner, A. Lyne et al., "The Parkes multibeam pulsar survey: VI. Discovery and timing of 142 pulsars and a Galactic population analysis", *Mon.Not.Roy.Astron.Soc.* **372** (2006) 777–800, arXiv:astro-ph/0607640.

[84] G. Case and D. Bhattacharya, "Revisiting the galactic supernova remnant distribution.", *AAPS* **120** (December, 1996) C437.

[85] K. M. Ferrière, "The interstellar environment of our galaxy", *Reviews of Modern Physics* **73** (October, 2001) 1031–1066, arXiv:astro-ph/0106359.

[86] Q. Yuan, S. Liu, and X.-J. Bi, "Unified model for the gamma-ray emission of supernova remnants", *Astrophys.J.* **761** (2012) 133, arXiv:1203.0085.

[87] C.-A. Faucher-Giguere and V. M. Kaspi, "Birth and evolution of isolated radio pulsars", *Astrophys.J.* **643** (2006) 332–355, arXiv:astro-ph/0512585.

[88] H. Nakanishi and Y. Sofue, "Three-dimensional distribution of the ISM in the Milky Way Galaxy: 1. The HI disk", *Publ.Astron.Soc.Jap.* **55** (2003) 191, arXiv:astro-ph/0304338.

[89] R. Lallement, B. Y. Welsh, J. L. Vergely et al., "3D mapping of the dense interstellar gas around the Local Bubble", *A&A* **411** (December, 2003) 447–464.

[90] M. Pohl, P. Englmaier, and N. Bissantz, "3D Distribution of Molecular Gas in the Barred Milky Way", *Astrophys.J.* **677** (2008) 283–291, arXiv:0712.4264.

[91] I. V. Moskalenko, A. W. Strong, J. F. Ormes et al., "Secondary anti-protons and propagation of cosmic rays in the galaxy and heliosphere", *Astrophys.J.* **565** (2002) 280–296, arXiv:astro-ph/0106567.

[92] A. W. Strong, I. V. Moskalenko, and O. Reimer, "Diffuse continuum gamma-rays from the galaxy", *Astrophys.J.* **537** (2000) 763–784, arXiv:astro-ph/9811296.

[93] I. V. Moskalenko, T. A. Porter, and A. W. Strong, "Attenuation of vhe gamma rays by the milky way interstellar radiation field", *Astrophys.J.* **640** (2006) L155–L158, arXiv:astro-ph/0511149.

[94] T. A. Porter, I. V. Moskalenko, and A. W. Strong, "Inverse Compton Emission from Galactic Supernova Remnants: Effect of the Interstellar Radiation Field", *Astrophys.J.* **648** (2006) L29–L32, arXiv:astro-ph/0607344.

[95] K. Beuermann, G. Kanbach, and E. M. Berkhuijsen, "Radio structure of the Galaxy - Thick disk and thin disk at 408 MHz", *A&A* **153** (December, 1985) 17–34.

[96] R. Beck, A. Brandenburg, D. Moss et al., "Galactic Magnetism: Recent developments and perspectives", *Ann.Rev.Astron.Astrophys.* **34** (1996) 155–206.

[97] M. Pshirkov, P. Tinyakov, P. Kronberg et al., "Deriving global structure of the Galactic Magnetic Field from Faraday Rotation Measures of extragalactic sources", *Astrophys.J.* **738** (2011) 192, arXiv:1103.0814.

[98] R. Jansson and G. R. Farrar, "A New Model of the Galactic Magnetic Field", *Astrophys.J.* **757** (2012) 14, arXiv:1204.3662.

[99] R. Beck, "Measuring interstellar magnetic fields by radio synchrotron emission", arXiv:0812.4925.

[100] R. Beck and R. Wielebinski, "Magnetic fields in galaxies", *Planets: Populations* (2013) arXiv:1302.5663.

[101] X. H. Sun, W. Reich, A. Waelkens et al., "Radio observational constraints on Galactic 3D-emission models", *A&A* **477** (January, 2008) 573–592, arXiv:0711.1572.

[102] L. J. Gleeson and W. I. Axford, "Solar Modulation of Galactic Cosmic Rays", *Astrophysical Journal* **154** (December, 1968) 1011.

[103] D. Maurin, F. Melot, and R. Taillet, "A database of charged cosmic rays", arXiv:1302.5525.

[104] O. Adriani, G. Barbarino, G. Bazilevskaya et al., "Time dependence of the proton flux measured by PAMELA during the July 2006 - December 2009 solar minimum", *Astrophys.J.* **765** (2013) 91, arXiv:1301.4108.

[105] H. Gast and S. Schael, "Charge-dependent solar modulation in light of the recent PAMELA data", *Proceeding to the 31st ICRC* (2009).

[106] D. Gaggero, L. Maccione, D. Grasso et al., "PAMELA and AMS-02 e^+ and e^- spectra are reproduced by three-dimensional cosmic-ray modeling", *Physical Review D* **89** (April, 2014) 083007, arXiv:1311.5575.

[107] Oulu Neutron Monitor website, "http://cosmicrays.oulu.fi/", (2014).

[108] V. L. Ginzburg and V. S. Ptuskin, "On the origin of cosmic rays: Some problems in high-energy astrophysics", *Reviews of Modern Physics* **48** (April, 1976) 161–189.

[109] D. Maurin, F. Donato, R. Taillet et al., "Cosmic rays below z=30 in a diffusion model: new constraints on propagation parameters", *Astrophys.J.* **555** (2001) 585–596, arXiv:astro-ph/0101231.

[110] R. Taillet, P. Salati, D. Maurin et al., "The effects of discreteness of galactic cosmic rays sources", *Astrophys.J.* **609** (2004) 173–185, arXiv:astro-ph/0308141.

[111] Galprop v.54 manual, "http://galprop.stanford.edu/download/manuals/galprop_v54.pdf", (2014).

[112] C. Evoli, D. Gaggero, D. Grasso et al., "Cosmic ray nuclei, antiprotons and gamma rays in the galaxy: a new diffusion model", *Journal of Cosmology and Astroparticle Physics* **10** (October, 2008) 18, arXiv:0807.4730.

[113] A. M. Atoyan, F. A. Aharonian, and H. J. Völk, "Electrons and positrons in the galactic cosmic rays", *Phys. Rev. D* **52** (Sep, 1995) 3265–3275.

[114] W. H. Press, S. A. Teukolsky, W. T. Vetterling et al., "Numerical Recipes in FORTRAN; The Art of Scientific Computing". Cambridge University Press, New York, NY, USA, 2nd edition, 1993.

[115] D. Gaggero, L. Maccione, G. Di Bernardo et al., "Three dimensional modeling of CR propagation", *ArXiv e-prints* (June, 2013) arXiv:1306.6850.

[116] R. Schlickeiser, "Cosmic Ray Astrophysics". Astronomy and Astrophysics Library. Springer, 2002.

[117] H. Ahn, P. Allison, M. Bagliesi et al., "Measurements of cosmic-ray secondary nuclei at high energies with the first flight of the CREAM balloon-borne experiment", *Astropart.Phys.* **30** (2008) 133–141, arXiv:0808.1718.

[118] Yanasak et al., "Astrophys.J. 563, 768", (2001).

[119] Davis et al., "AIP Conf Proc. 528, 421", (2000).

[120] Hams et al., "Astrophys.J. 611, 892", (2004).

[121] PAMELA Collaboration, "PAMELA Measurements of Cosmic-ray Proton and Helium Spectra", *Science* **332** (2011) 69–72, arXiv:1103.4055.

[122] PAMELA Collaboration, "PAMELA results on the cosmic-ray antiproton flux from 60 MeV to 180 GeV in kinetic energy", *Phys.Rev.Lett.* **105** (2010) 121101, arXiv:1007.0821.

[123] PAMELA Collaboration, "The cosmic-ray electron flux measured by the PAMELA experiment between 1 and 625 GeV", *Phys.Rev.Lett.* **106** (2011) 201101, arXiv:1103.2880.

[124] PAMELA Collaboration, "Cosmic-Ray Positron Energy Spectrum Measured by PAMELA", *Phys.Rev.Lett.* **111** (2013), no. 8, 081102, arXiv:1308.0133.

[125] V. Cavasinni, D. Grasso, and L. Maccione, "TeV Neutrinos from SuperNova Remnants embedded in Giant Molecular Clouds", *Astropart.Phys.* **26** (2006) 41–49, arXiv:astro-ph/0604004.

[126] R. M. Crocker, M. Fatuzzo, R. Jokipii et al., "The AGASA/SUGAR anisotropies and TeV gamma rays from the Galactic Center: A Possible signature of extremely high-energy neutrons", *Astrophys.J.* **622** (2005) 892–909, arXiv:astro-ph/0408183.

[127] C. G. T. Haslam, U. Klein, C. J. Salter et al., "A 408 MHz all-sky continuum survey. I - Observations at southern declinations and for the North Polar region", *A&A* **100** (July, 1981) 209–219.

[128] NASA's data center for Cosmic Microwave Background research (LAMBDA), "http://lambda.gsfc.nasa.gov/", (2014).

[129] WMAP Collaboration, "Five-Year Wilkinson Microwave Anisotropy Probe (WMAP) Observations: Galactic Foreground Emission", *Astrophys.J.Suppl.* **180** (2009) 265–282, arXiv:0803.0715.

[130] NASA HEALPix website, "http://healpix.jpl.nasa.gov/", (2014).

[131] A. Putze, L. Derome, D. Maurin et al., "A Markov Chain Monte Carlo technique to sample transport and source parameters of Galactic cosmic rays. I. Method and results for the Leaky-Box model", *A&A* **497** (April, 2009) 991–1007, arXiv:0808.2437.

[132] W. Hastings, "Monte Carlo Sampling Methods Using Markov Chains and Their Applications", *Biometrika* **57** (1970) 97–109.

[133] P. Neal, G. Roberts, and W. Kong Yuen, "Optimal scaling of random walk Metropolis algorithms with discontinuous target densities", *ArXiv e-prints* (October, 2012) arXiv:1210.5090.

[134] J. S. Liu, F. Liang, and W. H. Wong, "The Multiple-Try Method and Local Optimization in Metropolis Sampling", *Journal of the American Statistical Association* **95** (March, 2000) 121+.

[135] M. Matsumoto and T. Nishimura, "Mersenne Twister: A 623-dimensionally Equidistributed Uniform Pseudo-random Number Generator", *ACM Trans. Model. Comput. Simul.* **8** (January, 1998) 3–30.

[136] R. Brun and F. Rademakers, "ROOT: An object oriented data analysis framework", *Nucl.Instrum.Meth.* **A389** (1997) 81–86.

[137] J.-P. Meyer, L. O. Drury, and D. C. Ellison, "Galactic Cosmic Rays from Supernova Remnants. I. A Cosmic-Ray Composition Controlled by Volatility and Mass-to-Charge Ratio", *Astrophysical Journal* **487** (September, 1997) 182–196, arXiv:astro-ph/9704267.

[138] G. Di Bernardo, C. Evoli, D. Gaggero et al., "Unified interpretation of cosmic ray nuclei and antiproton recent measurements", *Astroparticle Physics* **34** (December, 2010) 274–283, arXiv:0909.4548.

[139] T. Kamae, N. Karlsson, T. Mizuno et al., "Parameterization of Gamma, e+/- and Neutrino Spectra Produced by p-p Interaction in Astronomical Environment", *Astrophys.J.* **647** (2006) 692–708, arXiv:astro-ph/0605581.

[140] I. Moskalenko and A. Strong, "Production and propagation of cosmic ray positrons and electrons", *Astrophys.J.* **493** (1998) 694–707, arXiv:astro-ph/9710124.

[141] F. W. Stecker, "The Cosmic γ-Ray Spectrum from Secondary Particle Production in Cosmic-Ray Interactions", *Astrophysics and Space Science* **6** (March, 1970) 377–389.

[142] G. D. Badhwar, S. A. Stephens, and R. L. Golden, "Analytic representation of the proton-proton and proton-nucleus cross-sections and its application to the sea-level spectrum and charge ratio of muons", *Phys. Rev. D* **15** (Feb, 1977) 820–831.

[143] C. D. Dermer, "Secondary production of neutral pi-mesons and the diffuse galactic gamma radiation", *A&A* **157** (March, 1986) 223–229.

[144] P. D. Serpico, "On the possible causes of a rise with energy of the cosmic ray positron fraction", *Phys.Rev.* **D79** (2009) 021302, arXiv:0810.4846.

[145] I. Cholis and D. Hooper, "Constraining the origin of the rising cosmic ray positron fraction with the boron-to-carbon ratio", *Phys.Rev.* **D89** (2014), no. 4, 043013, arXiv:1312.2952.

[146] S. Coutu, S. W. Barwick, J. J. Beatty et al., "Cosmic ray positrons: Are there primary sources?", *Astropart.Phys.* **11** (1999) 429–435, arXiv:astro-ph/9902162.

[147] J. Kopp, "Constraints on dark matter annihilation from AMS-02 results", *Phys.Rev.* **D88** (2013) 076013, arXiv:1304.1184.

[148] A. Ibarra, A. S. Lamperstorfer, and J. Silk, "Dark matter annihilations and decays after the AMS-02 positron measurements", *Phys.Rev.* **D89** (2014) 063539, arXiv:1309.2570.

[149] H.-B. Jin, Y.-L. Wu, and Y.-F. Zhou, "Implications of the first AMS-02 measurement for dark matter annihilation and decay", *JCAP* **1311** (2013) 026, arXiv:1304.1997.

[150] P. J. Fox and E. Poppitz, "Leptophilic Dark Matter", *Phys.Rev.* **D79** (2009) 083528, arXiv:0811.0399.

[151] V. Vagelli, "Measurement of the cosmic $e^+ + e^-$ flux from 0.5 GeV to 1 TeV with the Alpha Magnetic Spectrometer (AMS-02) on the International Space Station", *Ph.D. thesis, KIT, to be published in 2014.*

[152] Fermi-LAT Collaboration, "The Second Fermi Large Area Telescope Catalog of Gamma-ray Pulsars", *Astrophys.J.Suppl.* **208** (2013) 17, arXiv:1305.4385.

[153] Fermi-LAT Collaboration, "Searches for cosmic-ray electron anisotropies with the Fermi Large Area Telescope", *Physical Review D* **82** (November, 2010) 092003, arXiv:1008.5119.

[154] T. Linden and S. Profumo, "Probing the Pulsar Origin of the Anomalous Positron Fraction with AMS-02 and Atmospheric Cherenkov Telescopes", *Astrophys.J.* **772** (2013) 18, arXiv:1304.1791.

[155] G. di Bernardo, C. Evoli, D. Gaggero et al., "Implications of the cosmic ray electron spectrum and anisotropy measured with Fermi-LAT", *Astroparticle Physics* **34** (February, 2011) 528–538, arXiv:1010.0174.

[156] R. Battiston, "Precision measurements of e+ e- in Cosmic Ray with the Alpha Magnetic Spectrometer on the ISS", *Physics of the Dark Universe* **4** (2014), no. 0, 6 – 9.

[157] M. Cirelli, M. Kadastik, M. Raidal et al., "Model-independent implications of the e+-, anti-proton cosmic ray spectra on properties of Dark Matter", *Nucl.Phys.* **B813** (2009) 1–21, arXiv:0809.2409.

[158] P. Gondolo, J. Edsjo, P. Ullio et al., "DarkSUSY: Computing supersymmetric dark matter properties numerically", *JCAP* **0407** (2004) 008, arXiv:astro-ph/0406204.

[159] J. F. Navarro, C. S. Frenk, and S. D. White, "The Structure of cold dark matter halos", *Astrophys.J.* **462** (1996) 563–575, arXiv:astro-ph/9508025.

[160] J. Bovy and S. Tremaine, "On the Local Dark Matter Density", *Astrophysical Journal* **756** (September, 2012) 89, arXiv:1205.4033.

[161] HESS Collaboration, "The energy spectrum of cosmic-ray electrons at TeV energies", *Phys.Rev.Lett.* **101** (2008) 261104, arXiv:0811.3894.

[162] HESS Collaboration, "Probing the ATIC peak in the cosmic-ray electron spectrum with H.E.S.S.", *A&A* **508** (December, 2009) 561–564, arXiv:0905.0105.

[163] T. M. Dame, D. Hartmann, and P. Thaddeus, "The Milky Way in Molecular Clouds: A New Complete CO Survey", *Astrophysical Journal* **547** (February, 2001) 792–813, arXiv:astro-ph/0009217.

[164] A. W. Strong, I. V. Moskalenko, and O. Reimer, "Diffuse Galactic Continuum Gamma Rays: A Model Compatible with EGRET Data and Cosmic-Ray Measurements", *Astrophysical Journal* **613** (October, 2004) 962–976, arXiv:astro-ph/0406254.

[165] A. W. Strong, I. V. Moskalenko, O. Reimer et al., "The distribution of cosmic-ray sources in the Galaxy, γ-rays and the gradient in the CO-to-H_2 relation", *A&A* **422** (July, 2004) L47–L50, arXiv:astro-ph/0405275.

[166] Fermi-LAT Collaboration, "Constraints on the Cosmic-ray Density Gradient Beyond the Solar Circle from Fermi γ-ray Observations of the Third Galactic Quadrant", *Astrophysical Journal* **726** (January, 2011) 81, arXiv:1011.0816.

[167] D. Gaggero, C. Evoli, D. Grasso et al., "An alternative solution to the gamma-ray Gradient problem", *ArXiv e-prints* (November, 2011) arXiv:1111.1636.

[168] K. Gorski, E. Hivon, A. Banday et al., "HEALPix - A Framework for high resolution discretization, and fast analysis of data distributed on the sphere", *Astrophys.J.* **622** (2005) 759–771, arXiv:astro-ph/0409513.

[169] M. Su, T. R. Slatyer, and D. P. Finkbeiner, "Giant Gamma-ray Bubbles from Fermi-LAT: Active Galactic Nucleus Activity or Bipolar Galactic Wind?", *Astrophysical Journal* **724** (December, 2010) 1044–1082, arXiv:1005.5480.

[170] B. Y. Welsh, R. Lallement, J.-L. Vergely et al., "New 3D gas density maps of NaI and CaII interstellar absorption within 300 pc", *A&A* **510** (February, 2010) A54, arXiv:0912.3040.

[171] D. Gaggero, I. Gebauer, S. Kunz et al., "Impact of the Local Bubble on cosmic ray lepton spectra and anisotropy", *in preparation* (2014).

[172] C. D. Dermer and E. P. Liang, "Electron thermalization and heating in relativistic plasmas", *Astrophys.J* **339** (April, 1989) 512–528.

[173] A. Gelman and D. B. Rubin, "Inference from Iterative Simulation Using Multiple Sequences", *Statist.Sci.* **7** (1992) 457–472.

[174] C. Mao and C.S.Shen, "Anisotropy and Diffusion of Cosmic Ray Electrons", *Chinese Journal of Physics* **10** (November, 1971) 16.

[175] F. Keller, "Vorhersagen für die Anisotropien im leptonischen Fluss der kosmischen Strahlung", *Diploma thesis, KIT* (2014).

[176] Fermi-LAT Collaboration, "The Spectrum and Morphology of the Fermi Bubbles", *Astrophys.J.* (2014) arXiv:1407.7905.

Appendix

A. Energy Losses for Cosmic Nuclei and Leptons

A.1. Ionization losses

Nuclei

Ionization losses in the ISM can be expresses by the general formula [73]

$$\left(\frac{dE}{dt}\right)_{Ion}(\beta \geq \beta_0) = -2\pi r_e^2 c m_e c^2 Z^2 \frac{1}{\beta} \sum_{s=H,He} n_s[B_s + B'(\alpha_f Z/\beta)]. \tag{7.1}$$

Herein, α_s ist the fine structure constant, n_s is the number density of the considered particle species, $\beta = v/c$ is the speed of the nucleus in units of c, $\beta_0 = 1.4e^2/\hbar c = 0.01$ is the characteristic velocity, determined by the orbital velocity of electrons in hydrogen and

$$B_s = \left[ln\left(\frac{2m_e c^2 \beta^2 \gamma^2 Q_m ax}{\tilde{I}_s^2}\right) - 2\beta^2 - \frac{2C_s}{z_s} - \delta_s\right], \tag{7.2}$$

with the Lorentz factor of the ion γ. The largest possible energy transfer from the incident particle to the atomic electrons is given by

$$Q_{max} \approx \frac{2m_e c^2 \beta^2 \gamma^2}{1 + [2\gamma m_e/M]} \tag{7.3}$$

with the mass of the nucleon $M \gg m_e$ and the geometric mean of all ionization and excitation potentials of the atom $\tilde{I}_s$. The shell correction term C_s/z_s, the density correction term δ_s and the correction term β' for large Z or small β can be neglected, leading to

$$\left(\frac{dE}{dt}\right)_{Ion}(\beta \geq \beta_0) = -2\pi r_e^2 c m_e c^2 Z^2 \frac{1}{\beta} \sum_{s=H,He} n_s \left[ln\left(\frac{2m_e c^2 \beta^2 \gamma^2 Q_{max}}{\tilde{I}_s^2}\right) - 2\beta^2\right]. \tag{7.4}$$

Electrons

Ionization losses for electrons in neutral hydrogen and helium are given by the Bethe-Bloch formula

$$\left(\frac{dE}{dt}\right)_{Ion} = -2\pi r_e^2 c m_e c^2 \frac{1}{\beta} \sum_{s=H,He} Z_s n_s \left[ln\left(\frac{(\gamma-1)\beta^2 E^2}{2I_s^2}\right) + \frac{1}{8}\right] \tag{7.5}$$

with the charge of the nucleus Z_s, the gas number density n_s, the ionization potential I_s, the total electron energy E, the Lorentz factor γ and the velocity of the electron $\beta = v/c$.

A.2. Coulomb losses

Nuclei

In a completely ionized plasma, the Coulomb collisions are dominated by scattering off thermal electrons:

$$\left(\frac{dE}{dt}\right)_{Coul} \approx -4\pi r_e^2 c m_e c^2 Z^2 n_e \; ln\Lambda \frac{\beta^2}{x_m^3 + \beta^3}, \tag{7.6}$$

with the electron radius r_e, the electron rest mass m_e, the nucleon charge of the projectile Z, the electron number density in the plasma n_e and the definition $x_m \equiv (3\sqrt{\pi}/4)^(1/3) \cdot \sqrt{2kT_e/m_e c^2}$ with the electron temperature T_e. The 'Coulomb logarithm' in a cold plasma limit reads

$$ln\Lambda \approx \frac{1}{2} \; ln\left(\frac{m_e^2 c^4}{\pi r_e \hbar^2 c^2 n_e} \cdot \frac{M\gamma^2\beta^4}{M + 2\gamma m_e}\right), \tag{7.7}$$

with the nucleon mass M and the nucleon Lorentz factor γ.

Electrons

The Coulomb losses for electrons in a fully ionized medium are given by

$$\left(\frac{dE}{dt}\right)_{Coul} \approx -2\pi r_e^2 m_e c^2 Z n \frac{1}{\beta}\left[\; ln\left(\frac{E m_e c^2}{4\pi r_e \hbar^2 c^2 n Z}\right) - \frac{3}{4}\right], \tag{7.8}$$

where $Zn = n_e$ is the electron number density. For electron losses in a plasma of an arbitrary temperature, see [172].

A.3. Compton losses

The Compton energy losses can be calculated by using the *Klein-Nishina* cross section:

$$\frac{dE}{dt} = \frac{\pi r_e^2 m_e c^2 c}{2\gamma^2\beta} \int_0^\infty d\omega f_\gamma(\omega)(S(\gamma,\omega,k^+) - S(\gamma,\omega,k^-)), \tag{7.9}$$

where the background photon distribution $f_\gamma(\omega)$ is normalized on the photon number density as $n_\gamma = \int d\omega \omega^2 f_\gamma(\omega)$. ω is the energy of the background photon taken in the electron-rest-mass units, $k^\pm = \omega\gamma(1 \pm \beta)$ and

$$\begin{aligned} S(\gamma,\omega,k) = \omega \Bigg\{ &\left(k + \frac{31}{6} + \frac{5}{k} + \frac{3}{2k^2}\right) ln(2k+1) - \frac{11}{6}k - \frac{3}{k} + \frac{1}{12(2k+1)} + \frac{1}{12(2k+1)^2} + Li_2(-2k) \Bigg\} \\ -\gamma \Bigg\{ &\left(k + 6 + \frac{3}{k}\right) ln(2k+1) - \frac{11}{6}k + \frac{1}{4(2k+1)} - \frac{1}{12(2k+1)^2} + 2Li_2(-2k) \Bigg\}, \end{aligned} \tag{7.10}$$

with the dilogarithm

$$li_2(-2k) = -\int_0^{-2k} dx \frac{1}{x} ln(1-x). \tag{7.11}$$

A.4. Bremsstrahlung

Energy losses due to electron-proton bremsstrahlung in cold plasma are given the expressions

$$\begin{aligned}\left(\frac{dE}{dt}\right)_{Br,ep} &= -\frac{2}{3}\alpha_f r_e^2 m_e c^2 Z^2 n 8\gamma\beta[1-0.25(\gamma-1)+0.44935(\gamma-1)^2-0.16577(\gamma-1)^3], \text{ for } \gamma \leq 2,\\ \left(\frac{dE}{dt}\right)_{Br,ep} &= -\frac{2}{3}\alpha_f r_e^2 m_e c^2 Z^2 n \beta^{-1}[6\gamma ln(2\gamma)-2\gamma-0.2900], \text{ for } \gamma \geq 2.\end{aligned} \tag{7.12}$$

The electron-electron bremsstrahlung is given by

$$\left(\frac{dE}{dt}\right)_{Br,ee} = -\frac{1}{2}\alpha_f r_e^2 m_e c^2 Z n \beta \gamma^* Q_{cm}(\gamma^*), \tag{7.13}$$

where

$$Q_{cm}(\gamma^*) = 8\frac{p^{*2}}{\gamma^*}\left[1-\frac{4p^*}{3\gamma^*}+\frac{2}{3}\left(2+\frac{p^{*2}}{\gamma^{*2}}\right)\ ln(p^*+\gamma^*)\right]. \tag{7.14}$$

$$\gamma^* = \sqrt{(\gamma+1)/2}, \tag{7.15}$$

$$p^* = \sqrt{(\gamma-1)/2}, \tag{7.16}$$

The asterisk denotes the center of mass variable.

A good approximation for the total bremsstrahlung losses ($Br_{total} = Br_{ee} + Br_{ep}$) in an ionized gas is given by

$$\left(\frac{dE}{dt}\right)_{Br,total} \approx -4\alpha_f r_e^2 m_e c^2 Z(Z+1) n E\left(\ ln(2\gamma-\frac{1}{3})\right). \tag{7.17}$$

For a neutral gas one can obtain the energy losses by integration over the bremsstrahlung luminosity

$$\left(\frac{dE}{dt}\right)_{Br0} = -c\beta \sum_{s=H,He} n_s \int dk k \frac{d\sigma_s}{dk}. \tag{7.18}$$

A reasonable approximation with a maximal deviation of 10% near $E \sim 70$ MeV is

$$\begin{aligned}\left(\frac{dE}{dt}\right)_{Br0} &= -4\alpha_f r_e^2 m_e c^2 E\left(ln(2\gamma)-\frac{1}{3}\right)\sum_{s=H,He} n_s Z_s(Z_s+1), \text{ for } \gamma \lesssim 100,\\ \left(\frac{dE}{dt}\right)_{Br0} &= -cE\sum_{s=H,He}\frac{n_s M_s}{T_s}, \text{ for } \gamma \gtrsim 800,\end{aligned} \tag{7.19}$$

with a linear connection in between. M_s is the atomic mass and T_s ist the radiation length with $T_H \approx 62.8\,\mathrm{g/cm^2}$ and $T_{He} \approx 93.1\,\mathrm{g/cm^2}$ [74].

A.5. Synchrotron losses

The energy losses by synchrotron radiation are given by

$$\left(\frac{dE}{dt}\right)_{Synch} = -\frac{32}{9}\pi r_e^2 c U_B \gamma^2 \beta^2, \tag{7.20}$$

where $U_B = \frac{H^2}{8\pi}$ is the energy density of the random magnetic field.

B. Performance of the Markov Chain Monte Carlo

B.1. Performance of the MH and MTM Algorithm

Figures B.1 and B.2 illustrate the performance as development with time of the MH and MTM algorithm ($k = 8$ trials), respectively. Each point corresponds to an evaluated model for which the transport equation was solved. While the MH algorithm first has to rummage to interesting regions in parameter space until a characteristic scale of the fitness is accommodated, the MTM algorithm converges much faster by biasing the local parameter space.

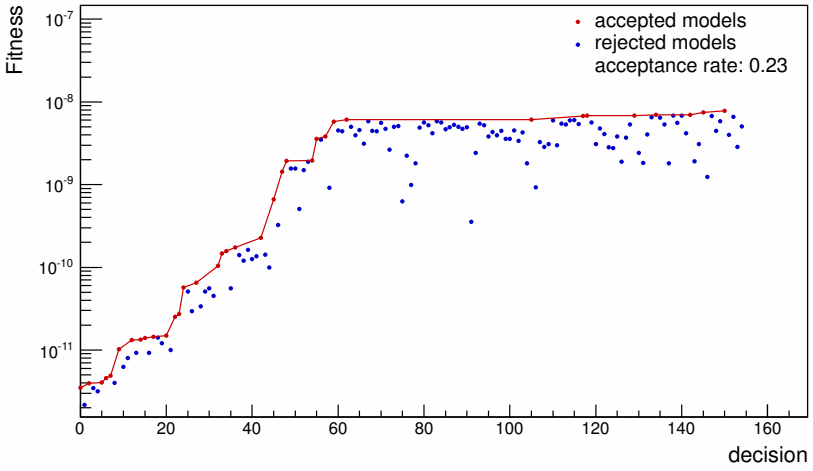

Figure B.1.: Performance of the Metropolis-Hastings algorithm. Shown is the Fitness versus the number of decision illustrating the development of a Markov chain over time. Each point corresponds to an evaluated model for which the transport equation was solved. Depending on the decision a model is marked blue (red) if rejected (accepted).

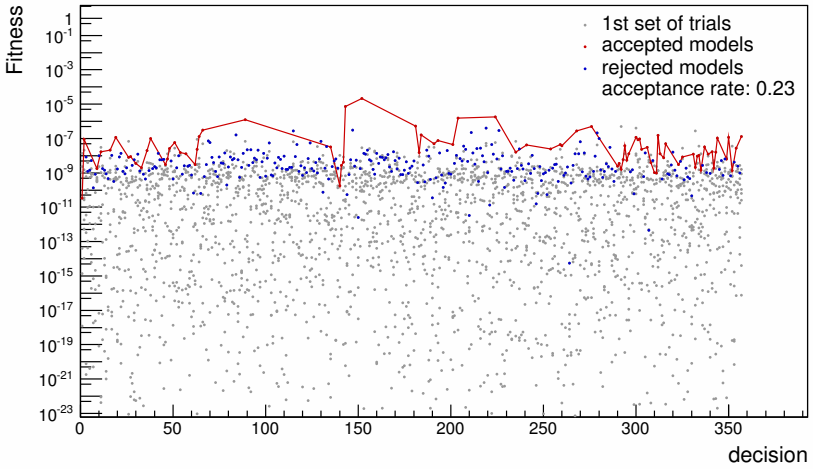

Figure B.2.: Performance of the Multiple-Try-Metropolis algorithm. Shown is the Fitness versus the number of decision illustrating the development of a Markov chain over time. Each point corresponds to an evaluated model for which the transport equation was solved. The first set consisting of 8 models is marked as gray points. The model chosen for decision is marked blue (red) if rejected (accepted). Note that the second set of evaluated models is not shown and the y-scale was cut on the lower edge for a better visualization.

B.2. The Gelman-Rubin Diagnostic

For an estimation of the length of the burn-in period the *Gelman-Rubin* diagnostic is used [173]. It requires $m \geq 2$ Markov chains that are compared in terms of within-chain and between-chain variances. Convergence is diagnosed as soon as the deviation between these two variances is sufficiently small and the chains output is indistinguishable, i.e. independent of the initial starting point.
The within-chain variance W of parameter θ of m Markov chains each with length n is defined as

$$W = \frac{1}{m} \sum_{j=1}^{m} s_j^2 \tag{7.21}$$

with

$$s_j^2 = \frac{1}{n-1} \sum_{i=1}^{n} (\theta_{ij} - \bar{\theta}_j)^2. \tag{7.22}$$

Herein θ_{ij} is the value of parameter θ of the ith entry of Markov chain j and $\bar{\theta}_j$ the averaged value of θ over all entries in Markov chain j.

The between-chain variance B reads

$$B = \frac{n}{m-1} \sum_{j=1}^{m} (\bar{\theta}_j - \bar{\bar{\theta}}) \tag{7.23}$$

with

$$\bar{\bar{\theta}} = \frac{1}{m} \sum_{j=1}^{m} \bar{\theta}_j. \tag{7.24}$$

The within-chain and between-chain variance are used to calculate the variance of the stationary distribution $\hat{V}(\theta)$:

$$\hat{V}(\theta) = \left(1 - \frac{1}{n}\right) W + \frac{1}{n} B. \tag{7.25}$$

The *potential scale reduction factor* $\hat{R}$ is

$$\hat{R}(\theta) = \sqrt{\frac{\hat{V}(\theta)}{W}}. \tag{7.26}$$

If all chains have reached the target distribution the variance of the stationary distribution $\hat{V}(\theta)$ should be very close to the within-chain variance W and therefore $\hat{R}(\theta) \approx 1$ for each parameter θ. If $\hat{R}$ is substantially above 1 the chains have not converged and should be run longer. The maximal recommended deviation of $\hat{R}$ to 1 depends on the application, but in general $\hat{R} < 1.05$ is used as a rule of thumb for which convergence can be assumed. In order to estimate the typical burn-in period of the MTM algorithm in combination with a 16 dimensional, realistic transport model as used in this work, $\hat{R}$ was calculated for a

number of 87 Markov chains. Figure B.3 shows $\hat{R}$ for each of the used 16 parameters as a function of the length of the Markov chains. The fast drop of $\hat{R}$ indicates that after a chain length of ~ 10 the sampling is independent of the starting point and the Markov chains sample the same distribution. The relatively fast burn-in process can be affiliated to the largely chosen step sizes by which the Markov chains move fast away from their initial starting point. A cross-check was performed by examining the local acceptance rates which at first drop but approach to constant values after typical chain lengths of the same order.

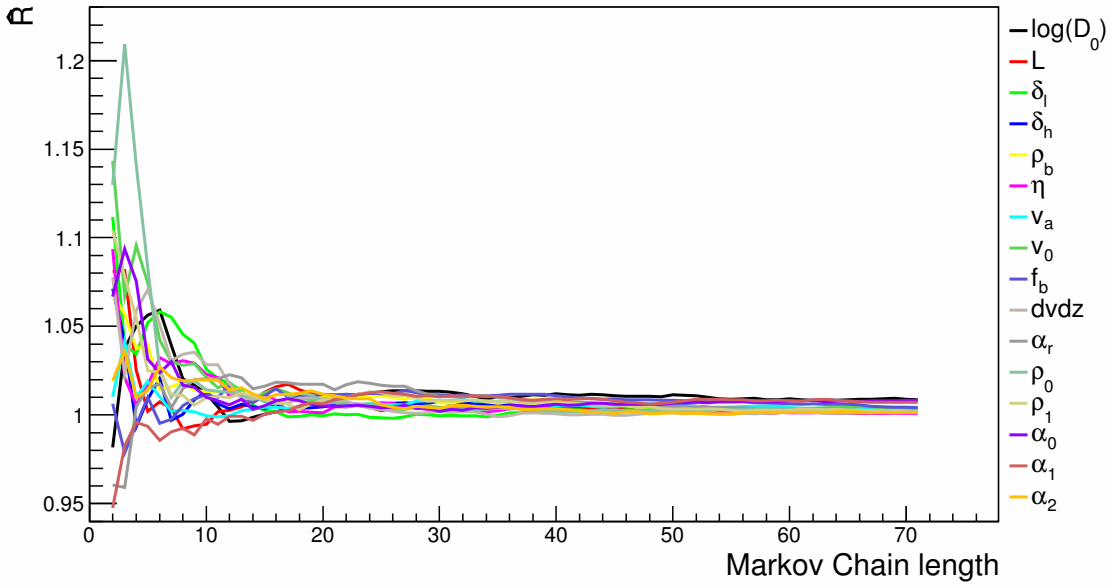

Figure B.3.: Potential scale reduction factor $\hat{R}$ of the Gelman-Rubin diagnostic. The quick drop of $\hat{R}$ indicates that the Markov chains are independent of their initial starting point and sample the same distribution after a relatively short length. As a rule of thumb $\hat{R} < 1.05$ is a typical value for which the sampled distributions of the particular Markov chains can be taken to be equal.

B.3. Proposal Functions

The variances of the Gaussian distributed proposal function were set for each parameter to 80% of the corresponding allowed parameter range in order to obtain a sufficient coverage of the allowed range. A total number of 1,421,149 models were evaluated by 270 Markov chains of which 15,393 models were accepted by those. The accepted models were used to calculate an approximation of the covariance matrix. The burn-in phase was taken to be 12 accepted models according to the Gelman-Rubin diagnostic and was subtracted before from each chain. The derived covariance matrix and the corresponding correlation matrix based on 12,150 models are shown in absolute values in figure B.4, respectively. 520 Markov chains were used to sample additional 1,072,938 models according to the multivariate normal distribution from which 30,521 were accepted. The kd-tree for the last iteration was built on all models evaluated up to that point and contained 3,938,870 models. These include primarily the models obtained with PFI and PFII but also a large number of models obtained during the test phase of the MCMC. Additional 480 Markov chains were run to sample another 5,042,021 models from which 24,221 were accepted. Table B.1 summarizes the quoted numbers.
In the following, the used proposal functions are compared in terms of their acceptance rate, coverage and the quality of the sampled models in general. Figure B.5 shows exemplarily

the number of evaluated and accepted models in the D_0-α_0 plane for each of the three proposal functions. By using PFI the whole allowed range was covered whereby the Markov chains show a preferred region in the parameter space indicated by the large number of proposed models. The number of accepted models points accordingly to a more constrained region but are washy distributed over a wide range. PFII takes correlations between the transport parameters into account and yields characteristic step sizes for a more efficient sampling of interesting regions of the parameter space. By the large amount of sampled models the approximated target distribution became sufficiently precise and PFIII allowed an exceedingly concentration on interesting regions.
Figure B.6 shows the sampled χ^2 values per Ndof for each proposal function. As expected from the concentrations on particular regions in parameter space the quality of the sampled models increased by PFII and a further increase was obtained by PFIII.

Table B.1.: Summary of the number of sampled and accepted models by MCMC.

Proposal function	Markov chains	Sampled models	Accepted models
Gaussian distribution	270	1,421,149	15,393
Multivariate normal distribution	520	1,072,938	30,521
Binary-space-partitioning-based	480	5,042,021	24,221

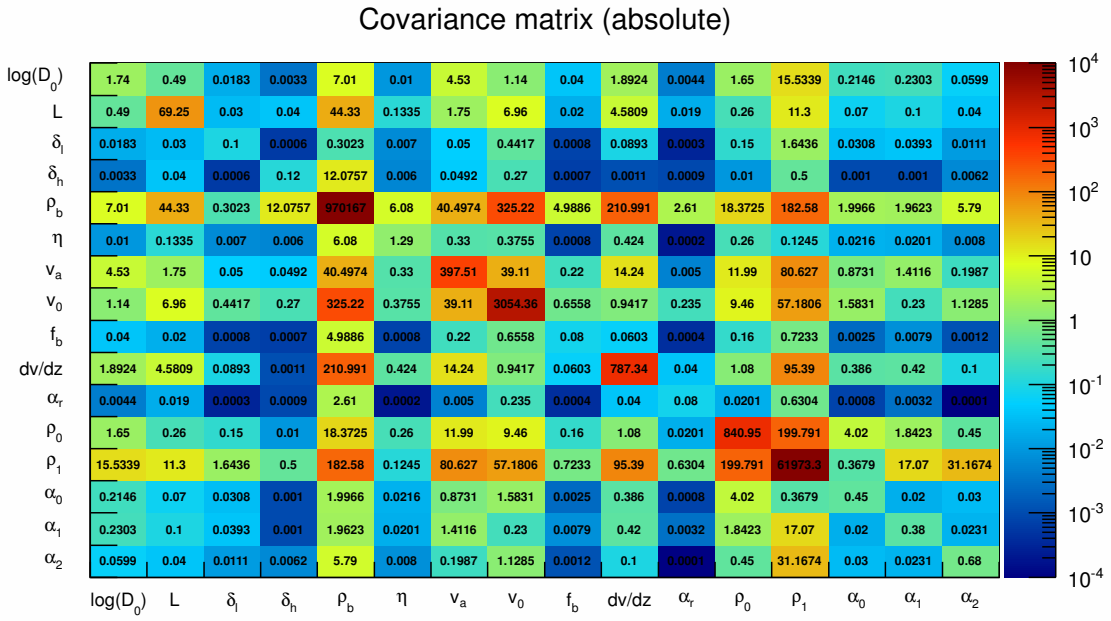

(a)

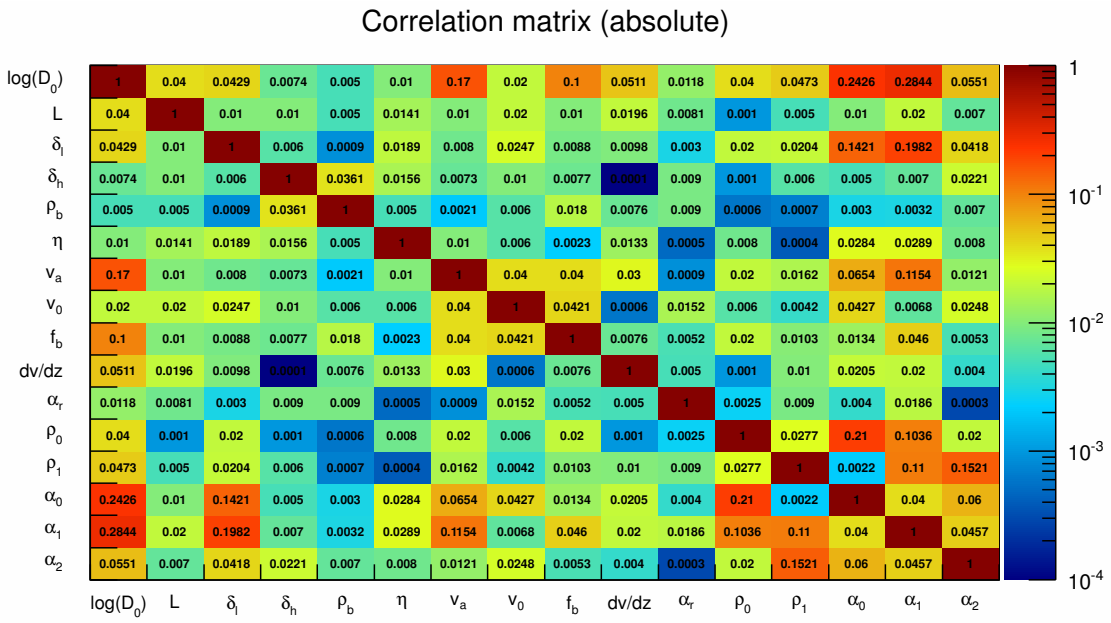

(b)

Figure B.4.: The covariance matrix and the corresponding correlation matrix used for the MCMC sampling. The largest correlations can be found between the diffusion constant D_0 and the injection indices α_0 and α_1. Although it is known that a correlation exists between D_0 and L the approximated correlation was determined to be only 0.04 since the correlation is of non-linear kind and the shown Pearson-correlation is merely sensitive to linear correlations.

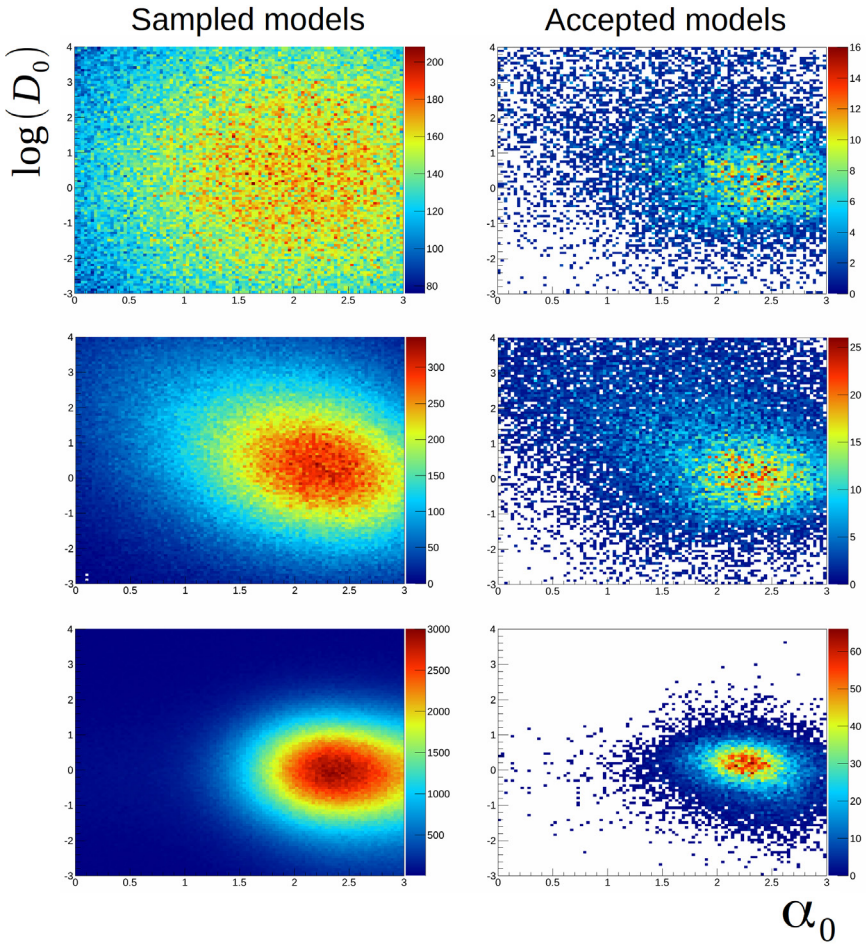

Figure B.5.: The distribution of sampled and accepted models in the plane of D_0-α_0. The z-axis corresponds to the number of sampled (left) and accepted models (right) for the three proposal functions PFI (top), PFII (middle) and PFIII (bottom).

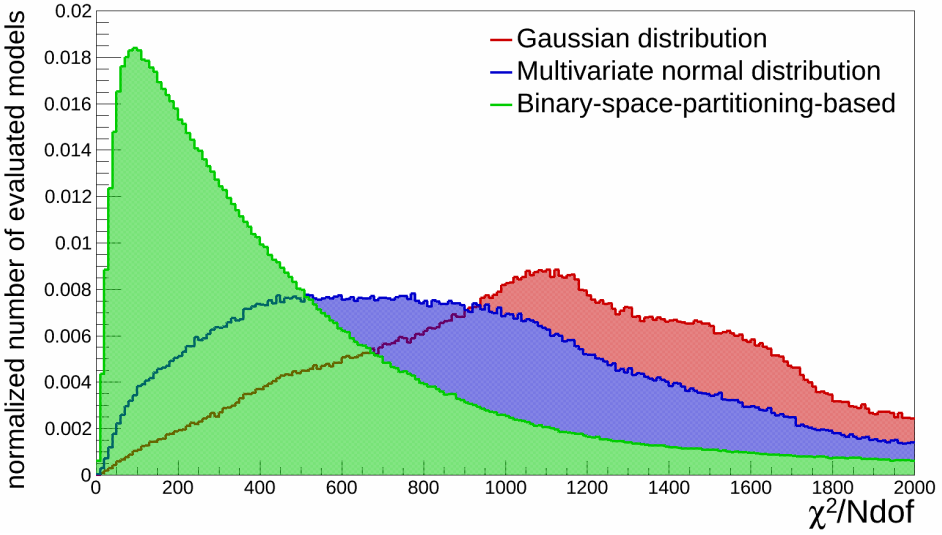

Figure B.6.: The distribution of the sampled χ^2 values per Ndof. By using more information about the parameter space obtained by sampling with the previous proposal function(s), the quality of the sampled models increased exceedingly.

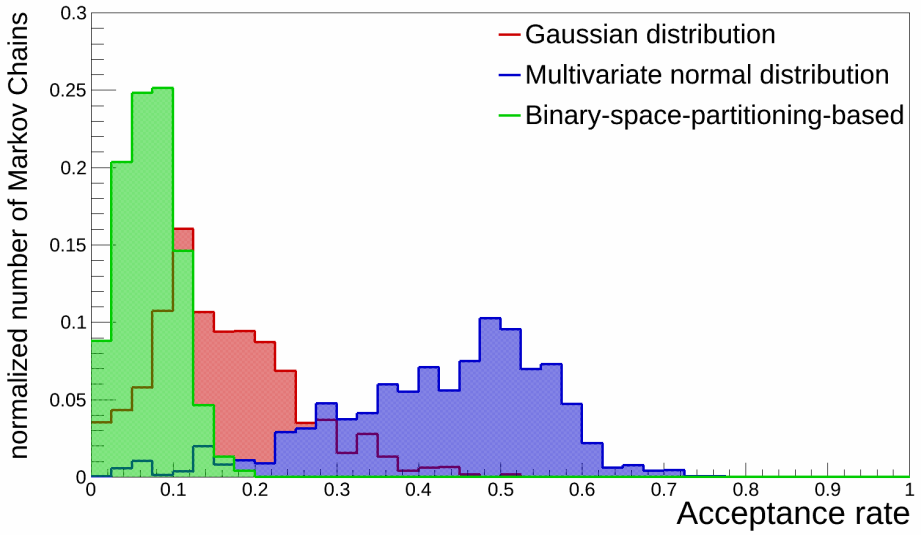

Figure B.7.: Acceptance rates of the proposal functions. While the acceptance rates of the Gaussian proposal function can be influenced by the chosen steps sizes, the acceptances rates of the other proposal functions are completely determined by the algorithm. Sampling according to the multivariate normal distribution yielded the largest acceptance rates around 50% whereas the binary-space-partitioning-based proposal function yielded rather low rates around 8%.

C. Minimal χ^2

C.1. Minimal χ^2 separated by observable

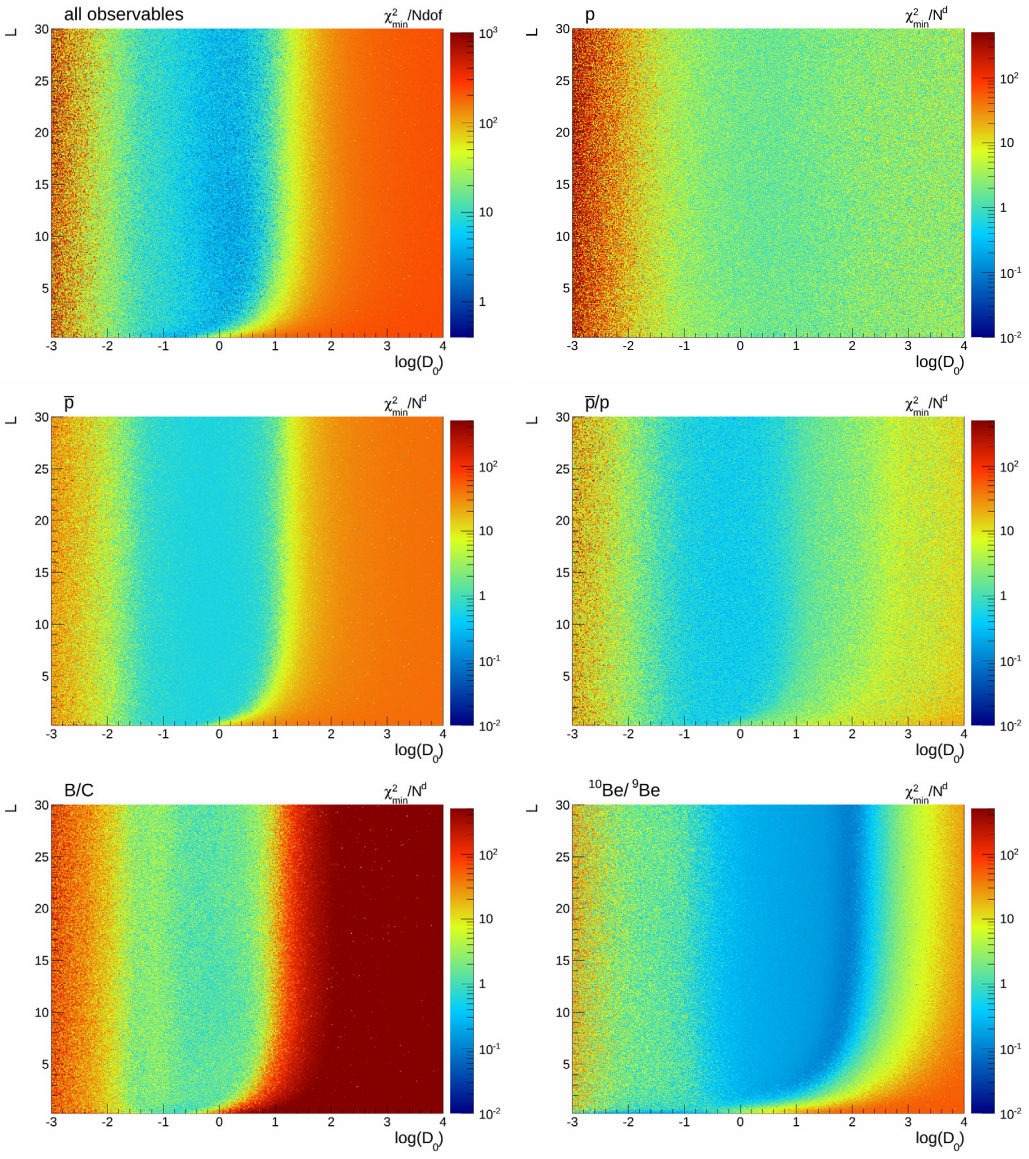

Figure C.8.: Minimal χ^2 values per Ndof in the plane of $L - log(D_0)$ for all observables and separated by observable.

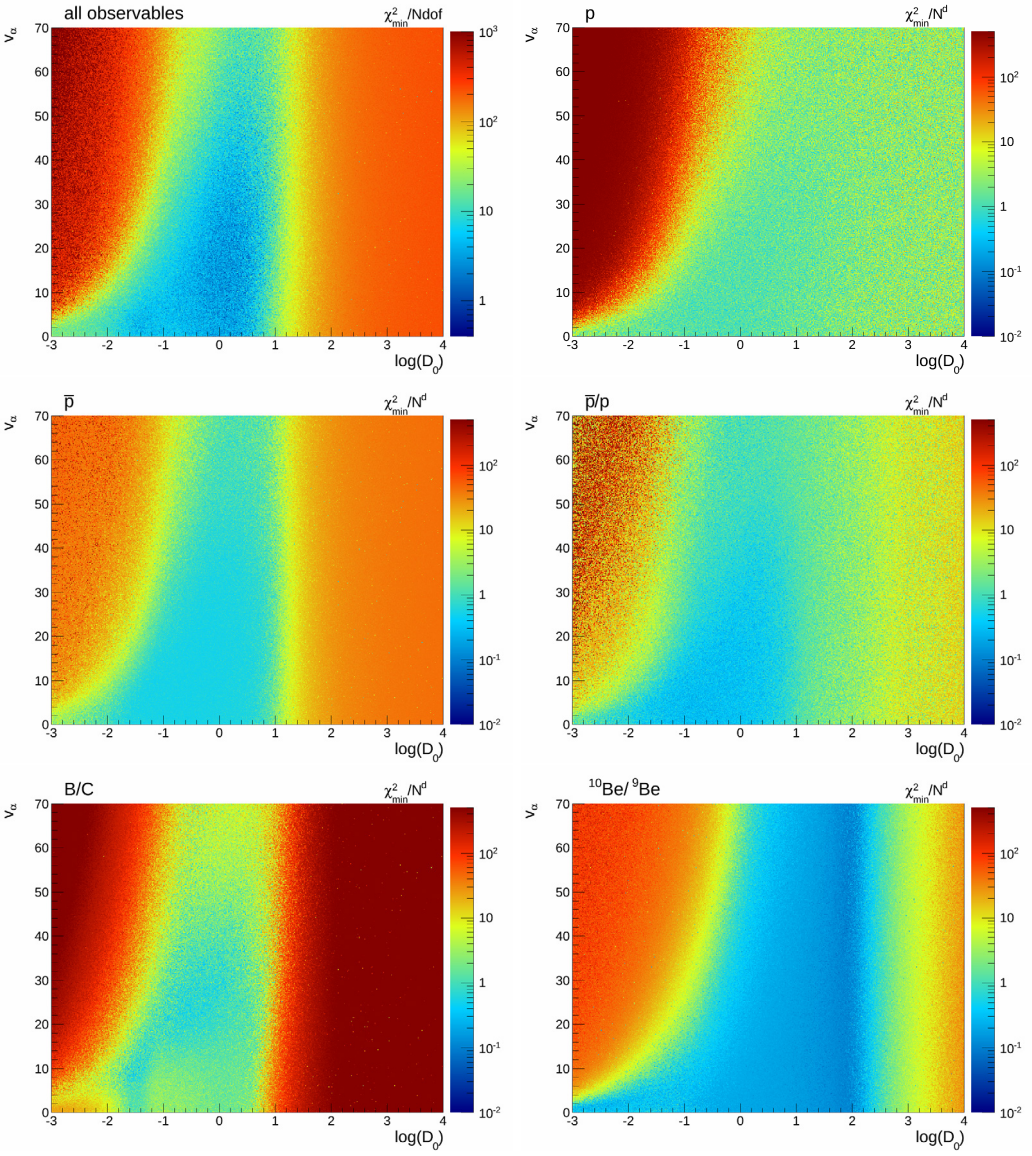

Figure C.9.: Minimal χ^2 values per Ndof in the plane of $v_\alpha - log(D_0)$ for all observables and separated by observable.

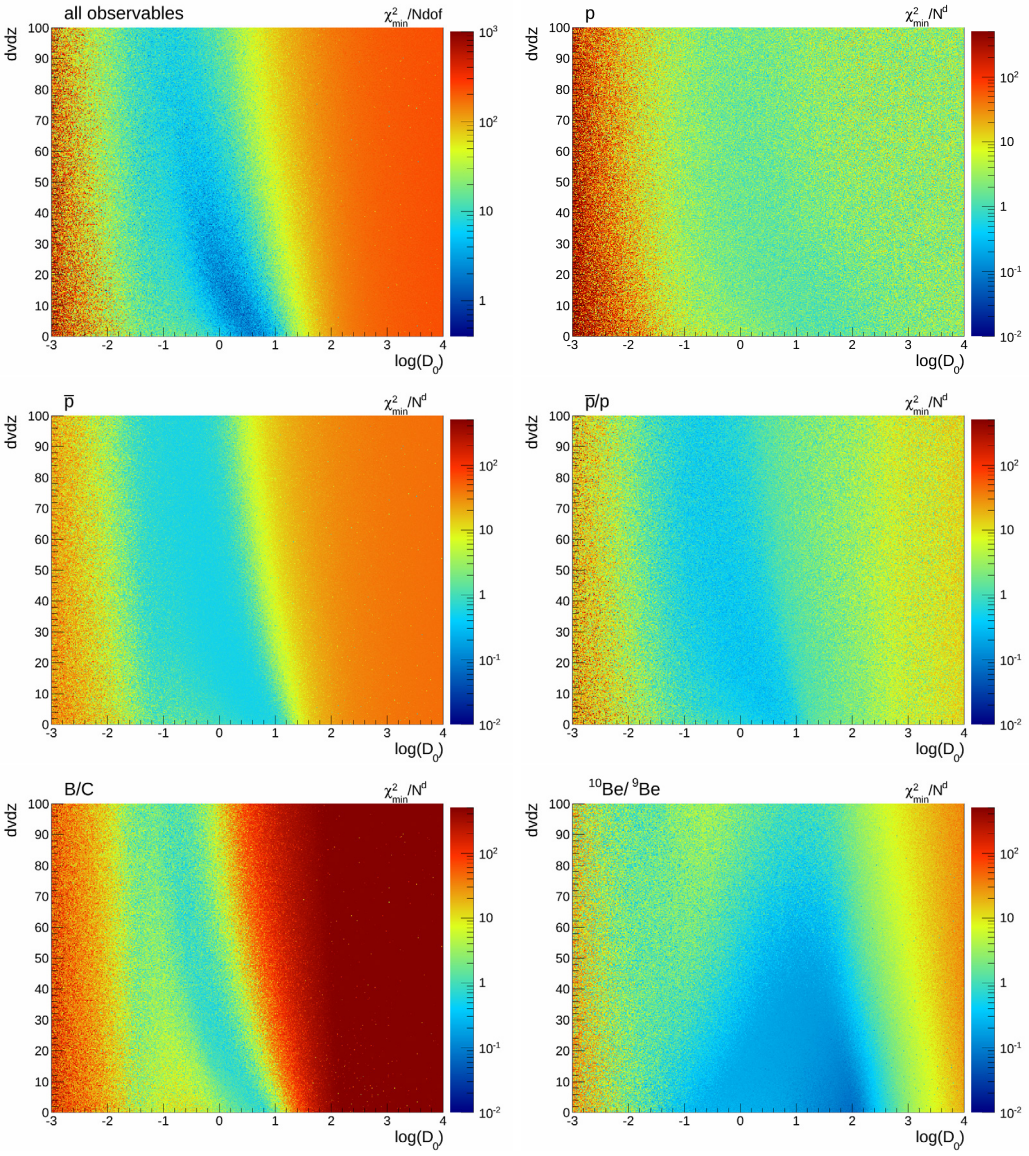

Figure C.10.: Minimal χ^2 values per Ndof in the plane of $dV/dz - log(D_0)$ for all observables and separated by observable.

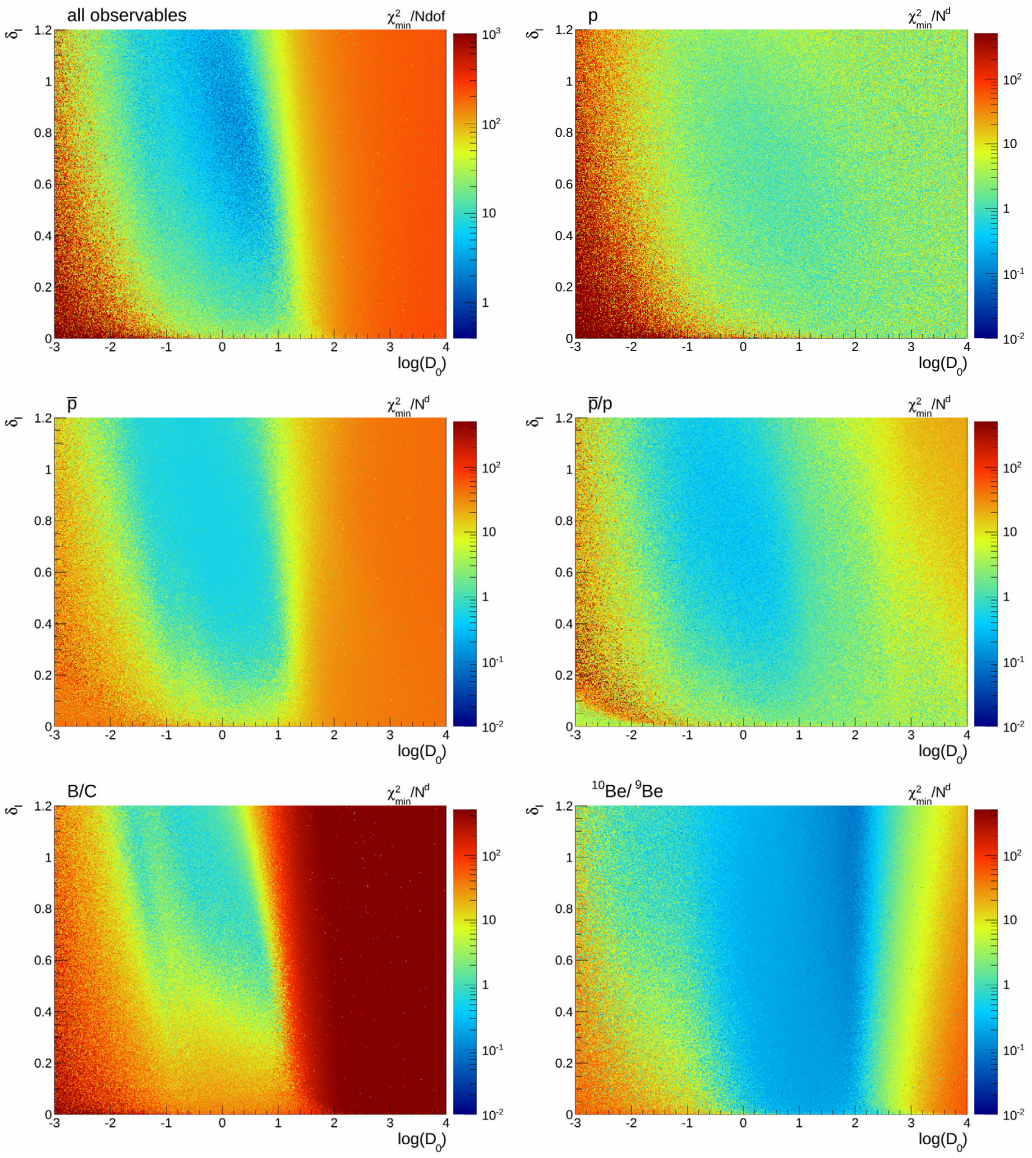

Figure C.11.: Minimal χ^2 values per Ndof in the plane of $\delta_l - log(D_0)$ for all observables and separated by observable.

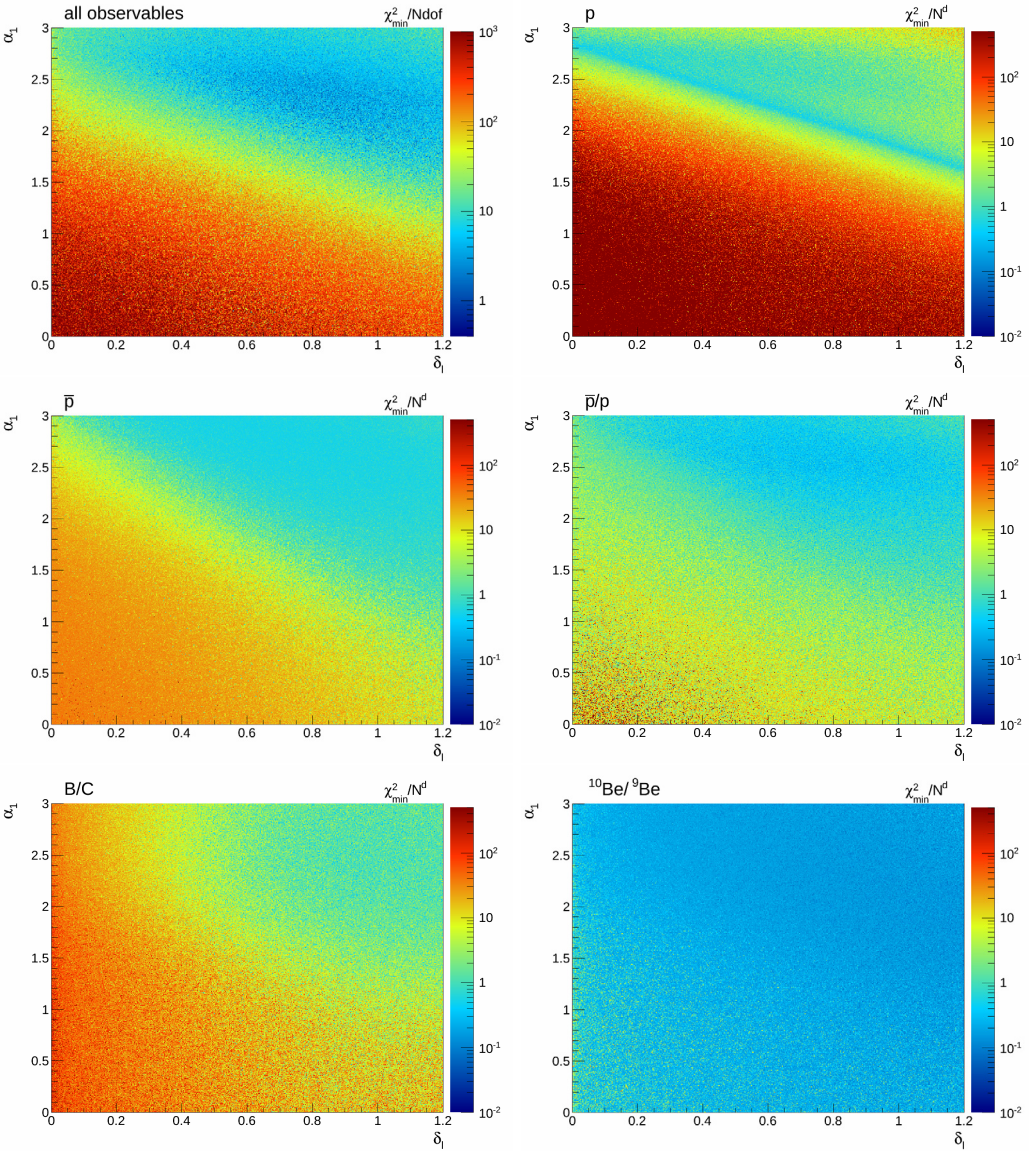

Figure C.12.: Minimal χ^2 values per Ndof in the plane of $\alpha_1 - \delta_l$ for all observables and separated by observable.

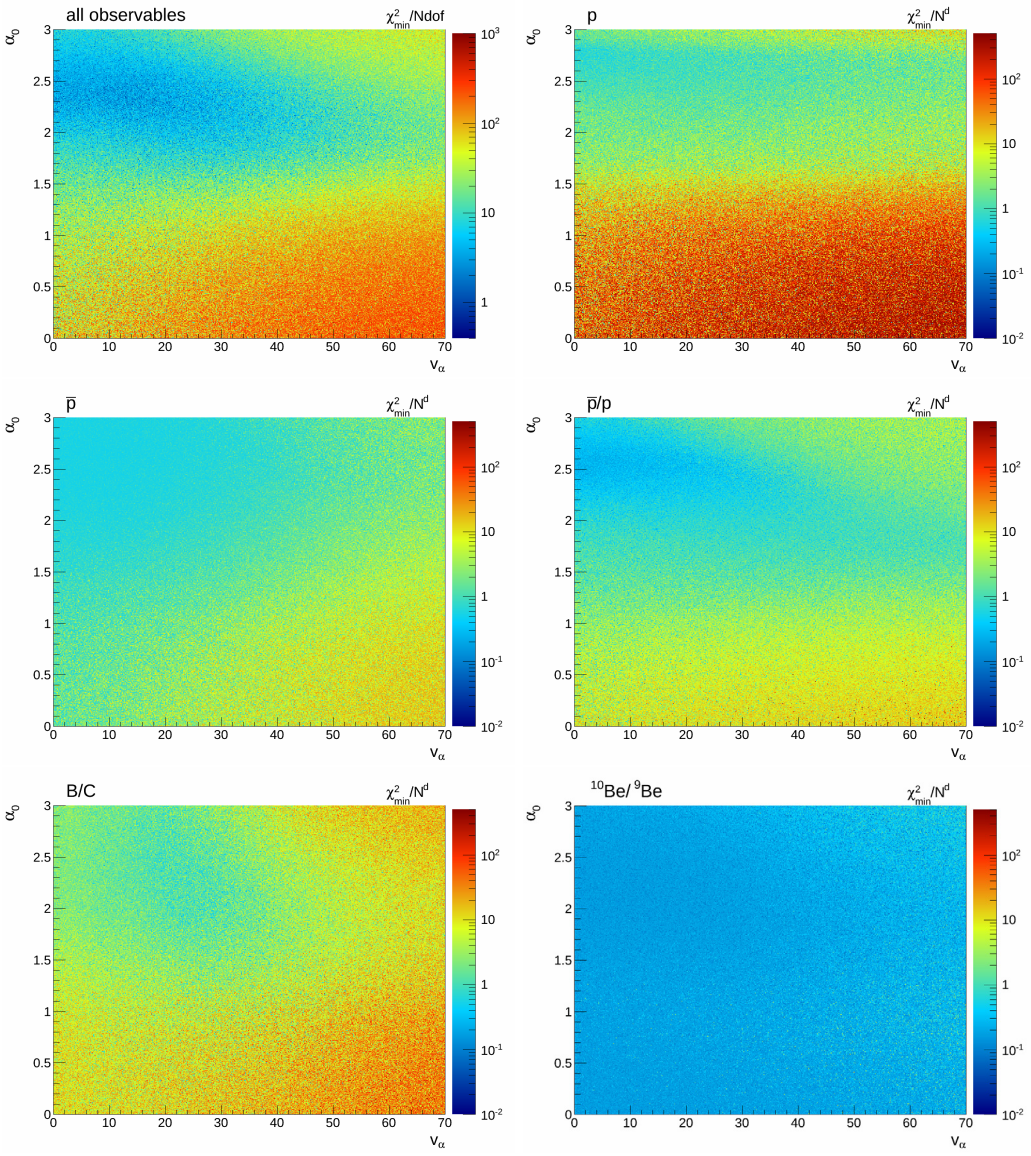

Figure C.13.: Minimal χ^2 values per Ndof in the plane of $\alpha_0 - v_\alpha$ for all observables and separated by observable.

C.2. Minimal χ^2 for each parameter combination

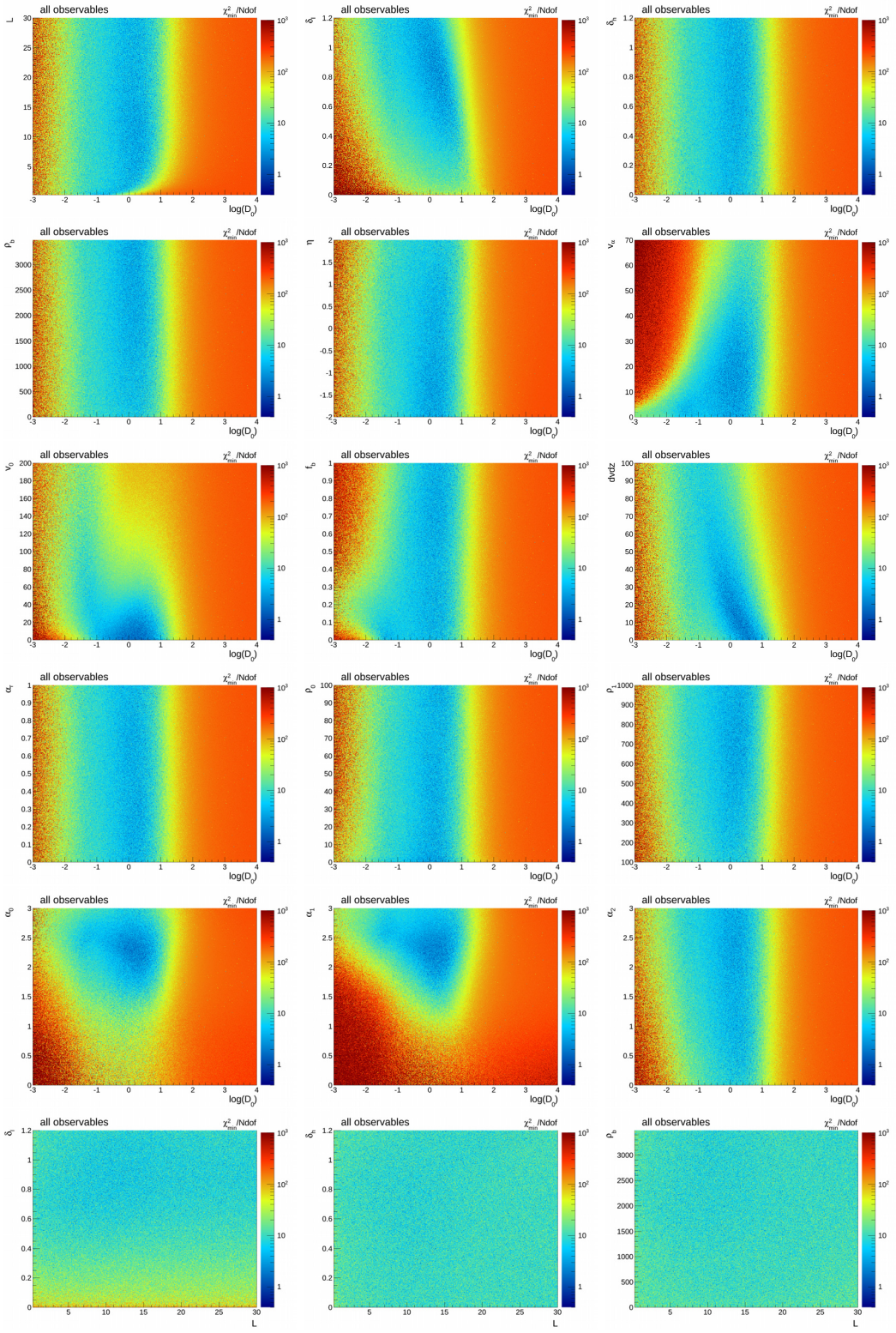

Figure C.14.: Shown is the combined, minimal χ^2 value per degrees of freedom for selected parameter combinations of the 16 dimensional transport model setup (continued on next page).

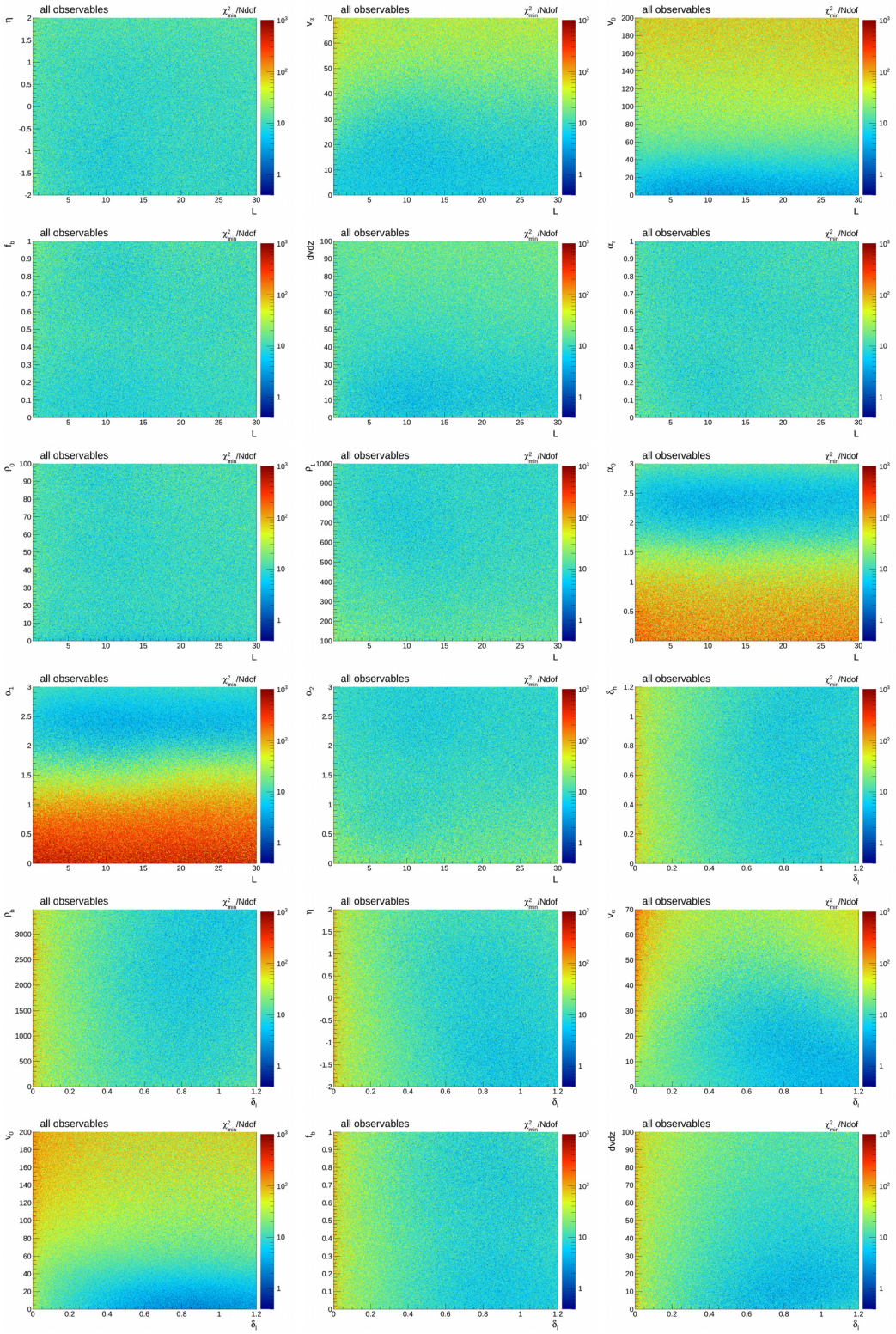

Figure C.15.: Shown is the combined, minimal χ^2 value per degrees of freedom for selected parameter combinations of the 16 dimensional transport model setup (continued on next page).

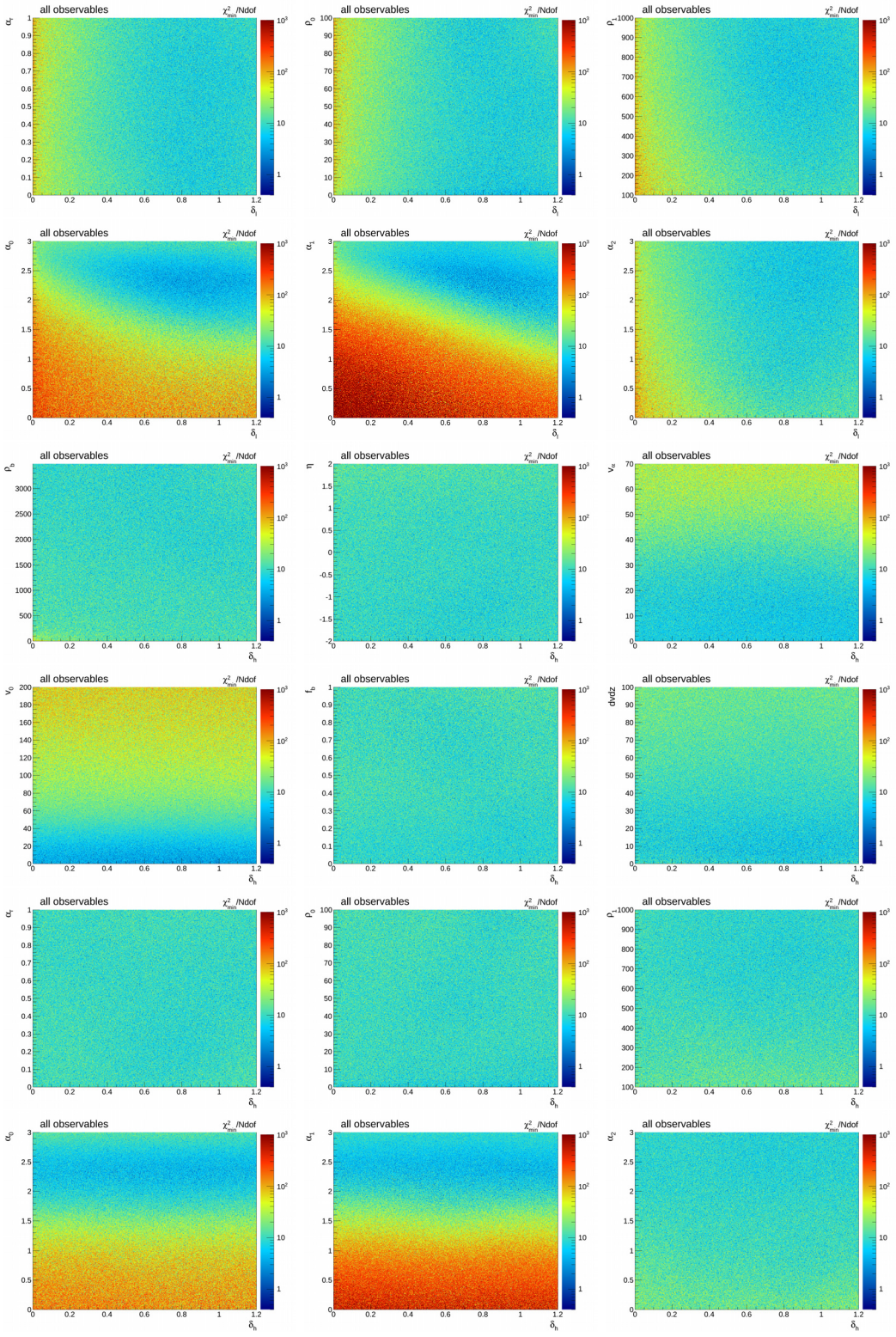

Figure C.16.: Shown is the combined, minimal χ^2 value per degrees of freedom for selected parameter combinations of the 16 dimensional transport model setup (continued on next page).

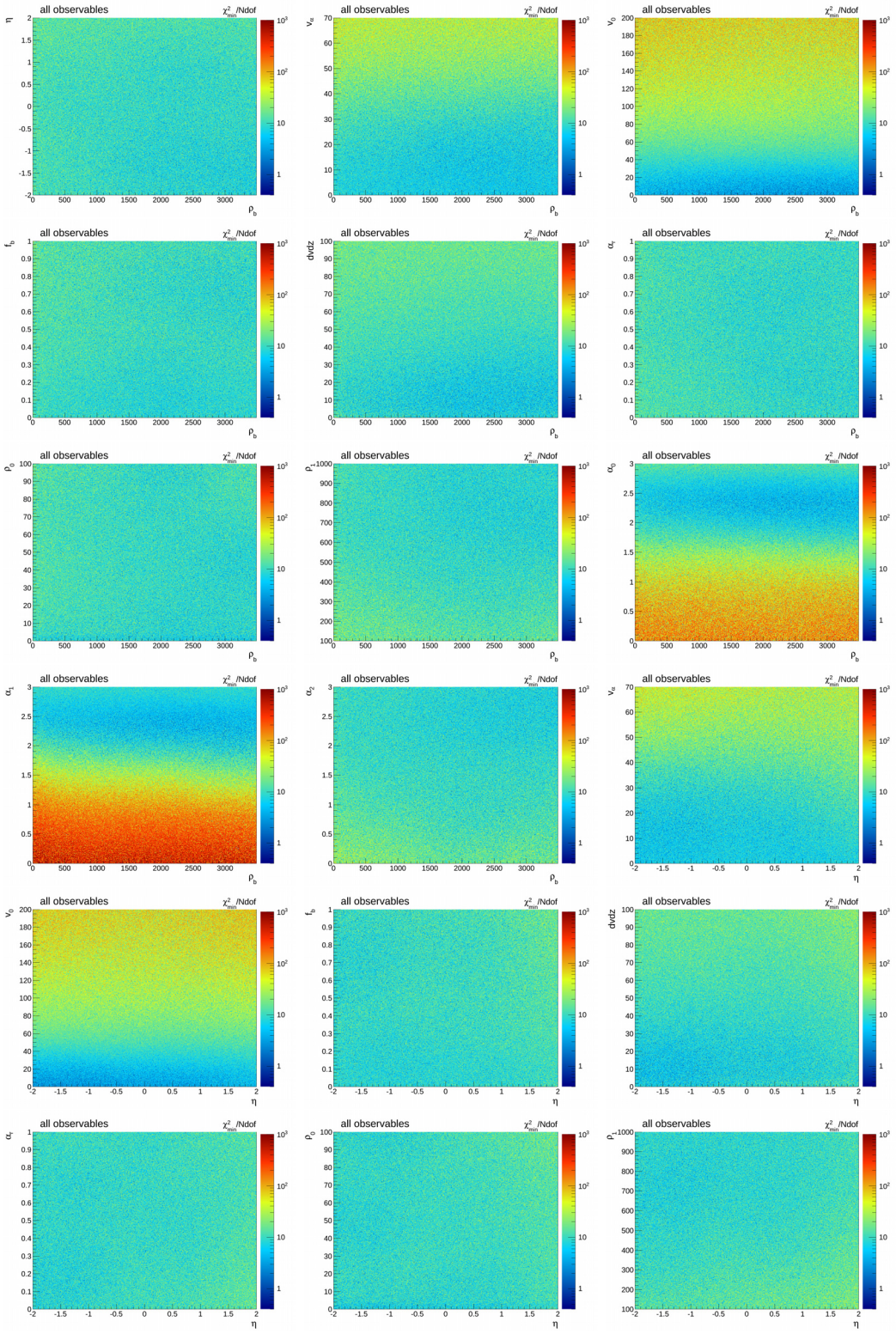

Figure C.17.: Shown is the combined, minimal χ^2 value per degrees of freedom for selected parameter combinations of the 16 dimensional transport model setup (continued on next page).

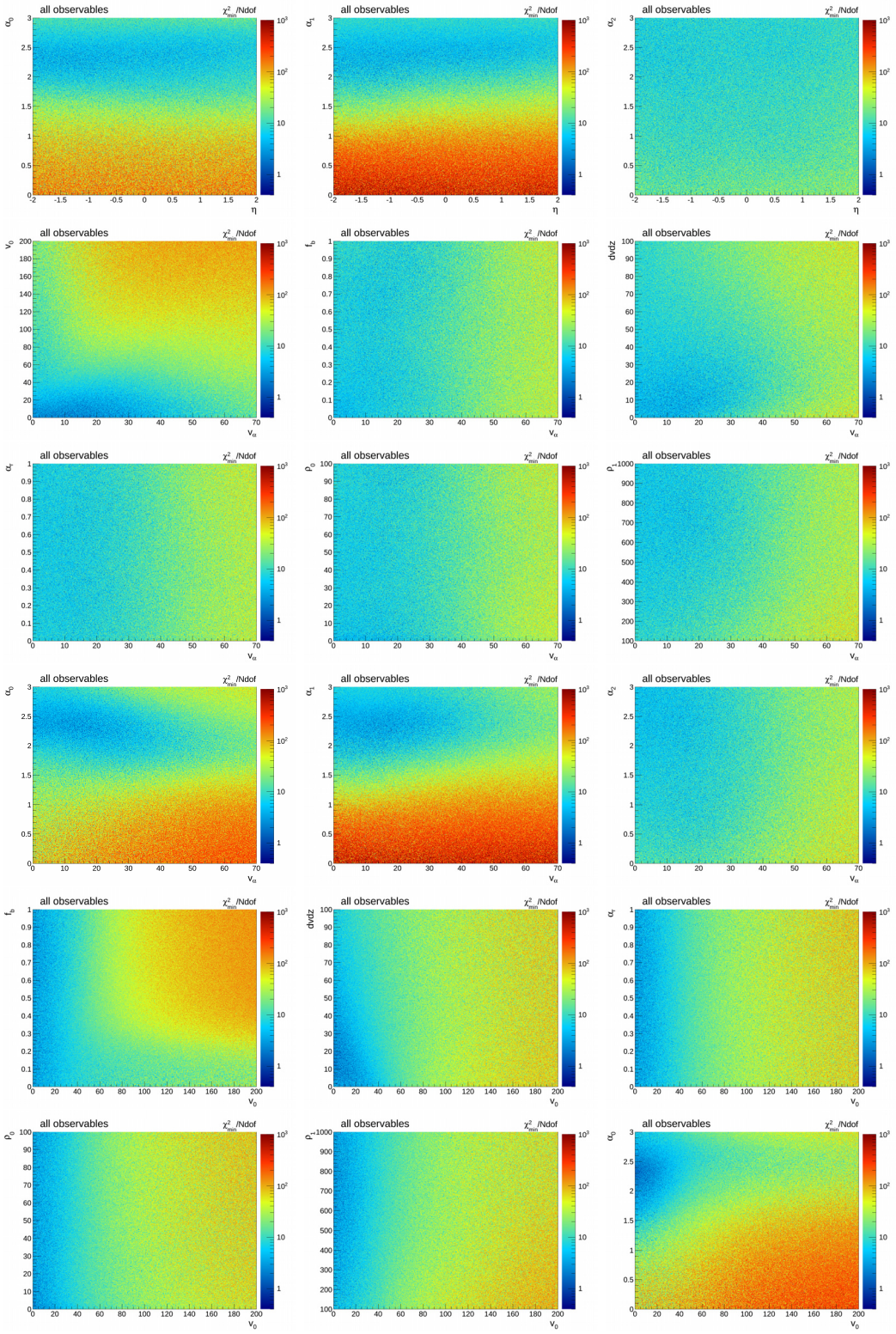

Figure C.18.: Shown is the combined, minimal χ^2 value per degrees of freedom for selected parameter combinations of the 16 dimensional transport model setup (continued on next page).

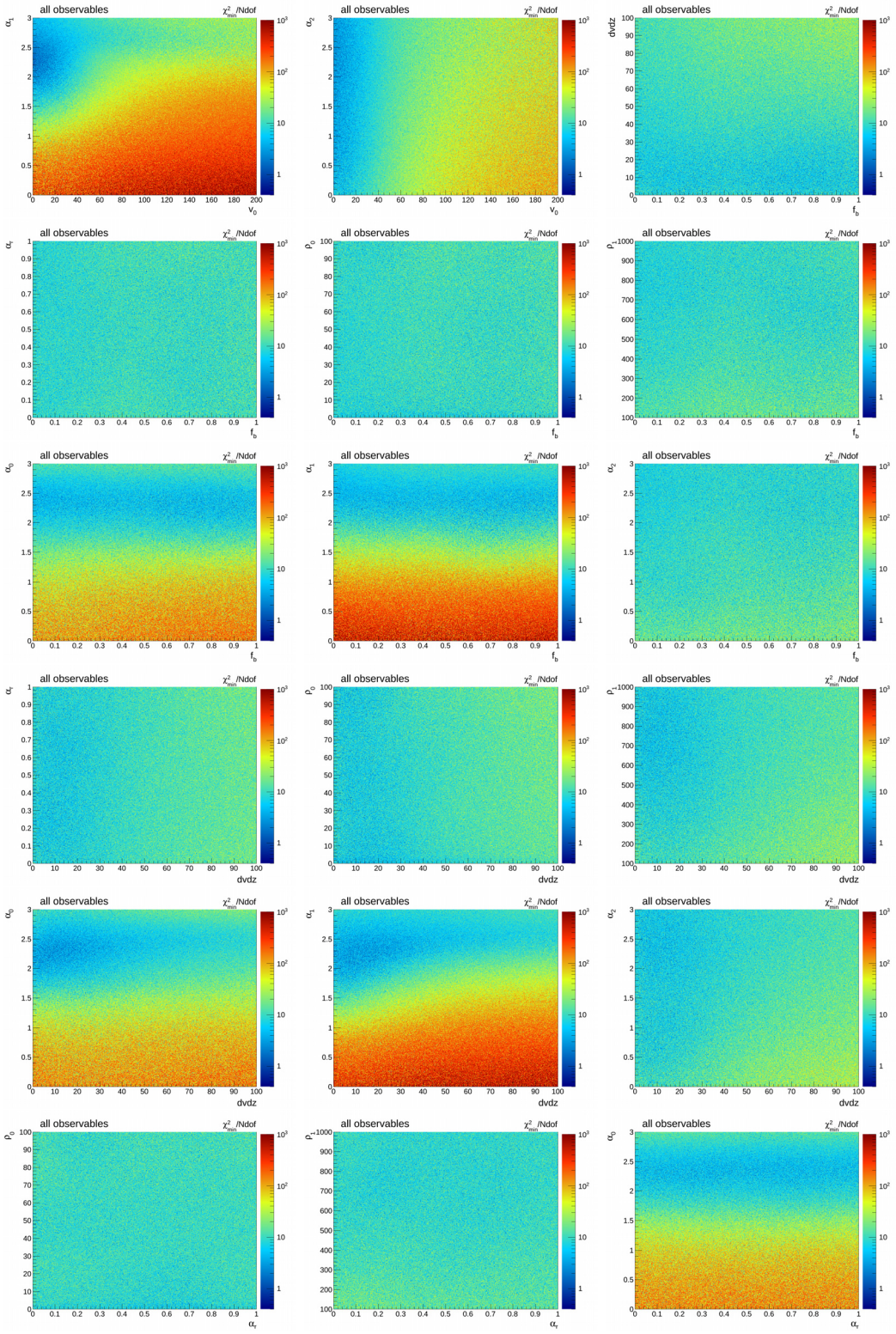

Figure C.19.: Shown is the combined, minimal χ^2 value per degrees of freedom for selected parameter combinations of the 16 dimensional transport model setup (continued on next page).

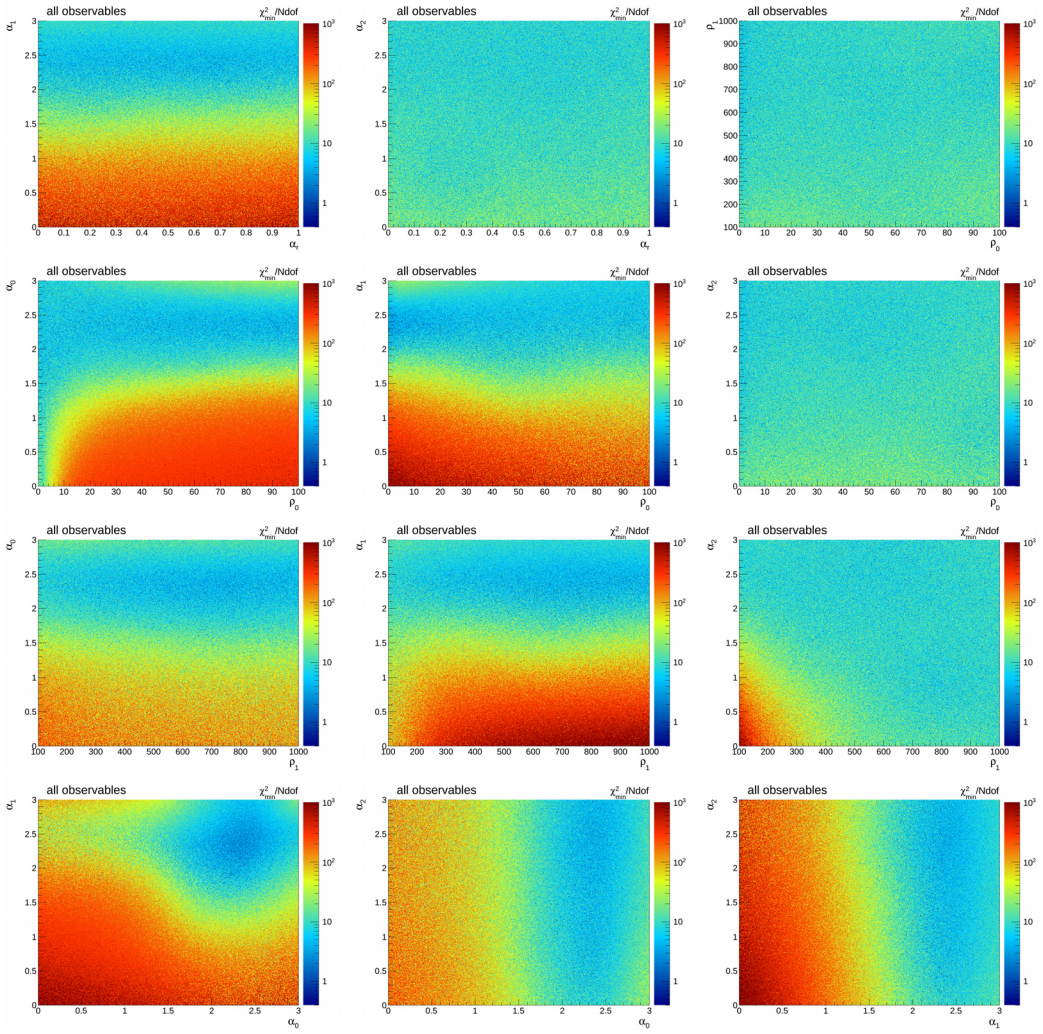

Figure C.20.: Shown is the combined, minimal χ^2 value per degrees of freedom for selected parameter combinations of the 16 dimensional transport model setup.

C.3. Minimal χ^2 of the minimal transport setup separated by observable

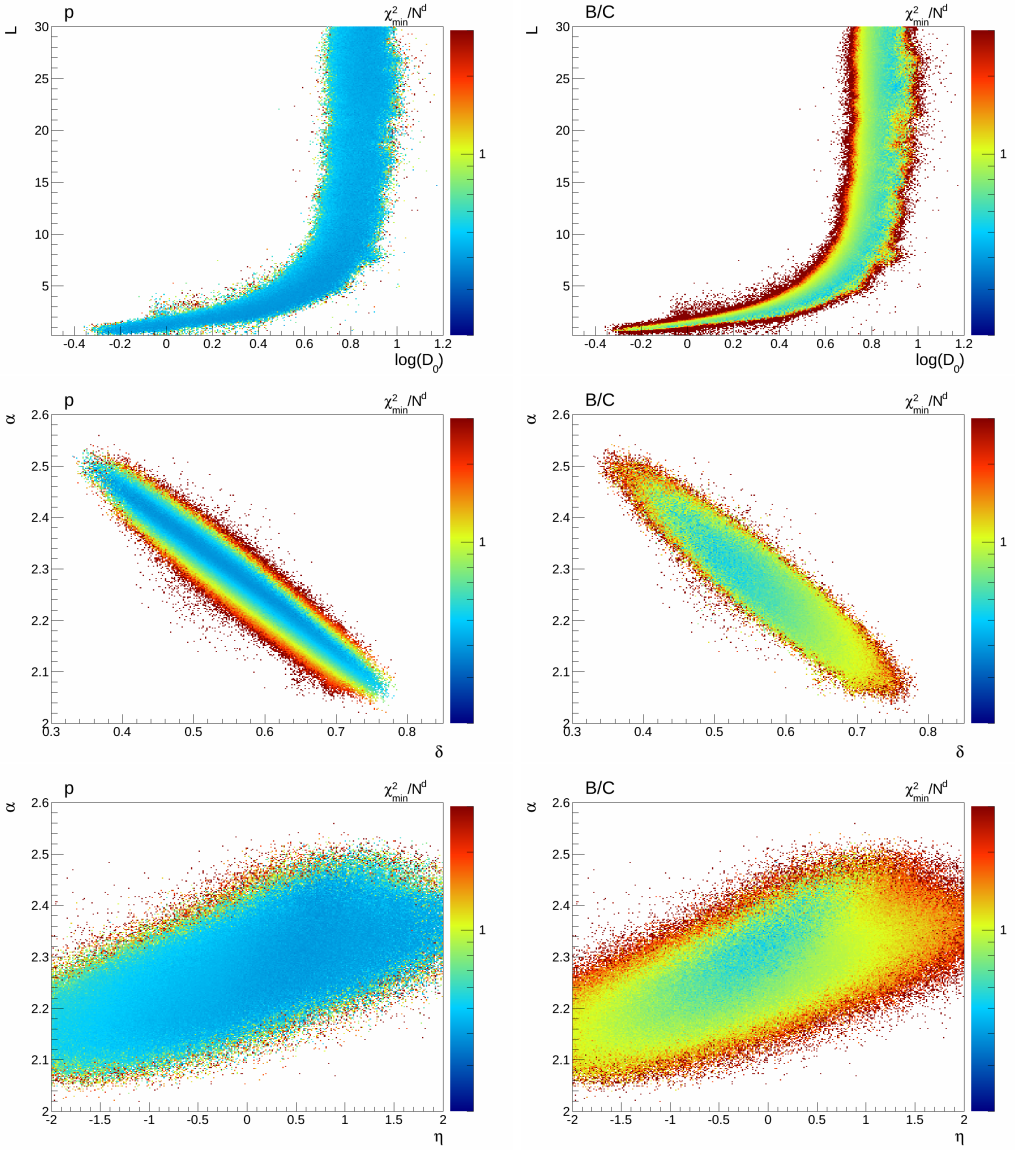

Figure C.21.: Minimal χ^2 per number of data points of the minimal transport setup separated by the proton spectrum **(left)** and the ratio B/C **(right)**

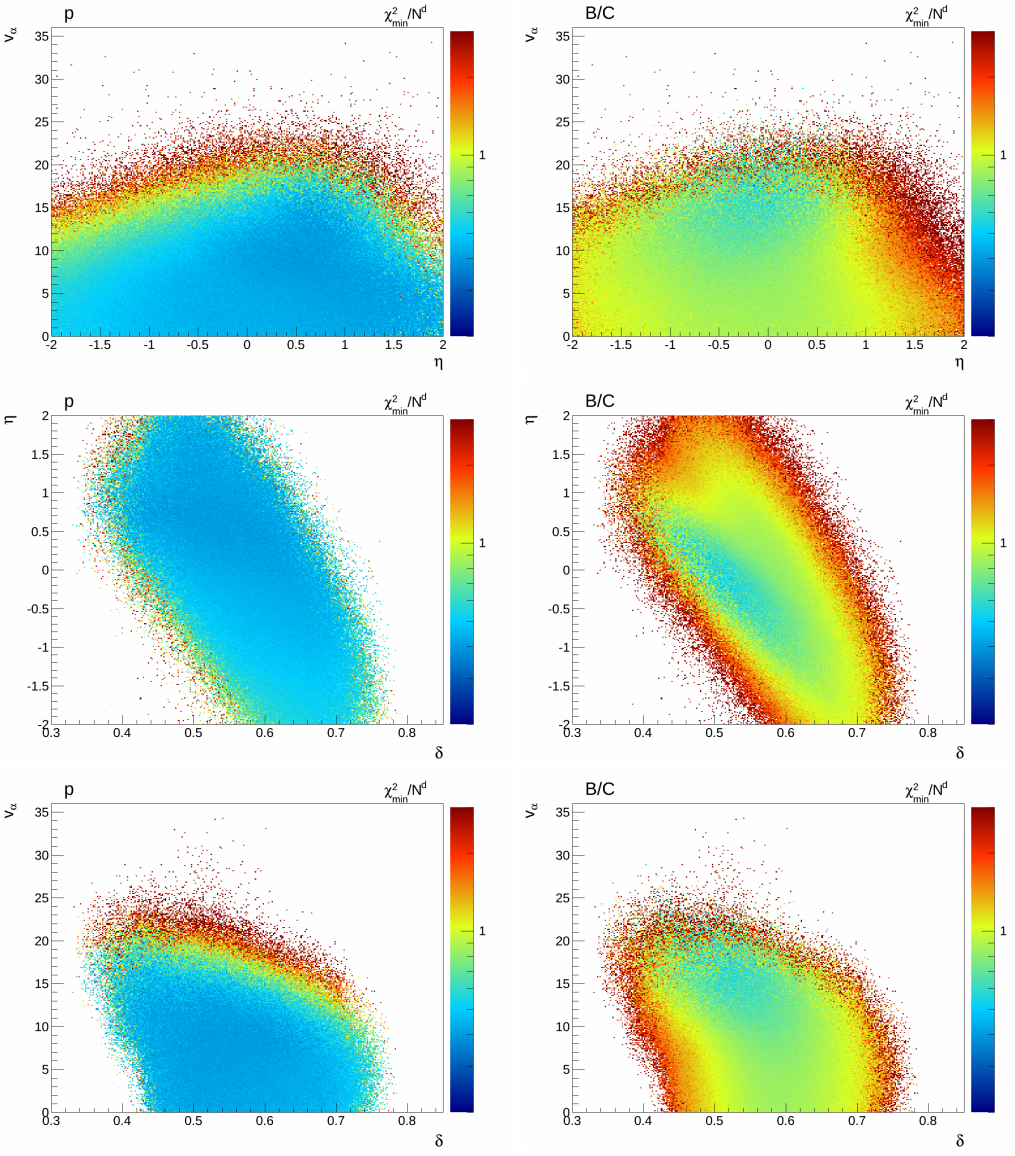

Figure C.22.: Minimal χ^2 per number of data points of the minimal transport setup separated by the proton spectrum **(left)** and the ratio B/C **(right)**

D. Estimation of Synchrotron Energy Losses by Observations

For a correct estimation of synchrotron induced energy losses the parameters of the applied magnetic field (eq. 3.21) were tuned to best match the synchrotron foreground maps of 9-year WMAP data and the Haslam synchrotron map. The positron and electron densities in steady-state derived by solving the transport equation for a reasonable transport model were extended by additional components to describe the electron and positron data measured by PAMELA and the high energy positron fraction measured by AMS-02. The intensity I of the synchrotron emission in particular directions of the sky (l,b) was calculated by the integration of the emissivity $\epsilon(\nu)$ along the LOS for an observer at the solar position:

$$I = \int_{LOS} \epsilon(\nu) ds \tag{7.27}$$

The emissivity $\epsilon(\nu, \gamma)$ for a given synchrotron frequency ν and electron (positron) energy of $E = mc^2\gamma$ is

$$\epsilon(\nu, \gamma) = \sqrt{3}\frac{e^3}{mc^2} BF(x), \tag{7.28}$$

with the regular magnetic field B. $F(x)$ is defined in terms of the modified Bessel function $K_{5/3}$:

$$F(x) = x \int_x^\infty K_{5/3}(x')dx', \tag{7.29}$$

with x defined as $x = \nu/\nu_c$ with

$$\nu_c = \frac{3}{4\pi}\frac{e}{mc} B\gamma^2. \tag{7.30}$$

The calculation is self-consistently performed by applying the same magnetic field strengths for the calculation of the synchrotron emission and the synchrotron energy losses during propagating.
The regions which were considered in the fit are illustrated in fig. D.23. Cutted out are the Galactic Center, the galactic bar as well as the major part of the WMAP-haze: giant bubble shaped regions above and below the Galactic Disc from which an excess of microwave emission with a slightly harder photon spectrum can be observed. These structures were also seen by FERMI in high energetic gamma-rays and became known as the *Fermi Bubbles*. Their origin is ascribed to a fresh CR component which is not considered in the models whereby the relevant sky regions have to be excluded. Although the size of the bubbles may be larger at synchrotron frequencies a spatial template was used which was derived by gamma-ray observations [169] and masks the major part of the bubbles. In addition, a spatial masking of strong point sources was adopted using an exclusion mask[1] provided by [128].
It was found that the parameters of the magnetic field could not be tuned to match the overall observed spectral shape of the synchrotron emission. Variations of the assumed electron and positron densities, still conform with locally measured spectra, were additionally checked but were found to affect the results only marginally compared to the strong influence of the magnetic field. Fig. D.24 shows the results of the best-fit model

[1] `wmap_temperature_source_mask_r9_7yr_v4.fits`

with $B_0 = 10.5$ μG, $r_0 = 7.97$ kpc and $z_0 = 0.79$ kpc. Especially in regions including the Galactic Disc (regions B and C) the demanded spectrum is found to be slightly harder whereby the Haslam data are overestimated. Only at intermediate latitudes and at the galactic poles (regions E and F) the spectral shape is matched reasonably well due to the relatively fast drop of the magnetic field strength with z. Fig. D.25 shows skymaps of the synchrotron emission at 408 MHz, 23 GHz, 41 GHz and 94 GHz for the data, the model prediction and the absolute value of the normalized residual, defined as |data-model|/data. The complexity of the synchrotron sky compared to the simple model becomes apparent. Whereas at 408 MHz the emission in the whole Galactic Disc up to latitudes of 40° is overestimated the emission in the same region is reasonably described at higher frequencies. At those frequencies two structures are visible: the WMAP haze with an increased emission and a large, butterfly-shaped structure at negative longitudes with a reduced emission, overestimated by the model. The synchrotron emission is by far not perfectly described and the results call for a more extensive study. However, this study does not aim to perfectly model the synchrotron emission but rather to estimate the synchrotron induced energy losses during lepton propagation.

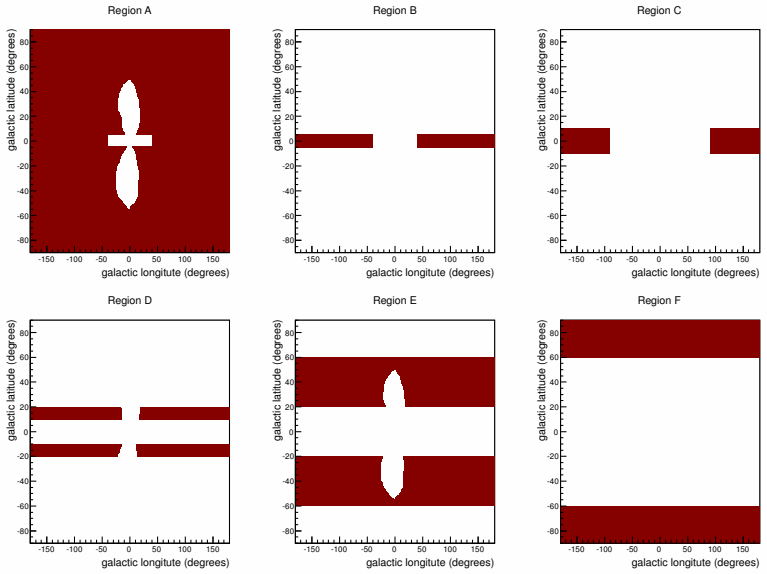

Figure D.23.: The 6 Considered sky regions A-F for the fit of the magnetic field parameters to match the synchrotron data. The white areas are excluded from the fit, respectively.

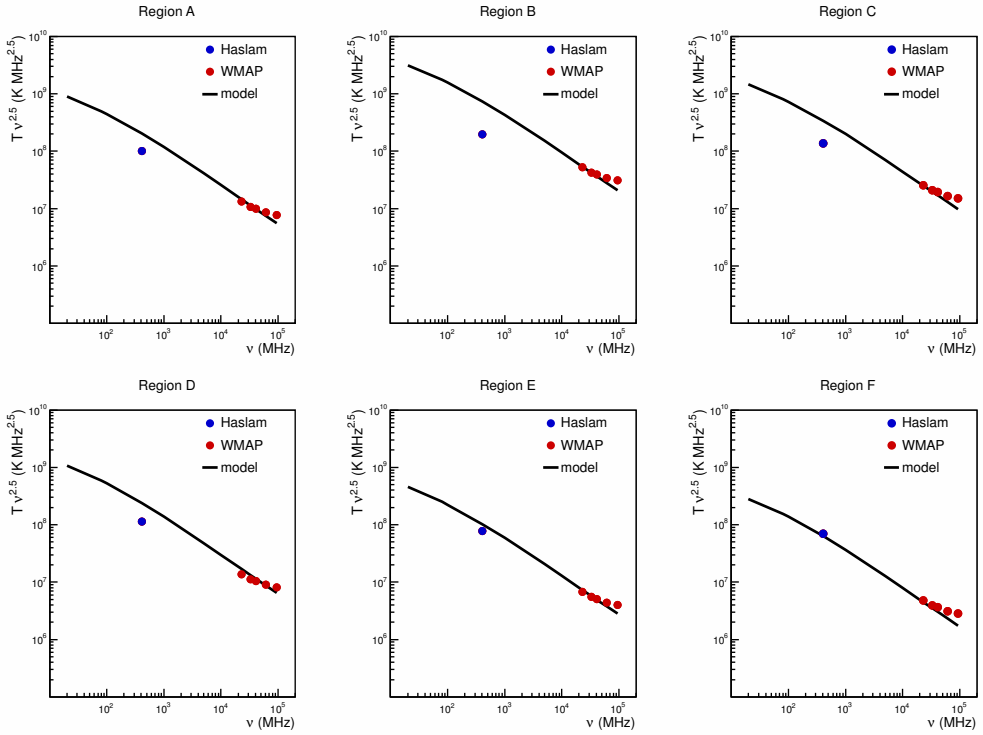

Figure D.24.: Model predictions for the synchrotron spectrum in the 6 sky regions A-F. At low frequencies the emission is overestimated in regions in or close to the Galactic Disc. Above galactic latitudes of 20° the spectral shape is predicted reasonably well. The parameters of the magnetic field for which the best match to the Haslam and WMAP spectra could be achieved are $B_0 = 10.5\ \mu$G, $r_0 = 7.97$ kpc and $z_0 = 0.79$ kpc.

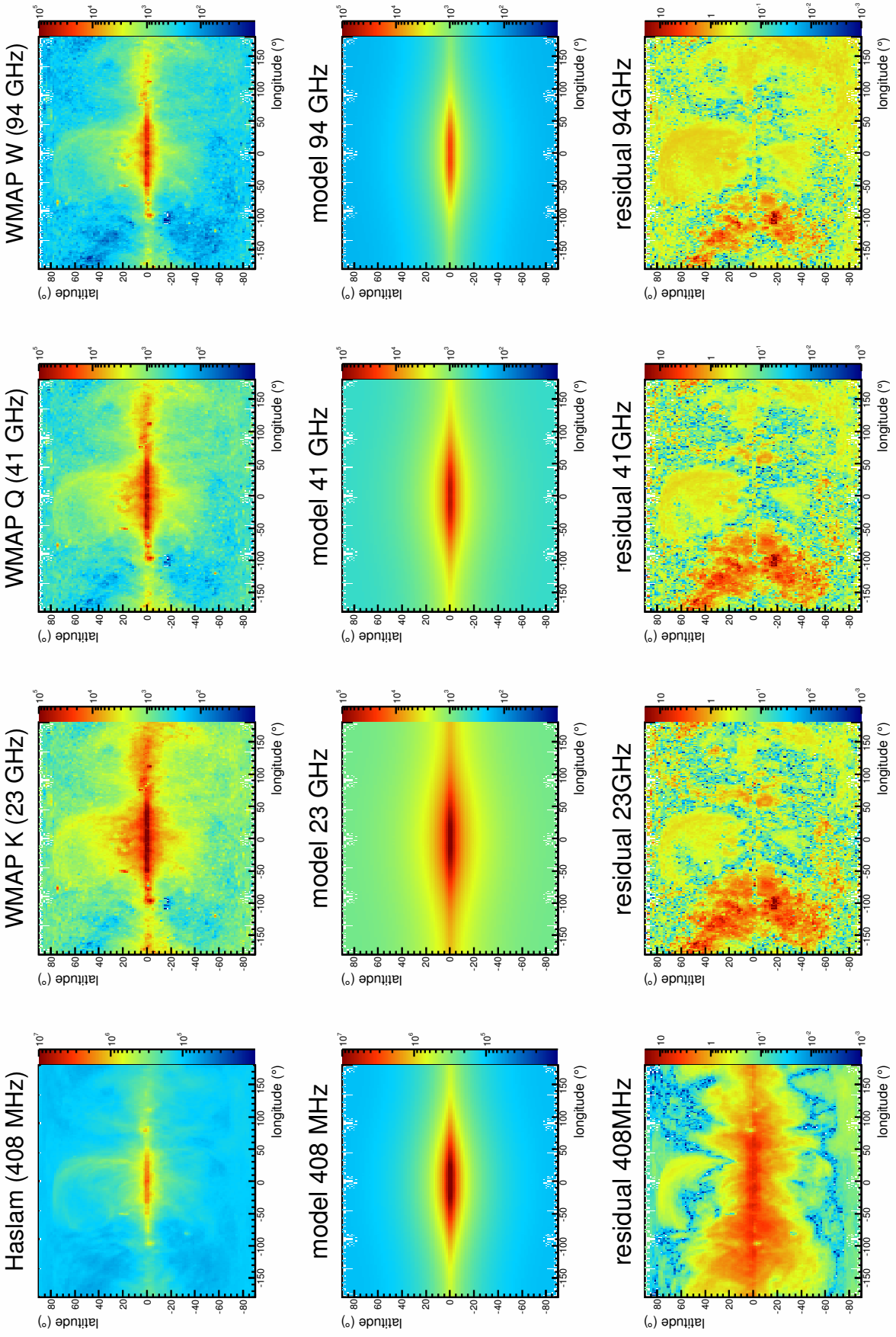

Figure D.25.: Skymaps of the synchrotron emission at 408 MHz, 23 GHz, 41 GHz and 94 GHz. Shown are the data, the model prediction and the absolute value of the normalized residual, defined as |data-model|/data.

E. Anisotropy Computations

E.1. Sum flux of e^+ and e^-

An expression for the anisotropy Δ of a single source in case of isotropic diffusion can be derived by utilizing that the flux F is the first moment of the intensity I with respect to the solid angle $d\Omega$ [174]:

$$\begin{aligned} F(0) - F(\Theta) &= \int I(\Theta) cos(\Theta) d\Omega \\ &= 2\pi \int_0^\pi I(\Theta) cos(\Theta) sin(\Theta) d\Theta, \end{aligned} \tag{7.31}$$

where $F(\Theta)$ is the flux from the direction given by the angle Θ. For a dipole anisotropy with $I = \bar{I}(1 + \Delta cos(\Theta))$ with the mean intensity $\bar{I} = \langle I(\Theta) \rangle$ the expression reads

$$\begin{aligned} F(0) - F(\Theta) &= 2\pi \int_0^\pi \bar{I}(1 + \Delta cos(\Theta)) cos(\Theta) sin(\Theta) d\Theta \\ &= \frac{4\pi}{3} \Delta \bar{I}. \end{aligned} \tag{7.32}$$

The flux in case of isotropic diffusion with the rigidity dependent diffusion coefficient D is given by

$$F(0) - F(\Theta) = D \left| \vec{\nabla} N \right|, \tag{7.33}$$

with the particle number density N. By equalizing equations 7.32 and 7.33 and exploiting the relation between N and $\bar{I}$ given by

$$N = \frac{1}{v} \int I d\Omega = \frac{4\pi \bar{I}}{v}, \tag{7.34}$$

the final expression reads

$$\Delta = \frac{3D}{c} \frac{\left| \vec{\nabla} N \right|}{N}, \tag{7.35}$$

if the particles are assumed to be highly relativistic and the average particle velocity v is approximated to $v = c$. The total anisotropy Δ_{tot} of several sources i is accordingly

$$\Delta_{tot} = \frac{3D}{c} \frac{\sum_i \left| \vec{\nabla} N_i \right|}{\sum_i N_i}. \tag{7.36}$$

E.2. Ratio of e^+ and e^-

For the calculation of the anisotropy of the ratio e^+/e^-, as for instance measured by AMS-02, an approximation is used in which the background contribution is assumed to be isotropic [175]. The fluxes of e^+ and e^-, denoted as F_+ and F_-, can be written as the sum of an isotropic flux $D_\pm$ and a signal S with a dipole anisotropy Δ:

$$\begin{aligned} F_{\pm} &= D_{\pm} + S \\ &= D_{\pm} + S_0(1 + \Delta cos(\Theta)). \end{aligned} \tag{7.37}$$

The flux F_+ can than be expressed as

$$F_+ = (D_+ + S_0)(1 + \frac{S_0}{D_+ + S_0})\Delta cos(\Theta). \tag{7.38}$$

With the definitions

$$\begin{aligned} d_+ &= \frac{S_0}{D_+ + S_0} \\ r_+ &= \frac{D_+ + S_0}{D_- + S_0}, \end{aligned} \tag{7.39}$$

the ratio of the fluxes F_+/F_- is

$$\frac{F_+}{F_-} = r_+ \frac{1 + d_+ \Delta cos(\Theta)}{1 + d_+ r_+ \Delta cos(\Theta)}. \tag{7.40}$$

With the approximation $d_+ \ll 1$ the ratio can be expressed as

$$\frac{F_+}{F_-} = r_+ \left[1 + (1 - r_+) d_+ \Delta cos(\theta)\right] \tag{7.41}$$

and the effective dipole anisotropy for the ratio Δ_{e^+/e^-} can be identified as

$$\Delta_{e^+/e^-} = (1 - r_+) d_+ \Delta. \tag{7.42}$$

F. Illustration of Selected Dark Matter Annihilation Models

Scans of the DM particle mass between 0 and 1 PeV/c^2 were performed and the scaling of the resulting, characteristic electron, positron and antiproton spectra were optimized to the data. The χ^2 calculation includes the complete energy range of lepton sum flux and the positron fraction as measured by AMS-02 and antiproton measurements by PAMELA. The large $\chi^2/Ndof$ values for various masses and optimized branching fractions are shown in fig. 5.16 and point out, that none of the models is able to describe the spectral shape of the lepton data in the whole energy range without violating constraints from the antiproton flux.
Three models will be shown exemplarily: A leptophilic model including annihilations into $e^{\pm}$ and $\tau^{\pm}$ (fig. F.26), the best-fit model which includes additionally annihilations into $b\bar{b}$ (fig. F.27) and a model including annihilations into gauge bosons and quarks optimized to the lepton data (fig. F.28). The latter predicts a large amount of antiprotons by which the PAMELA data are dramatically overshot and the model is strongly disfavoured.

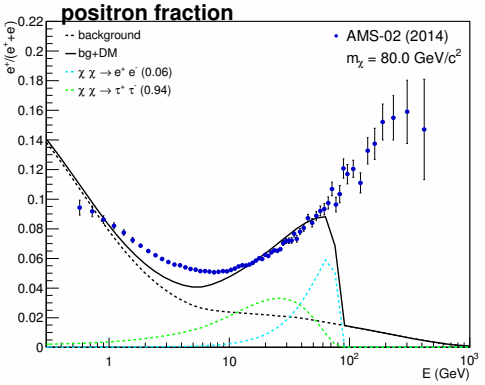

Figure F.26.: Leptophilic DM model with a particle mass of 80 GeV/c^2 and its poor description of the positron fraction. An additional annihilation into $\mu^{\pm}$ as also allowed in leptophilic models was found to not improve the fit. Leptophilic annihilation scenarios with DM masses of the order of 100 GeV/c^2 can therefore explain an increase in the positron fraction but can not account for the made observations in the whole energy range.

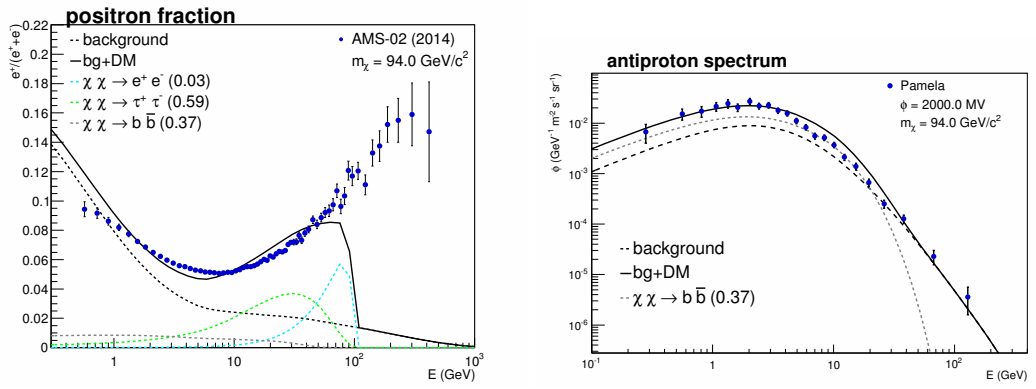

(a) (b)

Figure F.27.: Best-fit model optimized to the lepton data in the whole energy range and constraints from antiprotons. Compared to a the leptophilic model an additional annihilation into $b\bar{b}$ was found to improve the fit at energies of a few GeV. Even though the low energy antiproton data can be matched by assuming an exceedingly high modulation potential of 2000 MV, the intermediate data are overshot and constrain the contribution from $b\bar{b}$ annihilations.

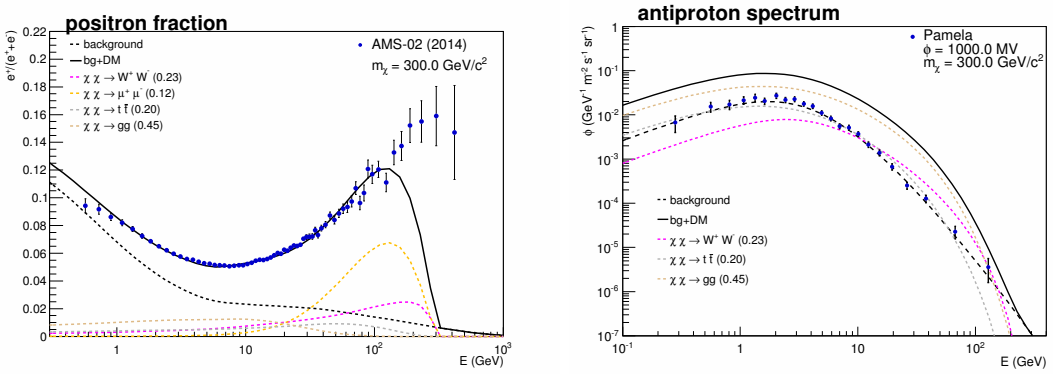

(a) (b)

Figure F.28.: DM annihilation model into leptons, gauge bosons and quarks with a DM particle mass of 300 GeV/c^2. While the positron fraction can be well reproduced up to energies of around 100 GeV, the antiproton flux as measured by PAMELA is dramatically overshot.

G. X_{CO} factor and Gamma-Ray Latitude Profiles

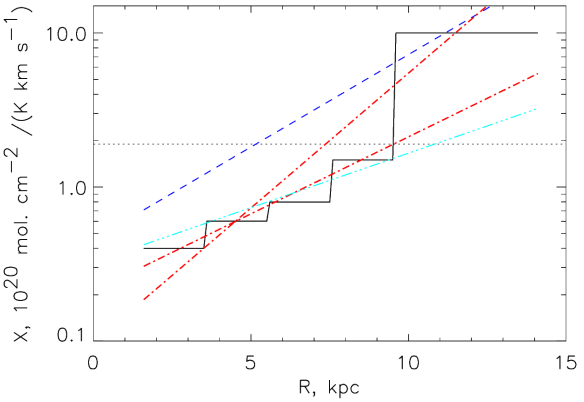

Figure G.29.: The calibration ratio X_{CO} as a function of the galactocentric radius. In [165] a radial rise of X_{CO} (solid black line) was assumed to explain the gamma-ray data. At around 10 kpc a sharp rise had to be adopted. In the present work a constant value of $X_{CO} = 1.9 \cdot 10^{20} \mathrm{cm}^{-2}(\mathrm{K\,km\,s}^{-1})^{-1}$ (dashed black line) is assumed. The colored lines represent models used by other groups. Figure taken from [165].

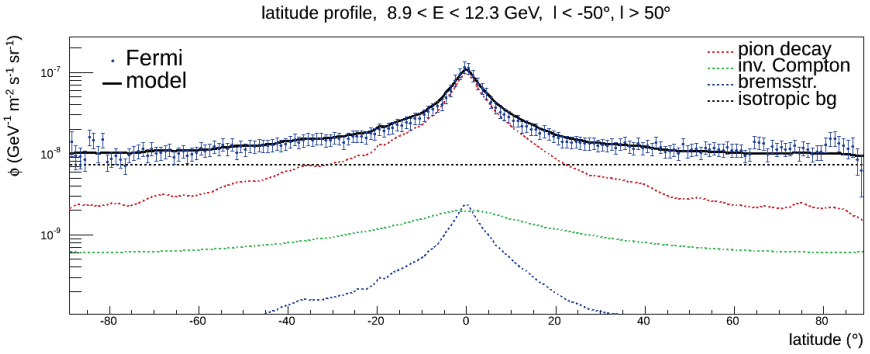

(a)

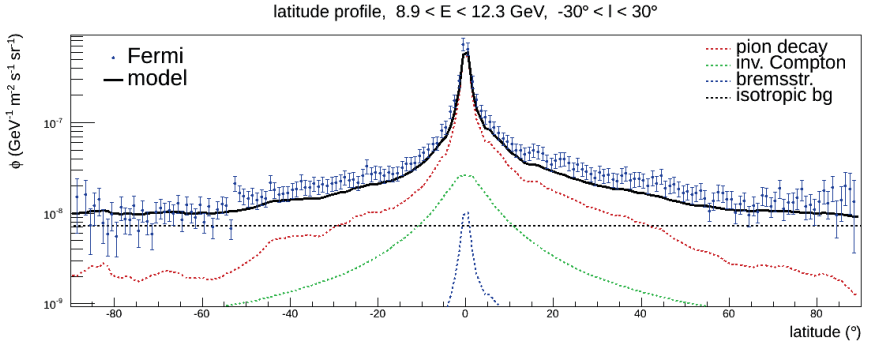

(b)

Figure G.30.: Latitude profile of the gamma-ray and nuclei optimized model. In **(a)** the profile is shown for $|l| > 50°$ and the data are well described by the model. In **(b)** the profile is shown for $|l| < 30°$ where the profile is influenced by the *Fermi Bubbles*. While for $|b| > 55°$ the data can be matched, the flux is underestimated for $|b| < 55°$ due to an increased gamma-ray emission originating from the bubbles. The height of the bubbles determined by the FERMI-LAT collaboration is around $|b| = 55°$ [176] in agreement with this analysis.